

# **MENISCUS TISSUE ENGINEERING WITH NANOFIBROUS SCAFFOLDS**

**Brendon M. Baker**

A Dissertation

in

Bioengineering

Presented to the Faculties of the University of Pennsylvania

in

Partial Fulfillment of the Requirements for the

Degree of Doctor of Philosophy

2010

## **Supervisor of Dissertation**

---

Dr. Robert L. Mauck  
Assistant Professor of Orthopaedic Surgery and Bioengineering  
University of Pennsylvania

## **Graduate Group Committee Chairperson**

---

Dr. Susan S. Margulies  
Professor of Bioengineering  
University of Pennsylvania

## **Dissertation Committee**

Dr. Jason A. Burdick, Associate Professor of Bioengineering,  
University of Pennsylvania

Dr. Dawn M. Elliott, Associate Professor of Orthopaedic Surgery and Bioengineering,  
University of Pennsylvania

Dr. G. Russell Huffman, Assistant Professor of Orthopaedic Surgery,  
University of Pennsylvania

Dr. Marc E. Levenston, Associate Professor of Mechanical Engineering,  
Stanford University

**MENISCUS TISSUE ENGINEERING WITH NANOFIBROUS  
SCAFFOLDS**

COPYRIGHT

2010

Brendon M. Baker

## ***ACKNOWLEDGEMENTS***

I'd like to thank first and foremost my advisor, Rob. If I have achieved anything as a graduate student, the credit is due entirely to Rob, who has been both a tremendous mentor and a steadfast friend to me. Rob identified in me some potential, and he spent his time and energy driving me to become something (which I admit has been no easy task, as I've often arrived at Rob's destination with my arm twisted behind my back). For five years, Rob has been a persistent source of motivation, inspiration, and education for me. He has always stood behind me, pushing me to aim higher, work harder, and achieve more. The small handful of decent ideas I've had have stemmed from my impassioned discussions with Rob, who has always welcomed argument (one of my few talents). Lastly, Rob has taken great efforts to educate me not only in conducting quality science ethically, but also in dealing with the realities of life with patience and poise. If in the future I should achieve any degree of success, I will not forget that it was Rob who tilled the soil, planted the seed, and watered the plant.

I would like to express my gratitude to the other members of my thesis committee: Drs. Jason Burdick, Marc Levenston, Dawn Elliott, and Russ Huffman. Each of these individuals has contributed in critical ways to this work, and on a larger scale, to my development as a scientist. As I move on to the next phase of my life, I'm grateful to know that I can rely on each of them for career guidance, scientific advice, and words of encouragement. Dr. Louis Soslowsky and Barb Gibson have kept the McKay ship afloat, often times in the most literal of senses. Lou has demonstrated the character of a leader needed to keep such a large and dissimilar group of people working in harmony. Barb

has been a constant reminder of the meaning of duty and of taking one's job seriously. Without her dedication, efficiency, and ability to confront facilities, my life as a graduate student would have been a whole lot more difficult.

I have had the great fortune of working with a slew of talented and dedicated undergraduate students. Without their contributions, this thesis would be considerably shorter. In chronological order, I've been incredibly lucky to be joined by the likes of Robert Metter, Ashwin Nathan, Giana Montero, and Amy Silverstein. Metter worked diligently at establishing the composite scaffold system, laying down the pilot work that motivated more than a third of this thesis. Giana and Amy have both been instrumental in the long-term studies using sacrificial fibers, which unexpectedly has proven to be the most difficult project I've undertaken. Without their persistence, patience, and encouragement, I probably would have given up. Lastly, I must make special mention of Ashwin, who has been more than an undergraduate research assistant, but also a great friend and a precious outlet for my competitive side. Ashwin has endured me the longest, joining the lab as a freshman and remaining until the very week he departed for Harvard-MIT to pursue an MD. Importantly, he has kept me in check and served as a constant reminder of the definition of being humble. At literally the top of many of his classes, I never once heard him brag or speak proudly of his accomplishments (with the exception of that one time he beat me at wall-ball). I thank all of the undergraduates I've worked with for being patient with me, and entertaining my obsessive compulsive disorder. I hope in some way I've had a positive impact on the lives of these young people, and I wish them all the best in their future pursuits.

I'd like to acknowledge several students who saw past my craggy exterior and allowed me the honor of calling them friends. These would include Ling Dong, Sounok Sen, and Albert Gee, and Nelly Andarawis. Each of these people has influenced my productivity as a graduate student through either contributions to the work itself, scientific discussion, or the issuance of encouragement. More importantly, they've been emotional pillars; without their friendships, I would have lost my sanity long ago. It's also been an honor to work alongside a number of McKay denizens, past and present, including Spencer Lake, John Boxberger, Isaac Erickson, Megan Farrell, Lachlan Smith, Daniel Cortes, Minwook Kim, Roshan Shah, Su-Chin Heo, and Tristan Driscoll. Through their dedication and good character, each of these people has served as daily reminders of how a proper scientist should function. I would like to think that I've influenced them reciprocally.

Last, but certainly not least, I'd like to end by acknowledging and thanking my two closest friends, Alice Huang and Nandan Nerurkar. I often reflect on how lucky I was to have met and joined Rob, but the probability of sharing my PhD experience with not one but two people who should become my best friends is imponderably smaller. These two have meant an incredible amount to me and without them, I'm certain I would not have made it. They have always been there for me, whether it be to discuss data, edit papers, provide advice, or simply listen to me whine. They are the very definition of the scientist I strive to be, and I am eternally grateful that they have stood in my corner for the past five years.

## ***ABSTRACT***

### **MENISCUS TISSUE ENGINEERING WITH NANOFIBROUS SCAFFOLDS**

Brendon M. Baker

Robert L. Mauck

The fibrocartilaginous menisci dwell between the articular surfaces of the knee and play a central role in joint function. Damage through trauma or degenerative changes is a common orthopaedic injury, disrupts the meniscus mechanical function, and leads to the precocious development of osteoarthritis. The current standard of treatment is removal of the damaged tissue, a procedure that does not re-establish normal knee mechanics. Given the frequency of meniscal injury, a restorative repair strategy remains a major unmet need in orthopaedic medicine. With the goal of replacing damaged meniscus with engineered biologic tissue that can restore meniscal function, this work focuses on scaffolds composed of aligned biocompatible and biodegradable nanofibers that mimic the length-scale and organization of fibrous tissues.

The highly ordered extracellular matrix of the meniscus is primarily composed of co-aligned collagen fibers, enabling the tissue to bear the high tensile loads seen with normal joint loading. To explore the use of nanofibrous scaffolds for engineering fibrocartilage, the effect of nanofiber alignment on the organization of cells and cell-deposited collagen was investigated. Cells seeded on randomly organized nanofibers produced disorganized

collagen, but on co-aligned nanofibers, collagen deposition was observed to occur parallel to the nanofiber direction. With the ability to generate organized collagenous tissues via nanofiber alignment, the remainder of this work focused on optimizing the combination of scaffold, relevant cell type, and inducers of tissue formation. Towards improving the functionality of aligned nanofibrous scaffolds, composites of multiple polymer fibers were investigated. Additionally, the tissue forming potential of cells isolated from human sources was examined in a nanofibrous context. Finally, the effect of modulating the mechanical environment on tissue formation was examined through cyclic tensile loading of nanofiber-based tissues.

Overall, this thesis establishes a novel approach to engineering meniscal fibrocartilage. Using a multi-pronged approach, the formation of fibrocartilage was optimized through scaffold design, cell source selection, and modulation of the mechanical environment. This work represents a significant advance in meniscus tissue engineering, and has bearing on other fibrous, anisotropic tissues such as the temporomandibular fibrocartilage, annulus fibrosus of the intervertebral disc, as well as tendon and ligament.

# **TABLE OF CONTENTS**

<b>ACKNOWLEDGEMENTS .....</b>	<b>iii</b>
<b>ABSTRACT.....</b>	<b>vi</b>
<b>LIST OF FIGURES .....</b>	<b>xiii</b>
<b>LIST OF TABLES .....</b>	<b>xxx</b>
<b>CHAPTER 1: INTRODUCTION.....</b>	<b>1</b>
<b>CHAPTER 2: BACKGROUND .....</b>	<b>8</b>
<b>2.1 Structure, Composition, and Function of the Meniscus.....</b>	<b>8</b>
2.1.1 Anatomy and Extracellular Matrix of the Meniscus.....	8
2.1.2 Mechanical Properties of the Meniscus .....	10
2.1.3 Physiologic Loading of the Meniscus.....	13
<b>2.2 Meniscal Injury and Current Treatment .....</b>	<b>14</b>
2.2.1 Meniscus Damage and Healing .....	14
2.2.2 Meniscectomy .....	16
2.2.3 Surgical Methods for Meniscus Repair.....	17
2.2.4 Meniscus Allografts.....	18
2.2.5 Enhancing Endogenous Repair.....	19
<b>2.3 Tissue Engineering of the Knee Meniscus .....</b>	<b>20</b>
2.3.1 Motivation for a Tissue Engineering Strategy for Meniscal Repair .....	20
2.3.2 Biomaterials for Meniscus Tissue Engineering .....	21
2.3.3 Cell Sources for Meniscus Tissue Engineering .....	22
2.3.4 Current Limitations in Meniscus Tissue Engineering .....	24
<b>2.4 Electrospinning .....</b>	<b>25</b>
2.4.1 Overview of Electrospinning .....	25
2.4.2 Electrospinning Synthetic and Natural Polymers .....	27
2.4.3 Optimization of Electrospinning Parameters .....	28
2.4.4 Inducing Anisotropy in Nanofibrous Scaffolds .....	30
<b>2.5 Nanofibrous scaffold mechanical characterization.....</b>	<b>32</b>
2.5.1 Mechanical Properties of Nanofibrous Assemblies.....	32
2.5.2 Uniaxial Tensile Testing of Fibrous Assemblies.....	34
<b>2.6 Summary.....</b>	<b>36</b>
<b>CHAPTER 3: THE EFFECT OF NANOFIBER ALIGNMENT ON THE MATURATION OF ENGINEERED MENISCUS CONSTRUCTS .....</b>	<b>38</b>
<b>3.1 Introduction.....</b>	<b>38</b>
<b>3.2 Materials and Methods.....</b>	<b>41</b>
3.2.1 Nanofibrous Scaffold Production .....	41
3.2.2 Cell Isolation and Expansion .....	41
3.2.3 Scaffold Seeding and Culture .....	42
3.2.4 Visualization of Cell-Scaffold Interactions .....	43
3.2.5 Mechanical Testing.....	44
3.2.6 Biochemical Content.....	44

3.2.7	Histological Analysis .....	45
3.2.8	Statistical Analysis.....	45
<b>3.3</b>	<b>Results .....</b>	<b>46</b>
3.3.1	Scaffold Characterization and Cellular Interactions .....	46
3.3.2	Biochemical Content of Cell-Laden Scaffolds .....	47
3.3.3	Histologic Appearance of Cell-Laden Scaffolds .....	53
3.3.4	Tensile Mechanical Properties of Cell-Laden Scaffolds .....	56
<b>3.4</b>	<b>Discussion.....</b>	<b>58</b>
<b>3.5</b>	<b>Conclusions.....</b>	<b>62</b>

**CHAPTER 4: SELECTIVE REMOVAL OF SACRIFICIAL FIBERS IMPROVES CELL INFILTRATION IN COMPOSITE FIBER-ALIGNED NANOFIBROUS SCAFFOLDS .....** **63**

<b>4.1</b>	<b>Introduction.....</b>	<b>63</b>
<b>4.2</b>	<b>Materials and Methods.....</b>	<b>68</b>
4.2.1	Formation of Single-Polymer and Composite Nanofibrous Scaffolds ..	68
4.2.2	Visualization of Sacrificial Fiber Removal.....	70
4.2.3	Mechanical Testing of Single-Polymer and Composite Scaffolds .....	71
4.2.4	Cell Seeding and Tissue Culture.....	72
4.2.5	Assessment of Cell Infiltration .....	73
4.2.6	Composite Scaffold Model .....	74
4.2.7	Statistical Analysis.....	74
<b>4.3</b>	<b>Results .....</b>	<b>75</b>
4.3.1	Production and Evaluation of Composite Nanofibrous Scaffolds .....	75
4.3.2	Tensile Properties of Single- and Dual-Polymer Composite Scaffolds	76
4.3.3	Tuning Scaffold Composition and Mechanics.....	79
4.3.4	MSC Infiltration with Increasing Sacrificial Content.....	80
4.3.5	Modeling Pore Size in Composite Scaffolds with Increasing Sacrificial Content.....	83
<b>4.4</b>	<b>Discussion.....</b>	<b>85</b>
<b>4.5</b>	<b>Conclusions.....</b>	<b>91</b>

**CHAPTER 5: TUNABLE NANOFIBROUS COMPOSITES WITH SACRIFICIAL CONTENT ENHANCE CELLULAR COLONIZATION AND FUNCTIONAL TISSUE FORMATION .....** **92**

<b>5.1</b>	<b>Introduction.....</b>	<b>92</b>
<b>5.2</b>	<b>Materials and Methods.....</b>	<b>96</b>
5.2.1	Fabrication of Nanofibrous Composites with Sacrificial Content .....	96
5.2.2	Tissue Culture .....	98
5.2.3	Mechanical Testing of Single-Polymer and Composite Scaffolds .....	99
5.2.4	Biochemical Content.....	100
5.2.5	Subcutaneous Implantation.....	100
5.2.6	Histological Analyses .....	101
5.2.7	Statistical Analysis.....	103
<b>5.3</b>	<b>Results .....</b>	<b>104</b>
5.3.1	Fabrication and Mechanics of Sacrificial Fiber Composites .....	104
5.3.2	Culture Conditions for Cell-seeded Sacrificial Fiber Composites.....	106

5.3.3	Effects of Sacrificial Fibers on Matrix Distribution and Content.....	108
5.3.4	Evolution of Mechanical Properties in Sacrificial Fiber Composites.	111
5.3.5	Cell and Matrix Organization with High Sacrificial Fiber Content....	113
5.3.6	In Vivo Colonization After Subcutaneous Implantation .....	116
<b>5.4</b>	<b>Discussion.....</b>	<b>117</b>
<b>5.5</b>	<b>Conclusion .....</b>	<b>124</b>
<b>CHAPTER 6: FABRICATION AND MODELING OF DYNAMIC MULTI-POLYMER NANOFIBROUS SCAFFOLDS.....</b>		
<b>6.1</b>	<b>Introduction.....</b>	<b>125</b>
<b>6.2</b>	<b>Materials and Methods.....</b>	<b>130</b>
6.2.2	Scaffold Fabrication.....	130
6.2.3	Imaging .....	133
6.2.4	Mechanical Testing.....	134
6.2.5	Determination of Fiber Fractions.....	135
6.2.6	Constitutive Modeling of Composites .....	135
6.2.7	Statistical Analyses .....	138
<b>6.3</b>	<b>Results .....</b>	<b>139</b>
6.3.1	Experimental .....	139
6.3.2	Theoretical .....	145
<b>6.4</b>	<b>Discussion.....</b>	<b>148</b>
<b>6.5</b>	<b>Conclusions.....</b>	<b>154</b>
<b>CHAPTER 7: TISSUE ENGINEERING WITH MENISCUS CELLS DERIVED FROM SURGICAL DEBRIS .....</b>		
<b>7.1</b>	<b>Introduction.....</b>	<b>156</b>
<b>7.2</b>	<b>Materials and Methods.....</b>	<b>160</b>
7.2.1	Scaffold Fabrication.....	160
7.2.2	Cell Isolation, Expansion, and Seeding .....	160
7.2.3	Mechanical Testing.....	162
7.2.4	Biochemical Analyses.....	162
7.2.5	Histology.....	163
7.2.6	Statistical Analyses .....	164
<b>7.3</b>	<b>Results .....</b>	<b>164</b>
7.3.1	Cell Isolation, Expansion, and Scaffold Seeding.....	164
7.3.2	Mechanical Properties of MFC-Laden Constructs .....	165
7.3.3	Biochemical Content of MFC-Laden Constructs .....	168
7.3.4	Structure-Function Correlations of MFC-Seeded Constructs.....	171
7.3.5	Histological Analysis.....	174
<b>7.4</b>	<b>Discussion.....</b>	<b>175</b>
<b>7.5</b>	<b>Conclusions.....</b>	<b>180</b>
<b>CHAPTER 8: THE INFLUENCE OF AN ALIGNED NANOFIBROUS TOPOGRAPHY ON HUMAN MESENCHYMAL STEM CELL FIBROCHONDROGENESIS.....</b>		
<b>8.1</b>	<b>Introduction.....</b>	<b>182</b>
<b>8.2</b>	<b>Materials and Methods.....</b>	<b>185</b>

8.2.1	Scaffold Fabrication.....	185
8.2.2	Cell Culture.....	186
8.2.3	Mechanical Testing.....	188
8.2.4	Transcriptional and Biochemical Analyses .....	189
8.2.5	Histology.....	190
8.2.6	Statistical Analyses.....	190
<b>8.3</b>	<b>Results .....</b>	<b>190</b>
8.3.1	Cell Isolation and Expansion .....	190
8.3.2	3D Pellet Culture.....	191
8.3.3	Nanofibrous Constructs .....	194
8.3.4	MSCs from Healthy Donors .....	199
<b>8.4</b>	<b>Discussion.....</b>	<b>200</b>
<b>8.5</b>	<b>Conclusions.....</b>	<b>206</b>
<b>CHAPTER 9: MECHANO-TOPOGRAPHIC MODULATION OF STEM CELL NUCLEAR SHAPE ON NANOFIBROUS SCAFFOLDS .....</b>		<b>208</b>
<b>9.1</b>	<b>Introduction.....</b>	<b>208</b>
<b>9.2</b>	<b>Materials and Methods.....</b>	<b>212</b>
9.2.1	Scaffold Fabrication.....	212
9.2.2	Cell Isolation and Seeding .....	213
9.2.3	Mechanical Loading.....	214
9.2.4	Quantification of Nuclear Morphology .....	216
9.2.5	Statistical Analysis.....	216
<b>9.3</b>	<b>Results .....</b>	<b>216</b>
9.3.1	Mechanical Response of Nanofibrous Scaffolds to Static Tensile Deformation .....	216
9.3.2	Translation of Topographical and Mechanical Cues to Nuclear Deformation.....	218
9.4.3	Temporal Changes in NAR and Orientation Angle.....	222
9.4.4	Cytoskeletal Mediation of Nuclear Changes .....	224
9.4.5	Directional Control of NAR and Orientation Angle.....	227
<b>9.4</b>	<b>Discussion.....</b>	<b>229</b>
<b>9.5</b>	<b>Conclusions.....</b>	<b>234</b>
<b>CHAPTER 10: DYNAMIC TENSILE LOADING IMPROVES THE FUNCTIONAL PROPERTIES OF MSC-LADEN NANOFIBER-BASED FIBROCARILAGE.....</b>		<b>236</b>
<b>10.1</b>	<b>Introduction.....</b>	<b>236</b>
<b>10.2</b>	<b>Materials and Methods.....</b>	<b>241</b>
10.2.1	Scaffold Fabrication.....	241
10.2.2	Cyclic Tension Bioreactor .....	241
10.2.3	Bioreactor Validation and Fatigue Testing.....	243
10.2.4	Cell Isolation, Expansion, and Seeding .....	244
10.2.5	Tensile Loading .....	245
10.2.6	Mechanical Testing.....	245
10.2.7	Biochemical and Gene Expression Analyses.....	246
10.2.8	Statistical Analysis.....	246

<b>10.3</b>	<b>Results .....</b>	<b>247</b>
10.3.1	Bioreactor Validation and Fatigue Loading.....	247
10.3.2	Construct Preculture and Effect of Dynamic Culture Conditions ..	249
10.3.3	Effect of Dynamic Loading on Construct Maturation .....	251
10.3.4	Transcriptional Changes with Dynamic Tensile Loading .....	254
<b>10.4</b>	<b>Discussion.....</b>	<b>255</b>
<b>10.5</b>	<b>Conclusions.....</b>	<b>262</b>
<b>CHAPTER 11:</b>	<b>SUMMARY AND FUTURE DIRECTIONS.....</b>	<b>264</b>
<b>11.1</b>	<b>Summary.....</b>	<b>264</b>
<b>11.2</b>	<b>Limitations and Future Directions .....</b>	<b>269</b>
11.2.1	Identifying shortcomings in MSC fibrochondrogenesis .....	269
11.2.2	Aproximating the Mechanical Environment of the Meniscus .....	273
11.2.3	Dynamic mechanical properties of engineered fibrocartilage .....	276
11.2.4	Tailorable, smart electrospun materials .....	278
11.2.5	Scaling up to anatomic form.....	281
11.2.6	Animal Models of Meniscus Repair .....	286
11.2.7	Outcome assessments for meniscus tissue engineering strategies..	289
<b>11.3</b>	<b>Conclusions.....</b>	<b>Error! Bookmark not defined.</b>
<b>APPENDIX I:</b>	<b>MATLAB SCRIPTS .....</b>	<b>293</b>
11.4	Tensile Stiffness Calculation .....	293
11.5	Cross-sectional Area Calculation.....	296
11.6	Cyclic tension data analysis .....	299
11.7	Compressive Equilibrium Modulus Calculation.....	300
11.8	Simple Model of Composite Scaffolds.....	302
11.9	Nuclear Aspect Ratio and Orientation Determination .....	303
11.10	Semi-quantitative Histology .....	305
11.11	Compilation of Mechanical and VIC2D Strain Data.....	306
11.12	Poisson Ratio Calculation .....	309
<b>APPENDIX II:</b>	<b>RELATED PUBLICATIONS.....</b>	<b>316</b>
<b>APPENDIX III:</b>	<b>RELATED CONFERENCE ABSTRACTS .....</b>	<b>318</b>
<b>BIBLIOGRAPHY .....</b>		<b>323</b>

## **LIST OF FIGURES**

- Figure 2-1: Anatomic location of the meniscus. Anterior (left) and side (right) view of the human knee joint depicting the semi-lunar fibrocartilaginous menisci. Courtesy of [www.aaos.org](http://www.aaos.org). ..... 8*
- Figure 2-2: Collagen organization in the meniscus. A) Image of the bovine knee joint, after transection of the cruciate and collateral ligaments. B) Schematic and drawing of collagen organization within the meniscus. Adapted from (Petersen et al. 1998). ..... 10*
- Figure 2-3: Histological and mechanical analysis of bovine meniscus. A) Hematoxylin and Eosin (H&E) staining shows limited cellularity (purple nuclei) and abundant extracellular matrix (orange). B) Alcian Blue staining for PGs is limited to the interstitial areas outside of dense collagen bundles. C) Dense collagenous matrix of the meniscus visualized through Picrosirius red staining. D) Polarized light microscopy analysis of collagen-stained sections reveals a highly organized network of collagen fibers within the macroscopic circumferential bundles. Scale bars: 50  $\mu\text{m}$ . E) Typical stress-strain response of meniscus samples tested in the circumferential and radial directions. F) The tensile modulus in the circumferential direction is ~6 times higher than that measured in the radial direction. .... 12*
- Figure 2-4: The mechanical role of the meniscus in bearing and distributing loads. A) A simple model of knee joint loading where the menisci are reduced to a single wedge-shaped annulus. With axial loading, the tissue resists radially-directed forces ( $F_r$ ) through the generation of circumferential hoop stresses ( $F_c$ ) with circumferential strains between 2-6%. Adopted from (Shrive et al. 1978). B) Schematics of loading in the intact joint (left) and following total meniscectomy (right). C) Representations of the resulting stress distributions on the underlying articular surface. Adopted from (McDermott et al. 2006). ..... 13*
- Figure 2-5: Meniscus damage and current treatment. A) Depictions of the numerous modalities by which tears occur in the meniscus. Courtesy of [www.jockdoc.ws](http://www.jockdoc.ws). B)*

*Depending on the type and severity of tearing, injured meniscus may be resected via partial or total meniscectomy or repair may be attempted. C) Arthroscopic images of a torn medial meniscus during (left) and following (right) tear resection. .... 15*

*Figure 2-6: Histology of the meniscus with increasing age. H&E staining of adult and fetal meniscus samples show region-specific and age-dependent variations in matrix content, cellularity, and blood vessel distribution. With increasing age, the menisci become less cellular (fewer nuclei) and less vascular (fewer vessels observed), particularly in the inner region. Scale bar: 100  $\mu\text{m}$ . .... 16*

*Figure 2-7: Electrospun scaffolds for meniscus tissue engineering. A) Scanning electron micrograph of bovine mesenchymal stem cells on a non-aligned nanofibrous scaffolds composed of poly( $\epsilon$ -caprolactone) (PCL). B) Schematic of electrospinning device incorporating a rotating collecting mandrel to generate aligned fibrous meshes. C-E) Mandrel velocity (top right) dictates the degree of alignment in forming nanofibrous scaffolds. Scale bars: 10  $\mu\text{m}$ . .... 27*

*Figure 2-8: Optimization of Electrospun Scaffolds. Solution, fabrication, and environmental parameters can be optimized to generate sheets with homogenous fiber populations. Shown in A) are several features that arise when electrospinning conditions are not optimized; \*: bead-like inclusions, large arrow: thick fibers, small arrowhead: thin fibers. Quality control of microstructure is required to ensure homogeneity across production runs. Even when precautions are taken, small changes in fiber properties can yield a range of mechanical properties in the resultant scaffolds. Shown in B) is the modulus of aligned PCL scaffolds produced over ten separate production runs. Note the deviations in mechanical properties within each batch, as well as the scatter of average properties across production runs. Gray area indicates  $\pm 1$  standard deviation for this grouping of scaffolds. .... 30*

*Figure 2-9: Tensile properties of common biodegradable polymers. A) Young's modulus and B) yield strain for non-aligned nanofibrous scaffolds fabricated from a common set of biodegradable polymers. A range of properties can be achieved, but few*

polymers can be distended to greater than 2% elongation. Adapted from (Li et al. 2006) with permission from Elsevier. .... 33

Figure 3-1: Biodegradable scaffolds with sub-micron fiber diameters may be formed with randomly oriented fibers or with a distinct fiber alignment. Fibrous architecture dictates initial cell-scaffold interactions, including shape and polarity. SEM images of acellular (A) non-aligned (NA) and (B) aligned (AL) scaffolds. SEM and fluorescent images of MSCs on NA (C, E) and AL (D, F) scaffolds after one day of culture. Scale bars: 50  $\mu$ m.....47

Figure 3-2: Cell-seeded constructs increase in mass and DNA content with time in culture. Construct mass (A) and DNA content (B) of MFC- and MSC-laden AL and NA nanofibrous scaffolds. \* indicates  $p < 0.05$  vs. day 1 within group for construct mass (bracket indicates all groups at time point); \* indicates  $p < 0.001$  vs. day 1 within group for DNA content,  $n = 5$  per group per time point. .... 49

Figure 3-3: MFCs and MSCs deposit a proteoglycan-rich matrix on NA and AL scaffolds with time in culture. Total s-GAG content per scaffold (A) and s-GAG content normalized to DNA (B) of MFC- and MSC-laden AL and NA nanofibrous scaffolds with time in culture. \* indicates  $p < 0.001$  vs. day 1 within group; # indicates  $p < 0.001$  vs. NA within same cell type at same time point; † indicates  $p < 0.001$  vs. MFC group of same alignment at same time point,  $n = 5$  per group per time point. .... 50

Figure 3-4: MFCs and MSCs deposit a collagen-rich matrix on NA and AL scaffolds with time in culture. Total collagen content per scaffold (A) and collagen content normalized to DNA (B) of MFC- and MSC-laden AL and NA nanofibrous scaffolds with time in culture. \* indicates  $p < 0.001$  vs. day 1 within group; # indicates  $p < 0.001$  vs. NA within same cell type at same time point; † indicates  $p < 0.001$  vs. MFC group of same alignment at same time point,  $n = 5$  per group per time point. .... 51

Figure 3-5: MFCs and MSCs infiltrate nanofibrous scaffolds in a time-dependent fashion, with full colonization occurring between days 42 and 70. H&E staining of cross sections of MSC- (A, C, E) and MFC- (B, D, F) laden AL scaffolds on days 14 (A, B), 42

(C, D), and 70 (E, F). NA scaffolds seeded with MSCs (G) and MFCs (H) on day 70 are shown for comparison. Scale bar: 500  $\mu\text{m}$ . ..... 53

Figure 3-6: Histological staining of collagen and proteoglycan (PG) deposition over the cross sections of cell-laden AL constructs on day 70. MFC- (A,B) and MSC- (C,D) laden AL nanofibrous stained with Alcian Blue (A,C) for PGs and Picrosirius Red (B,D) for collagens. PG deposition is observed throughout the scaffold, while collagen is restricted to the outer two-thirds. Scale bar: 500  $\mu\text{m}$ . ..... 54

Figure 3-7: Scaffold architecture influences the organization of forming neo-tissue with long term culture. Bright-field (A,C) and polarized light (B,D) microscopy images of en face sections of NA (A,B) and AL (C,D) scaffolds seeded with MSCs on day 70. Sections were taken  $\sim 200 \mu\text{m}$  deep to the scaffold surface and stained with Picrosirius Red (PSR) to enhance birefringence of collagen stained areas (orange). Scale Bar: 200  $\mu\text{m}$ . ..... 56

Figure 3-8: Time-dependent changes mechanical properties of cell-laden constructs are dependent on starting scaffold architecture but not cell type. Tensile properties (stiffness: A; modulus: B) of MFC- and MSC-laden AL and NA nanofibrous scaffolds with time in culture. \* indicates  $p < 0.001$  vs. day 1 within group; # indicates  $p < 0.001$  vs. NA within same cell type at same time point;  $n = 5$  per group per time point. .... 57

Figure 4-1: To improve cellular colonization of dense, aligned nanofibrous matrices, composite scaffolds were formed with two populations of interspersed nanofibers. Schematic depicting scaffold fabrication and subsequent removal of a sub-population of sacrificial fibers (green). ..... 67

Figure 4-2: Electrospinning setup for the fabrication of dual-polymer composite nanofibrous scaffolds. (A) Schematic depicting the electrospinning parameters implemented in generating PCL (red), PEO (green), and PCL/PEO composite scaffolds. (B) The electrospinning apparatus in operation with two syringe pumps delivering polymers distributed by 'fanners' along a common rotating mandrel. .... 69

*Figure 4-3: Composite nanofibrous scaffolds can be formed with individual fibers of distinct polymer composition. Removal of one sacrificial fiber population increases scaffold porosity. (A) Fluorescently-labeled PCL (red) and PEO (green) fibers showed pronounced alignment and interspersion. (B) Submersion of scaffolds in an aqueous solution removed the PEO component while the PCL fibers remained intact. SEM images of as-spun (C) and post-submersion (D) composite scaffolds reveal increases in pore size with the removal of sacrificial PEO fibers. Scale bars: 50  $\mu\text{m}$ . . . . . 76*

*Figure 4-4: The tensile properties of composite scaffolds is modulated by both the interspersion of multiple polymer components in distinct fibers, as well as by the removal of sacrificial fiber components. (A) Example stress-strain behavior of pure PCL, pure PEO, and PCL/PEO scaffolds as-spun (AS) and post-submersion (PS). (B) Maximum tensile stress achieved by samples from each group when tested in the fiber direction. (C) Tensile modulus of AS and PS samples from each group tested in the fiber and transverse directions. Note that pure PEO scaffolds dissolved completely upon submersion, and so could not be mechanically evaluated. Diamond-ended lines ( $\blacklozenge$ ) indicate significance with  $p < 0.05$ ; unmarked lines denote no significant difference between groups;  $n = 5/\text{group}$ . . . . . 77*

*Figure 4-5: The composition and tensile properties of composite scaffolds can be tuned along the length of the mandrel. (A) Off-setting spinnerets results in a graded fiber sheet ranging from nominal ( $\sim 5\%$ ) to  $\sim 90\%$  PEO content along the mandrel as determined by PS mass loss. Scaffold % PEO content correlated with maximum stress (B) and modulus (C) when samples were tested in the fiber direction. Correlations were significant with  $p < 0.001$ ;  $n = 3/\text{group}$ . . . . . 80*

*Figure 4-6: Increasing removal of sacrificial fiber content promotes mesenchymal stem cell (MSC) infiltration into composite nanofibrous scaffolds. Gross morphology (top row) and DAPI-stained cross-sections (bottom row) of MSC-seeded scaffolds with varying % PEO contents (% mass loss) after three weeks of in vitro culture. Scale bars: 5mm (top), 500 $\mu\text{m}$  (bottom). . . . . 81*

Figure 4-7: Quantification of MSC infiltration into composite scaffolds as a function of sacrificial fiber content. Corresponding phase (A) and fluorescent (B) images of DAPI-stained construct cross-sections were used to evaluate cellular infiltration into composite scaffolds. (C) The average % infiltration increased in scaffolds above a threshold of ~40% PEO content in the as-spun scaffolds. To quantify cell distribution, infiltration distance was binned with respect to scaffold thickness, as shown in (B). (D) Comparisons of the lowest (~5%) and highest (~60%) PEO content constructs analyzed showed significantly higher fractions of cells within the more central regions of the scaffolds with increased PEO content. (E) The degree of cellular infiltration (as indicated by the % of total cells in each bin) showed a linear correlations with of % PEO content across a range of scaffold compositions. Diamond-ended bars (◆) indicate significance differences observed with  $p < 0.05$ . A total of six samples were analyzed at each level of PEO content..... 83

Figure 4-8: A simple model of composite scaffolds with increasing sacrificial fiber removal shows a reduction in pore number, but an increase in average pore size. (A) Example composite scaffold layers representing scaffolds with 10, 50, and 90% sacrificial PEO fibers. (B) Increasing the PEO fiber fraction decreases the total number of pores (●) while increasing the average pore area (◆). (C) Pore area distribution shifts towards higher pore sizes with increasing PEO content. Data were averaged from 20 model iterations, each with a randomly generated fiber population..... 85

Figure 5-1: Nanofibrous composites were fabricated with a triple-jet electrospinning setup by modulating the balance of fiber sources. Using a custom electrospinning setup (A) capable of co-electrospinning from three unique fiber sources (B), the ratio of PEO to PCL fiber sources (C) was altered to control the content of sacrificial PEO fibers within the slow-degrading PCL scaffold..... 97

Figure 5-2: To improve cellular colonization of dense, aligned nanofibrous matrices, scaffolds were formed with tunable fractions of sacrificial fibers. (A) Schematic depicting scaffold fabrication and subsequent removal of a sub-population of fibers. (B) Slow-eroding poly( $\epsilon$ -caprolactone) (PCL, red) and water-soluble poly(ethylene oxide)

*(PEO, green) fibers were co-electrospun into composites. (C) Upon exposure to a humid environment, PEO fibers began to dissolve and further hydration removed these fibers from the structure completely. (D) By modulating the number of PCL and PEO fiber sources, scaffolds were fabricated with 0%, 20%, 40%, or 60% PEO fibers by mass. SEM images of scaffolds composed of 0% (E) and 60% (F) PEO fibers after hydration. All scales: 10  $\mu$ m..... 105*

*Figure 5-3: Increasing the sacrificial fiber population decreases scaffold mechanical properties and allows cell-mediated stresses to dictate construct form. (A) Tensile modulus of acellular scaffolds with varying initial mass fractions of PEO fibers. (B) Engineered tissues with high sacrificial fiber content buckle and contort over 3 weeks of culture. Custom fixtures (C & D) were employed to maintain the planar shape of constructs during cell culture, enabling samples formed with 60% PEO scaffolds to retain their initial geometry even after 12 weeks (E). (F) Dynamic culture conditions (via continual agitation of media) were necessary for even nutrient distribution across samples within fixtures. All scales: 10mm. .... 107*

*Figure 5-4: Removal of sacrificial fibers promotes cell infiltration and improves the distribution of cell-secreted extracellular matrix. Cross-sections (A) from 0%, 20%, 40%, and 60% PEO constructs were stained with DAPI and Picrosirius Red to visualize cell nuclei (B) and collagen deposition (C), respectively. Scale: 500  $\mu$ m. By week 12, increasing mass fractions of sacrificial PEO fibers led to a higher proportion of cells within the central 50% thickness of constructs (D), and a more homogeneous distribution of collagen through the scaffold depth (E). Bulk biochemical measures revealed increased DNA (F) and collagen (G) content in 60% PEO constructs relative to 0% controls after 12 weeks of culture.  $n=5$ ,  $p<0.05$  compared with time point-matched 0% constructs.....110*

*Figure 5-5: Increasing sacrificial content improved construct tensile properties with time in culture. (A) Tensile modulus of 0%, 20%, 40%, and 60% PEO constructs at weeks 3, 6, and 12. (B) Change in stiffness over 12 weeks of culture. (C) Average stress-*

strain responses of week 12 constructs.  $n=5$ , \*:  $p<0.05$  compared with time point-matched 0% constructs. .... 112

Figure 5-6: Despite the removal of significant fractions of sacrificial fibers from the composites, scaffolds retained their capacity to dictate cell and matrix organization. (A) Sections were collected in the plane of the fibers, approximately 200 $\mu\text{m}$  from the surface of the construct. (B) DAPI-stained nuclei of 60% PEO constructs were elongated and aligned in the direction of the surrounding nanofibers. Scale: 25  $\mu\text{m}$ . Fluorescent images were thresh-holded (C) and nuclear aspect ratio was determined in 12 week 0% and 60% PEO constructs (D). (E) Nuclear (blue) and collagen orientation (red) with respect to the fiber direction was measured in 0% (left) and 60% (right) PEO constructs. Transmission electron microscopy (TEM) revealed cells elongated in the nanofiber direction (F), and robust collagen deposition (G) parallel to the long axes of cells. Box in (F) depicts location of image featured in (G). TEM of construct cross-sections revealed a dense array collagen fibrils perpendicular to the plane of the image in both 0% (H) and 60% (I) PEO constructs. Boxes depict location of insets. Higher order collagen fibrillogenesis (arrows) was evident only in 60% PEO constructs. Scales: 2  $\mu\text{m}$  (F, H, I), 500 nm (G, H & I insets). Asterisks denotes fibrochondrocytes..... 115

Figure 5-7: Host cell colonization of scaffolds improves with increased sacrificial fiber content in a subcutaneous rat model. Cross-sections of 4 week explants DAPI-stained for cell nuclei. Asterisks denote host tissue. Scale: 1mm. .... 117

Figure 6-1: Composite nanofibrous scaffolds containing three distinct fiber populations were fabricated with a custom electrospinning device. A) Schematic of the formation of electrospun scaffolds containing fast, medium, and slow-degrading fiber populations. B) Diagram depicting the temporal evolution of porosity in composite scaffolds that lose fiber elements in a pre-programmed fashion via differing degradation profiles. C) Novel electrospinning device for forming single- and multi-polymer fibrous scaffolds by co-electrospinning from up to three jets onto a common rotating mandrel. D) Fiber morphology in composites imaged via SEM (scale bar: 10 $\mu\text{m}$ ). E) Composites

*fabricated with fluorescently labeled fiber populations show the presence and interspersions of each element (scale bar: 10 $\mu$ m). ..... 132*

*Figure 6-2: Study I: Electrospun PCL, PLGA, and PEO scaffolds have unique stress-strain profiles. When all three elements are combined, the Composite scaffold stress-strain behavior shares characteristics of each constituent. A) Stress-strain profiles of PCL, PEO, PLGA, and Composite scaffolds extended in the fiber direction. Modulus (B) and yield strain (C) for each scaffold (n=5/group). D) Samples from Composite scaffolds removed along the length of the mandrel showed a range of behaviors, dependent upon the relative fractions of PLGA or PCL fibers at each location. .... 141*

*Figure 6-3: Study II: Single- and multiple-fiber population scaffold tensile behavior is modulated by composition and degradation time. A) Stress-strain curves of day 0 PCL, Blend, and Composite scaffolds tested in the fiber direction. Yield strain (B) and modulus (C) of samples tested in the fiber direction over 63 days (n=5/group per time point). D) Modulus in the transverse direction as a function of time (n=5/group per time point). E) Percent mass loss relative to dry, as-formed samples over the 63 day time course (n=5/group per time point). Note that Composite scaffolds on day 0 lose ~22% of their starting mass due to removal of the PEO fiber population during hydration. \*: p<0.01 versus day 0. .... 143*

*Figure 6-4: Characterization of single-fiber population (PCL and Blend) scaffold tensile behavior with a hyperelastic fiber-reinforced constitutive model. Curve fit results (lines) on day 0 are shown along with experimental data (circles) for the transverse (A) and fiber (D) directions. From transverse direction testing, matrix parameters  $\mu$  (B) and  $\nu$  (C) were determined at each time point. These values, coupled with fits to fiber direction data at each time point were used to determine fiber parameters,  $\gamma$  (E) and  $\zeta$  (F). .... 146*

*Figure 6-5: Material parameters from single-component scaffolds successfully predict Composite scaffold behavior. A) Stress-strain curves for Composites tested in the fiber direction. Stress-strain profiles diminished as degradation occurred over 63 days, due to decreasing properties of the Blend fiber population. Model predictions of Composite*

stress response when tested in the fiber direction on days 0 (B), 7 (C), 21 (D), 42 (E), and 63 (F) showed good agreement with experimental measures. Each plot contains all five experimental curves (dotted lines) and the corresponding five model-generated predictions (solid lines)..... 147

Figure 6-6: Simulation of Composite scaffolds of any formulation. A) Stress-strain behavior of PCL/Blend composites (as indicated by the initial mass fraction of Blend fibers,  $\phi^B$ ) on day 0. Note that the color of each line serves only to illustrate the resulting modulus of the curve. B) Behavior of Composites covering the full range of possible PCL/Blend combinations was simulated for as-formed samples and with degradation over time. Modulus for each theoretical composite is denoted both by height as well as color. .... 148

Figure 7-1: Morphological appearance of human MFCs in monolayer and on fiber-aligned nanofibrous scaffolds. (A) Passage 2 MFCs in monolayer on tissue culture polystyrene demonstrate a fibroblast-like morphology. (B) Passage 2 MFC-seeded constructs cultured for one day reveal MFCs elongating in and aligning with the predominant fiber direction of the scaffold. Red: F-actin, white: fibers, blue: nuclei. Scale bar: 50 $\mu$ m..... 165

Figure 7-2: MFC-seeded scaffolds increase in mechanical properties with time in culture in a fibro-cartilaginous medium. (A) Force-elongation plots of five scaffolds either seeded (MFC) or maintained as unseeded controls (USC) on day 70 for Donor 8. (B) Maximum load of seeded scaffolds normalized to that of paired USC scaffolds on day 70 for all ten donors. Donor # is indicated on the x-axis. Data represent the mean and standard deviation of 5 samples per donor. (C) Normalized stiffness (indicating percentage change) of MFC-seeded scaffolds from each donor compared to their paired USC scaffolds at each time point. Donor # (and age) is indicated on the x-axis. .... 168

Figure 7-3: Donor-to-donor variation in time-dependent changes in biochemical composition of MFC-seeded engineered meniscus constructs. (A) Total collagen and (B) total s-GAG accumulation in engineered constructs with time in culture for each donor. Donor # (and age) is indicated on the x-axis. Data represent the mean and standard

deviation of 5 samples per donor per time point. (C) Percent dry weight (% DW) collagen and (D) % DW s-GAG for samples from each of the ten donors on day 70. Gray background in (C) and (D) indicates range of collagen and s-GAG found in 5 native tissue samples. Note the interrupted scale in (C) the % collagen by DW plot. USC constructs processed similarly showed no appreciable background content of s-GAG or collagen..... 171

Figure 7-4: Structure-function-composition correlations for MFC-seeded constructs with time in culture. (A) Total collagen content in constructs correlates well with change in stiffness for all donors at all time points (days 14, 42, and 70). (B) Total GAG content correlates poorly with change in stiffness for all donors at all time points (days 14, 42, and 70). (C) Donor age showed a weak correlation with change in stiffness of constructs on day 70..... 173

Figure 7-5: Histological analysis of constructs from best-case (Donor 8, A,C,E) and worst-case (Donor 6, B,D,F) samples on day 70. DAPI staining of cell nuclei demonstrate infiltration into the outer two-thirds of constructs under best-case conditions (A), and limited infiltration at the periphery under worst-case conditions (B). Similar findings are observed for collagen (C,D) and proteoglycan (E,F) deposition as indicated by Picrosirius Red and Alcian Blue staining, respectively. Scale Bar: 1mm. .... 175

Figure 8-1: MSCs isolated from OA donors are multipotent. MSCs cultured for 3 weeks under control (A, unstained), adipogenic (B, stained with Oil Red O), osteogenic (C, stained with Alizarin Red), and chondrogenic (D, stained with Alcian Blue) conditions. Scale: 100 $\mu$ m (A, C), 50 $\mu$ m (B), 500 $\mu$ m (D)..... 191

Figure 8-2: MSCs readily produce a GAG- and collagen-rich ECM comparable to MFCs in pellet culture. MSCs and MFCs isolated from four OA donors were formed into pellets and cultured in a pro-chondrogenic medium. On days 7 and 21, DNA (A), GAG (B), and collagen (C) contents were determined. Data is presented on a per pellet basis. 4 pellets/n, n=3. D) Representative day 21 MSC and MFC pellets stained for GAG (blue) and collagen (red). Scale: 500 $\mu$ m..... 193

*Figure 8-3: The nanofibrous topography defines cell morphology and modulates gene expression of key matrix constituents. A) Cells were seeded onto aligned nanofibrous scaffolds following the removal of sacrificial PEO fibers in order to hasten cell infiltration. Scale: 10 $\mu$ m. Type I collagen (B) and aggrecan (C) gene expression of MSC and MFC pellets and nanofibrous constructs after 7 days under identical culture conditions. n=4, \*: p<0.05. MSCs (D) and MFCs (E) seeded onto scaffolds (green: F-actin, red: fibers, blue: nuclei). Scale: 25 $\mu$ m..... 195*

*Figure 8-4: MSCs on nanofibrous scaffolds do not proliferate and produce less ECM than donor-matched MFCs. Donor-matched MSC and MFC populations were seeded onto aligned nanofibrous scaffolds and maintained in identical culture conditions. On days 21, 42, and 63, construct DNA (A), GAG (B), and collagen (C) content was determined. n=5, \*: p<0.05..... 196*

*Figure 8-5: Histological examination confirms the disparity in ECM production between MSC- and MFC-laden nanofibrous constructs. Representative cross-sections of MSC (A, B, C) and MFC (D, E, F) nanofibrous constructs on day 63 stained for cell nuclei (A, D), GAG (B, E), and collagen (C, F). Scale: 500 $\mu$ m. .... 197*

*Figure 8-6: Increases in construct biochemical content are paralleled by changes in mechanical properties. A) Tensile stiffness of MSC- and MFC-seeded constructs with time in culture, normalized to unseeded control scaffolds (grey bar). B) Tensile modulus of day 63 constructs and unseeded controls (grey bar). C) Compressive equilibrium modulus of MFC constructs on day 63. Note: MSC constructs and unseeded controls could not be tested in this manner (see Results). n=5 for tensile data, n=3 for compressive data..... 198*

*Figure 8-7: Limitations in the maturation of human MSC-seeded nanofibrous constructs are not dependent on age or disease-status. A) Tensile stiffness of healthy MSC constructs on day 63 normalized to unseeded control scaffolds (grey bar). GAG (B) and collagen (C) content of day 63 constructs. Dotted lines and gray regions represent the average and full range of response of OA MSCs, respectively. Cross-sections of day*

63 Donor 5 MSC-seeded nanofibrous constructs stained for cell nuclei (D), GAG (E), and collagen (F). Scale: 500 $\mu$ m. .... 200

Figure 9-1: Construction and validation of a custom system for prescribing controlled tensile deformation to cell-seeded nanofibrous scaffolds. A & B) Custom device for applying tension to constructs in vitro. C) Texture correlation of a speckled scaffold under 5% applied strain reveals surface strains that are relatively homogenous. D) Average surface strains correlate well with applied deformations (n=6). E) Representative stress (solid line) and strain (dashed line) response of an aligned nanofibrous scaffold held at 10% strain for 2 hours. .... 218

Figure 9-2: The organization of nanofibers dictates the initial morphology of seeded cells. SEM images of non-aligned (A) and aligned (B) PCL nanofibers (scale bar: 10 $\mu$ m). (C) To quantify subcellular morphologic changes, the nuclear aspect ratio (NAR) and orientation angle ( $\theta$ ) were quantified. The NAR was defined as the ratio of the long axis (a) to the short axis (b) of the nucleus and  $\theta$  was defined as the angle between the long axis (a) and the direction of stretch. Representative images of meniscal fibrochondrocytes seeded on NA (D) and AL (E) nanofibrous scaffolds, and AL constructs deformed to 5% (F) and 10% strain (G) (scale bar: 20  $\mu$ m). Cells were fluorescently labeled for F-actin (green) and DNA (blue). .... 219

Figure 9-3: Nuclear morphology and orientation are dependent upon scaffold architecture and applied strain. NAR of MSC- (A) and fibrochondrocyte- (B) seeded NA and AL scaffolds with increasing levels of applied strain (n>500, \*: p<0.05 vs. 0% NA, †: p<0.05 vs. 5% NA, ‡: p<0.05 vs. 0% AL,  $\alpha$ : p<0.05 vs. 5% AL). Dashed lines indicate the NAR of the same cell populations cultured in monolayer. Angular histograms of nuclear orientation of MSC (C) and fibrochondrocyte (D) NA and AL constructs at 0, 5, or 10% strain. The radial axis indicates the percentage of the total cell population and the solid line represents the mean angle of the distribution. .... 221

Figure 9-4: Time dependent nuclear relaxation with static scaffold deformation. A) The % change in NAR (relative to undeformed values) of fibrochondrocyte-seeded constructs at increasing time intervals after application of 10% strain (n>500, \*: p<0.05

vs. 0min, †:  $p < 0.05$  vs. 15min, ‡:  $p < 0.05$  vs. 60min). B) Angular histograms of nuclear orientation prior to stretch, immediately after stretch, and after 15 or 120 minutes ( $n > 500$ )..... 223

Figure 9-5: Selective disruption of cytoskeletal elements does not alter cell morphology on nanofibrous scaffolds. Fibrochondrocytes on AL scaffolds stained for microtubules (A, purple), intermediate filaments (B, red) and F-actin (C, green). Constructs were exposed to nocodazole (D), acrylamide (E), and cytochalasin D (F) to disrupt microtubule, intermediate filament, and F-actin networks, respectively. Additional samples were treated with nocodazole (G) or acrylamide (H) and stained with phalloidin to confirm the removal of these elements did not alter the actin cytoskeleton. All images were counterstained for cell nuclei (blue). Scale bar: 20  $\mu\text{m}$ ..... 225

Figure 9-6: Disruption of the actin cytoskeleton abrogates strain-induced alterations in NAR. MSC- (A) and fibrochondrocyte- (B) seeded constructs were cultured in either control media (CT), or identical media supplemented with nocodazole (NO), acrylamide (AC) or cytochalasin D (CD) prior to the application of 10% strain ( $n > 500$ , \*:  $p < 0.05$  vs. 0% CT, †:  $p < 0.05$  vs. 0% NO, ‡:  $p < 0.05$  vs. 0% AC). NAR was determined immediately after loading. .... 227

Figure 9-7: Alterations in nuclear morphology are dependent on nanofiber stretch. A) Schematic depicting strains applied parallel (//) and perpendicular ( $\perp$ ) to the predominant fiber direction. Fibrochondrocyte-seeded constructs were loaded in either direction in the presence or absence of CD. NAR (B), nuclear area (C), and angular histograms (D) were acquired from DAPI-stained images and normalized to pre-strain values ( $n > 500$ , \*:  $p < 0.05$  vs. 0% //CT, †:  $p < 0.05$  vs. 0%  $\perp$ CT, ‡:  $p < 0.05$  vs.  $\perp$ CD)... 229

Figure 10-1: Tensile bioreactor design. (A) The device consists of a computer programmable stepper motor which drives the opposing motion of two linear stages. (B) These stages are linked to mounting arms designed to engage and distract fixtures containing multiple cell-seeded scaffolds. (C) A heat sink is placed on the motor to remove excess heat during operation in a standard incubator. When not loaded, samples are cultured dynamically on an orbital shaker to ensure even nutrient distribution to

arrays of clamped constructs. (D) Schematics of the tensile bioreactor and fixture assembly.....243

Figure 10-2: Bioreactor validation and fatigue testing of acellular scaffolds. (A) Average surface strains determined by texture correlation of acellular scaffolds preloaded to 1% strain and cyclically loaded to 6% strain at 0.1Hz. Average stress-strain curves (B), tensile modulus (C), and percentage change in stiffness (normalized to nonloaded scaffolds) (D) after two weeks (108,000 cycles) or four weeks (216,000 cycles) of loading to 6% strain at 1Hz (n=6, \*: p<0.05 vs. nonloaded samples). ..... 248

Figure 10-3: Study design. Aligned nanofibrous scaffolds were seeded with MSCs and precultured for an initial six week period under static culture conditions. Following this, samples were either loaded daily or maintained as nonloaded controls for up to an additional four weeks. Constructs were harvested at weeks 6, 8, and 10 for analysis.. 249

Figure 10-4: Effect of dynamic culture and tensile loading on biochemical content. Total DNA (B), GAG (C), and collagen (D) content of MSC-seeded constructs after preculture (week 6), and with up to four weeks of daily cyclic loading (n=6, \*: p<0.05 vs. nonloaded controls, +: p<0.05 vs. precultured constructs). ..... 251

Figure 10-5: Histological assessment of long-term dynamically loaded MSC constructs. Representative cross-sections of precultured samples (week 6), and nonloaded controls and loaded constructs at week 10 stained with DAPI for cell nuclei, Picrosirius Red for collagens, and Alcian Blue for proteoglycans (scale: 500µm)..... 252

Figure 10-6: Mechanical stimulation increases construct tensile properties. (A) Tensile modulus of precultured samples at through week 6, and dynamically loaded constructs or nonloaded controls through week 10. (B) Changes in stiffness normalized to initial (week 0) values (n=6, \*: p<0.05 vs. nonloaded controls, +: p<0.05 vs. precultured constructs). (C) Average stress-strain curves of loaded and nonloaded constructs at the terminal time point, precultured samples at week 6, and acellular controls maintained in PBS for the duration of the study..... 253

Figure 10-7: Modulation of matrix-associated gene expression. Expression of collagen I, collagen II, fibronectin, and lysyl oxidase normalized to GAPDH for precultured samples (week 6) and loaded constructs or nonloaded controls at week 10 (n=6, \*: p<0.05 vs. nonloaded controls, +: p<0.05 vs. precultured constructs)..... 254

Figure 11-1: The effect of growth factors on MSC construct maturation. Tensile stiffness (A) and modulus (B) of adult human MSC-seeded constructs cultured with TGF- $\beta$ 3, bFGF, or a combination of both growth factors. Dashed lines indicate day 0 values. \*: p<0.05 vs day 21. Day 63 cross-sections stained for cell nuclei (C), proteoglycan (D), and collagen (E). Scale: 500 $\mu$ m. .... 271

Figure 11-2: Tension-compression bioreactor. A) Schematics of a combined tension-compression bioreactor featuring a unit culture cell (top left), locations of the tensile and compressive regions (top right), and the overall assembly capable of mechanically loading 24 samples simultaneously (bottom). B) Finite element modeling of scaffolds deformed against a cylindrical post, depicting magnitudes of tensile (left) and compressive (right) stresses..... 275

Figure 11-3: A) Tensile modulus of meniscus and engineered constructs cultured for 0, 50, or 100 days tested in the fiber direction at different strain rates. Average stress-strain response of day 100 constructs (B) and meniscus tissue (C) at each strain rate; note difference in scaling. Bars denote significant comparisons with p<0.05; constructs: n=5/group, tissue: n=10/group. .... 277

Figure 11-4: Benchmarks for the engineering of fibrous tissues. Healthy meniscus tissue tested in the fiber direction produces a non-linear stress-strain response (circles indicate average response; boundaries indicate high and low range of responses from 10 separate samples). Superimposed on this physiologic range are the stress-strain responses of nanofibrous scaffolds of varying polymer composition. .... 280

Figure 11-5: Approximating anatomic form. Fabrication algorithms involving lamellar folding (A) and spot-welding (B) were developed to generate constructs with 3D anatomic form (wedge shape) while preserving the orientation of nanofibers with respect

*to the circumferential collagen fibers of the meniscus. MSC-seeded wedge-shaped constructs took on a meniscus-like appearance after three weeks in culture (C), with collagen deposition occurring between each layer (D). Scale bar: 1 cm..... 283*

*Figure 11-6: Interfacing nanofibrous constructs. Scaffold-scaffold (A, S-S) and scaffold-meniscus (E, S-M) constructs were formed and cultured for up to 9 weeks in vitro. In both cases, mechanical strength of the interface increased with time (B and F), and new matrix was deposited at the interface (C: H&E and D: PSR for S-S constructs, G: H&E and H: PSR for S-M constructs)..... 285*

*Figure 11-7: Direct electrospinning of a wedge-shaped annulus. A) Schematic of a modified collection mandrel for direct electrospinning of meniscus implants. B-D) Images of the novel electrospinning device. E) Formation of a meniscus-shaped scaffold with gradual nanofiber deposition into the wedge-shaped crevice. F) Resulting semi-annular meniscus scaffold depicting the direction of constituent aligned nanofibers.... 286*

*Figure 11-8: Ovine meniscal defect model. A block osteotomy is performed on the medial femoral condyle (A), providing a birds-eye view of the meniscus (B). Using a custom defect tool (C) a 6×6mm portion of the inner medial meniscus is removed (D) and replaced with a suture-ready wedge-shaped construct (E). F) Radiograph of the sheep stifle following reduction of the osteotomy. .... 288*

## **LIST OF TABLES**

<i>Table 3-1: Change in measured parameters (compared to day 1) for two replicate studies of MFC- and MSC-laden AL and NA nanofibrous scaffolds over 70 days in free swelling culture.</i>	48
<i>Table 6-1: Scaffold Fabrication. Polymer formulations used to fabricate composite nanofibrous constructs in Study I and Study II.</i>	130
<i>Table 6-2: Model Validation. R<sup>2</sup> and Bland-Altman limit of agreements from least squares fits of experimental data for single fiber population scaffolds (PCL and Blend). Also shown are metrics comparing Composite scaffold experimental stress-strain response and model predicted values.</i>	147
<i>Table 7-1: Characteristics of Human Donor Tissue: Age, Gender, Tear Type, and Anatomic Location. Surgical debris from a total of ten donors ranging in age from 18-84 years was used in this study. Tissue was derived from seven donors who underwent partial meniscectomy and three who underwent total knee replacement.</i>	161
<i>Table 7-2: Structural and Mechanical Properties of Engineered Meniscus Constructs. Cross-sectional area (CSA, mm<sup>2</sup>), Stiffness (N/mm), Modulus (MPa), and Maximum Stress (MPa) achieved on day 70 are provided for constructs generated from each of the ten donors. Values indicate the mean (top number in bold) and standard deviation (bottom number) of five samples tested for each measure and donor at each time point. For each parameter, the highest magnitude of change is denoted with an (H), and lowest level of change is denoted with an (L). Average change in each parameter between days 14 and 70 for all donors is provided at the bottom of each column.</i>	166
<i>Table 7-3: Biochemical Composition of Engineered Meniscus Constructs. Dry mass (mg), total DNA content (μg), total sGAG content (μg), and total collagen content (μg) achieved on day 70 are provided for constructs generated from each of the ten donors. Values indicate the mean (top number in bold) and standard deviation (bottom number) of five samples tested for each measure and donor at each time point. For each</i>	

*parameter, the highest magnitude of change is denoted with an (H), and lowest level of change is denoted with an (L). Average change in each parameter between days 14 and 70 for all donors is provided at the bottom of each column. For this table, all comparisons between days 14 and 70 were significantly different with  $p < 0.05$  except when noted (+)..... 170*

*Table 8-1: MSCs were isolated from healthy and OA bone marrow sources. MSCs and MFCs isolated from the surgical waste tissue of four patients undergoing TKA were compared in this study. Healthy MSCs were examined to determine whether stem cell behavior was disease or age dependent..... 186*

## ***CHAPTER 1: INTRODUCTION***

The fibrocartilaginous menisci dwell between the articular surfaces of the knee and play a crucial role in healthy joint loading, functioning to transmit forces, absorb shock, and enhance the stability of the joint. Traumatic injury and/or degenerative changes disrupt the mechanical function of these tissues and lead to the early onset and accelerated development of osteoarthritis. The current standard of treatment is meniscectomy, or resection of the damaged portion of the meniscus, a procedure that fails to re-establish normal knee mechanics or prevent the initiation of osteoarthritic cascades. Given the high prevalence of meniscal injury, to date, a repair strategy that restores meniscus mechanical function remains a preeminent need in orthopaedic medicine.

Thus, the overarching goal of this thesis is to develop strategies and technologies for replacing damaged or diseased meniscus with tissue engineered, mechanically-competent fibrocartilage. Once implanted, this biologic tissue would be maintained by the body, avoiding the wear issues and limited lifespan of artificial implants and the numerous drawbacks associated with allografts. The functional properties of the meniscus stem from its highly ordered extracellular matrix, primarily composed of co-aligned collagen fibers which enable the tissue to bear high tensile loads. Towards recapitulating the structural features of the meniscus, this work focuses on scaffolds composed of aligned arrays of polymeric nanofibers fabricated with the electrospinning process. These biocompatible and biodegradable nanofibers can be formulated to mimic the length scale and organization of collagenous tissues, and as such, serve as a suitable foundation for engineering meniscal fibrocartilage. Using a multi-faceted approach, this work

investigates aspects of scaffold design, cell source selection, and modulation of the mechanical environment with the aim of engineering fibrocartilage that approximates the organization, composition, and mechanical function of the native meniscus.

To establish the functional metrics and target characteristics of tissue engineered fibrocartilage, Chapter 2 describes the structure, composition, and physiologic function of the native meniscus. Providing the motivation for this work, the failure modes of the meniscus are described, as well as the historical clinical approaches to repairing this tissue. The current state of meniscus tissue engineering is covered in detail, reviewing the different scaffolding materials that have been explored, potential cell sources suitable for reconstituting this tissue, and investigations into optimizing tissue formation with the use of bioreactors. Finally, an overview of the challenges associated with implementing engineered meniscus tissue is presented.

Demonstrating the utility of nanofibrous scaffolds for engineering anisotropic fibrous tissues such as fibrocartilage, Chapter 3 investigates the effect of nanofiber alignment on the organization of cells and cell-deposited collagen. Cells were seeded onto two distinct scaffold architectures formed from the same material: scaffolds where the nanofibers were randomly organized, or ones where the fibers were uniformly aligned in the same direction. With culture, collagen deposition parallel to the aligned nanofibers was observed, while only disorganized collagen was identified in nonaligned scaffolds. This chapter demonstrates that nanofiber alignment dictates the organization of collagen with

profound consequences on the load-bearing properties of the resultant tissue, and provides the foundation for the remainder of the work.

A significant limitation observed in these studies was the slow rates at which cells colonize these three-dimensional matrices. This problem arises from the dense packing of fibers during the electrospinning process which leads to small pore sizes. To increase pore sizes and hasten cell ingress, Chapters 4 and 5 develop composite scaffolds that contain both slow-eroding structural fibers, and removable elements that serve to hold space during the formation of the scaffold. Chapter 4 details the design and mechanics of these composite scaffolds, and shows that the use of sacrificial fiber elements leads to improvements in cell infiltration over short-term culture. In Chapter 5, the longer-term ramifications of sacrificial fiber inclusion on construct maturation were explored. With high sacrificial fiber content, increases in collagen distribution and content led to larger increases in mechanical properties. To underscore the widespread applicability of these composites, scaffold colonization by host cells was investigated in a rat subcutaneous model.

Findings from Chapters 4 and 5 demonstrate the utility of combining multiple types of polymer fibers into a composite, and motivate the addition of a fiber population that erodes concomitant with tissue formation. Thus, Chapter 6 focuses on engineering a tri-polymer composite with temporally dynamic mechanical properties. While the experimental aspects of this chapter focused on integrating a choice polymer with specific degradation rates and mechanical properties, the approach of combining multiple

fibers each with unique characteristics into a single composite could have bearing on numerous applications and tissues. To generalize this strategy, a theoretical model that describes the temporal mechanical behavior of composites was developed and validated with experimental data. This model was used to simulate the time-dependent stress-strain response of scaffolds of hypothetical formulations, and introduces a novel approach to the intelligent design of nanofibrous scaffolds with dynamic mechanical properties.

In addition to a well-designed biomaterial scaffold, an essential component to generating fibrocartilage *in vitro* is a cell type that can reconstitute the extracellular content of the meniscus. The two most accessible options are meniscal fibrochondrocytes (MFCs), the cells indigenous to the meniscus that assemble and maintain its extracellular matrix, and mesenchymal stem cells (MSCs), a multipotent cell type under widespread investigation for applications in musculoskeletal tissue engineering. The juvenile bovine MSCs and MFCs used in Chapter 3 (in order to compare healthy, donor-matched cell types) were found to synthesize a robust, fibrocartilaginous matrix on nanofibrous scaffolds. To move this technology towards clinical implementation, Chapter 7 examines the functional potential of human MFCs isolated from surgical waste tissue. These cells present a number of advantages: they possess the appropriate phenotype, would be autologous and so limit immune rejection, and can be obtained without an additional surgical site. Nanofibrous constructs were seeded with MFCs isolated from ten human donors and biochemical, mechanical, and histological features were assessed over long-term culture. While considerable donor-donor variability was noted, all ten cell lines synthesized load-

bearing fibrocartilaginous matrix, indicating MFCs isolated from surgical waste are a pertinent cell source for meniscus tissue engineering.

Chapter 8 assessed the ability of human marrow-derived MSCs to elaborate a mechanically functional, fibrocartilaginous matrix in a nanofibrous context. As MSCs can be readily harvested from bone marrow, their use for engineering replacement tissues would negate the need for multiple surgeries at the defect site. Based on results from Chapter 3 where juvenile bovine MSCs synthesized higher amounts of key fibrocartilaginous matrix components, we hypothesized that human MSCs would similarly outperform donor-matched MFCs. Instead, MSCs demonstrated limited proliferation and synthesized sparse extracellular matrix which led to negligible increases in construct mechanical properties as compared to donor-matched MFCs. Interestingly, there was no difference in matrix production of MSCs and MFCs when cultured in pellet form, highlighting the sensitivity of human MSCs to their three-dimensional microenvironment.

In the previous chapters, the highest tensile modulus achieved in an engineered construct after long-term free-swelling culture was approximately 30MPa, a value below adult meniscus by a factor of 2 or more. As these tissues require exposure to mechanical forces *in vivo* for proper formation and maintenance, it is perhaps not surprising that engineered tissue cultured in static, free-floating conditions failed to achieve native tissue properties. In an effort to hasten the *in vitro* maturation of these constructs and gain insights into how cells within a nanofibrous microenvironment respond to mechanical

stimulation, Chapters 9 and 10 investigate the primary loading modality of the meniscus: tensile deformation.

In Chapter 9, we begin at the cellular level by examining how tensile strains applied to the scaffold translate to cell and subcellular changes. Adult human MSCs and MFCs were sparsely seeded onto both aligned and nonaligned nanofibrous scaffolds which were deformed and held fixed at strains of up to 10% for analysis. Gross morphological changes in the cell as well as alterations in nuclear shape and organization were examined. With an applied deformation, the response of cells and their nuclei was found to be highly dependent upon the underlying scaffold architecture. Furthermore, by selectively removing cytoskeletal elements from these cells, the role of the actin, microtubule, and intermediate filament networks in mediating force transfer from the scaffold to the nucleus was interrogated.

Chapter 9 provides a basic understanding of how strains applied to aligned nanofibrous scaffolds affects adhering cells. We next scale up in complexity by examining cyclic tensile loading, which better approximates the dynamic mechanical environment of the meniscus. Chapter 10 focuses on the design and validation of a custom tensile bioreactor for applying cyclic loads to cell-seeded nanofibrous constructs during *in vitro* culture. Using this system, we asked whether daily administration of physiologic mechanical loading would positively impact the development of MSC-laden fibrocartilaginous constructs. Aligned nanofibrous were seeded with juvenile bovine MSCs and mechanically stimulated for four weeks. Dynamic loading led to increases in tensile

stiffness and total collagen content, and the expression of key matrix-associated genes were modulated with mechanical loading. These results have relevance to strategies for MSC-based tissue engineering, but also provide new insights on how stem cells can respond to external mechanical stimuli and modify their microenvironment.

Finally, Chapter 11 provides a summary of the major themes and findings stemming from this body of work, and proposes implications for engineering other anisotropic, load-bearing tissues. This is followed by an in-depth discussion of the key limitations to the described studies and drawbacks to the overall approach of engineering fibrocartilage with nanofibrous scaffolds. In addressing some of these limitations, future directions for this research are suggested, and some preliminary data is provided in support of these new avenues of investigation.

## **CHAPTER 2: BACKGROUND**

### **2.1 STRUCTURE, COMPOSITION, AND FUNCTION OF THE MENISCUS**

#### **2.1.1 Anatomy and Extracellular Matrix of the Meniscus**

The knee meniscus is a wedge-shaped fibrocartilaginous structure that transmits loads, absorbs shock, and enhances joint stability. These semi-lunar tissues reside between the femur and tibia within the medial and lateral compartments of the knee (**Figure 2-1**). Once considered fibrous remnants of joint formation, these unique tissues have come to be appreciated for their critical role in the mechanical function of the knee joint; their importance is demonstrated by their presence in numerous animal species, including mammals, birds, and amphibians (Arnoczky et al. 1988).

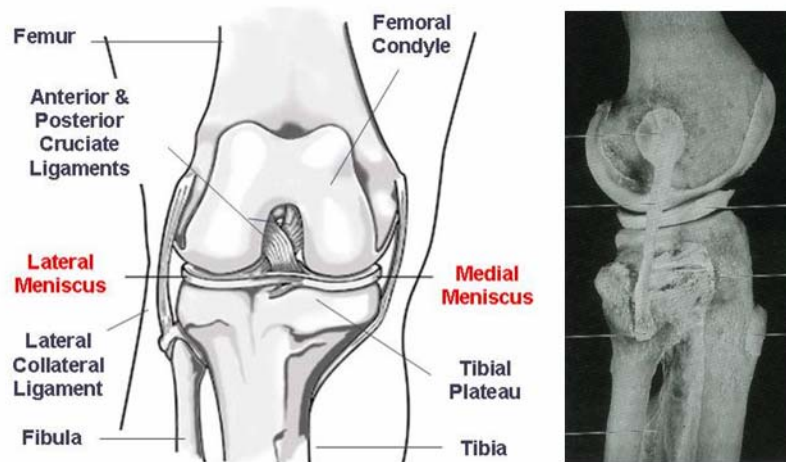


**Figure 2-1: Anatomic location of the meniscus. Anterior (left) and side (right) view of the human knee joint depicting the semi-lunar fibrocartilaginous menisci. Courtesy of [www.aaos.org](http://www.aaos.org).**

The meniscus is described as fibrocartilaginous as it shares characteristics of both fibrous tissues (tendon and ligament) as well as cartilaginous tissues (articular cartilage). In bulk, the meniscus extracellular matrix (ECM) contains 85-95% dry weight collagen, of which greater than 90% is type I (Eyre et al. 1983), with the remainder consisting mostly

of types II, III, V, and VI (McDevitt et al. 1990). Proteoglycans (PGs) makes up less than 2-3% of the dry weight, eight times less than is seen in articular cartilage (**Figure 2-3B**) (Fithian et al. 1990; McDevitt et al. 1990; Adams et al. 1992). The meniscus, like articular cartilage, is highly hydrated, with 72-77% of the wet weight comprised of water (Adams et al. 1992). Furthermore, the tissue ranges from being heavily vascularized in the outer periphery to completely lacking blood supply in the inner region (Arnoczky 1992). In the adult meniscus, the inner avascular region is more hyaline-like, while the outer vascular region is more fibrous in appearance. The resident cells of the tissue are known collectively as meniscal fibrochondrocytes (MFCs). These cells sparsely populate the tissue substance in the adult and function to maintain and remodel the extracellular matrix (McDevitt et al. 1990; Adams et al. 1992) (**Figure 2-3A, 2-4**). MFCs are an inhomogeneous population, with cells derived from the different meniscal regions exhibiting distinct morphologies. For example, MFCs in the peripheral region have numerous cellular processes, while those in the inner avascular region have a rounded morphology (Mauck et al. 2007).

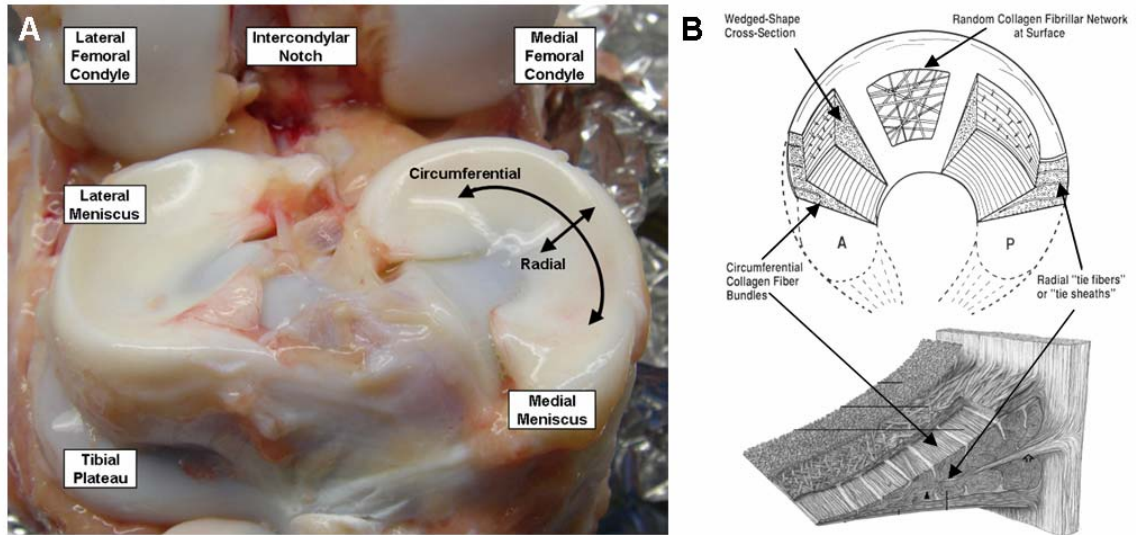


**Figure 2-2: Collagen organization in the meniscus. A) Image of the bovine knee joint, after transection of the cruciate and collateral ligaments. B) Schematic and drawing of collagen organization within the meniscus. Adapted from (Petersen et al. 1998).**

### **2.1.2 Mechanical Properties of the Meniscus**

Given its central position in the knee, there has been significant interest in elucidating the mechanical properties of the meniscus. Paramount to its mechanical function, the unique architecture of the meniscus consists of circumferentially oriented collagen fibers interspersed with radial collagen “tie” fibers (Fithian et al. 1990) (**Figures 2-2, 2-3C,D**). PGs are present at low levels in general, and are highest in the inner avascular zone (Petersen et al. 1998; Buma et al. 2004). As may be expected for such a fiber-reinforced matrix, the mechanical properties of this tissue are highly anisotropic (different in opposing directions), and strongly dependent on the prevailing fiber direction (Bullough et al. 1970; Setton et al. 1999). This can be seen in the tensile stress-strain response of samples oriented in the circumferential direction as compared to those oriented in the radial direction (**Figure 2-3E,F**). Circumferential samples show a pronounced ‘toe’ region common to fiber reinforced tissues, and a higher linear modulus thereafter. Radial

samples are relatively linear in their stress-strain response, with a much lower modulus. The tensile properties of the meniscus range from 48-259 MPa in the circumferential direction and 3-70 MPa in the radial direction, depending on anatomic location and species (Bullough et al. 1970; Proctor et al. 1989; Fithian et al. 1990; Setton et al. 1999). The compressive properties of the meniscus are low relative to articular cartilage (50-400 kPa, about one-half) (Sweigart et al. 2004; Bursac et al. 2009). The meniscus, while less stiff in compression, is also much less permeable than articular cartilage (Fithian et al. 1990), suggesting that the tissue is optimized to enhance congruency, load distribution, and shock absorption across the joint (Setton et al. 1999).

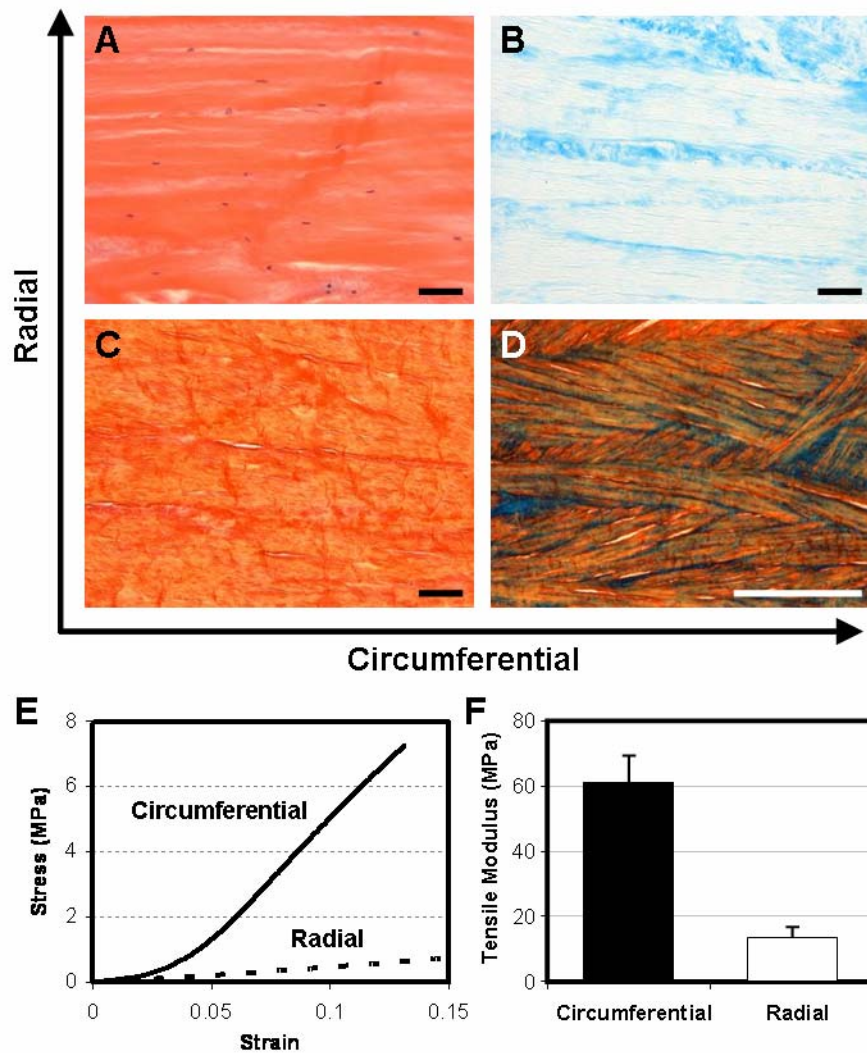


**Figure 2-3: Histological and mechanical analysis of bovine meniscus.** A) Hematoxylin and Eosin (H&E) staining shows limited cellularity (purple nuclei) and abundant extracellular matrix (orange). B) Alcian Blue staining for PGs is limited to the interstitial areas outside of dense collagen bundles. C) Dense collagenous matrix of the meniscus visualized through Picrosirius red staining. D) Polarized light microscopy analysis of collagen-stained sections reveals a highly organized network of collagen fibers within the macroscopic circumferential bundles. Scale bars: 50  $\mu\text{m}$ . E) Typical stress-strain response of meniscus samples tested in the circumferential and radial directions. F) The tensile modulus in the circumferential direction is  $\sim 6$  times higher than that measured in the radial direction.

### 2.1.3 Physiologic Loading of the Meniscus

The main functions of the meniscus are to transmit and distribute compressive load between the femur and the tibial plateau, increase joint congruency, stabilize the joint, and improve articular cartilage nutrition and lubrication (Ghosh et al. 1987). These functions are achieved by the unique load transfer that occurs between the more hyaline inner region and the more fibrous outer region of the meniscus. When the joint is loaded vertically, axial loads from the femoral condyles impinging on the wedge-shaped portion of the meniscus are redirected laterally (**Figure 2-4**) (Setton et al. 1999). Lateral extrusion of the meniscus is resisted by the osseous anchorage of the anterior and posterior horns (Setton et al. 1999), generating hoop stresses within the dense network of circumferentially oriented collagen fibers (Shrive et al. 1978). With normal use, the menisci transmit 50-100% of the loads in the knee (multiples of body weight) (Ahmed et al. 1983), with tensile deformations limited to 2-6% (Jones et al. 1996; Richards et al. 2003).

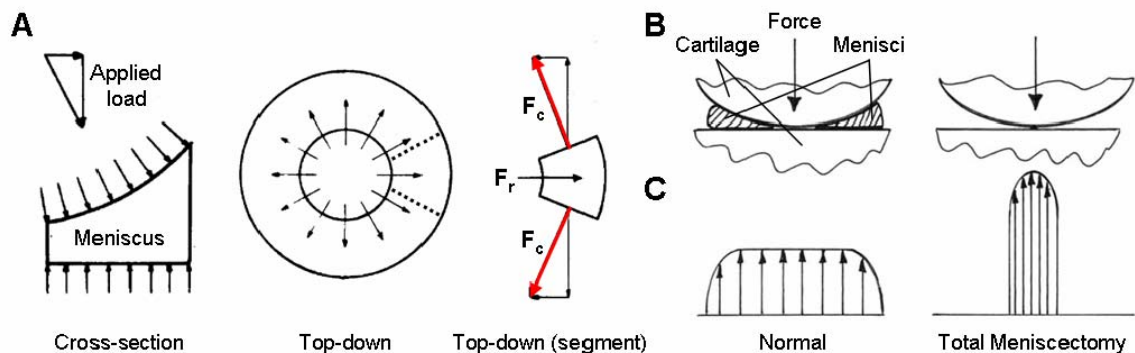


**Figure 2-4: The mechanical role of the meniscus in bearing and distributing loads. A) A simple model of knee joint loading where the menisci are reduced to a single wedge-shaped annulus. With axial loading, the tissue resists radially-directed forces ( $F_r$ ) through the generation of circumferential hoop stresses ( $F_c$ ) with circumferential strains between 2-6%. Adopted from (Shrive et al. 1978). B) Schematics of loading in the intact joint (left) and following total meniscectomy (right). C) Representations of the resulting stress distributions on the underlying articular surface. Adopted from (McDermott et al. 2006).**

## 2.2 MENISCAL INJURY AND CURRENT TREATMENT

### 2.2.1 *Meniscus Damage and Healing*

As the meniscus continually operates in a rigorous mechanical environment, damage is common with most patients over the age of 45 displaying some evidence of meniscal scarring. The annual incidence of meniscal injuries is estimated at 60 to 70 per 100,000 per year with the peak in male patients occurring between ages 21 to 30 and between 11 and 20 years of age in female patients (Hede et al. 1990; Nielsen et al. 1991). The cause of meniscal tears in young people is commonly traumatic due to sports injuries. Conversely, in people older than 40 years of age, tears are more often degenerative in nature (Greis et al. 2002). Meniscal injury occurs more frequently in the medial meniscus than the lateral, at a ratio of approximately 2:1 (Campbell et al. 2001), possibly due to the more stable fixation of the medial meniscus. Meniscal damage can manifest in a variety of forms (**Figure 2-5A**) including circumferential or longitudinal tears (where fracture occurs between collagen bundles), or radial tears (where collagen bundles are disrupted). Different tears commonly arise from different origins; trauma leads to bucket handle circumferential tears, while degeneration often results in horizontal and radial tears. Degeneration-associated tears occurring in older patients tend to be complex, involving a combination of the above and displaying largely in the posterior horn. Depending on the tear modality, symptoms manifest differently; for example, bucket handle tears frequently leads to mechanical locking of the knee.

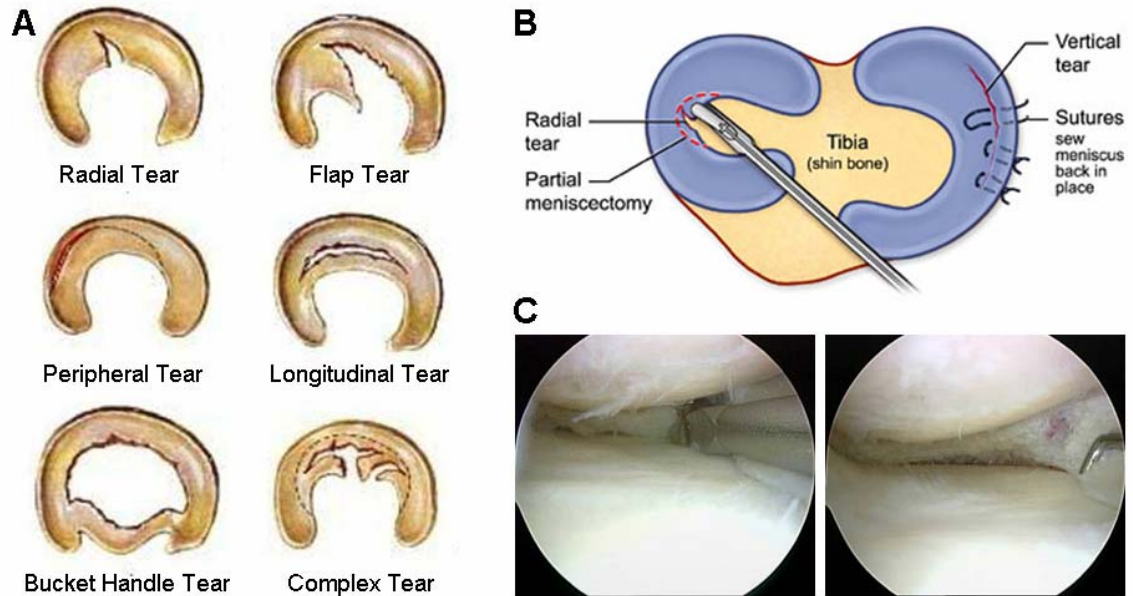


**Figure 2-5: Meniscus damage and current treatment.** A) Depictions of the numerous modalities by which tears occur in the meniscus. Courtesy of [www.jockdoc.ws](http://www.jockdoc.ws). B) Depending on the type and severity of tearing, injured meniscus may be resected via partial or total meniscectomy or repair may be attempted. C) Arthroscopic images of a torn medial meniscus during (left) and following (right) tear resection.

Like other dense connective tissues, the menisci are optimized for mechanical functionality at the expense of healing capacity. After birth and coincident with joint loading, the vasculature of the meniscus recedes to the periphery, cellularity decreases, and the collagenous ECM grows denser (**Figure 2-6**) (Clark et al. 1983). As vascularity is associated with healing responses, juvenile meniscus injuries heal readily while in the adult, complete healing only is observed in the vascularized periphery (Petrosini et al. 1996). More complicated tears, such as those that interrupt the circumferential fibers in the avascular zone have a poor long-term prognosis. Indeed, one potential strategy for accelerating healing in avascular regions is the drilling of channels to promote blood vessel invasion (Arnoczky et al. 1983). Even when healing does occur, radial tears often result in fibrovascular scars containing disorganized collagen with inferior mechanical

properties (Newman et al. 1989). Restoration of fiber arrangement in such tears has never been documented (DeHaven 1999).

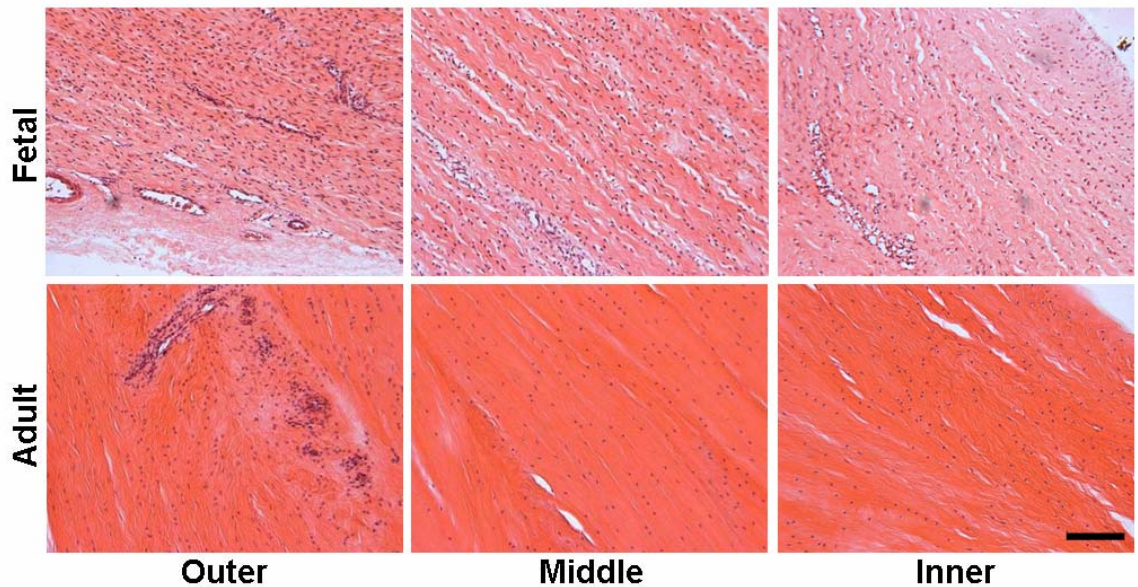


**Figure 2-6: Histology of the meniscus with increasing age. H&E staining of adult and fetal meniscus samples show region-specific and age-dependent variations in matrix content, cellularity, and blood vessel distribution. With increasing age, the menisci become less cellular (fewer nuclei) and less vascular (fewer vessels observed), particularly in the inner region. Scale bar: 100  $\mu$ m.**

### **2.2.2 Meniscectomy**

The most common treatment for meniscal damage is resection of meniscus tissue via partial or total meniscectomy, largely performed arthroscopically (**Figure 2-5B,C**) (McDermott et al. 2006). For irreparable tears located towards the inner rim of the meniscus, only the portion of tissue containing the disruption is resected. This procedure, termed partial meniscectomy, seeks to preserve as much healthy, functional tissue as possible while precluding further tear propagation (Andersson-Molina et al. 2002). Performed less frequently, the entirety of the tissue may be removed with total meniscectomy, prescribed in cases where tears are complex (**Figure 2-5A**), or when no healthy tissue remains (McGinity et al. 1977). Mechanical compromise of the meniscus

results from both injury or degeneration, as well as subsequent treatment via meniscectomy. The reduction in load-bearing meniscus decreases contact area and increases stress concentrations on the adjacent articular surfaces (**Figure 2-4B,C**) (Baratz et al. 1986; Rath et al. 2000). Such altered loading can in turn lead to detriment to the articular cartilage, inspiring osteoarthritic changes such as osteophyte formation and joint space narrowing (Petrosini et al. 1996; Rath et al. 2000). While complete meniscus removal was once considered the gold standard of treatment and a benign procedure, the biomechanical functions of these tissues have since been elucidated and current surgical resection seeks conservation whenever possible (McDermott et al. 2006). Numerous studies have now demonstrated that the incidence and severity of ensuing osteoarthritis is strongly correlated with the extent of tissue removed during surgery (McGinity et al. 1977; Higuchi et al. 2000; Andersson-Molina et al. 2002; Bonneux et al. 2002; Englund et al. 2003). Of note, while many of these studies dichotomized into partial or total meniscectomy, partial meniscectomies where the circumferential collagen bundles are completely disrupted may functionally represent total meniscectomies, as the hoop stresses intrinsic to the load-bearing function of the meniscus can not form (Hoser et al. 2001). Taken together, these studies confirm the importance of this tissue and identify the circumferentially-aligned collagen fibers as paramount to meniscus mechanical function and the tissue's role in maintaining the health of the adjacent articular surfaces.

### ***2.2.3 Surgical Methods for Meniscus Repair***

A number of surgical techniques have been adopted for augmenting the natural healing process of the meniscus. In some procedures, rasping of the synovium or the

intercondylar notch is employed to increase the vascular response (Okuda et al. 1999; Freedman et al. 2003). It has been suggested that whenever repair of the avascular zone is attempted, some form of healing enhancement technique should be considered (DeHaven 1999). The most common and successful repair technique is suturing and stabilizing the meniscal tears, bringing the torn portions back into apposition, either via open repair or arthroscopic surgery (Venkatachalam et al. 2001). These suturing techniques include “inside-out” (inside the joint capsule to the meniscus periphery) or “outside-in” (from the periphery to the internal space) approaches (DeHaven 1999; Rodeo 2000). There has also been a growing interest in the use of devices which employ an “all inside” arthroscopic technique for meniscal repair. These include commercially available biodegradable fixation devices (including screws, arrows, and darts) that provide for shorter surgical times, easier approaches for implantation and reduced surgical risk.

#### ***2.2.4 Meniscus Allografts***

Another approach to meniscus repair is allograft transplantation of a whole fresh-frozen or cryopreserved meniscus from a human donor. These tissue transplants, derived from cadaveric sources, are fixed to the tibial plateau via bone blocks or tunnels. Whole meniscus transplants can restore some aspects of load transmission after total meniscectomy. However, several studies have reported cartilage degeneration following implantation, most likely attributable to improper sizing of the implants (Garrett 1992; Jackson et al. 1992; Elliott et al. 2002; Mora et al. 2003). A recent study showed that the contact area of and resulting load transmission through cartilage and meniscus varied

considerably from normal if allografts were more or less than 10% of the original tissue size (Dienst et al. 2007). Furthermore, non-anatomic positioning of meniscus transplants can significantly impact load transmission (von Lewinski et al. 2008), and may explain some variation in clinical findings. Allografts also raise concerns regarding the methods of cryopreservation, graft sterility, and the proper method of fixation (Jackson et al. 1992). Clinical results of meniscal allografts suggest that function is only partially restored and that poor integration makes the grafts susceptible to premature failure (Rath et al. 2001). These findings highlight the need for a functional repair strategy short of total replacement for the clinical treatment of meniscal tears.

### ***2.2.5 Enhancing Endogenous Repair***

In addition to surgical fixation and replacement techniques, there are a number of emerging therapies designed to enhance endogenous repair. One of the first methods emerged from the observation that some repair occurred in canine meniscus where a fibrin clot had adhered to the cut surface (Arnoczky et al. 1985). This observation led to the introduction of vascular channels to improve access, as well as the implantation of fibrin clots (Arnoczky et al. 1988). In these first studies, a defect was created in the avascular region of the meniscus and filled with a fibrin clot. These clots (and the factors within) served as both chemotactic and mitogenic agents, encouraging cellular in-growth and division within the wound site (Arnoczky 1992). With clot treatment, healed tissue remained markedly different from the native tissue, though it was highly cellularized and of better quality than that found in untreated lesions (Arnoczky 1992). In a different approach, devitalized meniscal chips with autologous chondrocytes (Peretti et al. 2001)

were implanted into avascular longitudinal tears in a porcine model (Peretti et al. 2004). This strategy resulted in improved tissue formation compared to sutured controls, though complete healing of defects was not observed. These findings do suggest, however, a role for cell-based methods for enhancing meniscus repair.

## **2.3 TISSUE ENGINEERING OF THE KNEE MENISCUS**

### ***2.3.1 Motivation for a Tissue Engineering Strategy for Meniscal Repair***

Despite advances in surgical techniques and fixation devices, there remains a pressing clinical demand for new strategies for effecting repair of the knee meniscus. For many orthopaedic soft tissues, artificial prosthetics are currently on the market (e.g. total knee replacements for articular cartilage). While there has been some attempts to devise an artificial meniscus (Linder-Ganz et al.), it is widely believed that a successful replacement should incorporate with the surrounding host tissue and gradually be converted to biologic tissue with time *in situ*. Whether the scaffold is seeded prior to implantation, or is reliant upon host cell infiltration, cellularization will enable the production and homeostatic maintenance of biologic tissue. Such a strategy avoids the drawbacks associated with artificial replacements, including the failed restoration of physiologic joint motions required for high intensity sporting activities (e.g. squash), immunogenic wear debris, and limited implant lifetimes due to fatigue and failure of manmade materials. Thus, a number of meniscus tissue engineering approaches have emerged, combining biomaterials, cells, and/or drug and growth factor delivery systems to enhance repair and or replacement of damaged meniscus.

### ***2.3.2 Biomaterials for Meniscus Tissue Engineering***

At the foundation of most tissue engineering strategies seeking to replace load-bearing structures is a suitable scaffolding material. Importantly, this structure should be biocompatible with limited immunoreactivity, must support cells (either exogenously seeded, or invading from surrounding host tissue), and need ultimately foster the formation of tissue that approximates the form and function of the native tissue. Towards replacing the entire meniscus, scaffolds formed from a wide variety of biomaterials have been investigated. For example, in approaches that mirror allograft procedures, whole acellular polymeric menisci have been fabricated from polyvinyl alcohol, Dacron, and polyurethane (Sommerlath et al. 1993; Klompaker et al. 1996; Kobayashi et al. 2005), as have meniscus-shaped constructs formed from dense cell pellets shaped around molds (Aufderheide et al. 2007). Most recently, sophisticated MRI imaging and injection molding techniques have been coupled to create anatomic constructs composed of cell-seeded alginate hydrogels (Ballyns et al. 2008). Other cell-seeded scaffolds, such as PLLA porous foams with embedded carbon fibers (Veth et al. 1986), PGA felts (Ibarra et al. 2000), and macroporous PCL/PU and PCL/PLLA constructs have also been investigated. Such structures can be produced with compressive properties similar to the native tissue while promoting cellular in-growth after implantation (Heijkants et al. 2004), though these implants often result in cartilage erosion in *in vivo* studies (van Tienen et al. 2002).

Beyond synthetic materials, investigators have explored the “reassignment” of processed, natural tissues for use in repairing meniscal defects. Most notably, porcine small

intestinal submucosa (SIS) grafts have been examined for applications in both meniscus, as well as tendon and ligament healing (Dejardin et al. 2001; Gastel et al. 2001; Cook et al. 2006). Additionally, perichondral tissue taken from the rib has been tested in a complete meniscectomy model in sheep (Bruns et al. 1998). Along similar lines, there are numerous naturally-derived biopolymers currently being investigated either in the lab or the clinic. These would include type I collagen-glycosaminoglycan-supplemented scaffolds (Stone et al. 1992), fibrin gels (Connelly et al. ; Vanderploeg et al. 2004), hyaluronic acid (Tan et al.), agarose (Gunja et al. 2009), and even cellulose (Bodin et al. 2007). Of note, one biologic scaffold, the ‘collagen meniscus implant’ (now called Meniflex by ReGen Biologics, produced from homogenized decellularized bovine Achilles tendon) was recently used in a randomized clinical trial in humans (Rodkey et al. 2008). Despite lacking a fiber architecture that recapitulates meniscal structure and restores hoop stresses in the tissue, these implants showed some promise in maintaining knee function in patients with degenerative meniscus damage, although they were less effective in the treatment of traumatic lesions.

### ***2.3.3 Cell Sources for Meniscus Tissue Engineering***

Fibrochondrocytes, the cell type that resides within the meniscus, are the most direct choice for engineering meniscal tissue, given their possession of the appropriate phenotype (Benjamin et al. 2004). As mentioned earlier, the phenotype of fibrochondrocytes ranges depending on the anatomic location of the cells, where those in the inner, avascular region are more chondrocyte-like while those in the meniscus periphery adopt morphologies more akin to fibroblasts (Tanaka et al. 1999; Mauck et al.

2007). These cells have been isolated from the tissue and explored *in vitro* both for the sake of understanding fibrochondrocyte biology (Webber et al. 1985; Mueller et al. 1999; Verdonk et al. 2005), as well for assessing their potential to form meniscus constructs . For instance, Upton and coworkers explored the effects of biaxial strain on meniscus fibrochondrocytes (MFCs), showing these cells even when removed from their native extracellular environment are responsive to mechanical perturbation (Upton et al. 2006). Pangborn treated isolated MFCs with different growth factors and identified TFG- $\beta$ 1 as a suitable promoter of collagen and proteoglycan synthesis (Pangborn et al. 2005). Additionally, MFCs have been explored as a cell source for engineering *in vitro* fibrocartilage, either with (Vanderploeg et al. 2004; Pangborn et al. 2005; Gruber et al. 2008; Gunja et al. 2009) or without (Tumia et al. 2004; Hoben et al. 2007; Gunja et al. 2009) a supporting scaffolding material.

Mesenchymal stem cells (MSCs) are another potential cell type for engineering meniscus tissue. MSCs are thought to be key players in the maintenance of healthy tissues and in the repair processes that follow injury or disease. These self-renewing progenitor cells are capable of differentiating into cell types indigenous to bone, cartilage, muscle, tendon, ligament, and connective tissues, amongst others (Caplan 1991). Given this multipotency, and the relative ease with which they may be isolated, these cells are of significant interest for musculoskeletal tissue engineering (Caplan 2005). MSCs can be readily harvested from numerous adult tissues (da Silva Meirelles et al. 2006), and in the case of meniscal repairs, could negate the need for multiple surgeries at the defect site. Strategies for meniscus restoration involving MSCs have primarily sought to either use

these cells in combination with a scaffold or carrier to fill and repair a defect, or take advantage of the broad array of regenerative paracrine factors released by these cells and enhance the endogenous healing response (Caplan 2007). MSCs have been seeded onto type I collagen sponges (Walsh et al. 1999) and decellularized meniscus (Yamasaki et al. 2008) or encapsulated in fibrin gels (Connelly et al.) or glues (Port et al. 1996; Izuta et al. 2005) and hyaluronan/gelatin composites (Angele et al. 2008). Such constructs have been implanted in meniscal defect animal models ranging in aggressiveness from partial transections to total meniscectomy. While many of these studies demonstrated localization of implanted MSCs to the defect site and the formation of new matrix, no strategy proved to be consistent in protecting the adjacent articular surfaces. Alternatively, MSCs have been introduced into the injured joint space through intraarticular injections with the goal of encouraging a regenerative microenvironment via the MSC-mediated release of trophic factors (Caplan et al. 2006). In these studies, and similar to studies using scaffolds or carriers, traced MSCs were identified in defect zones and observed to be contributing to an anabolic response, but chondroprotection was not afforded (Murphy et al. 2003; Agung et al. 2006; Centeno et al. 2008; Horie et al. 2009). Unfortunately, few of these studies examined the mechanics of either the repair tissue or its integration with the host. Furthermore, none of these studies reported on the organization of the *de novo* matrix, a factor that likely contributes to long-term outcomes.

#### ***2.3.4 Current Limitations in Meniscus Tissue Engineering***

As evidenced above, a considerable number of biomaterial, cell, and growth condition combinations have been explored. Despite this, the vast majority of these result in the

formation of isotropic tissue, failing completely to recapitulate the highly-aligned organization of meniscal fibrocartilage. As such, while a plethora of both acellular and cell-based tissue-engineering therapies have emerged from these, no one approach has shown functional *in vivo* repair and the reconstitution of fiber architecture of the native tissue. Quite possibly, the application of a scaffold that provides a 3D template for the formation of organized ECM would prove a suitable starting point for engineering anisotropic tissues such as the meniscus.

## **2.4 ELECTROSPINNING**

### ***2.4.1 Overview of Electrospinning***

The technique of electrospinning to create fibrous scaffolds is becoming increasingly prevalent in the extant literature. While the basic technique was first patented in the 1930s (Formhals 1934), a search for ‘electrospinning’ in the Pubmed database yields nearly 400 entries in the past year alone, with applications as diverse as bone tissue engineering to drug delivery to treatment of burns. Several recent reviews on electrospinning (Li et al. 2004; Li et al. 2005; Burger et al. 2006; Pham et al. 2006; Teo et al. 2006; Barnes et al. 2007) highlight much of this literature and provide an excellent foundation for this technology and its potential applications.

The basic electrospinning setup consists simply of a polymer source (or sources), a high voltage power supply, and a grounded target (**Figure 2-7**). The solution is expressed through a fine capillary or syringe (called the ‘spinneret’) by gravity or positive pressure, and forms a pendant droplet. Application of a high voltage to this solution causes charge

buildup and charge-charge repulsion amongst the individual polymer chains within the droplet, until these intermolecular forces overcome the surface tension holding the droplet in place. Once this critical threshold is reached, the polymer emits from the spinneret as a fine jet, and rapidly travels to the nearest grounded surface (Reneker et al. 1996; Shin et al. 2001). As the jet is drawn from its source through the high voltage gradient, solvent evaporation and whipping instability produces ultra-fine fibers (50-1000 nm) (Deitzel et al. 2001). With time, these fibers accumulate on the grounded surface to create a mesh composed of randomly-oriented fibers. Mesh thickness can be controlled by simply increasing the time of deposition. Nanofiber features in the network depend on the polymer composition as well as several controllable processing variables (Deitzel et al. 2001) (discussed below). Nanofibers can be tuned to range from as small as 50 nm up to several microns in diameter, and as such are many times smaller than most mammalian cells (and in fact are similar in scale to collagen fibers normally present in the ECM (Riesle et al. 1998)). This nano- and micro-scale topography has been shown to modulate cell signaling pathways (Nur et al. 2005) and to elicit superior metabolic and matrix forming activities by seeded cells (Li et al. 2006). Nanofibrous meshes are porous structures with a continuous distribution of pore sizes in the range of 2-465  $\mu\text{m}$  and void volumes of 80-90% (Li et al. 2002).

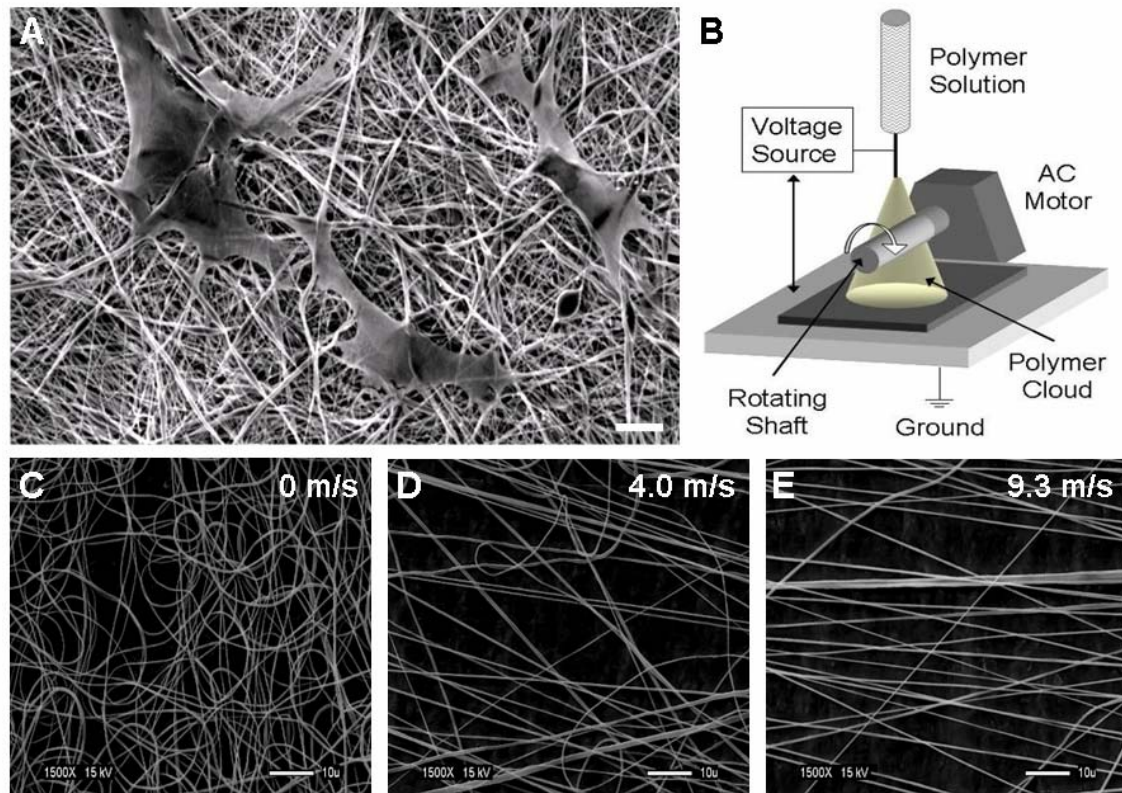


**Figure 2-7: Electrospun scaffolds for meniscus tissue engineering. A) Scanning electron micrograph of bovine mesenchymal stem cells on a non-aligned nanofibrous scaffolds composed of poly( $\epsilon$ -caprolactone) (PCL). B) Schematic of electrospinning device incorporating a rotating collecting mandrel to generate aligned fibrous meshes. C-E) Mandrel velocity (top right) dictates the degree of alignment in forming nanofibrous scaffolds. Scale bars: 10  $\mu$ m.**

#### **2.4.2 Electrospinning Synthetic and Natural Polymers**

Production of meshes via electrospinning has been carried out with numerous polymers, including polyurethanes (Khil et al. 2003), biodegradable polyesters (e.g., polycaprolactone (PCL) (Li et al. 2002; Yoshimoto et al. 2003; Xu et al. 2004; Venugopal et al. 2005), polyglycolic acid (PGA) (Boland et al. 2004), polylactic acid (PLA) (Yang et al. 2004; Yang et al. 2005; Li et al. 2006), and polydiacaxone (Boland et al. 2005)), as well as natural biopolymers including collagen (Matthews et al. 2002; Li et al. 2005; Venugopal et al. 2005; Buttafoco et al. 2006; Rho et al. 2006), elastin (Li et al.

2005; Buttafoco et al. 2006), silk fibroin (Min et al. 2004; Min et al. 2004), chitosan (Bhattarai et al. 2005; Geng et al. 2005), dextran (Jiang et al. 2004), and wheat gluten (Woerdeman et al. 2005). Additionally, liquid blends of biosynthetic and natural components have been electrospun (with components thus mixed in every fiber) to create meshes with enhanced cell compatibility (Stitzel et al. 2006; Lee et al. 2007). The most common appearance of such blends is in the combination of two dissimilar synthetic materials to result in a blend fiber that has properties of both, or a natural and a synthetic fiber combined to impart biologic functionality to the fibers as they form (Sell et al. 2006). Additional studies have modified fiber surfaces to enhance cell binding and/or growth factor retention (Casper et al. 2005; Ma et al. 2005; Casper et al. 2007). Further, methacrylate-based copolymers have been electrospun to form nanofibrous coatings that can be crosslinked after formation (Kim et al. 2005; Pornsopone et al. 2005). Clearly, there exists a wide range of polymers that can be processed into the nanofibrous format.

### ***2.4.3 Optimization of Electrospinning Parameters***

For each polymer utilized, spinning parameters are optimized to generate a homogeneous fiber array. Common intrinsic parameters that can be varied include the solvent type and composition, the mass concentration of the polymer, molecular weight of the polymer, solution viscosity, applied voltage, electric field strength, spinneret-to-collector distance, and polymer flow rate (Reneker et al. 1996; Deitzel et al. 2001; Fridrikh et al. 2003; Li et al. 2005). Additional extrinsic parameters include atmospheric conditions such as ambient temperature and humidity. These individual parameters are tuned to generate fibers that meet the criteria of the intended application, most commonly that the fibers

minimize their diameter, be free of defects (beads), and show little fiber-fiber welding at the interstices. **Figure 2-8A** shows examples of such defects in a PCL scaffold formed with sub-optimal electrospinning conditions. Fiber diameter and defects can usually be controlled by adjusting the solution mass concentration, voltage gradient, and distance over which fibers are collected. Solvent characteristics strongly influence these features. A recent study by Kidoaki and co-workers showed that when electrospinning PEUU, increasing N,N-dimethylformamide (DMF) content in the spinning solution led to enhanced fiber-fiber welding (Kidoaki et al. 2006). Even after spinning conditions have been optimized, some variation exists between batches, most likely due to small changes in extrinsic and intrinsic conditions on the day of production. Indeed, some in the field have suggested that electrospinning is an ‘art’ rather than a science because of this inherent variability. An example of this is shown in **Figure 2-8B**, where the mechanical properties of 10 different batches of PCL nanofibers (aligned, tested in the fiber direction) show some intra-scaffold variability, and extensive intra-batch variability.

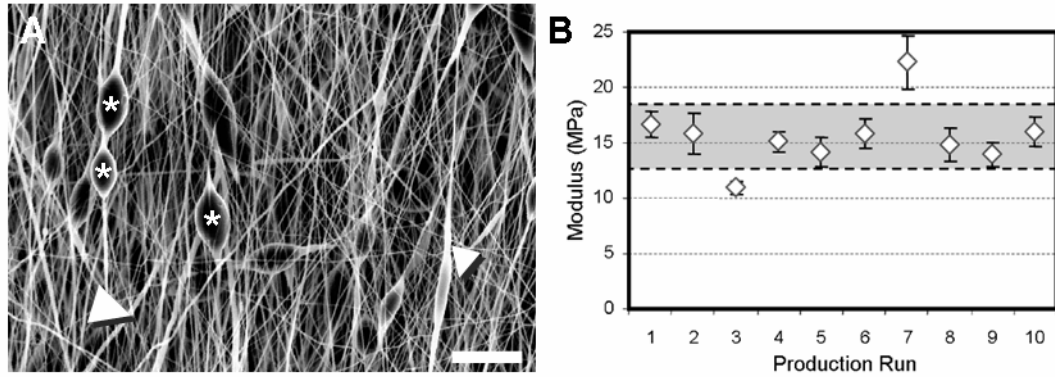


**Figure 2-8: Optimization of Electrospun Scaffolds.** Solution, fabrication, and environmental parameters can be optimized to generate sheets with homogenous fiber populations. Shown in A) are several features that arise when electrospinning conditions are not optimized; \*: bead-like inclusions, large arrow: thick fibers, small arrowhead: thin fibers. Quality control of microstructure is required to ensure homogeneity across production runs. Even when precautions are taken, small changes in fiber properties can yield a range of mechanical properties in the resultant scaffolds. Shown in B) is the modulus of aligned PCL scaffolds produced over ten separate production runs. Note the deviations in mechanical properties within each batch, as well as the scatter of average properties across production runs. Gray area indicates  $\pm 1$  standard deviation for this grouping of scaffolds.

#### 2.4.4 Inducing Anisotropy in Nanofibrous Scaffolds

When standard electrospinning methods are employed, and fibers are collected onto a stationary grounded plate, the resultant mesh contains fibers organized in a random fashion. As indicated above, most fiber-reinforced tissues show pronounced mechanical anisotropy (different properties in different directions), which is based on the underlying organized collagen ultra-structure. Methods to induce fiber alignment in nanofibrous scaffolds have thus been of great interest to the fiber-reinforced tissue engineering community (and were recently reviewed by Teo and Ramakrishna (Teo et al. 2006)). One of the first instances of nanofiber alignment was presented by Theron and colleagues (Theron et al. 2001), who focused fiber collection on the thin edge of a rotating disk. Nanofiber alignment was also demonstrated by Xia and colleagues, using a system in which the collecting surface was composed of pairs of electrodes that could be

differentially grounded and separated by an air gap or insulating surface. In this way, linear arrays of fibers were generated, and by varying the state of the electrodes (grounded or not), different rosette patterns were achieved (Li et al. 2004; Li et al. 2004; Li et al. 2005). More recently, Sun and colleagues demonstrated the capabilities of near-field electrospinning, where a point spinneret is situated only a few microns from the grounded surface. The probe tip, which is dipped in polymer solution, becomes a stylus from which polymer is ejected, and its position relative to the ground can be controlled to fabricate ordered structures. These methods are somewhat limited in their throughput, however, and so the most common method for aligning fibers for the generation of tissue engineering scaffolds (and the method used in the following work) is to deposit fibers onto a rotating drum or mandrel (**Figure 2-7**) (Boland et al. 2001; Sundaray et al. 2004; Ayres et al. 2006; Courtney et al. 2006; Li et al. 2007; Nerurkar et al. 2007). From high speed imaging studies, it has been shown that a single fiber can transit from the source spinneret to the ground at speeds  $> 2$  meters/second (Kowalewski 2005). Thus presenting a surface moving faster than the fiber jet will pull fibers into alignment as they are deposited. Numerous groups have shown that the degree of alignment is a function of the rotation speed of the collecting surface (**Figure 2-7**) (Ayres et al. 2006; Courtney et al. 2006; Li et al. 2007). Furthermore, this structural anisotropy is reflected in the measured mechanical properties, with more highly aligned scaffolds possessing greater levels of mechanical anisotropy (Li et al. 2007).

## 2.5 NANOFIBROUS SCAFFOLD MECHANICAL CHARACTERIZATION

### 2.5.1 *Mechanical Properties of Nanofibrous Assemblies*

Most load-bearing tissue engineering applications with nanofibrous scaffolds require some level of mechanical functionality. Therefore, the most common assay (aside from scanning electron microscopy (SEM) visualization) of any nanofibrous scaffold is the assessment of mechanical properties. These properties are typically assessed at the time of formation, as well as with subsequent degradation under physiologic conditions or with cell-mediated matrix deposition. When formed into random or non-aligned meshes, nanofiber scaffolds exhibit isotropic properties (same in all directions) that are reflective of the mechanical properties of their polymer composition. For example, polymers such as PLGA produce meshes that are quite stiff in tension, while scaffolds composed of PCL are 10 times less stiff and remain elastic over a wider range (up to 8-10%) (Li et al. 2006) (**Figure 2-9**). When biologic and synthetic molecules are mixed (in the same solution) before electrospinning, mechanical properties vary with composition (Barnes et al. 2007; Zhang et al. 2008). Given the large number of polymers (and biopolymers) that have been successfully electrospun, there is a correspondingly wide range of mechanical properties that can be achieved. Multi-jet electrospinning systems have also been developed to increase production rates (Yarin et al. 2004; Theron et al. 2005; Burger et al. 2006; Dosunmu et al. 2006). These systems may be used to create composite scaffolds (with a different polymer in each jet) whose properties reflect the properties (and ratios) of the individual components (Madhugiri et al. 2003; Ding et al. 2004; Kidoaki et al. 2005; Kwon et al. 2005).

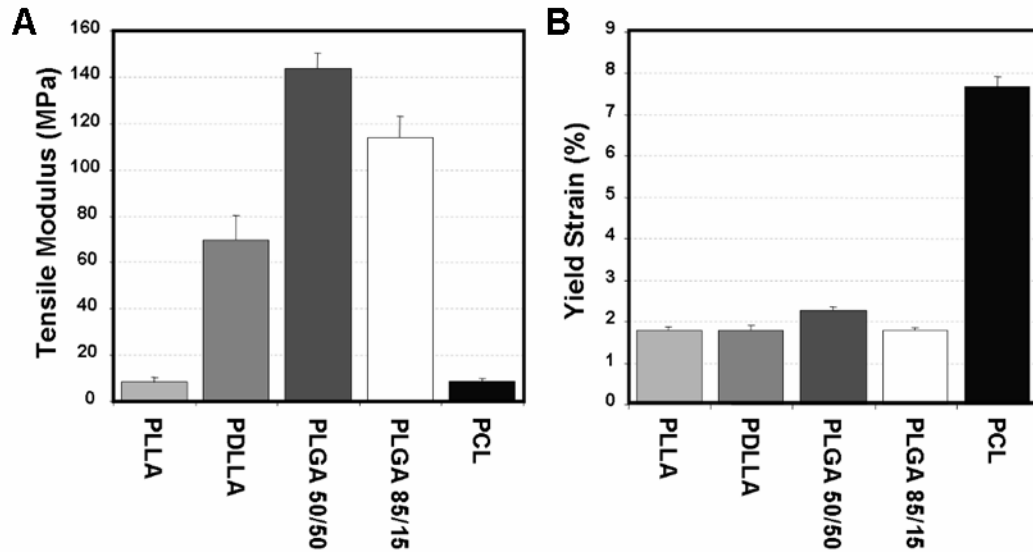


**Figure 2-9: Tensile properties of common biodegradable polymers. A) Young's modulus and B) yield strain for non-aligned nanofibrous scaffolds fabricated from a common set of biodegradable polymers. A range of properties can be achieved, but few polymers can be distended to greater than 2% elongation. Adapted from (Li et al. 2006).**

In addition to properties imparted by the polymer composition itself, several other factors may influence the measured mechanical properties. As noted above, recent studies have shown that alignment (and mechanical properties in the fiber direction) increase substantially as the collecting surface (rotating mandrel) increases in velocity (Ayres et al. 2006; Courtney et al. 2006; Li et al. 2007). For example, for PCL scaffolds, the ratio of properties in the fiber direction compared to transverse to the fiber direction can increase by 10-20 fold with increasing alignment (Li et al. 2007). Testing aligned scaffolds in directions that do not correspond to the prevailing fiber orientation also influences the measured mechanical properties in a predictable fashion (Nerurkar et al. 2007). Random scaffolds exhibit a relatively linear stress strain response in the pre-yield region, and extend linearly after yield. Aligned scaffold tested in the fiber direction have a sharper increase in stress with increasing deformation, and yield and fail at similar

points earlier in the strain regime. When these same scaffolds are tested in the transverse direction, a much lower stress-strain profile is observed. Other factors that can change mechanical properties include the amount of solvent remaining in a fiber when it reaches the collecting plate (and consequently the number of fiber-fiber welds that form). Kidoaki and co-workers showed a 4-fold increase in properties of electrospun scaffolds with increasing degrees of fiber-fiber welding (Kidoaki et al. 2006). Some materials show profound changes in mechanical properties when they are tested in a dry versus hydrated state. For example, collagen nanofibers (which must be cross-linked in order to be hydrated) decrease in tensile properties by approximately 100-fold with hydration (Shields et al. 2004; Barnes et al. 2007). Clearly, given the large number of factors at play, mechanical properties should be assessed for any fiber-reinforced tissue engineering application.

### ***2.5.2 Uniaxial Tensile Testing of Fibrous Assemblies***

While scaffolds are comprised of individual fibers with their own set of distinct mechanical features, the mechanical function is most commonly characterized in bulk samples, where the individual fibers combine to produce an aggregate response. In uniaxial testing of bulk scaffolds, load is applied along a single specified direction, while the sample is free to contract laterally. A rectangular or dumbbell shaped sample is typically loaded into a test-frame and pulled at a specified rate of displacement (displacement controlled) or force (load controlled), and both the load and displacement are measured. Normalizing force to undeformed cross-sectional area (engineering stress) and displacement to undeformed length (engineering strain), the stress-strain behavior

can be calculated. To evaluate cross sectional area, non-contacting methods such as imaging or laser systems are preferable; this avoids permanent deformation of scaffolds, particularly at early culture periods. The typical metric for the elastic behavior of linear elastic materials (those in which the plot of stress vs. strain reveals a linear relationship) is the Young's Modulus ( $E$ ), or slope of the stress-strain curve. Some electrospun polymers, such as aligned PCL fibers (as well as many fiber-reinforced soft tissues), exhibit a nonlinear stress-strain behavior and so are characterized by reporting a slope of the beginning of the curve, known as the toe-region modulus, in addition to the elastic region modulus. The strain at which the curve transitions from toe to linear regions is the transition strain, and is an additional parameter of interest in nonlinear materials. When electrospun scaffolds are stretched beyond their elastic regime, they may experience either of two primary failure modes: plastic deformation (deformations that are not reversed upon removal of load) and/or catastrophic failure (load goes instantly to zero or decreases markedly). The onset of plastic deformation occurs distinctly at a strain/stress level known as the yield point. As noted above, electrospun polymers have distinct failure properties, and may involve a combination of yielding and catastrophic failure (Li et al. 2007). In this case, an additional material property, the ultimate tensile strength (UTS), or the maximum stress prior to failure, is often reported. However, post yield measures, such as UTS, are less valuable for tissue engineering than properties of the elastic behavior, because post-yield deformations are not recoverable upon unloading. Due to the dynamic loading that most tissues encounter, it is critical that an engineered construct recover following deformation, and not be fully expended after a single loading event. Further, native soft tissues often undergo more than 25% deformation before

yielding or failure, while many common polymers in electrospinning are limited to 1-2% strain prior to yielding (Li et al. 2006). Therefore the yield point is an important design criterion to consider when selecting polymers for specific tissue applications.

## **2.6 SUMMARY**

The knee meniscus is a complex tissue whose structural properties allow it to carry out its physiologic role over a lifetime of use in a demanding mechanical environment. When damaged, intrinsic repair processes are limited, particularly in the poorly vascularized regions of the tissue. Annually, 60 to 70 meniscal injuries occur per population of 100,000 (Hede et al. 1990; Nielsen et al. 1991). Given this high rate of occurrence, arthroscopic meniscectomy has become one of the most commonly performed orthopaedic surgeries, comprising 10-20% of all surgeries at some centers (Renstrom et al. 1990). Considering this high incidence, the complete absence of a restorative therapy, and the poor long-term prognoses for these patients, the need for a repair strategy that re-establishes meniscal function and delays or prevents the onset of osteoarthritis is evident. Thus, there is considerable interest in engineering fibrocartilaginous tissue for the replacement of damaged meniscus. To be effective, this tissue substitute must possess mechanical properties that approximate that of the native meniscus. Furthermore, the organization of matrix within this construct will be crucial to its performance *in situ*. In the following work, three-dimensional arrays of aligned electrospun fibers will serve as a micropattern for instructing cells to lay down organized fibrocartilaginous matrix. The essential components of this construct – the cells, scaffold, and culture conditions – will then be examined in detail. Taken together, these studies will advance the state of

meniscus tissue engineering, and establish the use of aligned electrospun scaffolds for building anisotropic tissues.

# ***CHAPTER 3: THE EFFECT OF NANOFIBER ALIGNMENT ON THE MATURATION OF ENGINEERED MENISCUS CONSTRUCTS***

## **3.1 INTRODUCTION**

The menisci are a pair of fibrocartilaginous wedges that play a central role in knee mechanics, increasing congruency and joint stability (Messner et al. 1998; Greis et al. 2002). With normal use, forces of several times body weight arise within the knee, with the menisci transmitting 50-100% of this load (Seedhom 1976; Ahmed et al. 1983) through its dense network of circumferentially aligned collagen (Shrive et al. 1978; Fithian et al. 1990; Petersen et al. 1998; Setton et al. 1999). This ordered architecture engenders very high tensile properties in the fiber direction (50-300 MPa) (Proctor et al. 1989; Fithian et al. 1990; Setton et al. 1999). Collagens make up 85-95% of the tissue (Eyre et al. 1983; McDevitt et al. 1990), while proteoglycans (PGs) comprise 2-3% of the dry weight, are concentrated in the cartilage-like inner regions (O'Connor 1976; Adams et al. 1992), and contribute to the compressive properties of the tissue. ECM is generated and maintained by meniscal fibrochondrocytes (MFCs), a heterogeneous cell population sparsely distributed throughout the tissue (McDevitt et al. 1990; Adams et al. 1992; Benjamin et al. 2004).

While the meniscus functions well with normal use, failures may occur as a result of traumatic injury or degenerative processes (MacAusland 1931; Cravener et al. 1941).

Repaired tears in the vascular periphery heal well, while those in the avascular inner region fail to do so, and thus damaged elements are commonly resected via partial meniscectomy. Removal of tissue results in higher cartilage contact stresses which may predispose patients to osteoarthritic (OA) progression. Replacing damaged regions of the meniscus with a living, biodegradable, mechanically competent construct may restore function and protect against further deleterious changes in the joint.

To this end, a number of tissue engineering strategies for restoring the meniscus have been developed. These strategies include the delivery of cells to the defect site, including chondrocytes, MFCs, and mesenchymal stem cells (MSCs) (Port et al. 1996; Peretti et al. 2004; Izuta et al. 2005). Additionally, direct replacement has been performed using both natural and synthetic scaffolds, including collagen-based grafts and macroporous polymeric meshes (Stone et al. 1992; Buma et al. 2004; Cook et al. 2006). These studies suggest that cell- and scaffold-based interventions hold promise for effective meniscus repair.

To further this area of inquiry, we focus on the generation of engineered meniscus constructs using nanofibrous biodegradable scaffolds formed via electrospinning. In this process, non-woven fibrous meshes are generated with fiber diameters on the order of hundreds of nanometers (Reneker et al. 1996; Deitzel et al. 2001). These nanofibrous scaffolds can be produced from a range of polymers and biopolymers (Matthews et al. 2002; Li et al. 2005; Li et al. 2005; Courtney et al. 2006; Li et al. 2006), with composition dictating the as-formed mechanical properties of the mesh and its

degradation rate. Numerous cell types attach to, differentiate on, and infiltrate these scaffolds, including MFCs and MSCs (Li et al. 2005; Li et al. 2007).

As described above, the fiber architecture and alignment of the meniscus endows the tissue with its unique functional properties. As such, this architecture must be one of the first considerations when engineering replacement constructs. To address this issue, nanofibrous meshes with controlled fiber alignment were produced by directing fiber deposition onto a rotating shaft (Boland et al. 2001; Theron et al. 2001), with the degree of alignment controlled by the target rotation speed. This controllable architecture in turn dictates the anisotropic mechanical properties of the scaffold (Ayres et al. 2006; Courtney et al. 2006; Nerurkar et al. 2006; Li et al. 2007). In this study, we hypothesize that, when seeded with cells, aligned scaffolds will serve as a 3D micro-pattern for directing neo-tissue formation, resulting in a mature construct with enhanced matrix content, organization, and mechanical properties compared to non-aligned scaffolds similarly maintained. Further, we test the hypothesis that MSCs may serve as a viable alternative to MFCs. To evaluate these hypotheses, MSCs and MFCs were seeded on both non-aligned (NA) and aligned (AL) nanofibrous scaffolds and cultured over a 10-week period in a chemically defined chondrogenic medium. We evaluated initial cell-scaffold interactions and long-term accumulation and distribution of ECM and the resulting change in mechanical properties.

## **3.2 MATERIALS AND METHODS**

### ***3.2.1 Nanofibrous Scaffold Production***

Poly( $\epsilon$ -caprolactone) (PCL) nanofiber meshes were produced via electrospinning as described in (Li et al. 2005). Briefly, a 14.3% w/v solution of PCL (Sigma, 80 kD) was prepared in a 1:1 solution of tetrahydrofuran and N,N-dimethylformamide (Fisher Chemical, Fairlawn, NJ) with continuous agitation over 72 hours. A total of 10 ml of the polymer solution was gravity-fed from a vertically-oriented 10 ml syringe fitted with a stainless steel 18G blunt needle, the end of which was positioned 20 cm above a grounded collecting surface. For nonaligned scaffolds (NA), the collecting surface consisted of a stationary copper plate covered with aluminum foil. To produce aligned scaffolds (AL), the copper plate was replaced with a mandrel (1" diameter, 8" length) rotating at ~7500 rpm, corresponding to a linear velocity of ~10 meters/sec (Li et al. 2007). A power supply (Gamma High Voltage Research, Inc., Ormond Beach, FL) was used to apply a 13 kV potential difference between the needle and the collecting surface. Nanofibers were collected for 12-16 hours, resulting in a fiber mat ranging in thickness from 0.9 to 1.3 mm. NA and AL scaffolds used in this study were of similar thicknesses and distribution (NA: 1.14 mm, AL: 1.11 mm,  $p > 0.487$ ).

### ***3.2.2 Cell Isolation and Expansion***

Meniscal fibrochondrocytes (MFCs) were isolated from the lateral and medial menisci of 3-6 month old calves. Mesenchymal stem cells (MSCs) were isolated from the tibial trabecular bone marrow of the same animals. For each replicate study, cells isolated from a minimum of 3 donors were pooled. For MFC isolation, menisci were diced into 1-2

mm<sup>3</sup> pieces and placed in tissue culture dishes with basal medium (DMEM containing 1X PSF (100 units/ml Penicillin, 100 µg/ml Streptomycin, 0.25 µg/ml Fungizone) and 10% Fetal Bovine Serum (FBS)). MFCs emerged from these pieces over a 1-2 week period and were sub-cultured at a 1:3 ratio through passage 2 as in (Mauck et al. 2007). MSCs were harvested from the tibial trabecular bone marrow of the same donors as in (Mauck et al. 2006). Briefly, the proximal end of the tibia was sectioned and trabecular marrow freed into DMEM supplemented with 300 units/mL heparin. After centrifugation for 5 minutes at 500 × g, pelleted matter was resuspended in basal medium and plated in 150 mm tissue culture dishes. Adherent cells formed numerous colonies through the first week, and were subsequently expanded through passage 2 at a ratio of 1:3 as above.

### ***3.2.3 Scaffold Seeding and Culture***

To produce cell-seeded constructs, individual scaffolds were excised as strips from nanofibrous sheets at 25 mm length by 5 mm width. For AL sheets, the long axis of the construct corresponded to the prevailing fiber direction. Strips were disinfected and rehydrated with decreasing concentrations of ethanol (100, 70, 50, 30%; 30 minutes per step). For acellular degradation studies, constructs were incubated in phosphate buffered saline (PBS) at 37°C. For cell seeding studies, the rehydration step was concluded by incubation in 20µg/mL fibronectin in PBS for 12 hours followed by two 5 minute washes in PBS. To seed scaffolds, 50 µl aliquots containing 2.5×10<sup>5</sup> cells (MSCs or MFCs) were loaded onto each scaffold four times (twice per side) at 30 minute intervals. After allowing an additional 2 hours for cell attachment, seeded constructs were cultured in 3 mL of chemically defined medium (high glucose DMEM with 1X PSF, 0.1 µM

dexamethasone, 50  $\mu\text{g}/\text{mL}$  ascorbate 2-phosphate, 40  $\mu\text{g}/\text{mL}$  L-proline, 100  $\mu\text{g}/\text{mL}$  sodium pyruvate, 1X ITS+ (6.25  $\mu\text{g}/\text{ml}$  Insulin, 6.25  $\mu\text{g}/\text{ml}$  Transferrin, 6.25  $\text{ng}/\text{ml}$  Selenous Acid, 1.25  $\text{mg}/\text{ml}$  Bovine Serum Albumin, and 5.35  $\mu\text{g}/\text{ml}$  Linoleic Acid) with 10  $\text{ng}/\text{mL}$  TGF- $\beta$ 3) in non-tissue culture treated 6-well plates. This chemically defined media formulation was used as it has previously been shown to both induce chondrogenesis of MSCs as well as promote deposition of fibrocartilaginous ECM by MFCs in pellet culture (Mauck et al. 2007). Media (and PBS) were changed twice weekly over a 10-week period.

### ***3.2.4 Visualization of Cell-Scaffold Interactions***

NA and AL scaffolds seeded with MSCs were examined with the Live/Dead kit (Molecular Probes, Eugene, OR) after 24 hours of culture to visualize cell morphology. Images of calcein AM-stained MSCs on AL and NA scaffolds were acquired with an inverted fluorescent microscope (Axiovert 200, Carl Zeiss MicroImaging, Inc., Thornwood, NY) at a magnification of 20 $\times$ . Additional samples were fixed in phosphate-buffered 4% paraformaldehyde for imaging with scanning electron microscopy (SEM). These specimens were dehydrated in ethanol (four steps, 30-100%, 60 minutes per step) with terminal dehydration in hexamethyldisilane under vacuum (Venugopal et al. 2005). After AuPd sputter coating, SEM was used to image both acellular and cell-seeded scaffolds (JEOL 6400, Penn Regional Nanotechnology Facility).

### ***3.2.5 Mechanical Testing***

Uniaxial tensile testing was performed with an Instron 5848 Microtester equipped with serrated vise grips and a 50N load cell (Instron, Canton, MA). A 0.5N preload was applied for 180 seconds to ensure proper seating of the sample. An externally mounted digital camera was used to obtain sample thickness and width from front and side views of the preloaded sample. After noting gauge length with a digital caliper, samples were preconditioned with 10 cycles of 0.5% of gauge length at 0.1Hz and subsequently extended to failure at 0.1% of gauge length per second. Construct stiffness was determined from the linear region of the force-elongation curve. Engineering stress (load normalized to cross-sectional area) and strain (displacement normalized to gauge length) was calculated, and construct modulus was determined from a 1% strain range within the linear region of the stress-strain curve.

### ***3.2.6 Biochemical Content***

After testing, samples were stored at -80°C until processing for biochemical composition. Samples were lyophilized in a Freezone 4.5 Freeze Dry System (LabConco, Kansas City, MO) for 24 hours and weighted to determine dry weight. After papain digest as in (Mauck et al. 2006), samples were processed for DNA, sulfated glycosaminoglycan (s-GAG), and collagen content using the Picogreen double-stranded DNA (dsDNA) (Molecular Probes, Eugene, OR), DMMB dye-binding (Farndale et al. 1986), and orthohydroxyproline (Stegemann et al. 1967) assays, respectively. These data are reported as mass of ECM element (s-GAG or collagen) per construct and as ECM content normalized to DNA content.

### ***3.2.7 Histological Analysis***

At each time point, samples were fixed overnight at 4°C in 4% phosphate-buffered paraformaldehyde, washed in PBS, and frozen in Optimal Cutting Temperature compound (OCT, Sakura Finetek USA, Inc., Torrance, CA). Cross-sections (spanning the depth and width of the scaffold) were cut to 8 microns with a Cryostat (Microm HM500, MICROM International GmbH, Waldorf, Germany). Sections were rehydrated and stained with Haematoxylin and Eosin (H&E), Alcian Blue (AB, pH 1.0), or Picrosirius Red (PSR) for cells, proteoglycans, or collagens, respectively. On separate samples at the terminal time point (Day 70), serial 8 micron sections through the depth were removed en face (in the length-width plane of the scaffold). En face sections taken deep to the scaffold surface were stained with PSR to enhance birefringence and imaged using a polarizing light microscopy system (DMLP, Leica Microsystems, Germany) to assess collagen organization. Images were acquired at a magnification of 5× for cross-sections and 10× for en face sections with a color CCD digital camera.

### ***3.2.8 Statistical Analysis***

Analysis of variance (ANOVA) was carried out with SYSTAT (v10.2, Point Richmond, CA) with Fisher's LSD post-hoc tests used to make pair-wise comparisons between groups, with significance set at  $p \leq 0.05$ . For both cellular and acellular (degradation) studies, two replicate studies were carried out with distinct donors and scaffold productions, with  $\geq 5$  samples analyzed per assay per replicate. Data from cellular studies

are presented as mean  $\pm$  standard deviation (SD) for a single replicate study, with terminal data from both replicates shown in Table 1.

### **3.3 RESULTS**

#### ***3.3.1 Scaffold Characterization and Cellular Interactions***

As we have previously reported (Nerurkar et al. 2006; Li et al. 2007), non-aligned (NA) nanofibrous scaffolds can be generated with deposition onto a stationary, grounded collecting plate (**Figure 3-1A**), while an organized aligned array (AL) of these same fibers may be generated by replacing the plate with a rotating mandrel (**Figure 3-1B**). In this study, orientation and shape of cells (MFCs or MSCs) were dictated by the scaffold architecture. For example, after 1 day in culture, MSCs viewed via SEM (**Figure 3-1C,D**) and by vital staining (**Figure 3-1E,F**) appeared polygonal on NA scaffolds while those on AL scaffolds took on a polarized morphology with their long axis oriented in the prevailing fiber direction. When acellular NA and AL scaffolds were incubated for 70 days in PBS, no change in mechanical properties was observed (data not shown, NA:  $p > 0.83$ , AL,  $p > 0.09$ ,  $n = 5-10$  per time point).

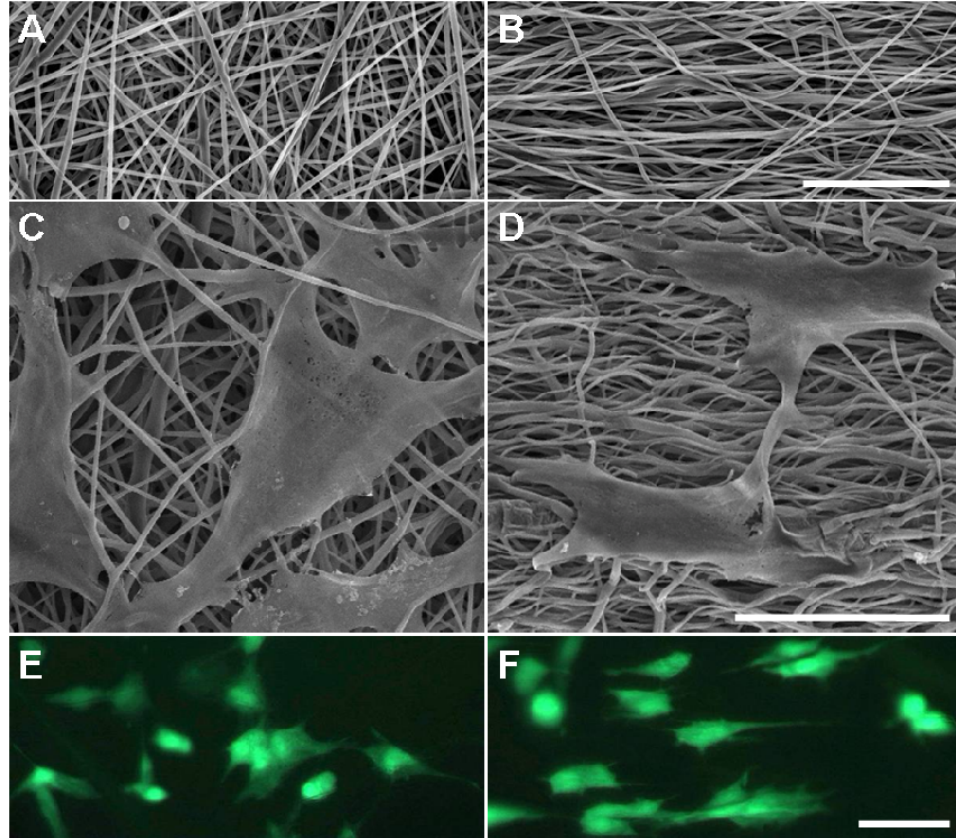


**Figure 3-1: Biodegradable scaffolds with sub-micron fiber diameters may be formed with randomly oriented fibers or with a distinct fiber alignment. Fibrous architecture dictates initial cell-scaffold interactions, including shape and polarity. SEM images of acellular (A) non-aligned (NA) and (B) aligned (AL) scaffolds. SEM and fluorescent images of MSCs on NA (C, E) and AL (D, F) scaffolds after one day of culture. Scale bars: 50  $\mu\text{m}$ .**

### ***3.3.2 Biochemical Content of Cell-Laden Scaffolds***

To assess long-term maturation of constructs, cell-seeded scaffolds were cultured for 10 weeks in a chemically defined medium in two replicate studies. Data from one representative study is shown, with the change in measured parameters over the time course for each replicate provided in **Table 3-1**.

**Table 3-1: Change in measured parameters (compared to day 1) for two replicate studies of MFC- and MSC-laden AL and NA nanofibrous scaffolds over 70 days in free swelling culture.**

	<b>Study 1*</b>				<b>Study 2</b>			
<b>Cell Type</b>	<b>MFC</b>		<b>MSC</b>		<b>MFC</b>		<b>MSC</b>	
<b>Scaffold Alignment</b>	<b>NA</b>	<b>AL</b>	<b>NA</b>	<b>AL</b>	<b>NA</b>	<b>AL</b>	<b>NA</b>	<b>AL</b>
<b>Δ Mass (mg)</b>	<b>3.3</b>	2.8	<b>2.5</b>	2.5	<b>5.6</b>	5.1	<b>8.8</b>	6.5
<b>Δ DNA (ng)</b>	<b>8.9</b>	9.2	<b>5.3</b>	7.3	<b>11.8</b>	13.0	<b>9.6</b>	10.2
<b>Δ GAG (μg)</b>	<b>104</b>	161	<b>151</b>	303	<b>165</b>	203	<b>325</b>	405
<b>Δ Collagen (μg)</b>	<b>119</b>	173	<b>162</b>	213	<b>124</b>	133	<b>139</b>	206
<b>Δ Stiffness (N/mm)</b>	<b>0.4</b>	4.2	<b>0.7</b>	4.5	<b>0.1</b>	5.6	<b>1.0</b>	6.8
<b>Δ Modulus (MPa)</b>	<b>1.0</b>	7.6	<b>1.4</b>	7.2	<b>-0.4</b>	4.4	<b>1.3</b>	7.2

\*Data from Study 1 are plotted in this manuscript.

With time, both MSC- and MFC-laden constructs increased in mass (**Figure 3-2A**). Irrespective of scaffold architecture, an ~3 mg increase in mass was observed for both cell types over 10 weeks ( $p < 0.05$ ). Additionally, constructs thickened with time (data not shown,  $p < 0.005$ ), increasing by ~40% by day 70. Cell number, as measured by DNA content, was dependent on time in culture ( $p < 0.001$ ), scaffold alignment ( $p < 0.001$ ), and cell type ( $p < 0.001$ ). Notably, DNA content increased in both MSC and MFC-seeded constructs up to day 42, after which levels plateaued (**Figure 3-2B**). At the final time point, MSC-seeded constructs contained fewer cells than MFC-seeded constructs (AL:  $p < 0.05$ , NA:  $p < 0.001$ ).

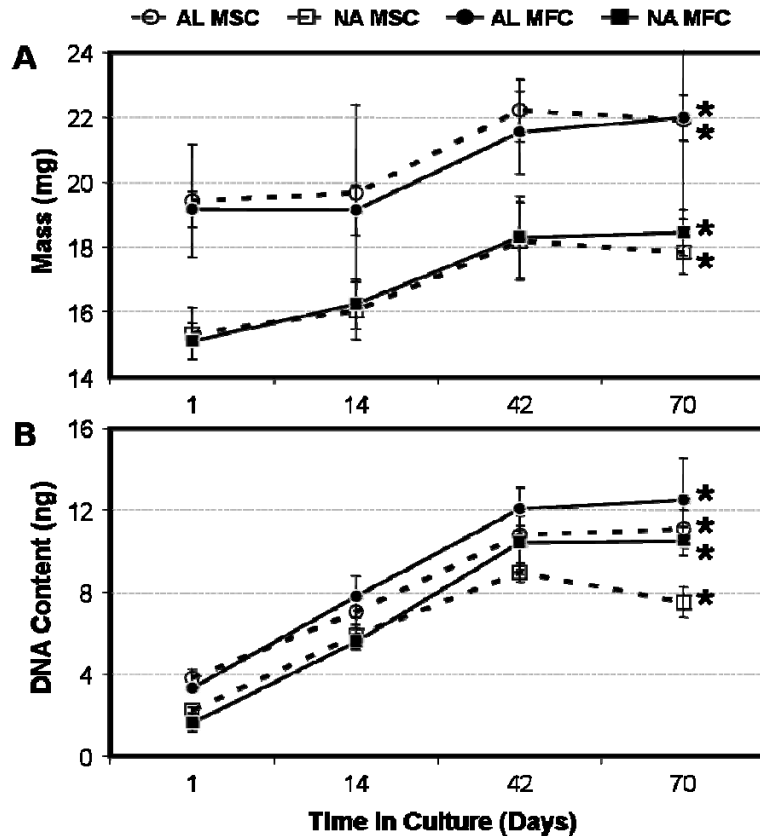


**Figure 3-2:** Cell-seeded constructs increase in mass and DNA content with time in culture. Construct mass (A) and DNA content (B) of MFC- and MSC-laden AL and NA nanofibrous scaffolds. \* indicates  $p < 0.05$  vs. day 1 within group for construct mass (bracket indicates all groups at time point); \* indicates  $p < 0.001$  vs. day 1 within group for DNA content,  $n = 5$  per group per time point.

ECM content also increased in constructs in a time-dependent manner. s-GAG content increased in all groups by day 42 (Figure 3-3A,  $p < 0.001$ ). For this replicate study, all groups, with the exception of NA-MSc, continued to increase in s-GAG content through day 70. Overall, the total s-GAG per construct was highly dependent on time in culture ( $p < 0.001$ ) and cell type ( $p < 0.001$ ). While there were differences in s-GAG content observed between AL and NA scaffolds at certain time points (particularly at day 70), neither architecture resulted in consistently higher s-GAG content at every time point. Similar trends were seen after normalizing s-GAG to DNA content. By day 42, MSCs

seeded on both NA and AL scaffolds produced higher amounts of s-GAG (and s-GAG/DNA) than their MFC counterparts (Figure 3-3A,B,  $p < 0.001$ ).

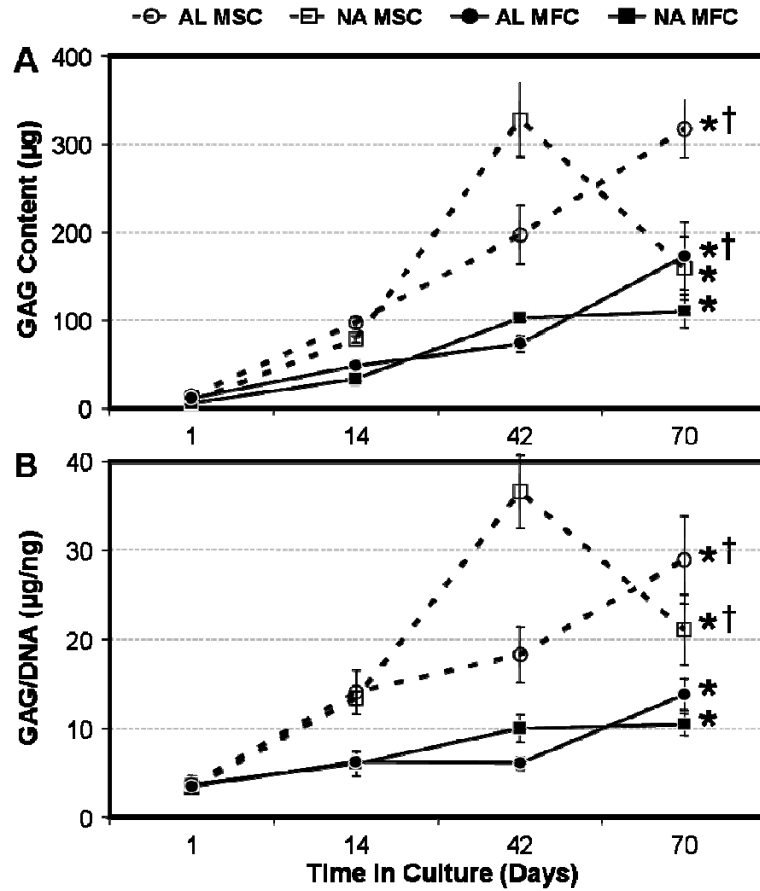
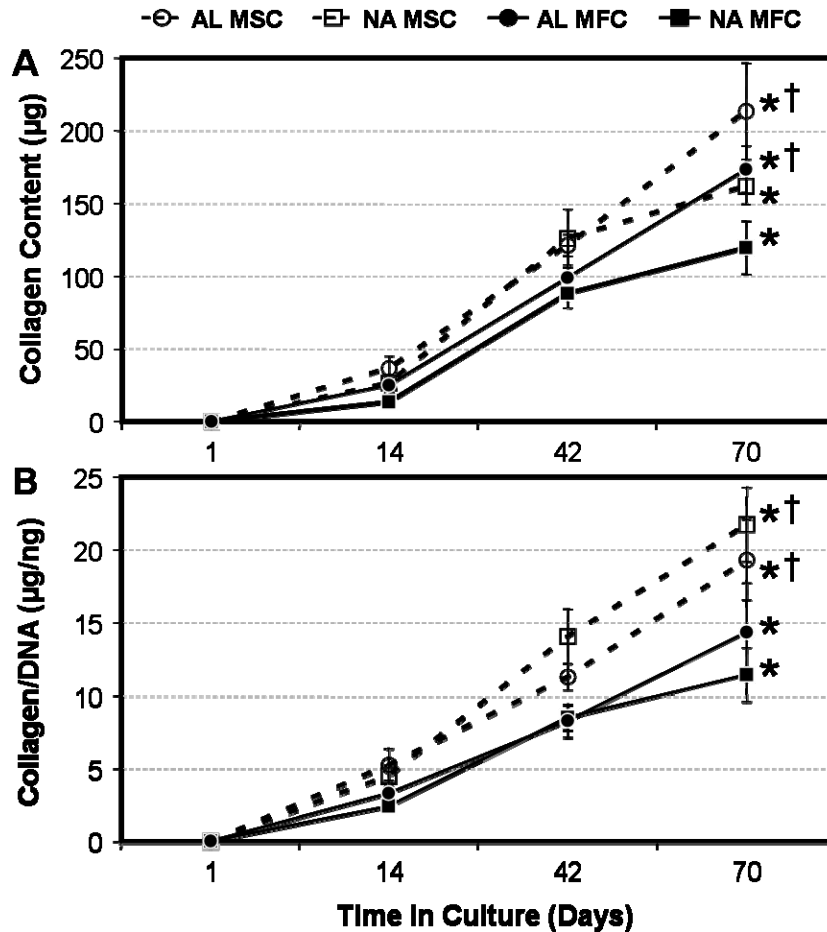


Figure 3-3: MFCs and MSCs deposit a proteoglycan-rich matrix on NA and AL scaffolds with time in culture. Total s-GAG content per scaffold (A) and s-GAG content normalized to DNA (B) of MFC- and MSC-laden AL and NA nanofibrous scaffolds with time in culture. \* indicates  $p < 0.001$  vs. day 1 within group; # indicates  $p < 0.001$  vs. NA within same cell type at same time point; † indicates  $p < 0.001$  vs. MFC group of same alignment at same time point,  $n = 5$  per group per time point.



**Figure 3-4:** MFCs and MSCs deposit a collagen-rich matrix on NA and AL scaffolds with time in culture. Total collagen content per scaffold (A) and collagen content normalized to DNA (B) of MFC- and MSC-laden AL and NA nanofibrous scaffolds with time in culture. \* indicates  $p < 0.001$  vs. day 1 within group; # indicates  $p < 0.001$  vs. NA within same cell type at same time point; † indicates  $p < 0.001$  vs. MFC group of same alignment at same time point,  $n = 5$  per group per time point.

Total collagen per construct was dependent on time ( $p < 0.001$ ), cell type ( $p < 0.001$ ), and alignment ( $p < 0.001$ , **Figure 3-4A**). Collagen was not detectable in day 1 samples. By day 14, collagen was detected in all groups and significant increases were observed between days 14 to 42 ( $p < 0.001$ ), as well as from day 42 to 70 ( $p < 0.001$ ). As with s-GAG content, MSC-seeded constructs contained higher collagen than MFC-seeded constructs, irrespective of underlying architecture, from day 42 forward ( $p < 0.001$ ). Within a cell type, no difference was observed between AL and NA constructs at days 14

(MSC:  $p>0.16$ , MFC:  $p>0.23$ ) and 42 (MSC:  $p>0.20$ , MFC:  $p>0.57$ ). On day 70, modest increases were seen in the collagen content of AL compared to NA constructs for both cell types ( $p<0.001$ ). These findings suggest that scaffold alignment has less effect on collagen production than time in culture or cell type. For collagen data normalized to DNA content (**Figure 3-4B**), cell type had a strong influence ( $p<0.001$ ) while scaffold architecture had no effect ( $p>0.75$ ), even on day 70. Irrespective of architecture, MSC-laden constructs contained more collagen per cell than MFC-laden constructs on days 14 ( $p<0.05$ ), 42 ( $p<0.001$ ), and 70 ( $p<0.001$ ).

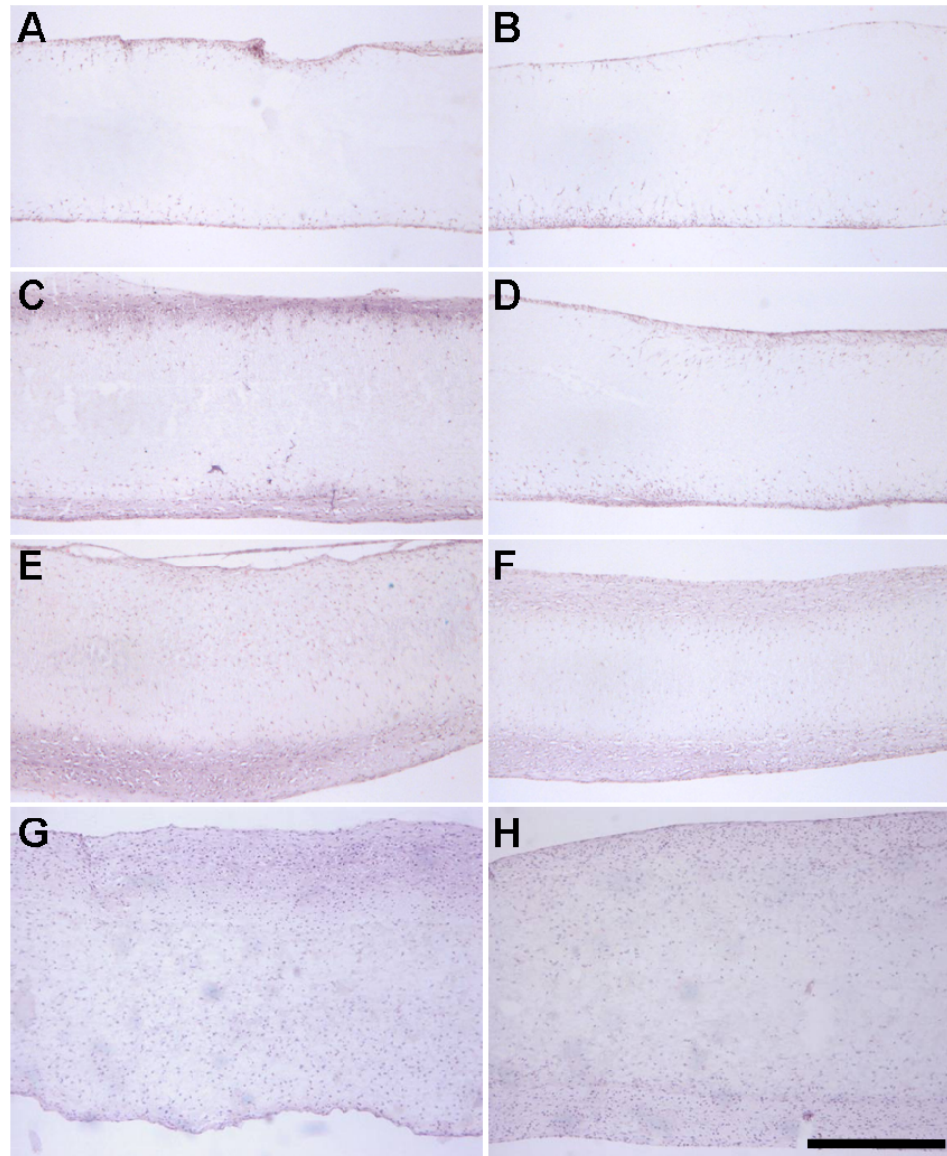


**Figure 3-5: MFCs and MSCs infiltrate nanofibrous scaffolds in a time-dependent fashion, with full colonization occurring between days 42 and 70. H&E staining of cross sections of MSC- (A, C, E) and MFC- (B, D, F) laden AL scaffolds on days 14 (A, B), 42 (C, D), and 70 (E, F). NA scaffolds seeded with MSCs (G) and MFCs (H) on day 70 are shown for comparison. Scale bar: 500  $\mu$ m.**

### **3.3.3 Histologic Appearance of Cell-Laden Scaffolds**

Cell localization and regional distribution of matrix deposition were assessed by staining of construct cross sections with time in culture (1-70 days), cell type (MFC and MSC), and scaffold architecture (NA and AL). No striking differences were observed between

NA and AL scaffolds, and so the time course of cell infiltration is shown only for AL scaffolds for each cell type. H&E staining revealed a time-dependent progression of cellular infiltration (**Figure 3-5**). On day 1 a sparse cell population was observed on the periphery (data not shown) that by day 14 completely covered the construct and had penetrated through the outer 100-200  $\mu\text{m}$  (**Figure 3-5A,B**). By day 42, constructs were covered with a multi-layer sheath of cells (**Figure 3-5C,D**), with some cells penetrating to depths of  $\sim 300$   $\mu\text{m}$  from each edge. By day 70, MFCs and MSCs colonized the entire scaffold thickness, though they remained less dense at the center compared to the edge (**Figure 3-5E,F**). A similar time course and final degree of colonization was observed for NA scaffolds seeded with both cell types (**Figure 3-5G,H**).

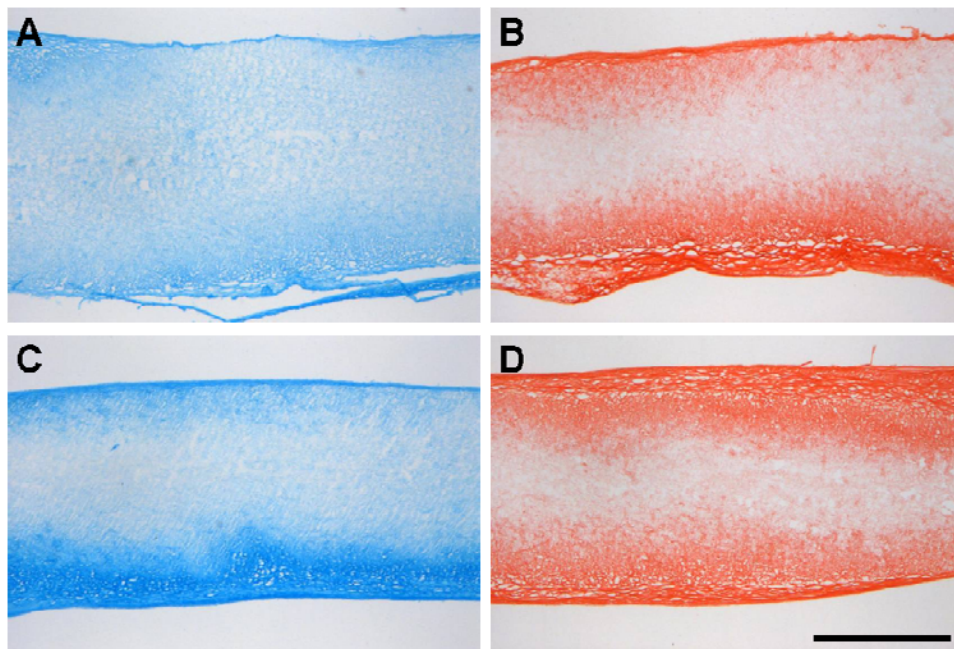


**Figure 3-6:** Histological staining of collagen and proteoglycan (PG) deposition over the cross sections of cell-laden AL constructs on day 70. MFC- (A,B) and MSC- (C,D) laden AL nanofibrous stained with Alcian Blue (A,C) for PGs and Picrosirius Red (B,D) for collagens. PG deposition is observed throughout the scaffold, while collagen is restricted to the outer two-thirds. Scale bar: 500  $\mu\text{m}$ .

Over the same time course, proteoglycan (PG) staining became more intense for both cell types, irregardless of scaffold alignment (data not shown). At early times, PG was most concentrated at the scaffold periphery (coincident with cells), though a deep and homogenous distribution was seen by day 70 for both MSC- and MFC-seeded constructs (**Figure 3-6A,B**). PG staining was generally greater for MSC- than for MFC-seeded constructs. Compared to PG staining, collagen was more heavily concentrated at the scaffold boundary (**Figure 3-6C,D**). By day 70, the outer ~300  $\mu\text{m}$  of each side of the scaffold showed similar staining intensity. Differences between MSC- and MFC-seeded constructs were less prominent than for PG staining. Alignment of collagenous matrix in day 70 en face sections taken ~200 microns deep to the construct surface showed a marked difference in organization in AL compared to NA constructs for both cell types (**Figure 3-7**). Specifically, while abundant PSR staining was observed in en face sections for both NA and AL scaffolds, more intense birefringence (orange in polarized images) corresponded to aligned collagen deposition only in AL constructs.

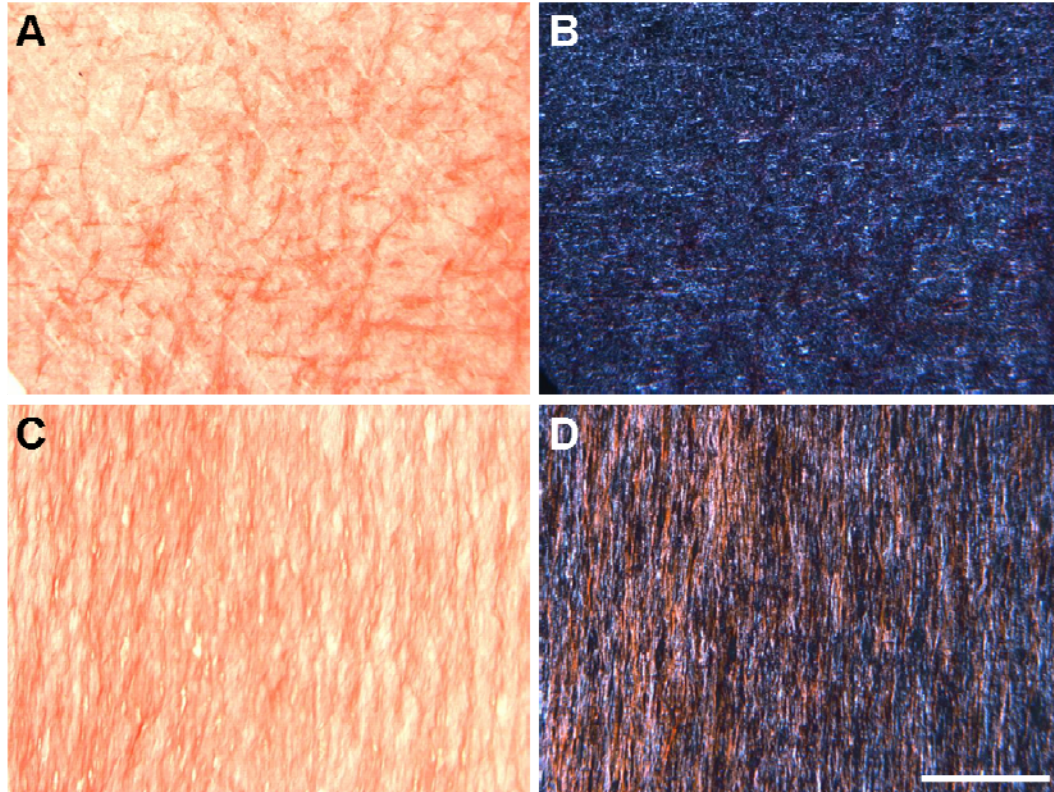


**Figure 3-7:** Scaffold architecture influences the organization of forming neo-tissue with long term culture. Bright-field (A,C) and polarized light (B,D) microscopy images of *en face* sections of NA (A,B) and AL (C,D) scaffolds seeded with MSCs on day 70. Sections were taken ~200  $\mu\text{m}$  deep to the scaffold surface and stained with Picrosirius Red (PSR) to enhance birefringence of collagen stained areas (orange). Scale Bar: 200  $\mu\text{m}$ .

### 3.3.4 Tensile Mechanical Properties of Cell-Laden Scaffolds

Tensile testing was carried out to determine the contribution of newly formed matrix to the load-bearing capacity of constructs with time in culture (stiffness, **Figure 3-8A**; modulus, **Figure 3-8B**). At the outset of culture (day 1), stiffness and modulus of AL scaffolds were ~3-fold higher than NA scaffolds ( $p < 0.001$ ). For cell-seeded scaffolds, both time in culture ( $p < 0.001$ ) and scaffold alignment ( $p < 0.001$ ) were determining factors in the mechanical properties of each construct, while cell type was not ( $p > 0.344$ ). NA constructs, irregardless of cell type, showed a nominal increase in modulus. For example MFC-seeded NA constructs increased from 4.0 MPa on day 1 to 5.0 MPa on day 70, a

25% increase. Similarly, the stiffness of these constructs increased from 1.5 N/mm to 1.8 N/mm. In contrast, MFC-laden AL constructs increased in modulus over the same time course, from 12.1 MPa to 19.7 MPa, a 63% increase ( $p < 0.001$ ). Likewise, these constructs nearly doubled in stiffness from 4.5 N/mm on day 1 to 8.7 N/mm on day 70. Notably, these increases in mechanical properties were directed by the aligned scaffold architecture and not cell type, as MSCs performed similarly to MFCs in both replicate studies (Table 3-1).

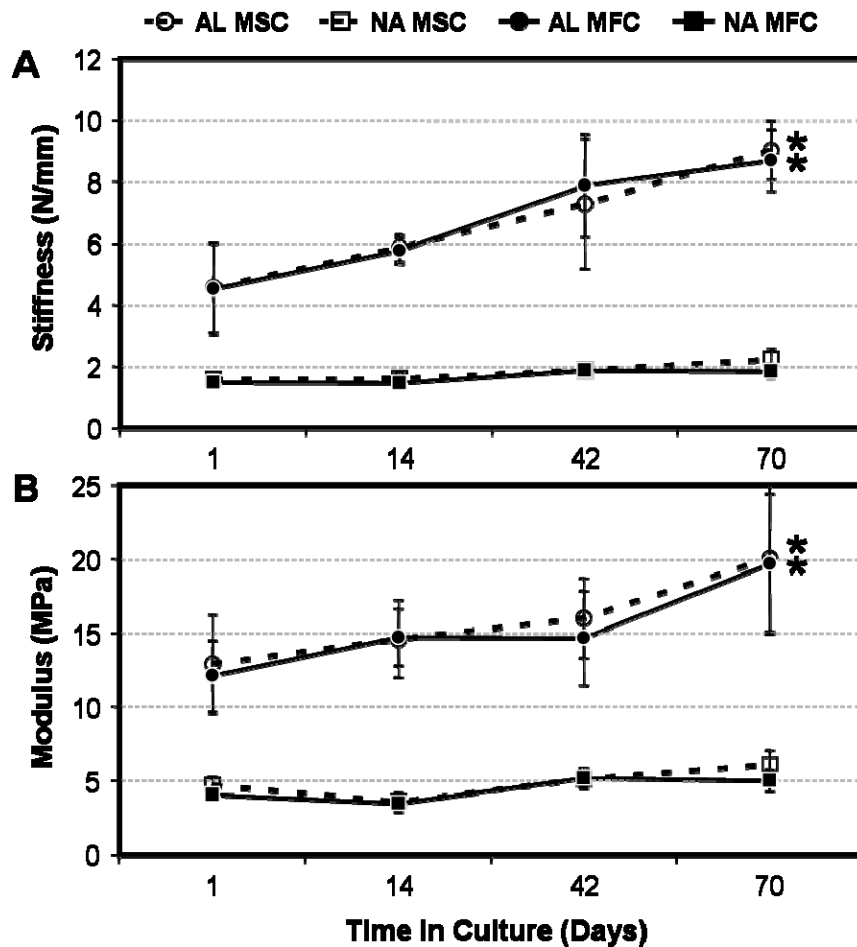


**Figure 3-8:** Time-dependent changes mechanical properties of cell-laden constructs are dependent on starting scaffold architecture but not cell type. Tensile properties (stiffness: A; modulus: B) of MFC- and MSC-laden AL and NA nanofibrous scaffolds with time in culture. \* indicates  $p < 0.001$  vs. day 1 within group; # indicates  $p < 0.001$  vs. NA within same cell type at same time point;  $n = 5$  per group per time point.

### 3.4 DISCUSSION

The mechanical function of the meniscus is dependent on its unique fiber-aligned collagen architecture. When damage occurs, this architecture is interrupted and the ability of the meniscus to transmit load is compromised (Messner et al. 1998). In this study, we address the repair of such defects with the fabrication and maturation of meniscus constructs using nanofibrous scaffolds whose architecture and anisotropy mimic that of the native tissue. We evaluated non-aligned (NA) and aligned (AL) nanofibrous meshes (**Figure 3-1**) formed from poly( $\epsilon$ -caprolactone) (PCL), a slow degrading polyester. As we have previously reported (Nerurkar et al. 2006), deposition of PCL nanofibers onto a rotating mandrel results in scaffolds with significant anisotropy, such that AL scaffolds tested in the fiber direction were 3 times stiffer than NA scaffolds at the outset of the study (**Figure 3-8**). Further, nanofibrous meshes formed from PCL maintain their organization and fiber diameter for long time periods in physiologic conditions, offering a stable micro-pattern for directed matrix deposition (Li et al. 2006).

When seeded with MFCs or MSCs, the underlying architecture of the nanofibrous scaffolds directed cellular morphology. The aligned cellular arrays produced in this study are similar to those observed when cells are exposed to micro-contact printed strips (Mrksich et al. 1997; Wheeler et al. 1999) and topographic channels (Wang et al. 2003) in monolayer cultures. During culture in a chemically defined medium, cells divided and occupied the entirety of the scaffold, and deposited a fibrocartilaginous matrix similar in composition to the native tissue. This ECM contributed to time-dependent increases in

the mechanical properties of the construct. Most strikingly, these increases depended primarily on underlying scaffold architecture – both MSC- and MFC-seeded NA scaffolds increased by ~1 MPa, while these same cells increased AL scaffold properties by >7 MPa. Interestingly, while marked increases in mechanical properties only occurred with AL scaffolds (**Figure 3-8**), both cell types on NA and AL scaffolds resulted in similar cell content and degree of infiltration as well as comparable bulk quantities of ECM (**Figures 3-3, 3-4**). This finding is counter to that previously observed on aligned polyurethane nanofibers after one week of culture, where AL scaffolds increased collagen deposition by ligament fibroblasts compared to NA scaffolds (Lee et al. 2005). In aligned monolayer cultures, linear arrays of fibroblasts organize their collagen deposition with respect to the underlying surface topography (Wang et al. 2003). Preliminary analysis of collagen organization suggests a similar mechanism at work in AL scaffolds, with pronounced collagen alignment observed under polarized light (**Figure 3-7**). These findings suggest that AL scaffolds serve as 3D micro-pattern for directing both the short- and long-term organization of cells and newly deposited ECM, and that this organization, rather than the amount of matrix produced, dictates the functional maturation of these meniscal constructs.

At the outset of this study, we hypothesized that, given their ability to undergo mixed fibrous/cartilaginous differentiation, MSCs may serve as a useful alternative to MFCs for the production of meniscus constructs. The clinical need for an alternative to MFCs arises from the scarcity of healthy autologous cells, and the fact that invasive surgical procedures are required for their isolation. MSCs may be suitable for this application, as

they are readily available from bone marrow (Pittenger et al. 1999), and can be isolated from aged donors without significant loss in fibrocartilaginous potential (Barry et al. 2001). The results of this study show that MSC-laden constructs produce higher levels of collagen and proteoglycan than MFC-laden scaffolds similarly maintained. Importantly, the MSC-deposited matrix is functional, leading to equivalent gains in the mechanical properties of constructs seeded with either cell type. It should be noted that the analyses carried out in this study were solely bulk measures of proteoglycan and collagen accumulation. Quantitative assessment of meniscus-specific matrix components, such as collagen types as well as expression and distribution of decorin, versican, and biglycan (Benjamin et al. 2004; Upton et al. 2006), may shed further light on similarities and differences between MFCs and MSCs, as well as the macromolecular underpinnings of the improvement of functional mechanical properties seen in AL compared to NA scaffolds in this study. Nevertheless, these findings do demonstrate the potential of MSCs to colonize and produce mechanically functional ECM in AL nanofibrous scaffolds in a manner similar to healthy primary MFCs, indicating their potential for meniscus tissue engineering applications.

While the results of this study are promising and repeatable (Table 1), several issues remain to be optimized in the production of a functional construct for meniscus repair. First, the mechanical properties of cell-seeded aligned scaffolds approach only ~20 MPa, a value ~1/10th (Proctor et al. 1989) to ~1/4th (Bursac et al. 2009) that of the native tissue measured in the fiber direction. One explanation for this finding may be tied to development. Similar to such tissues as the annulus fibrosus of the intervertebral disc

(Hayes et al. 1999), aligned meniscus cells arise first, prior to organized matrix deposition (Clark et al. 1983). At this stage of development, if mechanical forces resulting from in utero muscle contraction are abrogated, the meniscus fails to mature and ultimately regresses (Mikic et al. 2000). Conversely, with continued normal motion, and more strikingly with load-bearing use, initial cellular organization presages a rapid and robust accumulation of dense fiber-reinforced ECM (Clark et al. 1983). In this study, matured cell-seeded AL scaffolds possess the appropriate cell and matrix organization, but, like the developing native tissue, may require additional signals such as mechanical preconditioning to achieve properties comparable to the functionally differentiated adult load-bearing tissue.

A second limitation found in this study was the long time course required for mechanical properties to emerge. This slow accumulation in properties may be related to the rate at which cells colonize the scaffold interior. In this study, full colonization of ~ 1 mm thick scaffolds was achieved, but only between the six and ten week culture time points (**Figure 3-5**). Further, while cells colonized the entirety of the scaffold, their distribution and that of the forming matrix remained biased towards the outer periphery (**Figure 3-6**). Similar findings have been noted in nanofibrous meshes of various compositions implanted in a rat model (Telemeco et al. 2005). A number of strategies have been proposed to address this issue, including electrospraying cells directly into the forming nanofibrous scaffold during deposition (Stankus et al. 2006). Alternatively, design criteria may be imposed on polymer composition such that scaffold degradation is tuned to promote cellular colonization.

### **3.5 CONCLUSIONS**

The results of this study demonstrate that AL nanofibrous scaffolds serve as a micro-pattern for directed tissue growth and that, when seeded with either MFCs or MSCs, produce constructs with improved mechanical properties compared to NA scaffolds. Importantly, these improvements were dependent on the organization of the forming neo-tissue, and not on its overall content. Furthermore, we showed that MSCs serve as a viable alternative, colonizing and forming ECM and mechanical properties on par with that formed by native MFCs. While properties improve substantially on AL scaffolds, these studies highlight the need for further optimization to achieve native tissue properties. Additional considerations, such as the inclusion of radial tie fibers and recapitulation of the anatomic wedge-shaped form, may also be important for improving construct integrity and in vivo application. If successful, these scaffolds will find wide application in the repair of meniscal defects, a prevalent and otherwise untreatable orthopaedic condition. Further, these AL nanofibrous scaffolds may in general offer a ready solution to the challenge of tissue engineering other dense fibrous tissues of the musculoskeletal system whose mechanical function is critical to locomotion but whose endogenous repair is limited.

# ***CHAPTER 4: SELECTIVE REMOVAL OF SACRIFICIAL FIBERS IMPROVES CELL INFILTRATION IN COMPOSITE FIBER-ALIGNED NANOFIBROUS SCAFFOLDS***

## **4.1 INTRODUCTION**

Fibrous tissues are the primary soft tissue element of the musculoskeletal system. These dense, collagen-rich connective tissues serve critical load-bearing roles, with their fibrous architectures organized to optimize mechanical function. For example, tendons, ligaments, the knee menisci, and the annulus fibrosus of the intervertebral disc all transmit tensile loads generated with physiologic motion through their aligned extracellular matrix (ECM) (Setton et al. 1999; Lynch et al. 2003; Holzapfel et al. 2005). This ECM organization imbues the tissues with mechanical properties that are highly anisotropic and highest in the prevailing fiber orientation. While critical for musculoskeletal function, the demanding mechanical environment in which these tissues perform predisposes them to damage and endogenous repair processes do not restore normal tissue structure and function. Instead, the once highly-ordered tissue is replaced by a disorganized scar that is mechanically inferior and prone to re-injury (Newman et al. 1989; Beredjikian et al. 2003). Thus, there exists an unmet clinical need for an implantable tissue or tissue substitute that can guide repair or replace damaged fiber-reinforced tissues.

Towards this end, we and others have focused on the development of electrospun scaffolds composed of aligned nanofibers for soft tissue repair (Reneker et al. 1996; Li et al. 2005; Ayres et al. 2006; Courtney et al. 2006; Li et al. 2007). These scaffolds are formed through the process of electrospinning, in which charge repulsion initiates fiber jets from a polymer solution that are subsequently drawn through a large voltage gradient (Deitzel et al. 2001). At the collecting surface, micron to nanometer scale fibers build up layer-by-layer into a fibrous scaffold assembly. Numerous polymers have been electrospun, including both non-degradable and degradable synthetics as well as several biopolymers and proteins (for review, see (Li et al. 2005)). When formed into scaffolds, these fibers mimic the length scale of native ECM, and because of their tissue-mimetic topographies, can promote improved ECM deposition in comparison to other scaffolding architectures (Li et al. 2006). Additionally, when these same fibers are collected on a rotating mandrel, fiber alignment increases with increasing collector rotation speed, resulting in scaffolds that possess controllable and predictable mechanical and structural anisotropy (Courtney et al. 2006; Ayres et al. 2007; Li et al. 2007; Nerurkar et al. 2007). This organization recapitulates that of the ECM of fiber-reinforced tissues, and when seeded with cells, can serve as a 3D micro-pattern for promoting organized neo-tissue formation. In Chapter 3 using aligned poly( $\epsilon$ -caprolactone) (PCL) nanofiber scaffolds, we showed that mesenchymal stem cells (MSCs) aligned, deposited organized collagen, and increased the construct tensile properties in the predominant nanofiber direction. Conversely, when these same cells were seeded on non-aligned or randomly-oriented scaffolds, disorganized cell orientations and matrix deposition was observed to coincide with lesser improvements in mechanical properties.

While aligned nanofibrous scaffolds show promise for fiber-reinforced tissue engineering applications, several important limitations remain to be addressed. The most significant of these is the slow rate of cellular infiltration into these dense structures. This is more prevalent in scaffolds formulated from slow or non-degradable polymers. Even in non-aligned scaffolds, where solid content is on the order of 10% (and porosity on the order of 90%), cell infiltration is slow. When aligned, more efficient fiber packing results in increased scaffold density and reduced pore sizes, further limiting cellular ingress. For example, in our previous studies employing PCL, a slow-eroding polyester, human and bovine meniscus fibrochondrocytes infiltrated only the outer two-thirds of 1mm thick aligned scaffolds after ten weeks of *in vitro* culture (Chapter 3 & 7). Although it is not known if complete infiltration would have occurred given a longer culture period, more rapid colonization is clearly required for clinical applications.

To address this issue, a number of methodologies for improving infiltration have been proposed. Most directly, a novel system has been developed in which cells are electrosprayed directly into the forming nanofibrous scaffold (Stankus et al. 2006). While this method can generate cell-interspersed nanofibrous networks, issues of layering and challenges in sterility and time (for the production of thicker scaffolds) may limit its application. Others have noted that many of the synthetic polymers employed are not particularly amenable to dictated remodeling and have electrospun biopolymers such as collagen, elastin, and fibrinogen (Li et al. 2005; Buttafoco et al. 2006; McManus et al. 2006). Telemeco and coworkers compared cell infiltration into various electrospun

collagen or polyester meshes implanted in rat muscle interstitium. They reported that while the synthetic scaffolds induced fibrosis and were minimally colonized, electrospun collagen scaffolds were fully infiltrated after one week (Telemeco et al. 2005). However, the mechanical properties of electrospun biopolymers are several orders of magnitude lower than that of most synthetic polymer based meshes, even after crosslinking (Matthews et al. 2002; Li et al. 2006), limiting their application in situations where load bearing is required.

Another method for improving infiltration in dense nanofibrous networks may be by increasing scaffold porosity. Ongoing work with porous foams and sponges suggests that there exists an optimal pore size to promote cell infiltration (van Tienen et al. 2002). For nanofibrous scaffolds, this approach has been addressed by mixing fibers of different diameters to limit fiber packing (Pham et al. 2006). Alternatively, pores may be introduced by including salt particles at the time of production and subsequently leaching them out (Nam et al. 2007). Using this technique, some improvement in cell infiltration was observed in non-aligned scaffolds, though significant delamination was observed at the salt induced interfaces.

As our goal is to create and preserve structural anisotropy to foster fiber-reinforced tissue formation, we developed an approach based on the inclusion of sacrificial fibers in a composite nanofibrous scaffold (**Figure 4-1**). We hypothesized that the selective removal of sacrificial elements from a mixed fiber population would increase scaffold porosity, and thereby accelerate cell infiltration. We also hypothesized that the

mechanical properties of the composite scaffolds before and after sacrificial fiber removal would reflect the fractions of each interspersed fiber population, and that anisotropy would be preserved. To test these hypotheses, we developed a dual-electrospinning process for creating aligned scaffolds containing both a slow degrading and a sacrificial component. PCL and poly(ethylene oxide) (PEO) were selected based on their characteristic degradation and dissolution times; PCL is a slow degrading polymer and serves as a long-term structural element, while PEO dissolves immediately in aqueous solution and serves as the sacrificial fiber component. Using this system, we created fully interspersed nanofibrous constructs containing a range of sacrificial fiber (PEO) fractions. We evaluated the mechanical properties and anisotropy of these scaffolds in their ‘as formed’ state and after removal of the sacrificial component. Further, we measured MSC infiltration after 3 weeks into composite fiber-aligned scaffolds with a range (0-90%) of sacrificial fiber fractions.

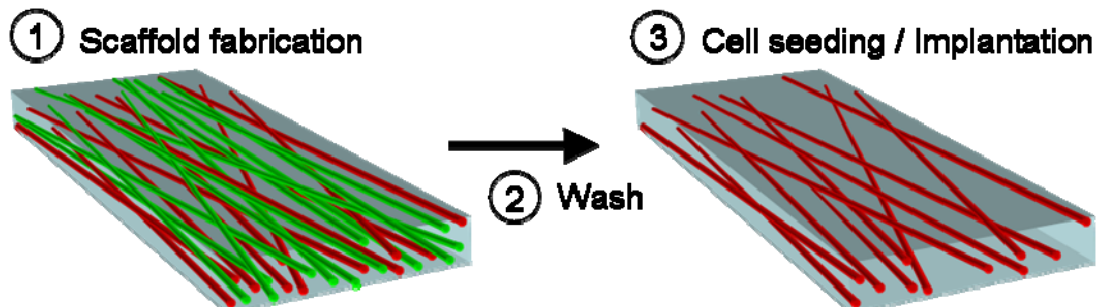


**Figure 4-1: To improve cellular colonization of dense, aligned nanofibrous matrices, composite scaffolds were formed with two populations of interspersed nanofibers. Schematic depicting scaffold fabrication and subsequent removal of a sub-population of sacrificial fibers (green).**

## 4.2 MATERIALS AND METHODS

### 4.2.1 *Formation of Single-Polymer and Composite Nanofibrous Scaffolds*

In this study, composite fiber-aligned nanofibrous scaffolds were produced by dual-component electrospinning. A 14.3% w/v solution of PCL (80kDa, Sigma-Aldrich, St. Louis, MO) was made in a 1:1 mixture of tetrahydrofuran and N,N-dimethylformamide (Fisher Chemical, Fairlawn, NJ) by stirring at 40°C for 18 hours. PEO (200kDa, Polysciences, Inc., Warrington, PA) was dissolved in 90% ethanol with stirring at room temperature for six hours to yield a 10% w/v solution. The polymer solutions were electrospun using a custom electrospinning device to generate fiber-aligned meshes comprised of PCL, PEO, or a mixture of discrete PCL and PEO fibers (**Figure 4-2**). To electrospin each component, separate 20ml syringes were filled with PCL or PEO and fitted with a 5cm length of flexible silicon tubing connected to a 12" long stainless steel 18G blunt-ended needle that served as the charged spinneret. Spinnerets reciprocated over an 8cm path (6.4cm/sec) along the mandrel under the control of two custom-built 'fanners'. The flow rate of both solutions was maintained at 2.5ml/h via syringe pump (KDS100, KD Scientific, Holliston, MA). A power supply (ES30N-5W, Gamma High Voltage Research, Inc., Ormond Beach, FL) was used to apply a +13kV potential difference between the spinnerets and the grounded aluminum mandrel ( $\text{\O} = 2''$ ), which was rotated via a belt mechanism conjoined to an AC motor (Pacesetter 34R, Bodine Electric, Chicago, IL) to achieve a linear velocity of  $\sim 10\text{m/s}$ . PCL and PEO fibers were collected over a spinneret-mandrel distance of 15 and 10cm, respectively. Additionally, two aluminum shields charged to +10kV were placed perpendicular to and on either side of the mandrel to better direct the electrospun fibers towards the grounded mandrel.

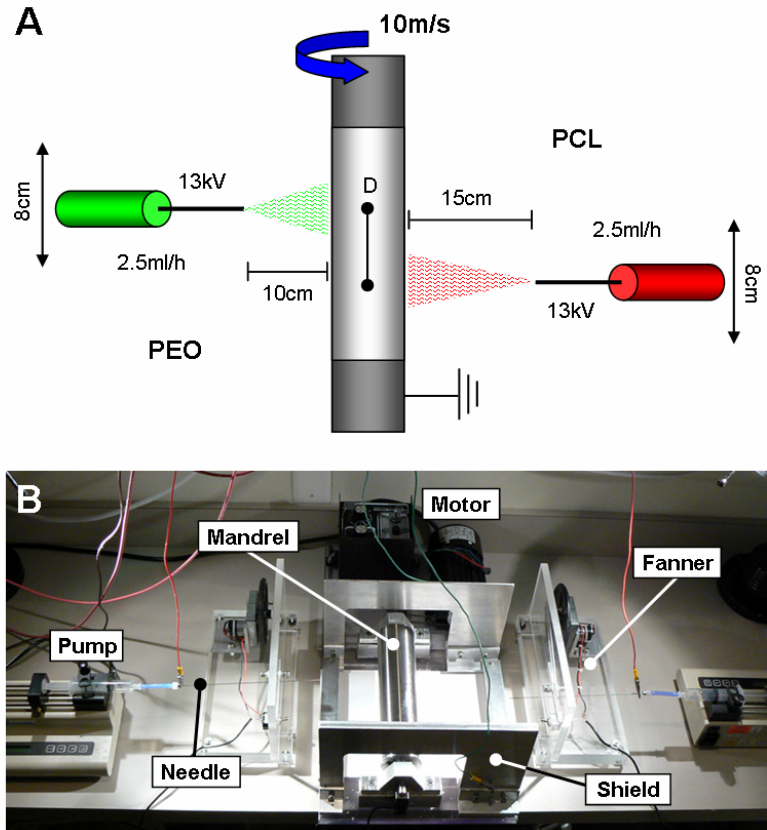


**Figure 4-2:** Electrospinning setup for the fabrication of dual-polymer composite nanofibrous scaffolds. (A) Schematic depicting the electrospinning parameters implemented in generating PCL (red), PEO (green), and PCL/PEO composite scaffolds. (B) The electrospinning apparatus in operation with two syringe pumps delivering polymers distributed by ‘fanners’ along a common rotating mandrel.

Three distinct types of fiber meshes were formed. Pure PCL and PEO meshes were generated by electrospinning the respective single polymer from one spinneret. A 60:40 PCL/PEO dual-polymer scaffold was produced by aligning the axes of the two opposing spinnerets (**Figure 4-2**, offset distance  $D=0$ ). From each of these three fiber mats, 30mm long by 5mm wide strips were excised in either the fiber or transverse-fiber direction (with the long-axis of strip parallel or perpendicular to the predominant fiber direction, respectively). Samples of each scaffold type and fiber orientation were divided into two groups ( $n=3$ /group), one of which was immediately tensile tested as-spun (AS) while the other was tested post-submersion (PS), after removal of the PEO fibers. PS samples were

weighed dry, submerged with agitation in 90% EtOH for three hours followed by distilled water for an additional three hours. PS samples were then dehydrated overnight in a vacuum desiccator and reweighed to determine mass loss. Percentage mass loss was taken as an indication of the PEO content of dual-polymer samples, as pure PCL scaffolds did not change with this treatment.

In order to tune different compositions in dual-polymer composite scaffolds, the above setup was modified by offsetting the axes of the spinnerets (i.e., offset distance,  $D=4\text{cm}$ ). This setup produced a graded fiber mesh ranging from nearly pure PCL at one end of the mandrel to nearly pure PEO at the other end. 25mm long by 5mm wide strips were excised in the fiber direction for analysis of mass loss and mechanical properties under AS and PS conditions as described above. From the same graded fiber mesh, samples indexed to mandrel position were excised for investigation of cellular infiltration. This nanofibrous mesh was generated over the course of six hours, resulting in a fiber mat ranging in thickness from 0.56 to 0.92 mm ( $0.80 \pm 0.10\text{mm}$ ).

#### ***4.2.2 Visualization of Sacrificial Fiber Removal***

To confirm the presence and interspersions of the two different fiber populations, PCL and PEO solutions were doped with Cell Tracker Red at 1% w/v or fluorescein at 0.5% w/v, respectively, and co-electrospun onto glass slides affixed to the rotating mandrel. Fibers were collected for one minute and imaged before and after PEO fiber removal at  $20\times$  using a Nikon T30 inverted fluorescent microscope equipped with a CCD camera and the NIS Elements software (Nikon Instruments, Inc., Melville, NY). Additionally, both AS

and PS full thickness scaffolds (pure PCL and 60:40 PCL/PEO) were examined by scanning electron microscopy. Samples were AuPd sputter coated and imaged with a JEOL 6400 scanning electron microscope (Penn Regional Nanotechnology Facility) operating at an accelerating voltage of 11kV.

#### ***4.2.3 Mechanical Testing of Single-Polymer and Composite Scaffolds***

Uniaxial tensile testing was carried out on AS and PS samples cut in the fiber and transverse to the fiber directions using an Instron 5848 Microtester equipped with serrated vise grips and a 50N load cell (Instron, Canton, MA). Prior to mechanical testing, three thickness measurements along the length of each sample were taken and averaged with a custom LVDT measurement system; three width measurements were acquired and averaged in similar fashion using a digital caliper. Samples were preloaded for 60 seconds to ensure proper seating and engagement of the sample; scaffolds cut in the fiber direction were loaded to 0.5N while those cut in the transverse-fiber direction were loaded to 0.25N. After noting the gauge length with a digital caliper, the sample was preconditioned with extension to 0.5% of the gauge length at a frequency of 0.1Hz for 10 cycles. Subsequently, the sample was extended to failure at a rate of 0.1% of the gauge length per second. Stiffness was determined over a 3% strain range from the linear region of the force-elongation curve using a custom MATLAB script. Incorporating sample geometry and the noted gauge length, a tensile modulus was calculated from the analogous portion of the stress-strain curve. Maximum stress was determined from the maximum load achieved by the sample normalized to its starting cross-sectional area.

#### ***4.2.4 Cell Seeding and Tissue Culture***

MSCs were isolated from the tibial trabecular bone marrow of two 3-6 month old calves (Research 87, Inc., Boylston, MA) as in Chapter 3. The proximal end of the tibia was sectioned and marrow freed from the trabecular spaces via shaking in DMEM supplemented with 300units/ml heparin. After centrifugation for 5 minutes at 500g, the pelleted matter was resuspended in DMEM containing 1X Penicillin/Streptomycin/Fungizone (PSF) and 10% Fetal Bovine Serum (FBS) and plated in 150mm tissue culture dishes. Adherent cells formed numerous colonies through the first week, and were subsequently expanded through passage 2 at a ratio of 1:3.

Six squares (5×5mm) cut from the graded PCL/PEO fiber mat describe above were sterilized and rehydrated with decreasing concentrations of ethanol (100, 70, 50, 30%; 30 minutes/step). A 20µl aliquot containing 100,000 MSCs was loaded onto each side of the scaffold followed by one hour of incubation to allow for cell attachment. Cell-seeded scaffolds were cultured in non-tissue culture treated 6-well plates with 3mL of chemically-defined medium (high glucose DMEM with 1X PSF, 0.1µM dexamethasone, 50µg/mL ascorbate 2-phosphate, 40µg/mL L-proline, 100µg/mL sodium pyruvate, 1X ITS+ (6.25µg/ml Insulin, 6.25µg/ml Transferrin, 6.25ng/ml Selenous Acid, 1.25mg/ml Bovine Serum Albumin, and 5.35µg/ml Linoleic Acid) with 10ng/mL TGF-β3), changed twice weekly.

#### ***4.2.5 Assessment of Cell Infiltration***

After three weeks of culture, samples were removed from culture and gross morphology was recorded via stereomicroscope. Samples were then fixed in 4% phosphate-buffered paraformaldehyde and embedded in Optimal Cutting Temperature compound (OCT, Sakura Finetek USA, Inc., Torrance, CA). 8 $\mu$ m thick cross-sections were cut with a Cryostat (Microm HM500, MICROM International GmbH, Waldorf, Germany) and stained with Prolong Gold Antifade with DAPI (Invitrogen) to visualize cell nuclei. Fluorescent and phase images of each sample were obtained at 4 $\times$  as above.

Cell infiltration was quantified with a custom MATLAB script (The Mathworks, Inc., Natick, MA). This program was written to minimize user bias and to speed data processing. The phase image of the construct cross-section was displayed and the user manually defined the periphery of the scaffold. At ten evenly-spaced positions along the periphery, the minimal distance to the adjacent face was determined; these ten measurements were averaged to yield the scaffold thickness. The user-defined boundary was then mapped to the corresponding DAPI image which had been thresholded and clustered. The thresholding level was selected to maximize noise removal without hampering the detection of nuclei; as all images were obtained at the same brightness and exposure time, this level was maintained for all image processing. The clustering algorithm scanned the thresholded image searching for groups of contiguous white pixels, resulting in the demarcation of each cell nucleus by a cluster of pixels. The minimal distance between the user-defined scaffold periphery and the centroid of each cluster was calculated. To account for variation in scaffold thickness, each nucleus-to-

boundary distance was normalized to the scaffold thickness to produce a percentage infiltration relative to the scaffold center. For each PCL/PEO formulation, six independently cultured samples were sectioned, imaged, and processed as above.

#### ***4.2.6 Composite Scaffold Model***

To better appreciate the dynamic characteristics of the composite scaffolds, a custom MATLAB script was written to model scaffolds with varying PEO content. A 1000 by 1000 pixel area was populated by 3 pixel diameter fibers whose angles ranged between  $\pm 20^\circ$  from the vertical axis. This angular deviation was taken from (Li et al. 2007) who measured angular dispersion of aligned fibers created using similar parameters. Fiber starting position was randomly assigned along the top edge and fibers were extended towards the bottom edge according to the randomly assigned angle. To model a layer of a X:100-X PCL/PEO scaffold, a total of 2·X fibers were produced. Thus, a 100% PCL scaffold contains 200 fibers and a 50:50 PCL/PEO scaffolds contains only 100 fibers, as PEO fibers are removed upon scaffold wetting. The void spaces defined by the fibrous array were then quantified and measured using a clustering algorithm (function `bwlabeln`, MATLAB Image Processing Toolbox). Total pore size, pore number, and the distribution of pore sizes were outputted for each of 20 model iterations, with a new random fiber starting position and angle generated with each iteration.

#### ***4.2.7 Statistical Analysis***

Analysis of variance and Pearson's correlations were carried out with SYSTAT (v10.2, Point Richmond, CA) with Fisher's LSD post-hoc tests used to make pair-wise

comparisons between groups. A level of significance was set at  $p \leq 0.05$ . For the assessment of single- and dual-polymer scaffold mechanical properties, five samples/group were analyzed. From the graded PCL/PEO fiber mesh, three samples/group were analyzed for mechanical properties and six samples/group were evaluated in cellular studies. Data are presented as the mean  $\pm$  the standard deviation.

### 4.3 RESULTS

#### 4.3.1 *Production and Evaluation of Composite Nanofibrous Scaffolds*

Composite scaffolds containing both individual PCL and PEO fibers were produced using the electrospinning device shown in **Figure 4-2**. For these initial studies, the spinnerets were positioned in direct opposition, resulting in a fiber mesh containing ~60% PCL and ~40% PEO (as determined by mass loss after wetting,  $41.6 \pm 0.3\%$ ). Fluorescent-labeling of the fibers within the scaffold (PCL: red, PEO: green) demonstrated that fibers could be successfully interspersed by co-electrospinning (**Figure 4-3A**). Submersion of the scaffold in an aqueous environment showed rapid removal of PEO fibers, leaving PCL fibers intact (**Figure 4-3B**). SEM visualization of these 60:40 PCL/PEO scaffolds as formed showed dense fibers organized along a predominant direction. After submersion in the aqueous solution, scaffolds appeared less dense and larger inter-fibrillar voids or pore spaces were apparent. Despite the removal of a significant fraction of the fiber population, the overall fiber alignment was retained (**Figure 4-3C,D**).

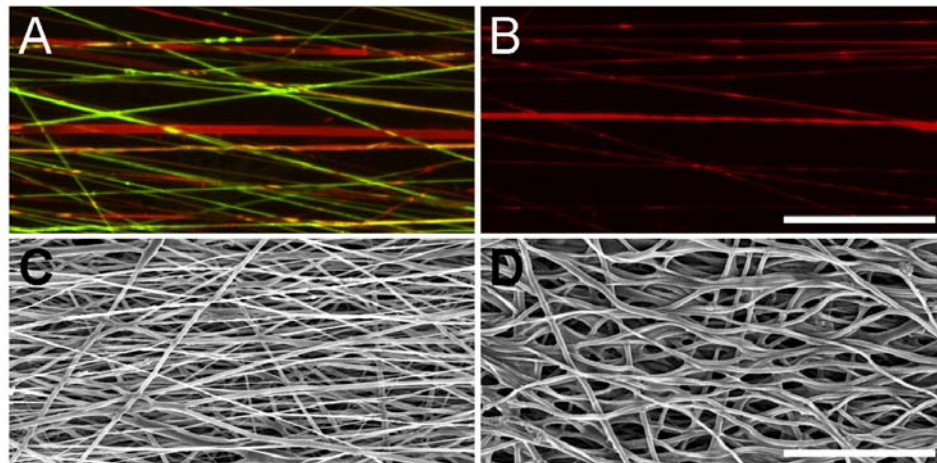


**Figure 4-3:** Composite nanofibrous scaffolds can be formed with individual fibers of distinct polymer composition. Removal of one sacrificial fiber population increases scaffold porosity. (A) Fluorescently-labeled PCL (red) and PEO (green) fibers showed pronounced alignment and interspersed. (B) Submersion of scaffolds in an aqueous solution removed the PEO component while the PCL fibers remained intact. SEM images of as-spun (C) and post-submersion (D) composite scaffolds reveal increases in pore size with the removal of sacrificial PEO fibers. Scale bars: 50  $\mu\text{m}$ .

#### **4.3.2 Tensile Properties of Single- and Dual-Polymer Composite Scaffolds**

To determine the effect of fiber interspersed on the mechanical properties of the composite scaffolds, tensile testing was performed on as-spun (AS) pure PCL, pure PEO, and 60:40 PCL/PEO scaffolds. Testing was carried out both in the fiber direction and perpendicular or transverse to the fiber direction. After evaluating the as-spun (AS) properties, paired samples for the PCL and PEO/PCL groups were tested post-submersion (PS) to examine the effect of fiber removal on tensile behavior. Pure PEO samples dissolved completely with submersion and could not be mechanically tested. Example stress-strain plots of samples tested in the fiber direction are shown in **Figure 4-4A**. From these plots, it is evident that pure PCL and PEO scaffolds possess a different mechanical response; PCL scaffolds show a significant toe region and a large post-yield linear extension while PEO scaffolds lacked a toe region and failed soon after reaching its

yield point. Composite scaffolds containing a mixture of both polymers showed characteristics of each individual constituent. AS PCL/PEO samples lacked a toe region (similar to pure PEO) but showed a long post-yield extension region (similar to pure PCL). After submersion in aqueous solution, the stress-strain profile of PS PCL/PEO samples was similar to pure PCL, though overall these scaffolds reached lower stress levels, indicative of the lower PCL fiber fraction present.

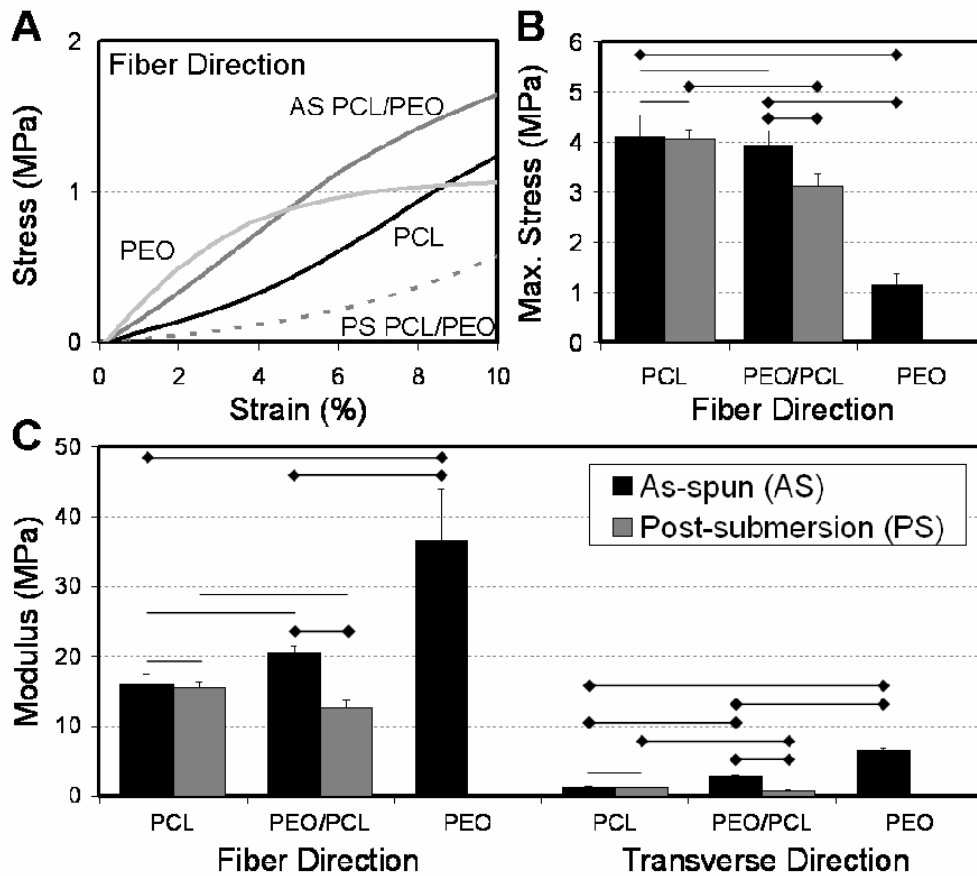


**Figure 4-4:** The tensile properties of composite scaffolds is modulated by both the interspersion of multiple polymer components in distinct fibers, as well as by the removal of sacrificial fiber components. (A) Example stress-strain behavior of pure PCL, pure PEO, and PCL/PEO scaffolds as-spun (AS) and post-submersion (PS). (B) Maximum tensile stress achieved by samples from each group when tested in the fiber direction. (C) Tensile modulus of AS and PS samples from each group tested in the fiber and transverse directions. Note that pure PEO scaffolds dissolved completely upon submersion, and so could not be mechanically evaluated. Diamond-ended lines (♦) indicate significance with  $p < 0.05$ ; unmarked lines denote no significant difference between groups;  $n = 5/\text{group}$ .

Quantification of these results showed that, in the fiber direction, AS PCL/PEO scaffolds reached similar maximum stresses as pure PCL ( $p=0.354$ ) and that both groups were significantly higher than the pure PEO scaffolds ( $p<0.001$ ). As expected, exposure of pure PCL scaffolds to aqueous solution did not change their tensile performance ( $p=0.783$ ). Conversely, the same treatment of PCL/PEO scaffolds resulted in a decline in the maximum stress achieved compared to AS PCL/PEO and PS PCL samples ( $p<0.001$ ). PCL samples tested in the transverse direction were distensible beyond the range of the testing device, and thus comparisons of maximum stress could not be made in this direction.

Tensile moduli were calculated from the linear portion of the stress-strain curves of scaffolds tested in the fiber or transverse directions. Pure PEO scaffolds had a higher modulus ( $36.5 \pm 7.5\text{MPa}$ ) than pure PCL scaffolds ( $16.1 \pm 1.5\text{MPa}$ ) when tested in the fiber direction ( $p<0.001$ , Figure 3C). Similar findings were observed in the transverse direction (PEO:  $6.6 \pm 0.3\text{MPa}$ ; PCL:  $1.4 \pm 0.1\text{MPa}$ ,  $p<0.001$ ). The modulus of composite 60:40 PCL/PEO scaffolds in the fiber direction ( $20.6 \pm 1.0\text{MPa}$ ) trended higher than pure PCL ( $p=0.054$ ), reflecting the contributions of the stiffer PEO component. In the transverse direction this difference in tensile modulus was significant ( $p<0.001$  vs. pure PCL). Submersion in an aqueous environment had no effect on PCL in either direction ( $p>0.55$ ), but resulted in a decrease in modulus in the composite PCL/PEO scaffolds in both testing directions ( $p<0.005$ ). The anisotropy ratio (AR) was calculated by normalizing the fiber direction modulus to that of the transverse-fiber direction. With

submersion, the AR of PCL was unaffected (AS:  $11.51 \pm 0.63$  vs. PS:  $11.67 \pm 0.08$ ) but that of PCL/PEO more than doubled (AS:  $7.17 \pm 0.38$  vs. PS:  $16.43 \pm 0.18$ ), due in part to the larger relative decline in properties in the transverse direction.

### ***4.3.3 Tuning Scaffold Composition and Mechanics***

To explore the relationship between sacrificial fiber content and tensile properties of the composite scaffolds, the PCL and PEO fiber jets were offset from one another and a graded PCL/PEO fiber sheet was generated. This sheet transitioned along the length of the mandrel from a nominal PEO content at one terminus to >90% PEO content at the other, as determined by the amount of mass lost with submersion (**Figure 4-5A**). Increasing the fraction of PEO fibers included in the as-spun (AS) scaffolds led to a larger decline in tensile properties when these fibers were removed. The maximum load and stiffness of samples post submersion (PS) were normalized that of their respective AS scaffolds (**Figure 4-5B,C**). Both maximum load and stiffness showed a significant negative correlation with the % PEO removed ( $R^2=0.87$ ,  $p<0.001$  and  $R^2=0.99$ ,  $p<0.001$ , respectively). These findings indicate that scaffold mechanics may be tuned according to the PEO content initially present.

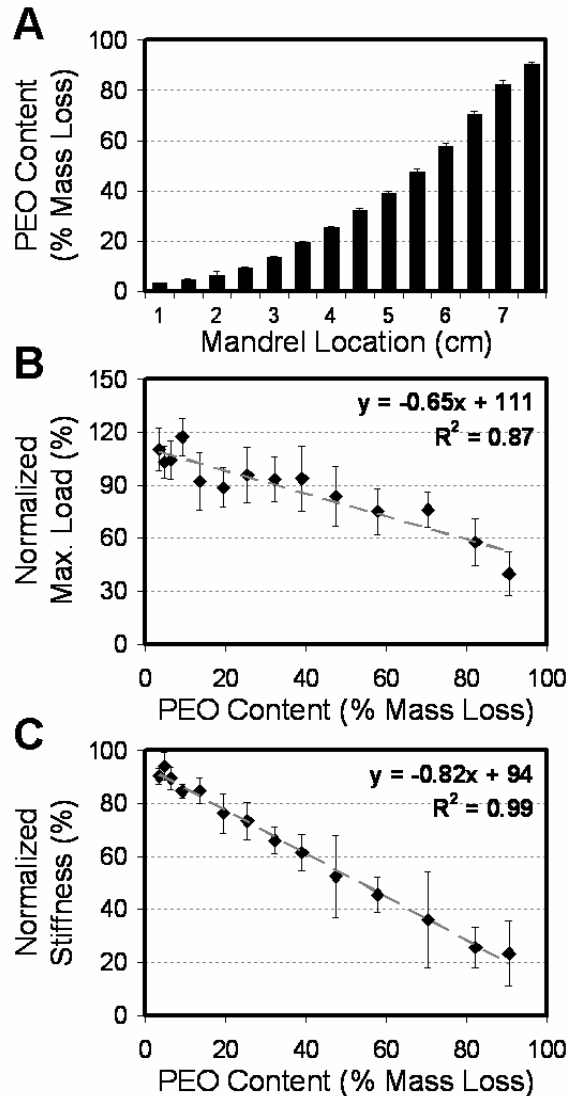


**Figure 4-5:** The composition and tensile properties of composite scaffolds can be tuned along the length of the mandrel. (A) Off-setting spinnerets results in a graded fiber sheet ranging from nominal (~5%) to ~90% PEO content along the mandrel as determined by PS mass loss. Scaffold % PEO content correlated with maximum stress (B) and modulus (C) when samples were tested in the fiber direction. Correlations were significant with  $p < 0.001$ ;  $n = 3/\text{group}$ .

#### 4.3.4 MSC Infiltration with Increasing Sacrificial Content

To determine whether sacrificial fiber removal would affect cell infiltration, scaffolds removed from graded PCL/PEO meshes were seeded with MSCs and cultured for three weeks. Gross scaffold morphology and nuclear position within the scaffold were

evaluated for a number of starting PEO contents (**Figure 4-6**). DAPI staining of construct cross-sections was used to assess the depth of infiltration into and distribution of cells throughout the scaffolds. Overall, cellular infiltration improved with increasing starting PEO content. For example, with 5% PEO, cells were present only at the periphery, with no cells reaching the middle third of the scaffold. At 50% PEO, cells reached the central region, though some regions remained devoid of cells. At 60% PEO, nearly complete infiltration was observed. Still further improvements in cell infiltration were seen at higher PEO contents. However, at these higher PEO contents, significant distortions of the starting scaffold shape was observed.

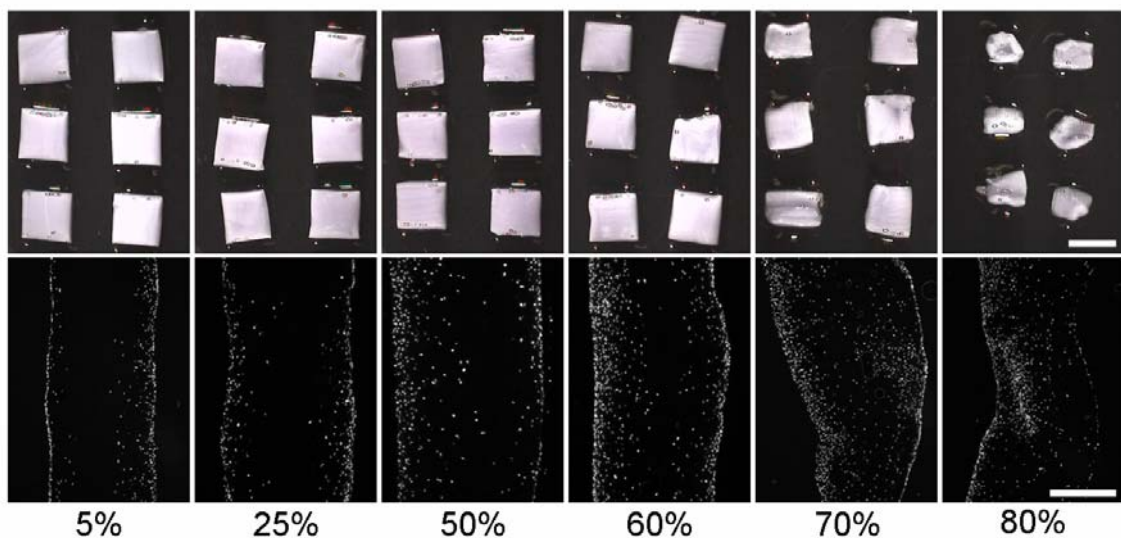


**Figure 4-6:** Increasing removal of sacrificial fiber content promotes mesenchymal stem cell (MSC) infiltration into composite nanofibrous scaffolds. Gross morphology (top row) and DAPI-stained cross-sections (bottom row) of MSC-seeded scaffolds with varying % PEO contents (% mass loss) after three weeks of in vitro culture. Scale bars: 5mm (top), 500 $\mu$ m (bottom).

To quantify these findings, cellular infiltration was evaluated from phase and DAPI images taken of construct cross-sections (**Figure 4-7A,B**). The boundary of the nanofibrous scaffold (NFS) was defined from the phase image and only cells within these

boundaries were analyzed. This excluded the contributions from the cell sheath (CS) that forms on all scaffolds. Next, the shortest distance between each cell nucleus and the NFS periphery was measured and normalized to the sample's half-thickness, yielding a percent infiltration. Thus when cells reach the center of the scaffold, 100% infiltration is achieved (**Figure 4-7B**). Results of this analysis showed that the % infiltration increased with PEO contents >40% (**Figure 4-7C**). Samples beyond 60% PEO could not be analyzed in this fashion due to their misshapen boundaries. To further this analysis, we also determined cellular distribution within the scaffold with varying PEO content. The % infiltration of each cell was determined and binned into ranges of 0-25% (outermost), 25-50%, 50-75%, and 75-100% (central region). These counts were normalized to the total number of cells within each scaffold. Results of this analysis for the lowest and highest PEO contents (5 and 60% PEO) are shown in **Figure 4-7D**, and the full range is quantified in **Figure 4-7E**. In the 0-25% infiltration range, the 5% PEO scaffolds contained a significantly higher fraction of cells than the 60% PEO group ( $p<0.001$ ). Conversely, in the 25-50% range, 60% PEO scaffolds contained more cells than 5% PEO ( $p<0.001$ ). This shift towards increased infiltration became more exaggerated in the 50-75% bin ( $p<0.001$ ). Finally, ~10% of the total cell population reached the center-most region for 60% PEO scaffolds, while no cells were present in this same region for the 5% PEO group. When considering all groups between 5 and 60% PEO content, a loose, but significant negative correlation was observed between percentage of cells in the outermost 0-25% region with increasing PEO content ( $p<0.05$ ). Conversely, the opposite trend was found in the 50-75% range, with an increasing percentage of the total cell population occupying this region with higher starting PEO contents ( $p<0.005$ ).

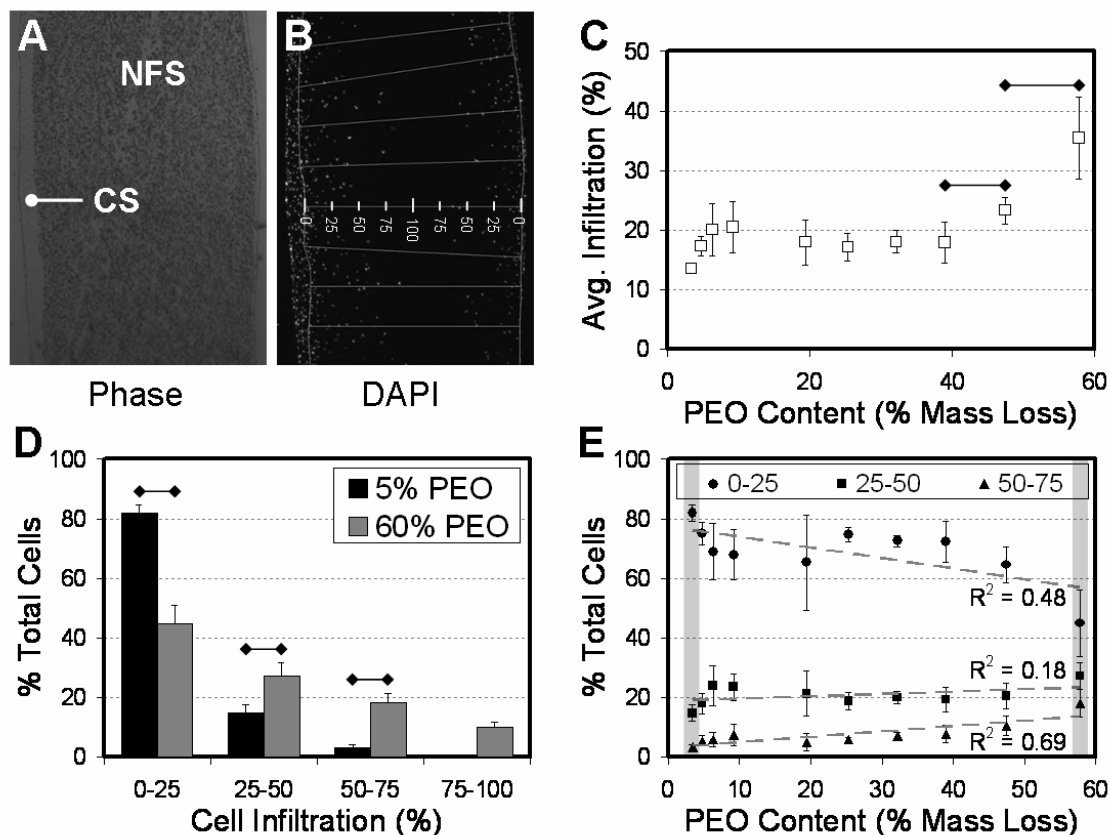


**Figure 4-7: Quantification of MSC infiltration into composite scaffolds as a function of sacrificial fiber content.** Corresponding phase (A) and fluorescent (B) images of DAPI-stained construct cross-sections were used to evaluate cellular infiltration into composite scaffolds. NFS: nanofibrous scaffold, CS: cell sheath. (C) The average % infiltration increased in scaffolds above a threshold of ~40% PEO content in the as-spun scaffolds. To quantify cell distribution, infiltration distance was binned with respect to scaffold thickness, as shown in (B). (D) Comparisons of the lowest (~5%) and highest (~60%) PEO content constructs analyzed showed significantly higher fractions of cells within the more central regions of the scaffolds with increased PEO content. (E) The degree of cellular infiltration (as indicated by the % of total cells in each bin) showed a linear correlations with of % PEO content across a range of scaffold compositions. Diamond-ended bars (◆) indicate significance differences observed with  $p < 0.05$ . A total of six samples were analyzed at each level of PEO content.

#### 4.3.5 Modeling Pore Size in Composite Scaffolds with Increasing Sacrificial Content

To better understand the effect of scaffold porosity on cellular infiltration, a simple mathematical model was created. Composite scaffolds occupying a single layer were generated with a range of starting PEO contents (0-95%) Representative scaffolds with

10, 50, and 90% of the total fibers removed are shown, depicting composite PCL/PEO scaffolds after submersion to remove the PEO content (**Figure 4-8A**). Analysis of the number of pores in these virtual scaffolds showed a steady decrease in pore number with increasing % PEO removal (**Figure 4-8B**). As the number of pores diminished, the average pore size increased. This change in average pore size steadily increased until 60% PEO, after which an exponential growth was observed. To evaluate pore size distribution in these composite scaffolds, the size of each pore in 10, 50, and 90% PEO content scaffolds was calculated, binned logarithmically, and reported as a percentage of the total pore number. Both 10% and 50% PEO layers behaved similarly, with the majority of pores below 10,000 pixels. However, a notable shift was observed in 90% PEO layers, where the bulk of pores were between 10,000 and 100,000 pixels in size.

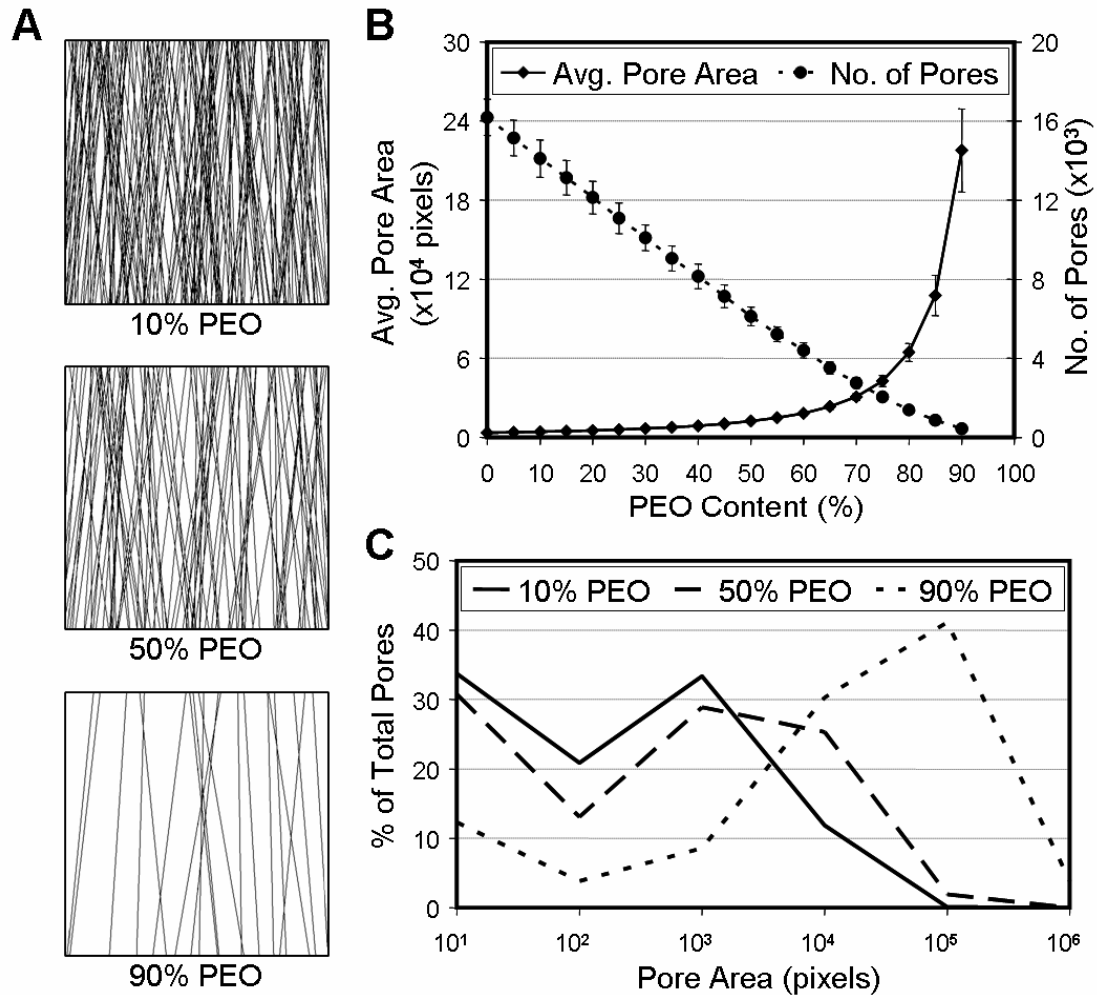


**Figure 4-8:** A simple model of composite scaffolds with increasing sacrificial fiber removal shows a reduction in pore number, but an increase in average pore size. (A) Example composite scaffold layers representing scaffolds with 10, 50, and 90% sacrificial PEO fibers. (B) Increasing the PEO fiber fraction decreases the total number of pores (●) while increasing the average pore area (◆). (C) Pore area distribution shifts towards higher pore sizes with increasing PEO content. Data were averaged from 20 model iterations, each with a randomly generated fiber population.

#### 4.4 DISCUSSION

Fiber-aligned nanofibrous scaffolds are a promising vehicle for the engineering of fiber reinforced tissues of the musculoskeletal system. In past work, we have shown that such scaffolds can promote ordered ECM deposition and functional maturation in the fiber

direction. However, considerable culture times were required to achieve full cellular colonization of even relatively thin scaffolds (~1mm). To address this issue, we developed a dual-polymer electrospinning process that intersperses a sacrificial fiber component within a composite nanofibrous scaffold. We hypothesized that the selective removal of these sacrificial fibers would increase scaffold porosity, and thereby accelerate cell infiltration.

To test this hypothesis, we developed a co-electrospinning process to produce and collect nanofibers from two distinct spinnerets. This blending process has previously been employed by several investigators to produce interspersed fibers within a randomly oriented nanofibrous assembly (Madhugiri et al. 2003; Ding et al. 2004; Kidoaki et al. 2005). In the present study (**Figure 4-3**) we show that interspersed fibers of differing composition can be achieved, while maintaining the organized fiber directionality within the scaffold. Furthermore, we show that combining individual fiber components with dissimilar mechanical properties influences the composite scaffold mechanics, and does so as a function of the fiber fractions employed. The modulus of PCL/PEO composite scaffolds was higher than pure PCL as a result of the inclusion of the stiffer PEO component (**Figure 4-4**). Notably, this inclusion also altered several key qualitative features of the stress-strain profile, including the toe region and the plastic deformation response of the scaffolds after reaching their yield point.

In this dual-component electrospinning process, water-soluble PEO was chosen as the sacrificial fiber component. Both visual inspection and mechanical testing of scaffolds

before and after removal of PEO fibers indicated that mechanical anisotropy was preserved. Further, we were able to show that by offsetting the source spinnerets with respect to one another, a graded fibrous mesh could be produced with varying PEO contents. The tensile properties (both in terms of maximum stress, stiffness, and modulus) reflected the amount of sacrificial component removed from the scaffold. Indeed, a linear relationship was found between PEO content removed and overall scaffold properties (**Figure 4-5**). These findings are consistent with the work of Ding and coworkers, who showed that differences in the mechanical properties in blended non-aligned meshes could be achieved by varying the relative number of spinnerets focused on a centralized collecting surface (Ding et al. 2004). Collectively, these results suggest that a tunable range of material properties can be achieved in these composite nanofibrous scaffolds.

To assess the degree to which removal of this sacrificial fiber population influenced cellular ingress, graded sacrificial content scaffolds were produced and seeded with MSCs for three weeks. MSCs were chosen for this application as they can assume a number of different phenotypes (Caplan 1991; Johnstone et al. 1998), and have been used in various attempts to engineer fibrous tissues with nanofibrous scaffolds (Li et al. 2005). At the end of the culture period, cellular infiltration was assessed by quantifying the position of nuclei within the scaffold cross-section. A demonstrable improvement in cellular infiltration was observed with removal of the sacrificial fiber fraction (**Figure 4-6**), particularly in meshes that started with greater than 40% sacrificial component. In scaffolds with 5% PEO content, more than 80% of the cells resided in the outer 25% of

the scaffold. Conversely, increasing the sacrificial PEO component to 60% resulted in less than 50% of the total cell population in this edge region. Instead, cells were found to migrate to a greater degree into the central regions of the scaffold. Indeed, in the 60% PEO scaffold, >10% of the total cells had reached the center at three weeks, while no cells had done so in the 5% PEO group. Evaluating scaffolds with a range of starting PEO contents showed that these trends were consistent across the groups considered. These findings show that cell infiltration into dense aligned nanofibrous scaffolds can be improved with removal of a sacrificial component.

One finding of interest in this study was that the improvement in cell infiltration only occurred above a certain threshold value of starting sacrificial content (in this case, at about 40%). To better understand this phenomenon, we created a simple model of composite scaffolds, and analyzed pore number, average pore size, and individual pore distribution within a series of ‘virtual’ scaffolds representing those produced experimentally (**Figure 4-8**). Results of this model show, as expected, a decrease in the number of pores and an increase in average pore size with increasing fiber removal. Unexpectedly, a marked transition from steady growth in average pore size to rapid changes in this parameter with further fiber removal was observed between 70% and 90% sacrificial fiber content. While this is a planar model and is not necessarily correlative with the experimental results of this study (in that a threshold exists over which cells invade to a greater extent), this finding is illustrative of the non-linear responses possible with sacrificial removal from these composite scaffolds.

While the results of this study are promising, several key limitations remain to be addressed. Although cell infiltration was improved, an even distribution throughout the scaffold was not achieved. Under the best conditions analyzed (~60% sacrificial fiber removal), ~45% of cells remain in the outer  $\frac{1}{4}$  of the scaffold, and only ~12% progressed into the central  $\frac{1}{4}$ . Additionally, this study was only designed to assess cellular position, and did not explore the cell-mediated production of extracellular matrix or changes in mechanical properties of these scaffolds with time culture. In previous studies we have shown that collagen deposition is localized to areas of high cell density, and that a strong positive correlation exists between scaffold tensile properties and collagen content (Chapter 3 & 7). Future studies will determine if longer culture durations result in a more even distribution of cells and matrix, and whether this process produces more rapid maturation and/or higher mechanical properties in these scaffolds.

Another limitation found in this study was the dimensional stability of the cell-seeded scaffolds at higher sacrificial fiber contents. We observed a threshold of sacrificial fiber removal above which cell infiltration increased markedly. However, in this same domain, significant changes in construct dimensions were observed. Most likely, this was due to cell-mediated contraction as unseeded PS scaffolds did not demonstrate comparable behavior. This suggests that the remaining fiber component was not sufficiently robust to resist this distortion. Control over this dimensional change could be affected in a number of ways. Scaffold peripheries might be clamped to maintain the as-formed shape of the construct. This is analogous to approaches that use rigid fixation of the boundaries of cell seeded-collagen gels, which contract significantly if left un-

tethered (Costa et al. 2003). Alternatively, the slow-degrading polymer could be altered to achieve greater structural resilience to deformation. For example, Li and coworkers have shown that nanofibrous PGA scaffolds are markedly stiffer in tension than PCL scaffolds (Li et al. 2006). Based on the linear relationship we observed in this study between sacrificial content and stiffness, a composite PGA/PEO scaffold would be expected to have higher tensile properties at any level of PEO content, and may therefore better resist contraction than the composite PCL-based scaffolds employed here. However, PGA is less elastically deformable than PCL which might limit application of the composite in certain physiologic scenarios. Alternatively, an entirely different class of polymers could be utilized. We have recently electrospun elements of a novel photopolymerizable library of poly( $\beta$ -amino ester)s (Anderson et al. 2006; Tan et al. 2008). These polymers have a wide range of tensile properties (modulus and elongation prior to yield), and so could be selected to specifically meet the design requirements. Another possibility is to use several polymers in a multi-polymer blend, rather than simply the two different components used in this study. In this work we created a situation in which increased porosity is either present or absent immediately after submersion in an aqueous environment. Tailoring overall degradation with the inclusion of a third component which degrades on a medium (weeks to months) time scale may maintain scaffold dimensions while still promoting cellular infiltration over the entire time course.

## 4.5 CONCLUSIONS

In summary, this study demonstrated that inclusion and subsequent removal of a sacrificial fiber population within a fiber-aligned nanofibrous scaffold enhances cellular infiltration. Moreover, removal of these sacrificial elements preserved structural and mechanical anisotropy, and could be tuned to generate composites with varying mechanical properties. The finding of increased rates of cell infiltration may similarly increase the rate of biochemical and mechanical maturation of these constructs, improving their efficacy at producing a functional tissue replacement, either *in vitro* or after *in vivo* implantation. While further work is required to optimize this process, these results suggest that sacrificial fibers provide one route for overcoming a significant barrier to the use of these dense, fibrous structures.

# ***CHAPTER 5: TUNABLE NANOFIBROUS COMPOSITES WITH SACRIFICIAL CONTENT ENHANCE CELLULAR COLONIZATION AND FUNCTIONAL TISSUE FORMATION***

## **5.1 INTRODUCTION**

Fiber-reinforced, anisotropic soft tissues such as the meniscus (as discussed in Chapter 1), tendon/ligament, and annulus fibrosus are composed of polarized cells embedded within a dense highly-aligned, collagenous extracellular matrix (ECM). This ordered composition underlies the refined and robust mechanical properties of these tissues, enabling them to transmit the extraordinary tensile loads generated with physiologic loading through their aligned ECM (Setton et al. 1999; Lynch et al. 2003; Holzapfel et al. 2005). Unfortunately, the extreme mechanical environment in which these tissues operate predisposes them to both traumatic injury and degenerative changes with aging. Repair processes in the adult are inadequate, replacing the once highly-ordered architecture of these structures with disorganized scar tissue. This replacement tissue is mechanically inferior and renders the tissue susceptible to re-injury (Newman et al. 1989; Beredjiklian et al. 2003). Thus, there exists tremendous clinical need for an implantable tissue or tissue template that can serve as a mechanically competent surrogate and guide the ordered repair of fiber-reinforced tissues.

Successful tissue engineering approaches for the repair or replacement of anisotropic fibrous tissues require the recapitulation of their microstructural organization. Aligned

nanofibrous scaffolds provide a useful biomimetic starting point for such endeavors, given their capacity to dictate cell alignment and subsequent cell-deposited ECM organization (Chapter 3). However, the dense layering of nanofibers during the electrospinning process results in small pore sizes which impede cellular infiltration into the depths of three-dimensional scaffolds, relegating tissue synthesis to essentially a surface phenomenon on scaffolds as thin as 1mm. This was the case with multiple cell lines (Chapter 3) isolated from both bovine and human sources (Chapter 7) despite significant durations of culture *in vitro* of up to 10 weeks. At the conclusion of these studies, the maximal thickness of engineered tissues containing cells surrounded by collagenous matrix was ~200-300 $\mu\text{m}$ , dimensions far below that of the musculoskeletal tissues of interest (i.e. the knee meniscus) which are often several millimeters in thickness. Thus, while the nano-scale topography of nanofibrous scaffolds are an appropriate basis for engineering a number of collagen-based tissues, this severe limitation considerably hampers their potential for wide-spread application.

As such, a number of different strategies have been explored to improve cell infiltration into synthetic electrospun scaffolds (Pham et al. 2006; Nam et al. 2007). While these works have shown progress, improvements in cell infiltration have come at the cost of introducing inhomogeneities or micrometer-scale fibers to augment pore size, which would likely detract from the cell- and ECM-organizing capacity imbued by a homogeneous matrix of nanofibers. Towards engineering a solution to this problem, we developed dual-fiber composites containing a removable fiber population uniformly integrated into the three-dimensional structure of the scaffold during fabrication (Chapter

4). In the previous chapter, we demonstrated an electrospinning system and methodology for fabricating composites containing interspersed populations of slow degrading poly( $\epsilon$ -caprolactone) (PCL) and water-soluble poly(ethylene oxide) (PEO). PCL and PEO were selected based on their temporal profiles in hydrated states; PCL degrades slowly via hydrolysis and functions as a persisting structural element, while uncrosslinked PEO dissolves instantly in aqueous solution and serves as the sacrificial element. We demonstrated that the balance of these two fiber types could be tuned, and that with increasing amounts of PEO fibers, the post-hydrated scaffold possessed lower mechanical properties (e.g. tensile modulus). Despite this compromise in acellular mechanical properties, the high degree of scaffold anisotropy was preserved where the modulus in the predominant direction of the fibers was 16-fold higher than in the orthogonal direction (transverse to the fibers). In short-term studies, we found that increasing fractions of sacrificial PEO fibers led to improvements in the infiltration rates of bovine mesenchymal stem cells (MSCs). After three weeks of culture, MSCs remained localized to the scaffold surface in pure PCL scaffolds but had reached the center of composites formed with >50% PEO fibers. However, at this early time point, ECM production was scarce and the effect of sacrificial fiber content on the evolution of these constructs remained unclear.

Thus, the objective of the current study was to investigate the longer-term ramifications of sacrificial fiber inclusion on construct maturation. Specifically, we sought to identify the fraction of sacrificial PEO fibers required to fully infiltrate 1mm thick constructs with *in vitro* culture, and to examine how improved cellular colonization impacted the

biochemical and mechanical properties of fibrocartilage grown *in vitro*. We hypothesized that better distributed cells and enlargement in the void space surrounding these cells would lead to both an increase in the production of load-bearing collagenous ECM and improvements in the homogeneity of this matrix through the depth of the scaffold. As this technology potentially scales the synthesis of anisotropic tissue from two-dimensional surfaces to three-dimensional volumes which closer approximate the geometry of native tissues, the alignment of cells and collagen throughout these engineered tissues was scrutinized.

Given the high costs associated with *in vitro* manipulations of cell-based implants (Minas 1998), an alternative application for this technology could involve the direct implantation of an acellular scaffold. Once implanted, host cells from surrounding tissues would invade the scaffold and establish functional neo-tissue under the guidance of the organizational cues provided by the aligned nanofibers. Thus, a final objective to this study was to assess cell infiltration into aligned nanofibrous composites in an *in vivo* setting with the hypothesis that sacrificial content would hasten host cell infiltration in similar fashion to surface-seeded constructs cultured *in vitro*.

With these goals in mind, scaffolds were fabricated with a range of sacrificial content, seeded with human fibrochondrocytes, and cultured *in vitro* for up to 12 weeks. As high PEO fiber fractions translate to scaffolds with low initial mechanical properties, special culture conditions were derived to prevent cell-mediated stresses from altering construct shape. Cell infiltration, biochemical content, and mechanical properties were assessed

with time in culture. Additionally, the organization of cells and cell-deposited ECM within these scaffolds was examined at several length-scales using multiple imaging modalities. Finally, acellular sacrificial fiber composites were implanted subcutaneously in rat dorsa for 4 weeks and examined histologically for cell infiltration and matrix production.

## **5.2 MATERIALS AND METHODS**

### ***5.2.1 Fabrication of Nanofibrous Composites with Sacrificial Content***

Aligned nanofibrous scaffolds were produced by co-electrospinning solutions of poly( $\epsilon$ -caprolactone) (PCL) and poly(ethylene oxide) (PEO), yielding a composite structure containing two distinct but interspersed populations of fibers. Briefly, a 14.3% w/v solution of PCL (80kDa, Sigma-Aldrich, St. Louis, MO) 1:1 tetrahydrofuran and N,N-dimethylformamide (Fisher Chemical, Fairlawn, NJ) and a 10% w/v solution of PEO (200kDa, Polysciences, Inc., Warrington, PA) in 90% ethanol were dissolved by stirring at 40°C for 18 hours. To generate scaffolds containing tunable fractions of PCL and PEO nanofibers, a custom electrospinning apparatus was employed (described in Chapter 6). This device, enables simultaneous electrospinning from three fiber sources onto a single, centrally-located mandrel. By modulating the number and balance of PCL and PEO fiber sources, scaffolds composed of 0%, 20%, 40%, and 60% PEO fibers by mass were fabricated (**Figure 5-1**).

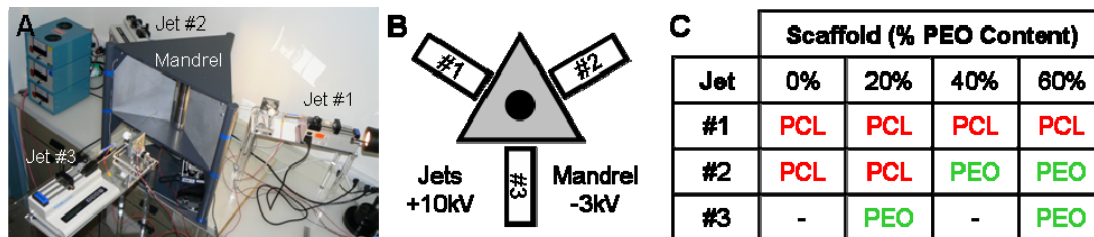


**Figure 5-1:** Nanofibrous composites were fabricated with a triple-jet electrospinning setup by modulating the balance of fiber sources. Using a custom electrospinning setup (A) capable of co-electrospinning from three unique fiber sources (B), the ratio of PEO to PCL fiber sources (C) was altered to control the content of sacrificial PEO fibers within the slow-degrading PCL scaffold.

To electrospin each component, separate 10ml syringes were filled with PCL or PEO and fitted with a 5cm length of flexible silicon tubing connected to a 12” long stainless steel 18G blunt-ended needle that served as the charged spinneret. Spinnerets reciprocated over an 6cm path along the mandrel under the control of custom-built ‘fanners’. The flow rate of all solutions was maintained at 2ml/h via syringe pump (KDS100, KD Scientific, Holliston, MA). A power supply (ES30N-5W, Gamma High Voltage Research, Inc., Ormond Beach, FL) was used to apply a +10kV potential difference between the spinnerets and the grounded aluminum mandrel ( $\varnothing=2''$ ), which was rotated via a belt mechanism conjoined to an AC motor (Pacesetter 34R, Bodine Electric, Chicago, IL) to achieve a linear velocity of  $\sim 10\text{m/s}$ . Both PCL and PEO fibers were collected over a spinneret-mandrel distance of 15cm. To aid in directing the transiting electrospun fibers towards the grounded mandrel, aluminum shields and the rotating mandrel were charged to +5kV and -3kV, respectively.

In additional studies, PCL and PEO solutions were doped with Cell Tracker Red at 0.0005% w/v or fluorescein at 0.5% w/v, respectively, and co-electrospun onto glass slides affixed to the rotating mandrel. To maintain a comparable fiber density, nanofibers

were collected for a range of durations dependent on the number of active fiber sources. The resulting thin layers of fibers were imaged before and after PEO fiber removal at 20× using a Nikon T30 inverted fluorescent microscope equipped with a CCD camera and the NIS Elements software (Nikon Instruments, Inc., Melville, NY). Additionally, both 0 and 60% PEO scaffolds post-hydration (removal of PEO fibers) were examined by scanning electron microscopy. Samples were Au/Pd sputter coated and imaged with a Philips XL 20 scanning electron microscope (University of Pennsylvania School of Medicine Microscopy Core).

### ***5.2.2 Tissue Culture***

Human meniscus fibrochondrocytes were isolated from surgical waste tissue. Briefly, resected meniscus tissue was collected according to an approved IRB protocol from two adult patients, finely minced, and plated on tissue culture polystyrene in basal medium (DMEM containing 1X PSF and 10% FBS). Fibrochondrocytes emerged over a two week period after which the tissue pieces were removed. Adherent colonies from both donors were expanded to passage 6 and combined to yield a sufficient quantity of cells for scaffold seeding.

Scaffolds (50×5mm, with the long axis oriented in the direction of nanofiber alignment) were sterilized and rehydrated in decreasing concentrations of ethanol (100, 70, 50, 30%; 30 minutes/step), concluding with two washes in PBS completely dissolving all PEO fibers. A 50µl aliquot containing 500,000 fibrochondrocytes was loaded onto each side of the scaffold followed by one hour of incubation to allow for cell attachment. Cell-

seeded scaffolds were cultured in non-treated 100mm plates with 4ml/scaffold of chemically-defined medium (high glucose DMEM with 1X PSF, 0.1 $\mu$ M dexamethasone, 50 $\mu$ g/mL ascorbate 2-phosphate, 40 $\mu$ g/mL L-proline, 100 $\mu$ g/mL sodium pyruvate, 1X ITS+ (6.25 $\mu$ g/ml Insulin, 6.25 $\mu$ g/ml Transferrin, 6.25ng/ml Selenous Acid, 1.25mg/ml Bovine Serum Albumin, and 5.35 $\mu$ g/ml Linoleic Acid) with 10ng/mL TGF- $\beta$ 3), changed twice weekly. After one week of culture, samples were transferred to custom polysulfone fixtures in order to maintain the planar shape of the constructs in the presence of cell-mediated stresses and cultured in dynamic media conditions on top of an orbital shaker (48RPM).

### ***5.2.3 Mechanical Testing of Single-Polymer and Composite Scaffolds***

Uniaxial tensile testing was performed on hydrated acellular scaffolds, and cell-seeded constructs after three, six, and twelve weeks of culture. For seeded samples, culture fixtures were removed and gross morphology was recorded via stereomicroscope. Tensile testing was performed with an Instron 5848 Microtester (Instron, Canton, MA). Prior to testing, the cross-sectional area was determined at four locations along the length of each construct with a custom laser-LVDT measurement system (Peltz et al. 2009). Samples were preloaded to 0.1N for 60 seconds to remove slack. After noting the gauge length with a digital caliper, samples were extended to failure at a rate of 0.1% of the gauge length per second. Stiffness was determined over a 1% strain range from the linear region of the force-elongation curve with a custom MATLAB script. Using the cross-sectional area and gauge length, Young's modulus was calculated from the analogous

stress-strain curve. Average gauge lengths were maintained across groups and time points, to enable the comparison of stiffness.

#### **5.2.4 Biochemical Content**

Constructs after tensile testing were stored at -20°C until determination of biochemical composition. Samples were desiccated, massed, and papain digested as in (Mauck et al. 2006). DNA and collagen content was determined using the Picogreen double-stranded DNA (dsDNA) (Invitrogen, Carlsbad, CA) and hydroxyproline (Stegemann et al. 1967) assays, respectively. Hydroxyproline content was converted to collagen as in (Neuman et al. 1950), using a factor of 7.14. This conversion is an estimate, and susceptible to slight bias based on the prevailing collagen type present.

#### **5.2.5 Subcutaneous Implantation**

Male SAS SD rats aged 63-67 days and weighing 276-300 gm (Charles River Laboratories, Wilmington, MA) were used for a subcutaneous implantation model. Sacrificial fiber composites were implanted into four sites just lateral to the dorsal midline at the shoulders and hips of each animal. Each rat received a 0%, 20%, 40%, and 60% scaffold (5×7mm); the placement of scaffolds at the four implantation sites was randomized for each animal.

Following anesthesia with 2% isoflurane in an oxygen carrier and 0.1 mg/kg of buprenorphine subcutaneously, rat dorsums were shaved and sterilized with betadine and ethanol. Gas anesthesia was continued using a mask and body heat was maintained with

a heating lamp. Following sterile draping, 2cm incisions were made just lateral to midline and with a curved mosquito clamp, the subcutaneous tissues were carefully dissected towards the ventral side of the rat to form a pocket. Following adequate exposure, a sterilized scaffold (after PEO fiber removal) was carefully placed in the base of the pocket, with care taken to insert the scaffold between the cutaneous tissue and fascia. Three metal staples were used to approximate the wound edges with eversion. The procedure was repeated for the other three implantation sites in each animal. Following this, the animal was allowed to awaken with room air under a heating lamp. Animals were assessed on post operative days 1 and 2 for signs of pain and discomfort. Food and water were available *ad libitum*.

#### **5.2.6 Histological Analyses**

A central portion from the center of each construct was divided into segments for imaging under multiple imaging modalities, and either in cross-section or *en face* (in the plane of the fibers). For light and fluorescence microscopy, these samples were fixed in 4% phosphate-buffered paraformaldehyde, embedded in Optimal Cutting Temperature compound (Sakura Finetek USA, Inc., Torrance, CA), and sectioned to 16 $\mu$ m thickness. Sections were stained with Picrosirius Red (PSR) and 4',6-diamidino-2-phenylindole (DAPI) to identify collagen and cell nuclei, respectively. For transmission electron microscopy (TEM), samples were washed and fixed in 2.5% glutaraldehyde/2% paraformaldehyde in 0.1 M sodium cacodylate buffer (pH 7.4), post-fixed in 2% osmium tetroxide, and embedded in PolyBed 812 (Polysciences, Warrington, PA). Samples were sectioned to 70nm thickness, stained with uranyl acetate and lead citrate, and imaged

with a Jeol 1010 (University of Pennsylvania School of Medicine Biomedical Imaging Core).

Cell infiltration was quantified with a custom MATLAB script (The Mathworks, Natick, MA) as described in Chapter 4. Briefly, the central portion of each cross-section was co-imaged under phase and fluorescence. The boundary between the cellular capsule and scaffold was demarcated from the phase image, and mapped to the corresponding DAPI image which had been thresholded and clustered. The distance from the scaffold boundary to the centroid of each nucleus was determined and normalized to the thickness of each construct. Data is presented as the % of the total population of cells within the scaffold that are located in the central 50% thickness and represents the average response of five samples.

The organization of nuclei was examined in DAPI-stained *en face* sections ~200 $\mu$ m deep from the surface of the construct. As a metric for the shape of the nucleus, the nuclear aspect ratio (NAR) was defined as the ratio of the long to short axis of each nucleus. In addition, the orientation of the long axis of each nucleus with respect to the prevailing direction of the nanofibers was determined. To quantify NAR and orientation angle, a custom script was developed in MATLAB. Briefly, grayscale images of DAPI-stained nuclei were thresholded and each nucleus was assigned a cluster identity. Each cluster of pixels representing a nucleus was subjected to principle component analysis in order to determine its long and short axis and orientation. These data are presented as the average of three samples from each group, where >1500 nuclei were analyzed in each sample.

Additionally, collagen orientation and distribution through the scaffold thickness was determined from *en face* and cross-sectional views of PSR-stained sections, respectively. Quantitative polarized light microscopy was carried out to quantify collagen alignment, as described previously in (Thomopoulos et al. 2003). Briefly, greyscale images were collected at 10° increments using a green band-pass filter (BP 546 nm) with a crossed analyser and polarizer coordinately rotated through 90°. This procedure was repeated with the filter replaced by a  $\lambda$  compensator. Custom software was then used to determine collagen fiber orientations for a series of 300 nodes within the region of interest. To quantify collagen distribution through the depth of each construct, PSR-stained cross-sections were converted to grayscale and the pixel intensity along 20 evenly-spaced transecting lines was acquired and averaged. Collagen orientation and distribution was quantified for 5 samples per group and averaged.

### ***5.2.7 Statistical Analysis***

Analysis of variance were carried out with SYSTAT (v10.2, Point Richmond, CA) with independent factors of time in culture and PEO content. Bonferroni post-hoc tests were used to make pair-wise comparisons between groups. A level of significance was set at  $p \leq 0.05$ . All data are presented as the mean  $\pm$  the standard deviation.

## 5.3 RESULTS

### 5.3.1 *Fabrication and mechanics of sacrificial fiber composites*

A triple-jet electrospinning device was used to fabricate composite scaffolds containing varying ratios of PEO and PCL nanofibers (**Figure 5-1**). By altering the number of PEO and PCL electrospinning sources, the resultant mass content of PEO fibers could be tuned to 20, 40, or 60%. In validation studies, polymer solutions were doped with fluorophores and thin layers of fibers were electrospun onto glass coverslips for imaging (**Figure 5-2A**). When exposed to a humid environment, PEO fibers immediately dissolved (**Figure 5-2B**). With submersion into an aqueous environment, residual PEO was completely removed from the enduring PCL fibers (not shown). As expected, modulating the balance of PEO and PCL fiber sources translated to changes in the resulting fiber populations (**Figure 5-2C**). As the electrospinning configuration was adjusted for fabricating scaffolds with 20, 40, and 60% PEO, the density of PEO fibers (green) increased and the quantity of PCL fibers (red) decreased at each level. Changes in pore size after fiber removal were greater with increasing PEO fiber density.

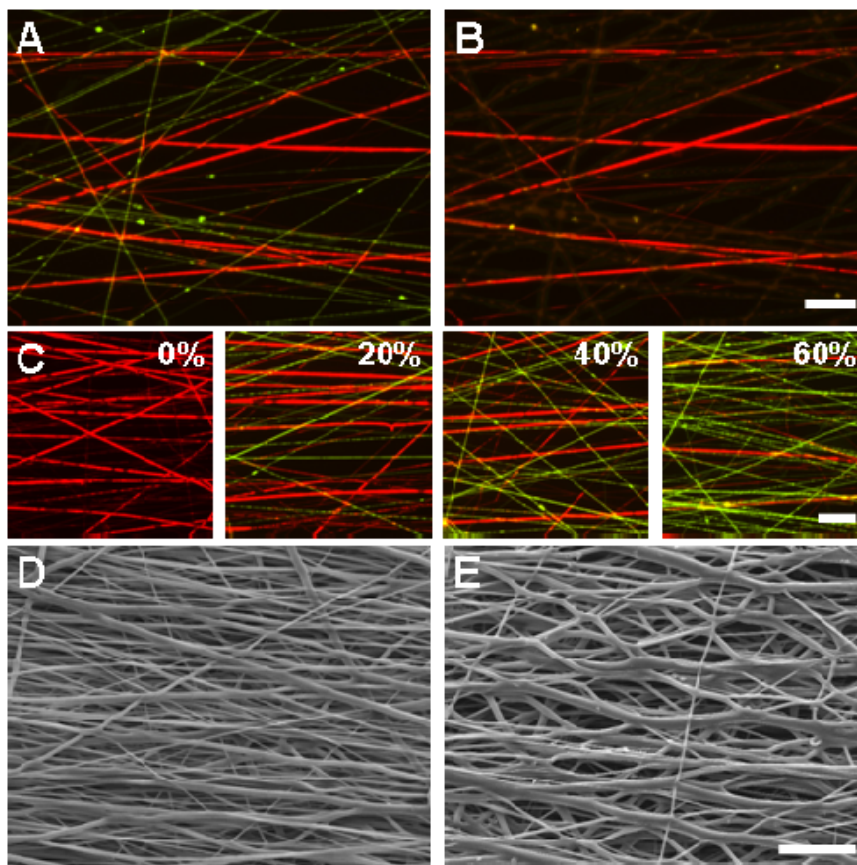


**Figure 5-2:** To improve cellular colonization of dense, aligned nanofibrous matrices, scaffolds were formed with tunable fractions of sacrificial fibers. (A) Schematic depicting scaffold fabrication and subsequent removal of a sub-population of fibers. (B) Slow-eroding poly( $\epsilon$ -caprolactone) (PCL, red) and water-soluble poly(ethylene oxide) (PEO, green) fibers were co-electrospun into composites. (C) Upon exposure to a humid environment, PEO fibers began to dissolve and further hydration removed these fibers from the structure completely. (D) By modulating the number of PCL and PEO fiber sources, scaffolds were fabricated with 0%, 20%, 40%, or 60% PEO fibers by mass. SEM images of scaffolds composed of 0% (E) and 60% (F) PEO fibers after hydration. All scales: 10  $\mu$ m.

After confirming that the fraction of PEO and PCL fibers could be tuned in thin layers, electrospinning was performed over longer durations to generate ~1mm thick scaffolds. To examine the changes in topography resulting from high sacrificial fiber content, scanning electron microscopy (SEM) was performed on 0% and 60% scaffolds after hydration and removal of PEO fibers (**Figure 5-2D,E**). Both scaffolds contained co-

aligned PCL fibers with a range of diameters, however increased pore size was apparent in 60% PEO scaffolds. Additionally, the PCL fibers in 0% PEO control scaffolds appeared to be better aligned than those in scaffolds originally containing 60% PEO fibers, although these differences were not quantified.

Acellular composites after sacrificial fiber removal were mechanically tested in uniaxial tension. As the PEO fiber content of composites increased, the tensile modulus of the hydrated scaffolds decreased, due to the lower PCL fiber density after PEO fiber removal (**Figure 5-3A**). While pure PCL (0% PEO) controls possessed a modulus of 30MPa, scaffolds that initially contained 60% PEO fibers were 3-fold less stiff, with a modulus of 10MPa.

### ***5.3.2 Culture conditions for cell-seeded sacrificial fiber composites***

In preliminary studies, scaffolds were seeded with human meniscus fibrochondrocytes and cultured in free floating conditions. Over the first 3 weeks of culture, constructs formed with scaffolds containing high sacrificial fiber content became increasingly contorted due to cell-mediated stresses (**Figure 5-3B**). While 0% and 20% PEO constructs retained their starting geometry, slight twisting was evident in 40% PEO constructs, and with the highest sacrificial content examined, samples formed helices. To maintain the planar form of the scaffolds in the presence of cell-mediated forces, constructs were clamped at both ends with the use of custom polysulfone and stainless steel fixtures (**Figure 5-3C,D**). Even in 60% PEO constructs after 12 weeks of culture,

the use of the culture grips successfully maintained the initial shape of the scaffolds, although some narrowing was observed (**Figure 5-3E**, arrows).

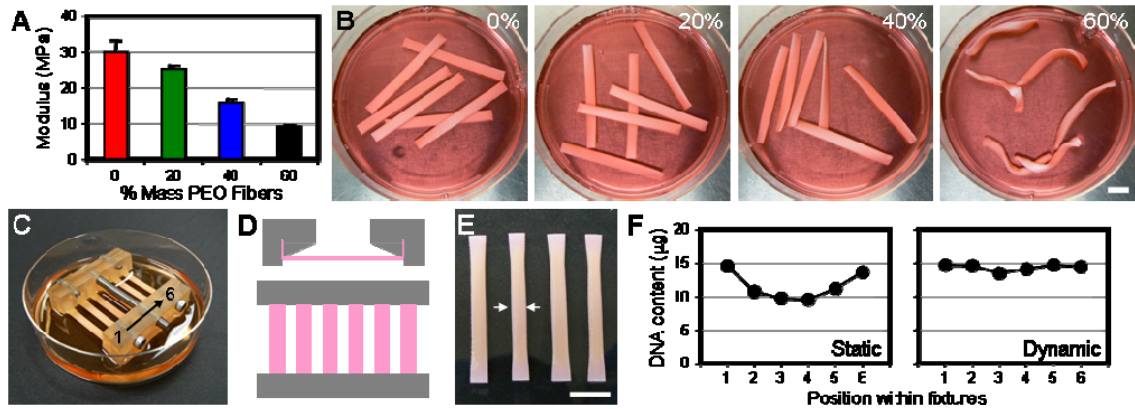


**Figure 5-3: Increasing the sacrificial fiber population decreases scaffold mechanical properties and allows cell-mediated stresses to dictate construct form. (A) Tensile modulus of acellular scaffolds with varying initial mass fractions of PEO fibers. (B) Engineered tissues with high sacrificial fiber content buckle and contort over 3 weeks of culture. Custom fixtures (C & D) were employed to maintain the planar shape of constructs during cell culture, enabling samples formed with 60% PEO scaffolds to retain their initial geometry even after 12 weeks (E). (F) Dynamic culture conditions (via continual agitation of media) were necessary for even nutrient distribution across samples within fixtures. All scales: 10mm.**

Additional preliminary studies were performed to ensure that clamped constructs arrayed in this fashion (six constructs with 5mm spacing) received equivalent nutrient supply independent of positioning. Constructs were cultured in polysulfone fixtures under either static conditions where the media was left unperturbed (except during media replacement), or under dynamic conditions atop an orbital shaker which continually mixed the media. After 3 weeks of culture, constructs were assayed for biochemical content. Under static media conditions, samples in the central positions possessed considerably less DNA (**Figure 5-3F**, left) and matrix content (not shown) than those located in the outer positions. As a result, centrally-located constructs increased in mechanical properties to a lesser extent compared to peripheral samples (not shown).

When constructs were maintained in dynamic media conditions, all six samples developed similarly independent of position (**Figure 5-3F**, right). Thus, dynamic media conditions were employed in long term studies to ensure homogeneous nutrient supply in arrays of clamped constructs with varying PEO fiber content.

### ***5.3.3 Effects of Sacrificial Fibers on Matrix Distribution and Content***

Cell-seeded constructs formed with 0%, 20%, 40%, or 60% PEO scaffolds were maintained in fixtures and incubated under dynamic conditions for up to 12 weeks. To assess cell infiltration into the depths of the scaffolds, constructs were sectioned in cross-section (**Figure 5-4A**) and stained for cell nuclei (**Figure 5-4B**). As observed in numerous previous studies, cells were sequestered to the fringe of 0% PEO controls, despite extensive durations of culture. With increasing sacrificial fiber content, cell infiltration improved, where 60% PEO constructs were well-colonized throughout the depth of the scaffold. The percentage of the total cell population located in the central 50% thickness was quantified via an image analysis program described previously in Chapter 4. With increasing PEO fiber content, the percentage of cells located in the center of scaffolds increased significantly, and in a manner dependent upon PEO fiber content (**Figure 5-4D**).

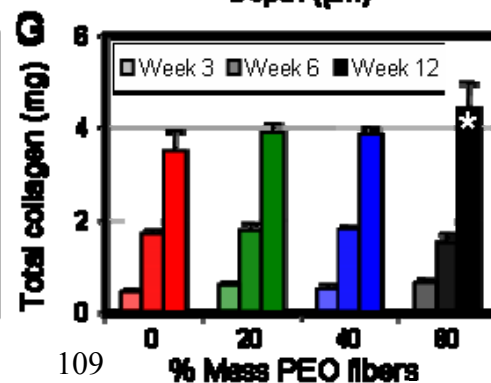
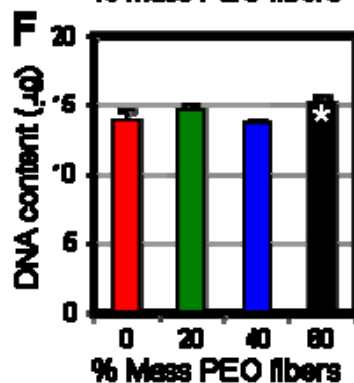
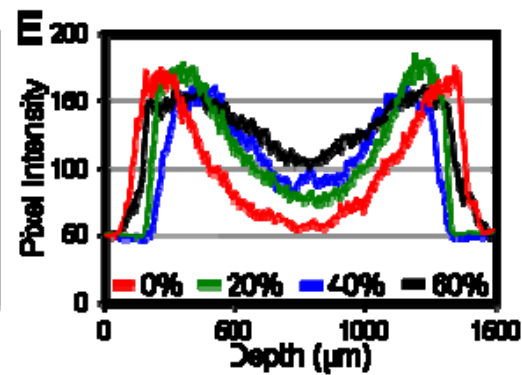
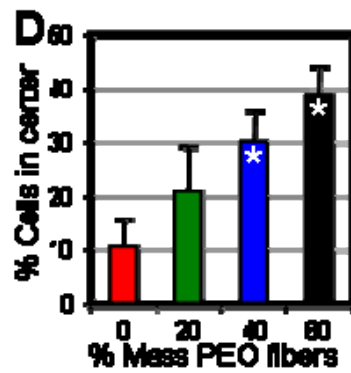
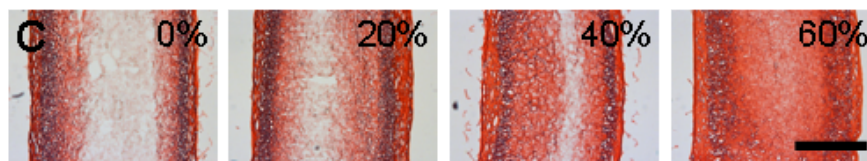
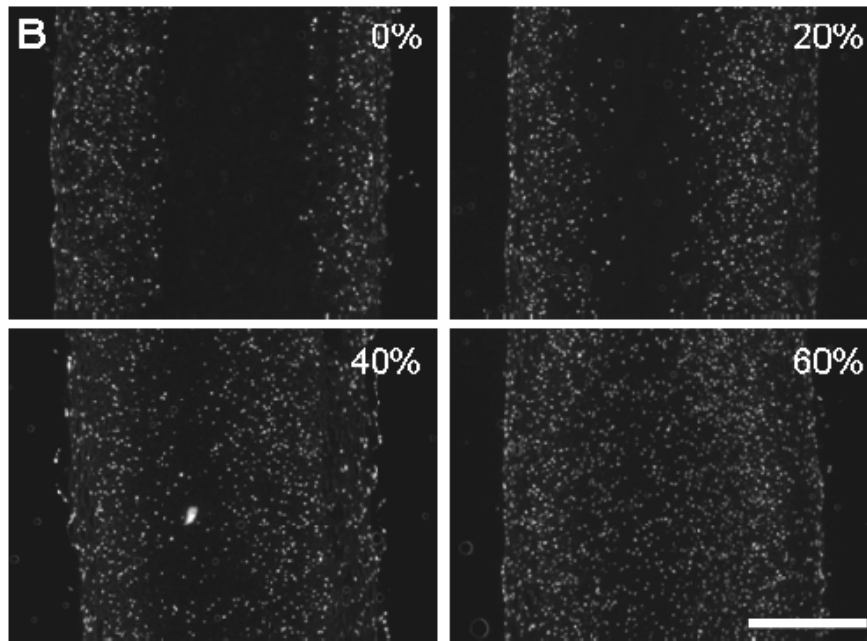
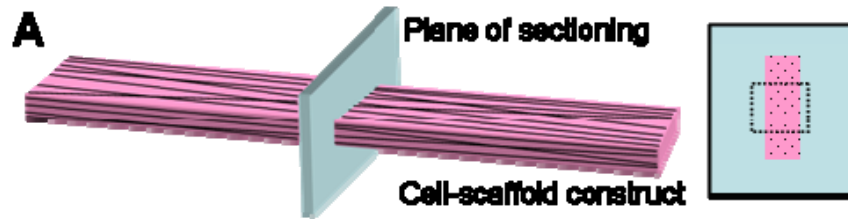


**Figure 5-4: Removal of sacrificial fibers promotes cell infiltration and improves the distribution of cell-secreted extracellular matrix. Cross-sections (A) from 0%, 20%, 40%, and 60% PEO constructs were stained with DAPI and Picrosirius Red to visualize cell nuclei (B) and collagen deposition (C), respectively. Scale: 500  $\mu$ m. By week 12, increasing mass fractions of sacrificial PEO fibers led to a higher proportion of cells within the central 50% thickness of constructs (D), and a more homogeneous distribution of collagen through the scaffold depth (E). Bulk biochemical measures revealed increased DNA (F) and collagen (G) content in 60% PEO constructs relative to 0% controls after 12 weeks of culture.  $n=5$ ,  $p<0.05$  compared with time point-matched 0% constructs.**

Due to the more even distribution of cells, the deposition of collagenous matrix (as indicated by Picrosirius Red (PSR) staining) appeared more homogeneous through the scaffold depth (**Figure 5-4C**). In 0% PEO scaffolds, PSR staining was completely absent in the central central region of the scaffold. As the front of infiltrating cells approached the center of the scaffold with increasing PEO fiber content, the region devoid of collagen narrowed such that collagen deposition pervaded the entire thickness of 60% PEO scaffolds. Average densitometric profiles were acquired from PSR stained cross-sections to demonstrate the consistency of these observations (**Figure 5-4E**). In 0% PEO constructs, collagen staining was robust at the scaffold periphery and diminished to background intensity values at the center of the scaffold, represented by a concave profile. With increasing sacrificial fiber content, the concavity of these curves decreased. However, despite the marked improvement in matrix distribution in 60% PEO constructs, densitometric measurements revealed the persistence of a depth-dependent gradient.

Biochemical assays were performed to determine the total DNA and collagen content in constructs. Corroborating histological assessments, total DNA content after 12 weeks of culture was significantly higher in 60% PEO constructs as compared to 0% controls

(**Figure 5-4F**), although levels were overall fairly comparable (due to the high density of cells present in the encapsulating cell sheath). At 3 and 6 weeks of culture, collagen content was identical across all groups (**Figure 5-4G**). However, with an additional 6 weeks, total collagen content in 60% PEO constructs surpassed that of 0% controls, despite robust collagen deposition in the cell periphery present in all samples. Thus, the inclusion of sacrificial PEO fibers during scaffold formation led to not only a more homogeneous distribution of cells and matrix, but also contributed to increases in the bulk content of these key tissue components.

#### ***5.3.4 Evolution of Mechanical Properties in Sacrificial Fiber Composites***

The production of a collagen-rich extracellular matrix translated to increases in the tensile properties of all constructs with time in culture. At week 3, there was an inverse correlation between sacrificial fiber content and tensile modulus, where 60% PEO constructs were significantly lower than 0% controls (**Figure 5-5A**). At this early time point when collagen deposition was limited (**Figure 5-4G**), this trend reflected measurements of acellular scaffolds (**Figure 5-3A**). With an additional 3 weeks of culture, the disparity between groups became less pronounced. By week 12, the relationship between sacrificial fiber content and tensile modulus reversed, and the modulus of 60% constructs was significantly higher than that of 0% controls. Average stress-strain plots of week 12 constructs typify the improved stress-strain response occurring with increasing levels of PEO content (**Figure 5-5B**).

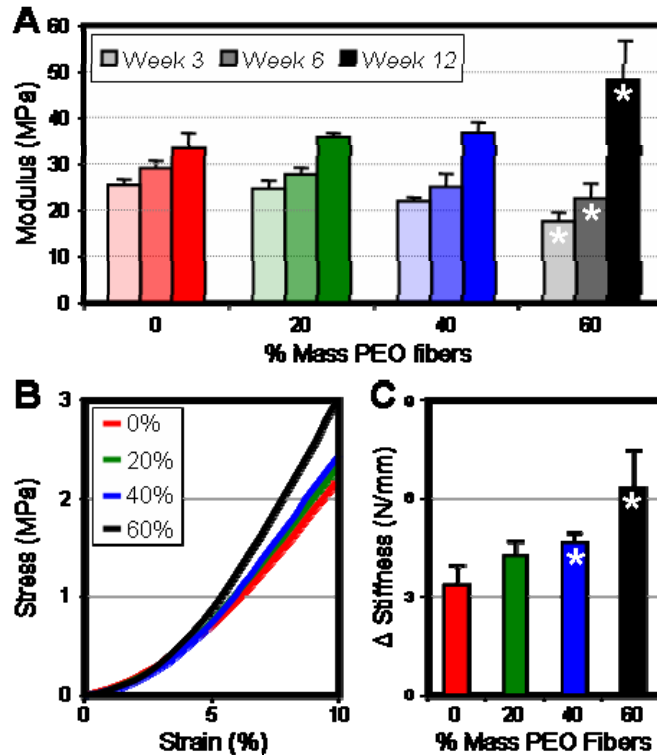


**Figure 5-5:** Increasing sacrificial content improved construct tensile properties with time in culture. (A) Tensile modulus of 0%, 20%, 40%, and 60% PEO constructs at weeks 3, 6, and 12. (B) Change in stiffness over 12 weeks of culture. (C) Average stress-strain responses of week 12 constructs. n=5, \*: p<0.05 compared with time point-matched 0% constructs.

While modulus is an intrinsic property of a material, alterations in cross-sectional area (most evident in 60% constructs, **Figure 5-3E**) can misrepresent actual changes in stiffness due to the production of load-bearing matrix. To eliminate any error introduced by changes in cross-sectional area due to tissue remodeling, gauge lengths were maintained identically across the entire study to enable the fair comparison of stiffness. Quantifying the change in stiffness over the latter 9 weeks of culture, the tensile contribution of newly synthesized ECM was isolated (**Figure 5-5C**). While less exaggerated than differences observed in tensile modulus, the effect of sacrificial fiber content on the mature construct stiffness was still evident. The change in stiffness due to

matrix elaboration was dependent upon sacrificial fiber content ( $p < 0.001$ ), and was highest in 60% PEO scaffolds.

### **5.3.5 Cell and Matrix Organization with High Sacrificial Fiber Content**

To examine the effect of sacrificial fiber content on the organization of fibrochondrocytes and the collagenous matrix they synthesized, sections were taken *en face* (i.e. in the plane of the fibers) from 0 and 60% PEO constructs after 12 weeks of culture (**Figure 5-6A**). DAPI-stained nuclei (**Figure 5-6B**) were imaged and nuclear aspect ratio (length divided by width) as well as orientation were quantified (**Figure 5-6C**). In both control scaffolds as well as sacrificial fiber composites, nuclei appeared columnar and oriented in the direction of nanofiber alignment, independent of location with respect to scaffold depth. While populated arrays of organized nuclei were present throughout the entire thickness of 60% scaffolds, cell density diminished beyond depths of  $\sim 250\mu\text{m}$  in 0% PEO controls. Thus all comparisons were made from images taken at depths between 100-200 $\mu\text{m}$  from the surface of the construct. Nuclei in 0% and 60% PEO scaffolds were equally highly elongated, possessing aspect ratios of  $\sim 3$  (**Figure 5-6D**). The angle between the long axis of each nucleus with respect to the direction of nanofiber alignment was determined (**Figure 5-6E**, blue histograms). In both 0% and 60% PEO scaffolds, nuclei were oriented in the direction of the surrounding nanofibers, with  $>75\%$  of the entire cell population aligned within  $\pm 15^\circ$  of the fiber direction.

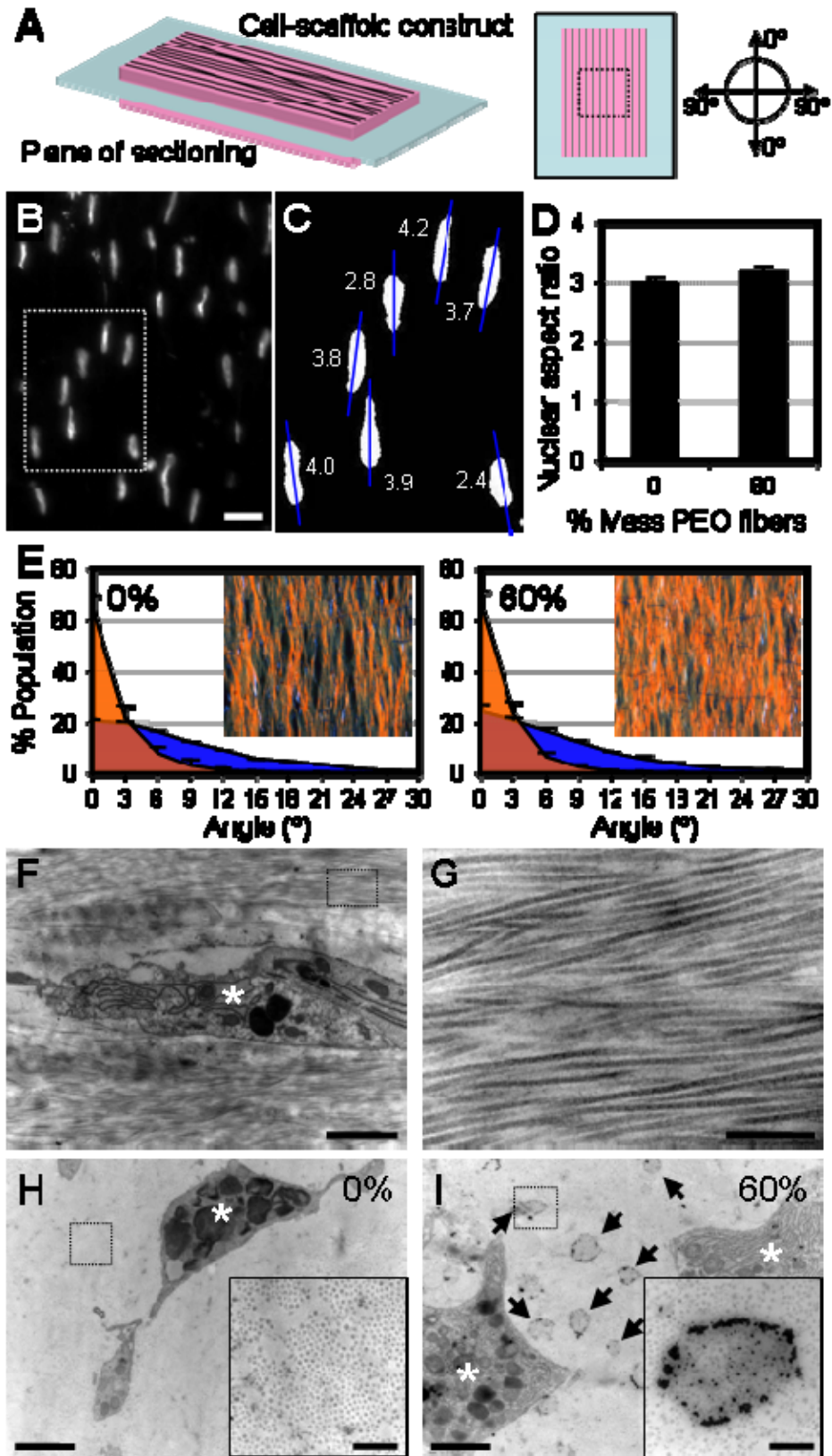


**Figure 5-6:** Despite the removal of significant fractions of sacrificial fibers from the composites, scaffolds retained their capacity to dictate cell and matrix organization. (A) Sections were collected in the plane of the fibers, approximately 200 $\mu$ m from the surface of the construct. (B) DAPI-stained nuclei of 60% PEO constructs were elongated and aligned in the direction of the surrounding nanofibers. Scale: 25  $\mu$ m. Fluorescent images were thresh-holded (C) and nuclear aspect ratio was determined in 12 week 0% and 60% PEO constructs (D). (E) Nuclear (blue) and collagen orientation (red) with respect to the fiber direction was measured in 0% (left) and 60% (right) PEO constructs. Transmission electron microscopy (TEM) revealed cells elongated in the nanofiber direction (F), and robust collagen deposition (G) parallel to the long axes of cells. Box in (F) depicts location of image featured in (G). TEM of construct cross-sections revealed a dense array collagen fibrils perpendicular to the plane of the image in both 0% (H) and 60% (I) PEO constructs. Boxes depict location of insets. Higher order collagen fibrillogenesis (arrows) was evident only in 60% PEO constructs. Scales: 2  $\mu$ m (F, H, I), 500 nm (G, H & I insets). Asterisks denotes fibrochondrocytes.

Polarized light microscopy, which can quantify the birefringent light transmitted by noncentrosymmetric materials such as collagen fibrils, was performed to examine the organization of collagen in *en face* sections from 12 week constructs (**Figure 5-6E**, inset images). In all constructs, birefringence peaked sharply when the polarizer and analyzer were aligned with the fiber direction of the scaffold. Quantification of grids of nodes within each image revealed that collagen organization in 0% and 60% PEO constructs was nearly identical (**Figure 5-6E**, orange histograms), and was more tightly coordinated with the alignment of surrounding nanofibers than nuclear orientation. Despite there being no change in collagen orientation with increasing sacrificial fiber content, the amount of birefringent collagen was notably higher in 60% PEO constructs than 0% controls (**Figure 5-6E**, inset images).

Transmission electron microscopy (TEM) of *en face* sections qualitatively confirmed these findings, revealing cell bodies extended in the direction of nanofiber alignment,

running parallel to dense arrays of collagen fibrils (**Figure 5-6F,G**). In cross-sections imaged with TEM, collagen fibrils transected the plane of viewing and were identified as punctate staining surrounding the cells; collagen fibrils running perpendicular to the direction of cell/nanofiber alignment were not observed (**Figure 5-6H,I**). Single collagen fibrils represented the bulk of the tissue in both 0% and 60% PEO constructs. However, and only in 60% PEO constructs, occasional fibril aggregates surrounded by electron-dense particulates were observed, providing some evidence of higher order fibrillogenesis (**Figure 5-6I**, arrows, inset).

### ***5.3.6 In Vivo Colonization After Subcutaneous Implantation***

Scaffolds fabricated with 0%, 20%, 40%, or 60% PEO fiber content were implanted subcutaneously into dorsal pockets of Sprague-Dawley rats. After 4 weeks of implantation, animals were sacrificed and scaffolds along with surrounding tissue were sectioned and stained for cell nuclei. Upon gross dissection, composite scaffolds with >40% sacrificial fiber content were well integrated with the surrounding host tissue. In 0% PEO controls, invading cells were sequestered to the scaffold periphery and the bulk of the scaffold remained devoid of any cellular content (**Figure 5-7**). With increasing amounts of PEO fibers, the front of cell colonization approached the center of scaffolds. In both 40% and 60% scaffolds, the central regions of scaffolds were densely populated with host cells. Cells within these subcutaneous implants elaborated a collagenous matrix as evidenced by Picrosirius Red staining (not shown).

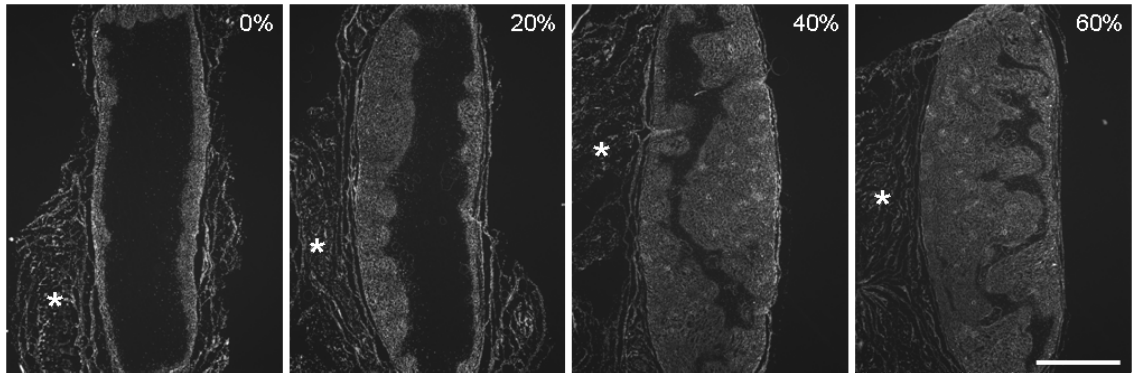


**Figure 5-7: Host cell colonization of scaffolds improves with increased sacrificial fiber content in a subcutaneous rat model. Cross-sections of 4 week explants DAPI-stained for cell nuclei. Asterisks denote host tissue. Scale: 1mm.**

#### 5.4 DISCUSSION

In Chapter 4, a dual-jet electrospinning system was employed in tuning the two populations of fibers in composites by offsetting the axes of the two spinnerets. While this method can generate composites with a full range of PEO fiber fractions, the yield is inadequate for performing longer term studies that are sufficiently powered. In order to fabricate the large quantities scaffolds needed for the present study, electrospinning was performed with a triple-jet electrospinning device (which will be described in further detail in the subsequent chapter). While it is possible to modulate the incorporation rate of PEO fiber mass by altering electrospinning conditions such as polymer flow rate, changes in electrospinning parameters alter the morphology of the resulting nanofibers without fail (Boland et al. 2001; Deitzel et al. 2001; Fridrikh et al. 2003; Bolgen et al. 2005; Dalton et al. 2006). As the goal of this study was to examine the effect of increasing the density of sacrificial fibers (without any differences in fiber morphology), we maintained identical electrospinning parameters for all scaffolds and simply varied the number of PCL and PEO fiber sources (**Figure 5-1**), thereby modulating the balance of fiber populations in composites (**Figure 5-2**). Thus, we could carefully dissect out the

effect of sacrificial fiber inclusion in a density-dependent manner without complicating effects due to differences in fiber morphology.

With increasing sacrificial fiber content, cell ingress into aligned nanofibrous scaffolds improved demonstrably. Constructs formed with 60% PEO scaffolds and culture *in vitro* were fully infiltrated by 12 weeks, while cells remained sequestered to the periphery of 0% PEO scaffolds (**Figure 5-4**). In comparison with construct maturation *in vitro*, the time course *in vivo* was accelerated where 1mm thick composites with >40% sacrificial fibers were fully infiltrated by host cells within 4 weeks of implantation (**Figure 5-7**). However, as seen *in vitro*, colonization of scaffolds lacking sacrificial fiber content was severely limited. As cells establish and maintain ECM locally, the improved colonization in sacrificial fiber composites led to a better distribution of collagen throughout 1mm thick constructs (**Figure 5-4**).

Concurrent with cell infiltration and matrix elaboration, constructs increased in tensile properties with time in culture. Notably, increases in construct stiffness after 12 weeks were proportional to the sacrificial fiber content of scaffolds, where the largest improvement was observed in 60% PEO constructs (**Figure 5-5**). In acellular scaffolds, tensile stiffness decreased with greater sacrificial fiber content such that pure 0% PEO scaffolds were 3 times stiffer than 60% PEO scaffolds post-hydration. After construct maturation, however, the larger gains in stiffness of 60% PEO constructs overcame this disparity in initial properties and translated to a higher final modulus than 0% PEO constructs (34 vs. 48 MPa).

As there was no differences in collagen alignment at varying levels of PEO fiber content, the improvement in tensile properties with increasing PEO fiber fractions likely lies in the more rapid distribution of cells. With increasing sacrificial fiber fractions, a larger percentage of the entire structure was filled with matrix-synthesizing cells (**Figure 5-4**). The number of cell nuclei and the amount of collagen staining within the scaffold increased with PEO fiber content. In scaffolds with the highest sacrificial fiber content, total DNA and collagen contents were significantly higher than pure PCL controls (the considerable portion of cells and matrix encapsulating the construct obstructed significance in 20% and 40% comparisons). Therefore, enhanced cell colonization led to a more homogeneous tissue containing greater amounts of organized collagen, which in turn led to larger increases in tensile properties. Furthermore, 60% PEO constructs viewed under TEM revealed evidence of higher order collagen fibrillogenesis, where collagen fibril aggregates surrounded by electron-rich particulates (possibly proteoglycan) were common. The mechanism underlying the formation of these structures, which were completely absent in 0% PEO constructs, and their contribution to the developing tensile properties of constructs will be examined in future work.

The concept of extracting fibers from a scaffold prior to cell seeding raised the concern that the thinned population of remaining fibers would be unable to dictate cell and matrix organization, especially in the case of 60% PEO scaffolds where the majority of constituent fibers were dissolved upon hydration. Indeed, qualitative assessment of scanning electron micrographs indicated the degree of fiber alignment was decreased in

60% PEO composites post-hydration (**Figure 5-2**). As nanofiber alignment dictates scaffold anisotropy (Ayres et al. 2006; Courtney et al. 2006; Li et al. 2007), and the organization of cell-deposited ECM (Chapter 3), increased fiber dispersion could lead to the formation of a less organized extracellular matrix. While we sought to improve cell infiltration with the goal of generating tissues that more closely approximate the dimensions of native structures, significant impairment to the instructional capacity of aligned nanofibrous scaffolds would be a severe limitation. After all, the anisotropy of these tissues and the mechanical function they serve are intimately coupled and of utmost importance.

To assess the alignment of cells and matrix within constructs, the organization of DAPI-stained nuclei and the birefringence of collagen was compared in 0% and 60% PEO constructs under fluorescence and polarized light microscopy, respectively (**Figure 5-6**). Independent of depth within the scaffold, cells and matrix were aligned with the direction of the surrounding nanofibers (and the long axes of the constructs). Histograms of nuclear and collagen orientation were identical for 0% and 60% constructs, indicating that the removal of the majority of fibers from 60% PEO composites did not diminish the ability of the remaining scaffold to serve as a micropattern for directing tissue organization. Interestingly, the angular profiles of nuclear and collagen alignment were markedly different, where collagen was strongly oriented with the fiber direction (95% of all nodes of analysis were within  $\pm 10^\circ$ ) but nuclear orientation was more dispersed (only 60% of all nuclei were within  $\pm 10^\circ$ ). The directionality of collagen assembly remains poorly understood, although there are several reports indicating that cellular orientation

plays an important role (Li et al. 2003; Wang et al. 2003; Manwaring et al. 2004). In the developing annulus fibrosus, cells are patterned in a thatch-like fashion prior to the formation of a cross-ply collagen network (Hayes et al. 1999). In this work, nuclear alignment was taken as an indicator of overall cell body alignment. It is certainly possible that there is variability or “wobble room” to the positioning of nuclei within the cytoplasm (Maniotis et al. 1997), and in actuality, perhaps cell body orientation was as tightly regulated as collagen organization in these constructs. Alternatively, as cells secrete short collagen fibrils which then self-assemble extracellularly (Birk et al. 1989), the geometrical constraints imposed by the fiber-aligned scaffold may serve to orient the aggregating fibrils. Whether cells actively deposit collagen oriented in a manner reflective of their own alignment, or simply secrete collagen that is organized by the surrounding microenvironment is a subject of future inquiry.

Beyond orientation in a predominant direction, cells in an aligned nanofibrous microenvironment also possessed highly elongated nuclei reminiscent of cells resident to anisotropic fibrous tissues such as tendon and annulus fibrosus (Bruehlmann et al. 2004; Egerbacher et al. 2008). For reference, meniscus fibrochondrocytes in monolayer on tissue culture plastic typically display nuclei with aspect ratios of  $\sim 1.5$  (Chapter 9). In contrast, the nuclei of fibrochondrocytes in both control scaffolds and 60% PEO composites after 12 weeks of culture revealed aspect ratios of  $\sim 3$ , with significant variability and numerous nuclei possessing values beyond 5. It is well known that for a plethora of cell types found throughout the body, shape and function are directly related. However, the significance of the lengthy cell bodies and polarized cytoskeletons

characteristic of these cells is not yet understood in the framework of the roles these cells play in establishing and maintaining their surrounding ECM. Furthermore, it remains to be shown whether a highly elongated nucleus provides a functional advantage, or if this morphology is merely the result physical constraints on the cell conferred by the surrounding matrix. Future studies mapping chromosomal territories in these cells may shed some light on the importance of the shape of the nucleus and the structuring of genes and regulatory regions within (Cremer et al. 2001).

The use of sacrificial fiber composites hastened cell and matrix distribution while still providing the necessary structural cues to generate a highly organized, load-bearing ECM. Recreating the microstructural features of native fiber-reinforced tissues is a fundamental component of successfully engineering tissues such as the meniscus. However, as the use of sacrificial fibers enables the production of larger, three-dimensional tissues that better approximate the anatomic form of native tissues, it is necessary to begin to consider the macroscopic form of these engineered tissues. In other words, as engineers we must be able to define the overall shape of the engineered tissue. For example, in the case of filling a meniscal defect, the implanted scaffold or precultured engineered tissue must meet prescribed dimensions within narrow tolerances (Ballyns et al. 2008). Thus, a proper construct should not only match the mechanical properties of the tissue we seek to replace (i.e. microstructural aspects), but also closely approximate its anatomic form (i.e. macrostructural aspects). A mismatch in tissue sizing would likely lead to incorrect loading of either the host or implant tissue, and undermine any efficacy provided by intervention (Dienst et al. 2007; Hommen et al. 2007).

In this work, there was a tradeoff between generating homogeneous tissues and maintaining their macroscopic form during *in vitro* culture or after subcutaneous implantation. With high PEO fiber content, scaffolds post-hydration lost structural integrity such that cell-mediated stresses altered the scaffold's initial geometry (**Figure 5-3**). To circumvent this *in vitro*, we employed fixed boundary conditions, a strategy common to work done with collagen gels which are prone to contraction (Thomopoulos et al. 2005). Despite these constraints, 60% PEO constructs contracted visibly in width and grew thicker with time in culture. Similarly, with increasing PEO content, scaffolds implanted in subcutaneous pockets of rat dorsa thickened and narrowed (**Figure 5-7**).

Although it is possible that changes in construct form will not occur upon implantation in a load-bearing site, the more ideal scenario is one where the scaffold provides the necessary structure to define the resulting shape of the tissue. In this work, we've created scaffolds containing two populations of fibers: those that disappear instantaneously, and those that undergo hydrolysis at a very slow rate. The use of a polymer that erodes at a more moderate pace could simultaneously provide the necessary organizational cues and minimum structural integrity needed to engineer an anisotropic tissue with defined form. This stiff and yet elastic polymer would need to degrade quickly enough to allow cells to further invade and fill the newly-vacated space with ECM, while persisting long enough to thwart the effects of cell-mediated stresses. Rather than relying on hydrolysis for fiber degradation and removal, it may prove more sensible to engineer biologically-sensitive fibers (e.g. MMP-cleavable nanofibers). By associating matrix synthesis with the

cleavage and removal of synthetic fibers, it may be possible to inversely couple tissue growth and scaffold degradation, a central tenet of functional tissue engineering.

## **5.5 CONCLUSION**

This work presents an enabling technology for the engineering of fiber-reinforced tissues; namely, the production of tunable nanofibrous scaffolds that provide instruction without impediment. Whether scaffolds are seeded with cells *in vitro*, or implanted acellularly and infiltrated by host cells, rapid colonization is essential for both tissue integration and maturation. As the dense packing of fibers cannot be controlled during the electrospinning process, the use of sacrificial fibers allows for better cellular access, and importantly, preserves the instructional capacity of the scaffold to direct cell and cell-secreted matrix organization. In essence, this work transforms what is an interesting surface phenomenon (cells on top of nanofibrous mats) into a method by which functional, three-dimensional tissues can be formed, both *in vitro* and *in vivo*. As such, it is marked step forward in material processing for the engineering of load-bearing fibrous tissues, and will find widespread applications in regenerative medicine.

# ***CHAPTER 6: FABRICATION AND MODELING OF DYNAMIC MULTI-POLYMER NANOFIBROUS SCAFFOLDS***

## **6.1 INTRODUCTION**

Fibrous tissues are collagen-rich structures present throughout the musculoskeletal system that serve a variety of vital load-bearing roles. The organization of these tissues is paramount to their mechanical function, and is to a great extent dictated by the mechanical environments in which they operate. For example, those tissues that function under cyclic, near-uniaxial tension (such as flexor tendons) are comprised of collagen fibers organized in a single, predominant direction (Lynch et al. 2003). On the other hand, tissues that function in more complex, multi-axial loading environments, such as the knee meniscus (Petersen et al. 1998; Setton et al. 1999; Petersen et al. 2004) and the annulus fibrosus of the intervertebral disc, reveal more complex hierarchical collagen organization (Iatridis et al. 2005). Despite the refined characteristics that function has imparted on the form of these tissues, traumatic injury and degeneration are common occurrences and can interrupt normal mechanical function. As a result, there remains unmet clinical need for engineered replacements for damaged or diseased native fibrous tissues.

When engineering fibrous tissue replacements, the demanding physical environment in which they will perform must be taken into consideration. Tissue engineered constructs should at minimum recapitulate the sub-failure stress-strain response of the tissue (Butler et al. 2004). Because success in such endeavors has been limited to date, the most

common clinical solution for fibrous tissue damage remains the autologous or allogeneic transfer of tissue to the defect site (for example, meniscus transplantation and bone-patella-bone autografts). However, low availability of suitable grafting tissues and high failure rates engender a need for tissue engineered solutions. To specifically address the hierarchical and structural organization of fibrous tissues, many tissue engineering strategies have focused on collagen gel-based constructs. Organization in such constructs is mediated by the traction forces that cells within the collagen gel exert against a fixed boundary, and can promote pronounced anisotropy in the forming construct (Awad et al. 2000; Costa et al. 2003). However, these collagen gel-based constructs remain very soft, even after long culture durations, in comparison to native fibrous tissue (Garvin et al. 2003; Thomopoulos et al. 2005). In other work, hierarchical structure has been imparted through the use of macro-scale polymer fibers (including biodegradable polyesters and silk) to engineer fiber-reinforced constructs (Altman et al. 2002; Cooper et al. 2005; Moutos et al. 2007). These scaffolds better recapitulate the native tissue mechanical response, and have moved toward clinical implementation.

An alternative strategy that has recently become more prevalent for engineering such tissues is based on the process of electrospinning (Reneker et al. 1996). This is an old technology, first patented in the 1930s (Formhals 1934), and has been extensively investigated for applications such as textile and filter manufacturing (Burger et al. 2006). Within the last decade, this process has found renewed interest for the engineering of a number of different tissues. Compared to macrofibrous construction methods, electrospinning generates nano- and micron-scale fibers, thereby providing a ready means

to recapitulate the organizational features and length-scales of many collagenous tissues (Li et al. 2007). In its most basic form, electrospinning involves the application of a high voltage potential and resulting gradient to draw a polymer solution into thin fibers which can then be collected *en masse*. Numerous processing variables can be varied to fine tune the electrospinning process, and both biologic and synthetic polymers can be processed in this fashion (Li et al. 2005; Barnes et al. 2007). Moreover, multiple polymers can be combined in the same fiber (intra-fibrillar) (Stitzel et al. 2006; Barnes et al. 2007), or separate jets can be used to deliver multiple polymers to the same collecting surface (Ding et al. 2004; Kidoaki et al. 2005) to modulate the as-formed mechanical properties.

More recently, numerous groups have begun to examine the role of fiber alignment in nanofibrous scaffolds, and its potential application for fiber-reinforced tissue engineering. Aligned fibers can be formed by simply focusing deposition onto a rapidly moving surface (Sundaray et al. 2004). We and others have shown that these aligned arrays mimic the structure of numerous fiber-reinforced and anisotropic tissues (Ayres et al. 2006; Courtney et al. 2006; Li et al. 2007; Nerurkar et al. 2007). In our previous studies, we used electrospun scaffolds composed of poly( $\epsilon$ -caprolactone) (PCL), and demonstrated that multiple cell types adhere to and organize themselves into aligned communities when cultured on aligned scaffolds. Importantly, with time in culture, the organization of the cell-generated extracellular matrix (ECM) paralleled the governing fiber direction defined by the nanofibrous array as shown in Chapter 3. However, we also observed a significant limitation in these scaffolds; surface-seeded cells have difficulty infiltrating through the small pore-sizes that result from the dense packing of

aligned fibers. This slow infiltration rate results in inhomogeneous ECM deposition and incomplete cell colonization even in relatively thin scaffolds (~1mm thick) and over long culture durations (>10 weeks).

To address this issue, we developed a dual-polymer electrospinning process that enables the interspersions of a sacrificial fiber population within a dual-component nanofibrous scaffold (Chapter 4). These sacrificial fibers, comprised of water-soluble poly(ethylene-oxide) (PEO), serve as space-holders during the formation of the scaffold, and their subsequent removal provides the necessary increase in pore size to accelerate cellular ingress. Unfortunately, while removal of a sufficient fraction of sacrificial fibers enhanced infiltration, it also resulted in an overall loss in scaffold structural integrity as cell-mediated traction forces compacted the construct. Thus, to maintain scaffold integrity while still implementing pore-forming sacrificial fibers, the present work focuses on the inclusion of a more slowly eroding third fiber population. This fiber population would serve to maintain scaffold integrity initially, and then gradually erode to augment pore size and porosity as the composite evolves. Inclusion of this third fiber population would provide time-dependent characteristics in the composite scaffold, and could also be used to further refine the mechanical properties.

In addition to experimental characterization of scaffold mechanics and porosity as described above, constitutive modeling of these structures can also provide additional insight by permitting investigations that, experimentally, may be laborious or even impossible. Constitutive models of electrospun scaffolds have varied widely in their

complexity, from simple geometrically motivated linear models (Mathew et al. 2006; Li et al. 2007; Nerurkar et al. 2007) to hyperelastic continuum models (Courtney et al. 2006; De Vita et al. 2006; Nerurkar et al. 2008). Hyperelastic models have the additional advantage of describing materials with nonlinear mechanical behaviors over large deformations. Because nonlinearity and finite deformations are functional hallmarks of many fiber-reinforced soft tissues, hyperelastic models are of great utility not only for characterizing acellular scaffolds and engineered constructs, but also for yielding comparisons of these materials with native tissue benchmarks (Nerurkar et al. 2007; Nerurkar et al. 2008). In these previous studies, a fiber-reinforced hyperelastic model was developed to characterize the mechanics of acellular electrospun scaffolds with a single population of PCL nanofibers, and used this model to quantify the functional evolution of cell-seeded scaffolds over 8 weeks as ECM was deposited and the constructs matured *in vitro*. The model was validated as a predictive tool for that system, and is expanded in the present work to account for the combined behavior of multiple constituent fiber populations.

To carry out this study, a novel multi-jet electrospinning device was developed for the production of aligned composite nanofibrous scaffolds with multiple and distinct fiber populations. Using this device, a composite scaffold containing slow, medium, and fast-eroding elements was fabricated, and its mechanical properties were evaluated over the course of degradation. To better understand the mechanical response of these novel composites, a hyperelastic model was used to assess the full nonlinear and anisotropic response of these meshes and developed numerical descriptions of how these properties

change over the time course of component degradation. We utilized data from scaffolds containing a single fiber population, coupled with a constrained mixture approach, to predict the time-dependent nonlinear tensile behavior of the evolving composite. Finally, we used this validated model to predict the mechanical response of any combination of fiber populations. This new fabrication method and modeling approach provides a means by which rational and directed design can be used to manufacture tissue-specific nanofibrous scaffolds for the engineering of dense connective tissues.

## 6.2 MATERIALS AND METHODS

Two separate studies were performed: Study I included device and methodology development to enable fabrication and testing of multi-component scaffolds; Study II analyzed and modeled dynamic multi-component scaffolds over a nine week time course.

**Table 6-1: Scaffold Fabrication. Polymer formulations used to fabricate composite nanofibrous constructs in Study I and Study II.**

	<b>Study I</b>		<b>Study II</b>	
	<b>Polymers</b>	<b>Solvent</b>	<b>Polymers</b>	<b>Solvent</b>
<b>Slow</b>	PCL	DMF:THF	PCL	DMF:THF
<b>Medium</b>	PLGA	DMF:THF	PCL/PLGA	DMF:THF
<b>Fast</b>	PEO	90% Ethanol	PEO	90% Ethanol
<b>Testing</b>	Dry (as-formed)		Wet (time course)	

### 6.2.2 Scaffold Fabrication

In Study I, solutions of PCL, PLGA, and PEO were electrospun either individually or simultaneously to generate scaffolds with a single fiber population or with multiple fiber populations (Composite), respectively. All polymers were dissolved by stirring over 18 hours at 40°C. PEO (10% w/v, 200kDa, Polysciences, Warrington, PA) was prepared in

90% ethanol while PLGA (50:50 lactic acid:glycolic acid, 22.2% w/v, 100kDa, Durect, Pelham, AL) and PCL (14.3% w/v, 80kDa, Sigma, St. Louis, MO) were each dissolved in equal parts dimethylformamide and tetrahydrofuran (DMF:THF, Sigma). Due to the undesirable mechanical characteristics of electrospun PLGA (see Results), the PLGA solution was replaced with a mixture of PCL and PLGA (termed Blend) in Study II. In study II, PCL and PEO solutions were prepared as described above, and PCL (7.2% w/v) and PLGA (11.1% w/v) were dissolved together in DMF:THF to produce the blended polymer solution (**Table 6-1**).

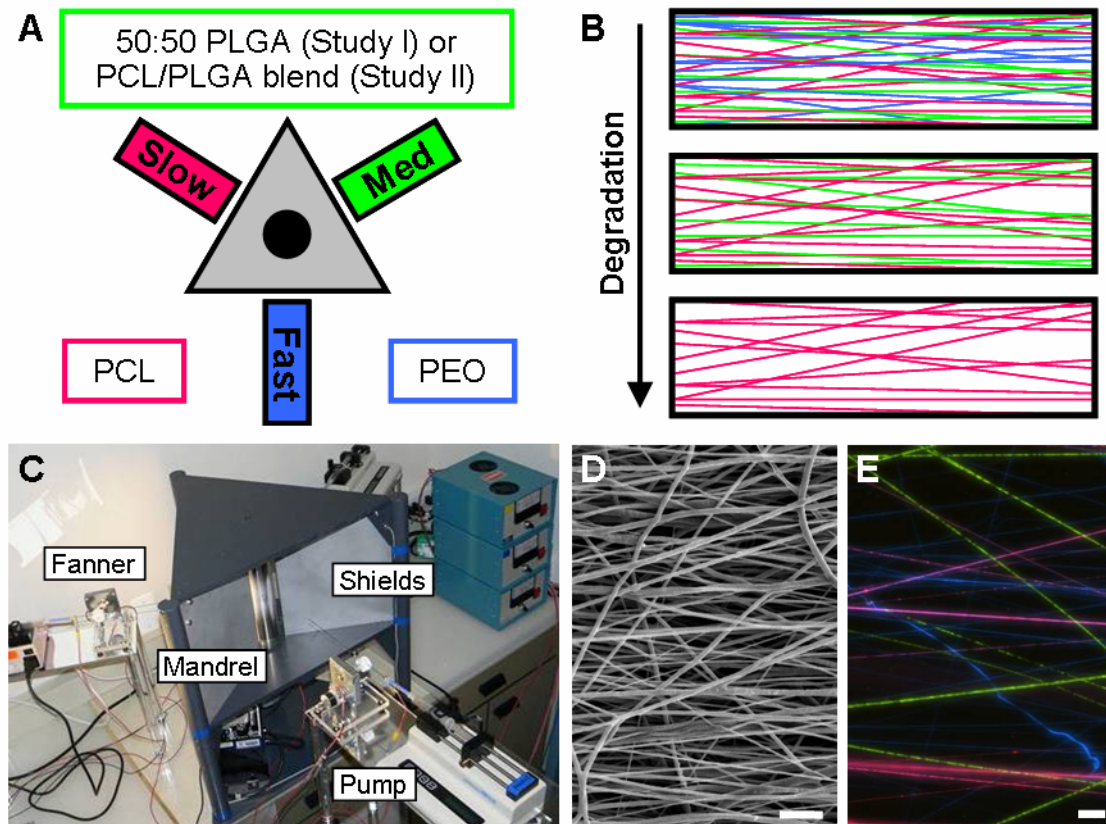


**Figure 6-1: Composite nanofibrous scaffolds containing three distinct fiber populations were fabricated with a custom electrospinning device. A) Schematic of the formation of electrospun scaffolds containing fast, medium, and slow-degrading fiber populations. B) Diagram depicting the temporal evolution of porosity in composite scaffolds that lose fiber elements in a pre-programmed fashion via differing degradation profiles. C) Novel electrospinning device for forming single- and multi-polymer fibrous scaffolds by co-electrospinning from up to three jets onto a common rotating mandrel. D) Fiber morphology in composites imaged via SEM (scale bar: 10µm). E) Composites fabricated with fluorescently labeled fiber populations show the presence and interspersed nature of each element (scale bar: 10µm).**

Electrospinning was performed using a custom device designed to focus three electrospun polymer jets from separate spinnerets towards a common, centralized rotating mandrel (**Figure 6-1**). Each solution was driven through the spinnerets via syringe pump (KDS100, KD Scientific, Holliston, MA) at 1ml/h (Study I) or 2.5ml/h (Study II) from an 18G needle that was translated (with custom fanning devices) over a 5cm distance along the vertical mandrel (which rotated at a linear surface velocity of  $\sim 10\text{m/s}$ ). All three

spinnerets were charged to +13kV and placed 15cm from the mandrel surface, which was itself charged to -2kV to enhance fiber collection. Additionally, aluminum plates were positioned at the vertices of this setup and charged to either +9kV (Study I) or +8kV (Study II) to focus the electrospun cloud so as to further aid in efficient fiber capture. In both studies, each polymer solution was electrospun individually to generate a mesh containing a single fiber population, then, all three polymers were co-electrospun onto the same mandrel simultaneously to generate multi-fiber composites.

### **6.2.3 Imaging**

In additional studies, polymer solutions were fluorescently doped and electrospun to confirm the presence and interspersions of the three distinct fiber populations. Cell Tracker Red, 7-dimethylaminocoumarin-4-acetic acid (Invitrogen, Carlsbad, CA), and fluorescein (Sigma) were added at 0.2% w/v to solutions of PCL, PEO, and blended PCL/PLGA, respectively. Fluorescently labeled solutions were then co-electrospun for 15s onto glass cover slips affixed to the rotating mandrel. Fibers were imaged at 20× magnification using a Nikon T30 inverted fluorescent microscope equipped with a CCD camera and the NIS Elements software (Nikon Instruments, Inc., Melville, NY). Additionally, PCL, Blend, and Composite scaffolds were examined by scanning electron microscopy at each time point. Samples were gold-palladium sputter coated and imaged with a JEOL 6400 scanning electron microscope operating at an accelerating voltage of 10kV (Penn School of Medicine Microscopy Core Center).

#### **6.2.4 Mechanical Testing**

From each mat, 30mm by 5mm strips were excised in the prevailing fiber direction (Fiber) or perpendicular to this direction (Transverse). For Study 1, all testing was performed on as-formed, dry samples. In Study 2, acellular scaffolds were rehydrated and maintained in a standard culture environment (37°C, 5% CO<sub>2</sub>) for nine weeks in order to measure degradation-dependent behavior. After determining the initial dry mass, samples were UV sterilized, rehydrated in diminishing fractions of ethanol (100, 70, 50, 30%), and incubated in DMEM containing 1x PSF at 37°C until testing. For samples from both studies, four measurements of the cross-sectional area were acquired with a custom LVDT/laser system. The strips were airbrushed with black enamel to generate texture before mounting in an Instron 5848 Microtester (Instron, Canton, MA). After a nominal preload of 0.1N, the samples were allowed 1min to equilibrate. Following this, the strips were extended beyond their yield point at a rate of 0.1% of the gauge length per second. Images of the central third of each specimen were captured at 0.5Hz for subsequent texture-correlation analysis via Vic2D to determine two-dimensional Lagrangian strain (E) (Correlation Solutions, Columbia, SC). Modulus was determined from the linear region of the stress-strain plot. Linear regressions were performed iteratively over ranges of 0.6% strain and the yield strain was demarcated when the R<sup>2</sup> transitioned below 0.996. This strain range and R<sup>2</sup> threshold was chosen as a conservative and reproducible method for defining the end of the linear portion of the stress-strain curve, and was maintained for analysis throughout the entire study. After tensile testing, samples were dried and reweighed to determine mass loss at each time point.

### ***6.2.5 Determination of Fiber Fractions***

Day 0 samples from Study II were enzymatically digested to estimate starting fiber fractions of Composite scaffolds. PCL, Blend, and Composite scaffolds were digested with 10U/ml of *Pseudomonas* sp. lipase (Type XIII, Sigma) in phosphate buffered saline and incubated at 37°C for 48h with agitation. After lipase-mediated digestion of the PCL component of each scaffold, samples were washed twice in distilled water before being dried and reweighed.

### ***6.2.6 Constitutive Modeling of Composites***

A hyperelastic fiber-reinforced constitutive model was employed to describe the tensile behavior of hydrated composite nanofibrous scaffolds in Study II. We first determined the constitutive laws for scaffolds composed of single fiber populations of Blend or PCL. These were then applied, using a constrained mixture approach, to predict the time-varying behavior of the two-component composite scaffold (after removal of PEO). Upon validation, the model was used to simulate time and composition dependent mechanics.

The composite and single component scaffolds were modeled using the constitutive theory of highly anisotropic solids as described by Spencer, in which the strain energy density function is decomposed into the sum of ‘fiber’ and ‘matrix’ functions (Spencer 1972).

### 6.2.6a Single Component Constitutive Laws

For each Blend and PCL scaffold, the matrix phase was described as a compressible Neo-Hookean material, while the fibers were described with an exponential law (Holzapfel 2000; Eberline et al. 2001; Nerurkar et al. 2008). As detailed in Nerurkar et. al., the resulting constitutive law is given by:

$$\mathbf{T}^i = I_3^{-1/2} [\mu^i (\mathbf{F}\mathbf{F}^T - I_3^{-\beta^i} \mathbf{I}) + 2\gamma^i (I_4 - 1) e^{\xi^i (I_4 - 1)^2} \mathbf{F}\mathbf{a} \otimes \mathbf{a}\mathbf{F}^T] \quad (1)$$

where the superscript  $i = B, C$  for Blend and PCL, respectively;  $\mathbf{T}$  is the Cauchy stress tensor,  $\mu^i$  and  $\nu^i = \frac{\beta^i}{1 + 2\beta^i}$  are the two matrix parameters that characterize matrix modulus and material compressibility;  $\gamma^i$  and  $\xi^i$  are fiber parameters representing the fiber stiffness and the degree of their stress-strain nonlinearity;  $I_3 = \det(\mathbf{C})$  is the third invariant of the Right Cauchy Green Tensor  $\mathbf{C} = \mathbf{F}^T\mathbf{F}$ , where  $\mathbf{F}$  is the deformation gradient tensor (Ogden 1997); the scalar  $I_4$  is an invariant defined as  $I_4 = \mathbf{a} \cdot \mathbf{C}\mathbf{a}$ , where  $\mathbf{a}$  is a unit vector along the fiber direction (Spencer 1972). Fiber contributions were restricted to tensile stresses only ( $I_4 = 1$  for  $I_4 < 1$ ) (Ateshian 2007).

Therefore, each single fiber population scaffold, Blend or PCL, was described by four scalar material parameters:  $\mu^i$  and  $\nu^i$  to describe the matrix phase, and  $\gamma^i$  and  $\xi^i$  to represent the fiber phase. The implementation of this model for single-component electrospun scaffolds was performed as described previously (Nerurkar et al. 2008). In brief, a least squares curve fit of the model to the transverse stress-strain data was performed at each time point to yield matrix material parameters,  $\mu^i$  and  $\nu^i$ . The average of the resulting values was used to fit the fiber direction stress-strain curves in order to

determine the time-matched values of fiber parameters,  $\gamma^i$  and  $\xi^i$ . Accordingly, the four material parameter values were obtained for each component (Blend and PCL) at each time point (days 0, 7, 21, 42, 63).

### 6.2.6b Composite Constitutive Law

To model the composite scaffold mechanics, it was assumed that the composite properties were determined entirely by the constituent material parameters and the relative amounts of each constituent present, or:

$$\mathbf{T}^t = \mathbf{T}^t(\phi^C, \mu^C, \nu^C, \gamma^C, \xi^C, \phi^B, \mu^B, \nu^B, \gamma^B, \xi^B, C)$$

where  $\mathbf{T}^t$  is the total stress of the composite and  $\phi^i$  is the mass fraction of each component. Specifically, a constrained-mixture approach was used, whereby each constituent deforms identically, according to the overall deformation of the composite, or in other words  $\mathbf{F} = \mathbf{F}^i$  for  $i = \text{Blend, PCL}$ . Additionally, the composite stress is the sum of constituent stresses scaled to their current mass fraction:

$$\mathbf{T}^t = \phi^B \mathbf{T}^B + \phi^C \mathbf{T}^C$$

Conventionally, it is required that the sum of mass fractions always be unity. Although this constraint was enforced at Day 0, it was relieved at subsequent time points in order to account for the loss of intact, load-bearing fibers with degradation; mass fractions were computed at each time point as the current constituent mass normalized to the initial total mass. At Day 0, it was assumed that  $\phi^B = \phi^C = 0.5$ , based upon experiments using lipase to remove the PCL component from both Blend and Composite scaffolds. From Days 7 to 63, mass fractions were approximated by assuming all mass loss of the composite (measured experimentally) was due to loss of the Blend component, while  $\phi^C = 0.5$  was

maintained for all time points (see Results). The contention that PCL mass does not degrade significantly over 63 days was supported by the experimental results. The model was then validated by *predicting* the fiber direction stress-strain behavior of the composite scaffold at each time point using time-matched material parameters and mass fractions. For each sample, the experimentally measured 2-D deformations were input into the model and the resulting model-computed stresses were compared with experimentally measured stress. Agreement of the model predicted stress with the corresponding experimental stress was assessed to indicate the suitability of the proposed model as a full quantitative description of the nanofibrous composite scaffold (Nerurkar et al. 2008).

#### **6.2.6c Model Simulation**

Upon validation, the model was used to simulate the time-varying mechanical behavior of composite nanofibrous scaffolds for a range of initial compositions. In order to approximate the time dependence of the material parameters, each parameter was assumed to vary linearly with time and linear regression were utilized. This assumption proved reasonably accurate for all time-varying parameters (see Results). The moduli of simulated composites were determined by fitting a tenth order polynomial to the model-generated stress-strain curve, and evaluating the derivative of the polynomial at  $E=0.05$ .

#### **6.2.7 Statistical Analyses**

For experimental data, a two-factor ANOVA with Bonferroni post-hoc tests was used to make comparisons between groups, with independent factors of degradation time

and scaffold type. Data is presented as the mean  $\pm$  standard deviation from a minimum of 5 samples for each condition and time point. The quality of model fits are reported by  $R^2$  values as well as the Bland-Altman limits of agreement (B-A, bias  $\pm$  standard deviation), reported in MPa (Bland et al. 1986).

## 6.3 RESULTS

### 6.3.1 *Experimental*

A custom multi-jet electrospinning device was successfully constructed and employed to generate single fiber population and multiple fiber population composite aligned nanofibrous scaffolds (**Figure 6-1**). Fluorescently labeled fibers demonstrated successful interspersions of discrete fibers throughout the composite scaffold. In Study I, PCL, PLGA, and PEO scaffolds were formed and tested in uniaxial tension in the fiber direction. Stress-strain profiles for each single fiber population scaffold were distinct (**Figure 6-2A**). PEO and PCL scaffolds had comparable tensile moduli while the modulus of PLGA scaffolds was  $\sim$ 20 times higher (**Figure 6-2B**). While PCL scaffolds exhibited a significant toe region and yielded at a higher strain ( $E=0.100$ ), both PEO and PLGA scaffolds lacked toe regions and were significantly less extensible, yielding at  $E=0.012$  and  $E=0.014$ , respectively (**Figure 6-2C**). When all three polymers were co-electrospun into a composite scaffold, the resulting mesh displayed characteristics of its constituents (**Figure 6-2A**). Composite scaffolds had a modulus intermediate to PCL and PLGA (**Figure 6-2B**) and a toe region was observed, though composite scaffolds still yielded at low strains ( $E=0.026$ ) relative to pure PCL scaffolds (**Figure 6-2C**). Of note, these scaffolds were all taken from the same location on the rotating mandrel. However,

when composite strips were excised from different locations along the length of the mandrel we observed a gradient in the deposition of PCL and PLGA fibers (**Figure 6-2D**). Where PLGA fibers were dominant, stress-strain profiles revealed a linear behavior with a higher modulus. Conversely, increases in the PCL fiber fraction resulted in a more pronounced toe region but a lower modulus. This suggests that care must be taken in ensuring full interspersions of composite fibers, particularly when one component has markedly higher mechanical properties than the others. We also noted that, upon hydration, both PLGA and Composite scaffolds contracted in length by ~70% and ~60%, respectively (data not shown). Due to this behavior, as well as the low yield strains of PLGA fibers, the PLGA solution was replaced with a blend of PCL and PLGA in Study II.

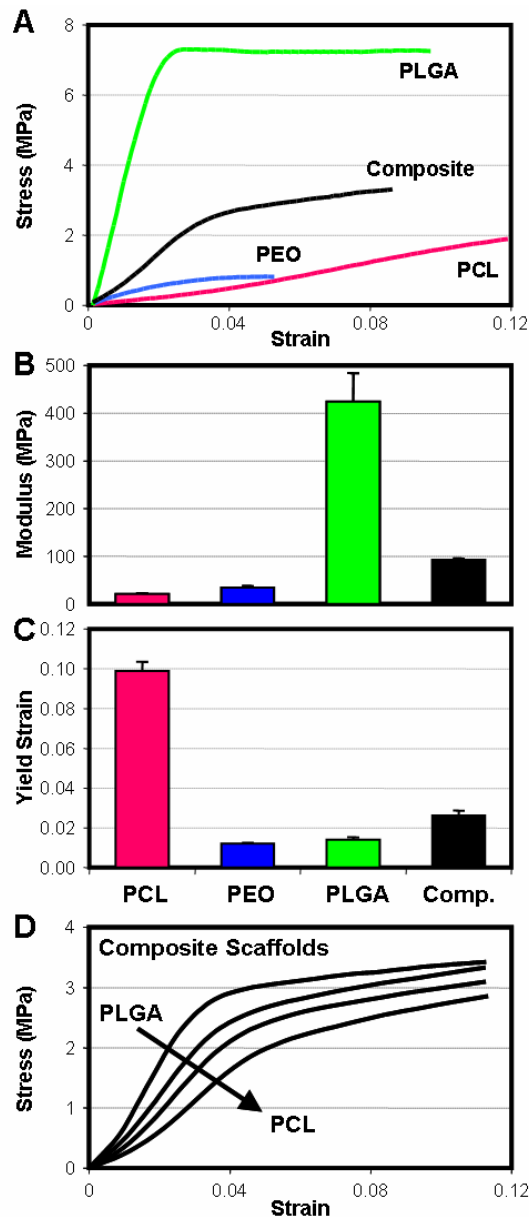


**Figure 6-2: Study I: Electrospun PCL, PLGA, and PEO scaffolds have unique stress-strain profiles. When all three elements are combined, the Composite scaffold stress-strain behavior shares characteristics of each constituent. A) Stress-strain profiles of PCL, PEO, PLGA, and Composite scaffolds extended in the fiber direction. Modulus (B) and yield strain (C) for each scaffold (n=5/group). D) Samples from Composite scaffolds removed along the length of the mandrel showed a range of behaviors, dependent upon the relative fractions of PLGA or PCL fibers at each location.**

In Study II, scaffolds comprised of a single fiber population of Blend PCL/PLGA fibers could be hydrated without noticeable decreases in scaffold length or fiber morphology in

SEM images (not shown). This allowed for evaluation of scaffold mechanical behavior over a time course of degradation, without the influence of complicating factors such as gross scaffold distortion. For this study, composite scaffolds were hydrated before mechanical analysis. As expected, upon hydration, PEO scaffolds dissolved completely, and so are excluded from further analysis of mechanics or mass loss. On day 0 (immediately after hydration), PCL and Blend scaffolds tested in the fiber direction demonstrated distinct stress-strain profiles (**Figure 6-3A**). As in Study I, PCL revealed a significant toe region with yield strains of  $E=0.115$  (**Figure 6-3B**). Blend scaffolds were linear and lacked a toe region, but were extensible to higher strains ( $E=0.080$ ) before yield (compared to yield at  $\sim 1\%$  for pure PLGA scaffolds evaluated in study I). Similar to Study I, composites comprised of PCL and Blend fibers showed characteristics of the two remaining constituents (recall that PEO is removed upon hydration). Initially, composite scaffolds had moduli intermediate to PCL and Blend (**Figure 6-3C**), but lower strains at yield than both of its constituents (**Figure 6-2B**). Testing performed on transverse samples revealed the high degree of anisotropy in all three types of scaffolds as evidenced by the significantly lower moduli in the transverse direction (**Figure 6-3D**).

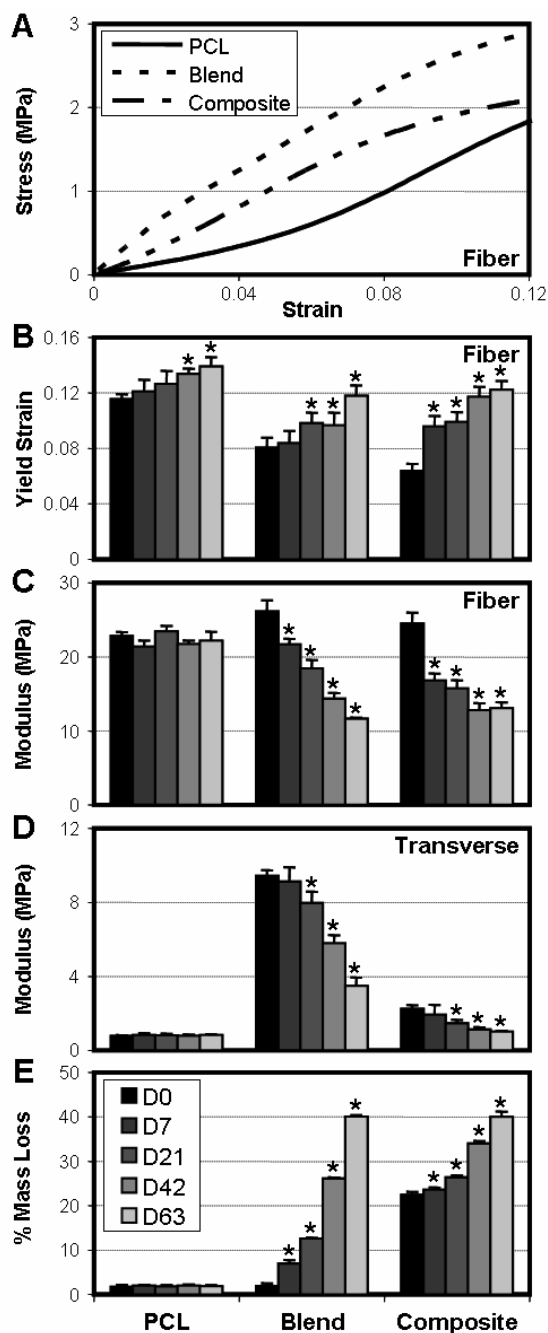


**Figure 6-3: Study II: Single- and multiple-fiber population scaffold tensile behavior is modulated by composition and degradation time. A) Stress-strain curves of day 0 PCL, Blend, and Composite scaffolds tested in the fiber direction. Yield strain (B) and modulus (C) of samples tested in the fiber direction over 63 days (n=5/group per time point). D) Modulus in the transverse direction as a function of time (n=5/group per time point). E) Percent mass loss relative to dry, as-formed samples over the 63 day time course (n=5/group per time point). Note that Composite scaffolds on day 0 lose ~22% of their starting mass due to removal of the PEO fiber population during hydration. \*: p<0.01 versus day 0.**

After the initial day 0 hydration and testing, scaffolds were incubated in DMEM+PSF at 37°C and fiber and transverse properties as well as changes in mass were assessed on days 7, 21, 42, and 63. As observed in previous studies, the mass of pure PCL scaffolds did not diminish up to 63 days (**Figure 6-3E**,  $p=1.0$ ). Paralleling the lack of mass loss, the mechanical behavior of PCL scaffolds did not change appreciably, with moduli in both the fiber and transverse directions remaining constant for the entire course of the study (**Figure 6-3C,D**,  $p=1.0$ ). Interestingly, the yield strain of PCL increased with time, and was significantly higher than starting values by day 42 (**Figure 6-3B**). Contrasting the immutability of PCL scaffolds, Blend scaffolds began degrading from the outset, as indicated by the significant mass loss by day 7. Additional decreases in mass were observed at all remaining time points, cumulating to a ~40% mass loss by day 63 (**Figure 6-3E**). Degradation of these Blend fibers resulted in decreases in both fiber and transverse moduli in the scaffolds (**Figure 6-3C,D**,  $p<0.001$ ). Additionally, yield strains of Blend scaffolds extended in the fiber direction increased with degradation time (**Figure 6-3B**,  $p<0.001$ ).

Composite scaffolds showed time dependent characteristics as well. These scaffolds lost ~22% of their original mass upon hydration as a result of the immediate dissolution of the PEO fiber population (**Figure 6-3E**). Lipase digestion after PEO removal showed that Blend fibers made up 54.3% of the remaining Composite scaffold, while pure PCL fibers made up 45.7%. Due to the presence of Blend fibers, Composites continually lost mass for the duration of the study resulting in an additional 18% decrease in mass by day 63. As observed in Blend scaffolds, Composite scaffolds showed temporal changes in

mechanical properties, with both fiber and transverse moduli decreasing in a time-dependent manner (**Fig 6-3C,D**,  $p < 0.001$ ). Contrasting Blend behavior, the fiber-direction modulus of Composites decreased dramatically by day 7 to levels well below PCL and Blend values ( $p < 0.001$ ), then appeared to stabilize towards later time points. As with PCL and Blend scaffolds, Composite yield strains increased with time ( $p < 0.001$ ) approaching  $E = 0.122$  by day 63.

### 6.3.2 Theoretical

The constitutive model was successfully fit to transverse PCL and Blend constructs at all time points to yield matrix constants  $\mu^i$  and  $\nu^i$  (**Figure 6-4B,C** and **Table 6-2**), with average  $R^2 = 0.986$  and B-A  $-0.002 \pm 0.004$  MPa. As an example, model fits to experimental data of day 0 samples tested in the transverse direction are shown in **Figure 6-4A**. The Blend matrix parameter  $\mu^B$  decreased linearly with time by up to 2.5-fold on day 63. No significant changes were observed in  $\mu^C$ ,  $\nu^C$  or  $\nu^B$  with time. The constitutive model also successfully fit Blend and PCL samples along the fiber direction to yield fiber parameters  $\gamma^i$  and  $\xi^i$  with average  $R^2 = 0.988$  and B-A  $-0.018 \pm 0.055$  MPa (**Figure 6-4E,F**). Model fits to fiber direction experimental data of day 0 samples are shown in **Figure 6-4D**. The fiber modulus parameter  $\gamma^i$  decreased approximately 2-fold with time for Blend samples, but did not change with time for PCL.  $\xi^C$  increased slightly by Day 63, and  $\xi^B$  was zero at all time points.

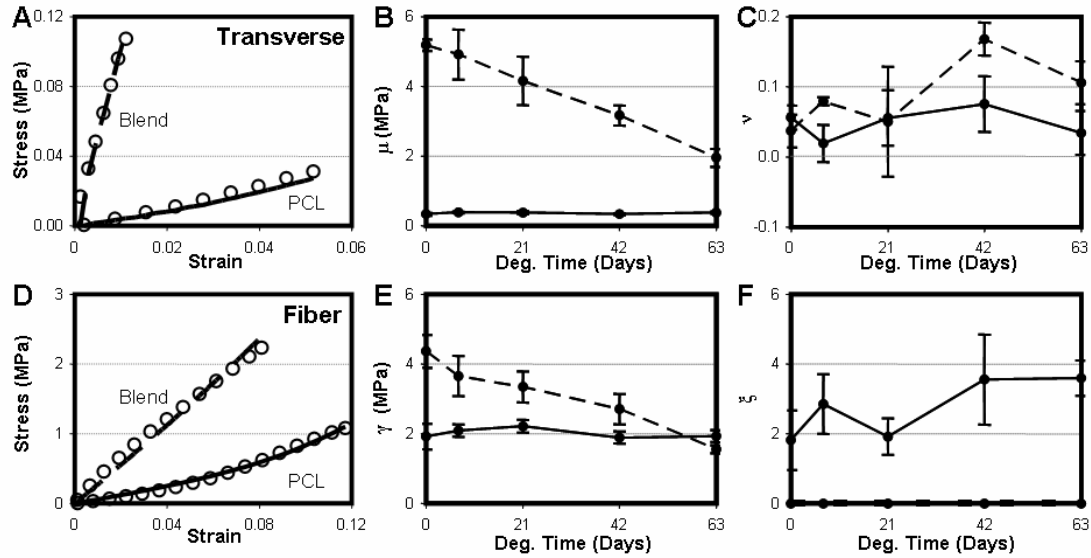


**Figure 6-4:** Characterization of single-fiber population (PCL and Blend) scaffold tensile behavior with a hyperelastic fiber-reinforced constitutive model. Curve fit results (lines) on day 0 are shown along with experimental data (circles) for the transverse (A) and fiber (D) directions. From transverse direction testing, matrix parameters  $\mu$  (B) and  $\nu$  (C) were determined at each time point. These values, coupled with fits to fiber direction data at each time point were used to determine fiber parameters,  $\gamma$  (E) and  $\xi$  (F).

Having determined the time-varying material parameters for each single fiber population scaffold, we next used this information to predict the behavior of the composite scaffold. Accurate prediction of the composite scaffold mechanics would indicate that the model is valid for this application. The model was successfully validated at each time point, using only the deformation, the relative amount of Blend to PCL fibers remaining, and the material parameters from each time point to *predict* the Composite scaffold stress under uniaxial extension in the fiber direction (**Figure 6-5**, average  $R^2=0.997$  and B-A -  $0.013\pm 0.053$  MPa, **Table 6-2**). Although at Day 0 the model under-predicted stresses, it provided strikingly close predictions of experimental stress-strain curves at each subsequent time point (**Table 6-2**).

**Table 6-2: Model Validation.**  $R^2$  and Bland-Altman limit of agreements from least squares fits of experimental data for single fiber population scaffolds (PCL and Blend). Also shown are metrics comparing Composite scaffold experimental stress-strain response and model predicted values.

	Model Fits								Model Predictions	
	PCL				Blend				Composite	
	Fiber		Transverse		Fiber		Transverse		Fiber	
	R2	B-A (MPa)	R2	B-A (MPa)	R2	B-A (MPa)	R2	B-A (MPa)	R2	B-A (MPa)
Day 0	0.987±0.005	0.010±0.044	0.998±0.002	0.000±0.001	0.984±0.004	-0.052±0.104	0.979±0.006	-0.005±0.009	0.997±0.002	-0.151±0.105
Day 7	0.995±0.001	0.005±0.025	0.999±0.000	0.000±0.001	0.967±0.003	-0.053±0.096	0.984±0.003	-0.004±0.008	1.000±0.000	0.028±0.027
Day 21	0.992±0.001	0.006±0.032	0.995±0.006	-0.001±0.002	0.989±0.005	-0.043±0.081	0.977±0.017	-0.004±0.008	0.998±0.001	0.064±0.049
Day 42	0.991±0.004	0.005±0.036	0.996±0.007	0.000±0.002	0.984±0.004	-0.049±0.083	0.965±0.005	-0.004±0.007	0.996±0.001	0.039±0.045
Day 63	0.994±0.001	0.005±0.023	0.995±0.008	0.000±0.001	0.994±0.002	-0.011±0.020	0.974±0.009	-0.002±0.004	0.995±0.001	-0.046±0.041

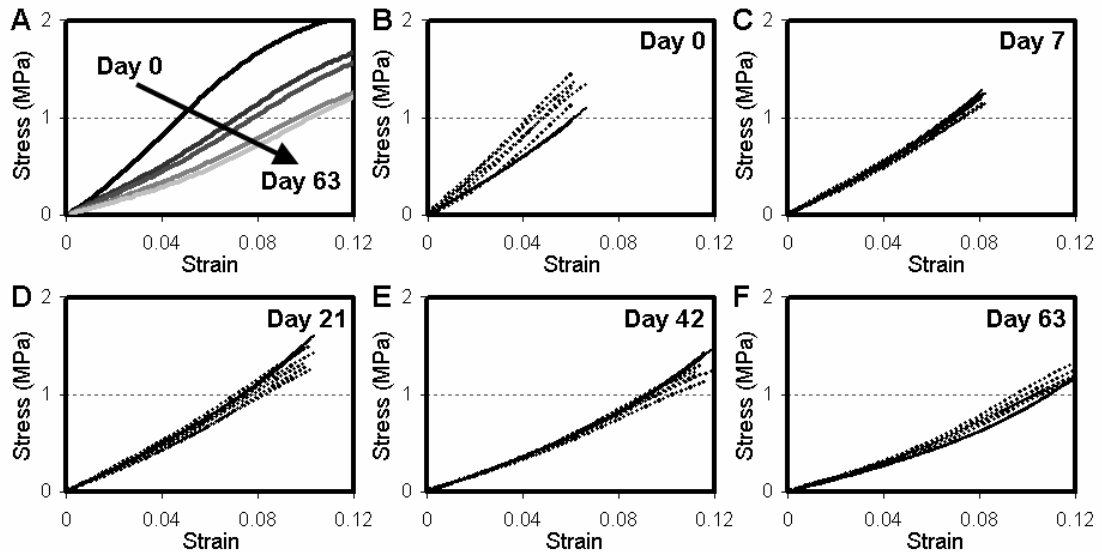


**Figure 6-5: Material parameters from single-component scaffolds successfully predict Composite scaffold behavior.** A) Stress-strain curves for Composites tested in the fiber direction. Stress-strain profiles diminished as degradation occurred over 63 days, due to decreasing properties of the Blend fiber population. Model predictions of Composite stress response when tested in the fiber direction on days 0 (B), 7 (C), 21 (D), 42 (E), and 63 (F) showed good agreement with experimental measures. Each plot contains all five experimental curves (dotted lines) and the corresponding five model-generated predictions (solid lines).

Using the validated model, we next predicted the modulus and curvature of theoretical scaffolds consisting of any combination of PCL and Blend at any time point. The model simulation demonstrated that the composite scaffold modulus can be tuned between 20

and 45 MPa, simply by varying the initial content of Blend or PCL (Figure 6-6). Additionally, the composite mechanics are increasingly sensitive to degradation with time as the Blend content is increased. Finally, by varying the balance between Blend and PCL fiber populations, the model demonstrated that the magnitude and the nonlinearity of the composite stress-strain behavior can both be modulated.

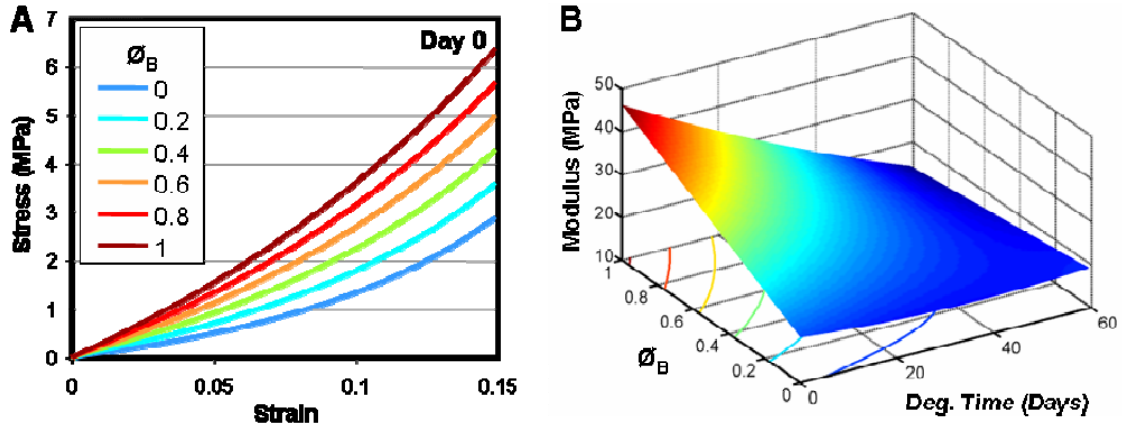


**Figure 6-6: Simulation of Composite scaffolds of any formulation. A) Stress-strain behavior of PCL/Blend composites (as indicated by the initial mass fraction of Blend fibers,  $\phi_B$ ) on day 0. Note that the color of each line serves only to illustrate the resulting modulus of the curve. B) Behavior of Composites covering the full range of possible PCL/Blend combinations was simulated for as-formed samples and with degradation over time. Modulus for each theoretical composite is denoted both by height as well as color.**

## 6.4 DISCUSSION

Electrospun nanofibrous scaffolds hold great promise for the tissue engineering of fibrous elements of the musculoskeletal system. The electrospinning process is inexpensive, straightforward, and easily modified to produce scaffolds with a range of mechanical and degradation characteristics (Li et al. 2006; Barnes et al. 2007). Furthermore, the alignment of nanometer- to micron-scale fibers engenders structural and mechanical anisotropy in scaffolds comparable to that of many soft tissues (Li et al. 2007; Nerurkar et al. 2007; Moffat et al. 2008). However, the mechanical behavior of native tissues is

complex, with most showing not only pronounced anisotropy but also non-linear stress-strain profiles (Fung 1982). Both ‘toe’ and ‘linear’ properties are critical for normal tissue response; ‘toe’ region properties are essential for flexibility, while ‘linear’ region properties resist extreme deformations at high loads. These non-linear properties are dependent on the complex interplay of numerous tissue constituents, including fibers (e.g., collagens), matrix (e.g., proteoglycans and water), and fiber-matrix interactions (e.g., cross linking molecules) (Guerin et al. 2005; Guo et al. 2006).

While the target tissues are complex, most electrospinning efforts to date have relied upon the use of a single polymeric fiber population for scaffold formation. The number of polymers that can be electrospun is increasing at a rapid rate and these fibers show a diverse array of mechanical properties, including some with non-linear behaviors. However, it is somewhat unreasonable to suppose that a single fiber population can recapitulate the intricate mechanical behavior of native tissues. This would therefore limit scaffold applications to non-load bearing situations, or rely on cell-mediated ECM deposition to provide tissue specific functionality. We have shown that, with extended periods of in vitro pre-culture, cells seeded onto aligned scaffold can improve functional properties and impart increasing non-linearity (Nerurkar et al. 2008). An ideal scaffold would, however, match the native tissue properties over the entire time course of maturation. We hypothesized that such complex features might be achieved by combining multiple fiber populations, each with distinct mechanical characteristics, into a single composite nanofibrous scaffold.

The particular polymer set chosen for this work are commercially available, widely applied, and are generally considered to be biocompatible upon implantation. Previous work from our group identified PCL as a suitable electrospun polymer as it is distensible to high strains before yield, exhibits a toe region akin to that of fibrous tissues, and is stable in culture for long durations (Li et al. 2006). However, due to the dense packing of nanofibers in aligned PCL scaffolds, pore size is limited and thus cell infiltration and matrix deposition is slow and inhomogeneous (Nerurkar et al. 2008, Chapter 3). To increase porosity of these scaffolds, we developed methods for the incorporation of sacrificial, pore-forming fibers (Chapter 4). In that study, it was observed that removal of increasing fractions of sacrificial fibers correlated linearly with decreases in scaffold properties. Since cell infiltration was enhanced only at >50% sacrificial fiber content, a 50% decline in initial scaffold properties would be required to hasten colonization. Furthermore, because dissolution of the sacrificial PEO fibers is ‘all-or-none’, these mechanical changes occur very rapidly, and so cell-mediated contraction can result in distortion of the scaffold shape.

To specifically address this issue, we sought to include a stiffer, slower degrading fiber population in these composite structures. Based on previous reports in the literature, PLGA was chosen for its high stiffness and moderate degradation rate. In Study I, PLGA was successfully electrospun and incorporated into composite scaffolds (**Figure 6-2**). Single fiber population PLGA scaffolds were very stiff (~20-fold higher than PCL), however, two significant limitations were observed. First, consistent with previous reports (Li et al. 2006), pure PLGA scaffolds could only be deformed by ~1% before

succumbing to permanent deformation and/or failure. Thus when PLGA was electrospun into the Composite scaffold, the resulting yield strain was reduced by a factor of four, to  $E=0.025$ . As most fibrous tissues experience deformations on the order of 5-10%, we considered this attribute to be a serious deterrent to using pure PLGA fibers. Additionally, and through a mechanism not yet fully understood, PLGA scaffolds underwent severe contraction and thickening immediately upon hydration, precluding a longitudinal study of mechanical properties with degradation.

Previous work by Barnes and co-workers had demonstrated that inelastic polymers (such as PLGA) could be made more elastic with the inclusion of PCL (Barnes et al. 2007). Thus, in Study II, we utilized a blended solution of PLGA and PCL to introduce temporal characteristics to the composite (**Figure 6-3**). The modulus of pure Blend scaffolds was significantly lower than that of pure PLGA, though its yield strain (~8%) was markedly higher. These changes are possibly due to alterations in crystallinity within each fiber strand, though this was not assessed in the current study. Blend scaffolds could be hydrated without the gross distortion, as had been observed for pure PLGA fibers. Interestingly, removal of the PCL component of Blend fibers on day 0 (via lipase digestion) caused the remaining PLGA portion to contract, confirming a secondary role of PCL as an intra-fibrillar stabilizer (not shown). With this Blend component, we evaluated the temporal characteristics of composite scaffolds (**Figure 6-3**). Instantaneous removal of PEO from the composite resulted in ~22% mass loss upon hydration. Conversely, Blend fibers (formed into single component scaffolds) degraded slowly over nine weeks, with corresponding decreases in mechanical properties. Composite scaffolds

containing Blend populations showed similar time-dependent decreases in mechanical properties, while pure PCL scaffolds did not change, suggesting that these dynamic characteristics arise from the degrading Blend component. The mechanism by which Blend scaffolds (or fibers) degrade was not assessed. While the idealized mechanism shown in **Figure 6-1B** suggests degradation resulting in complete fiber removal, Blend fibers may undergo scission and complete removal or may experience internal changes that leave the fiber present but in a weakened state. SEM imaging over the time course did not reveal obvious structural changes, although this may be an inherent limitation of the 2D imaging modality (not shown). The specific mode of degradation of the Blend fiber population, and its influence on scaffold porosity, will be important to characterize in future studies.

To better understand and predict the complex behaviors of nanofibrous scaffolds, which are further compounded when multiple fiber populations are combined, a hyperelastic constitutive model was employed. The model fit single fiber population Blend and PCL data well, despite the distinct stress-strain profiles of each (**Figure 6-4**). As evident from experimental results, PCL was nonlinear along the fiber direction, while Blend was mostly linear. The model reflected this, with a significant difference found between  $\xi^C$  and  $\xi^B$ . Without applying any constraints, fits to Blend along the fiber direction invariably resulted in  $\xi^B = 0$ , suggesting that the parameter values obtained were unique results of the curve-fits, and thus the physical interpretation of these parameters were preserved. The model also described time-varying mechanics of the PCL and Blend scaffolds, accounting for degradation through changes in the material parameters (**Figure**

**6-4).** Degradation of Blend scaffolds was mirrored functionally by a significant decline in both the matrix ( $\mu^B$ ) and fiber ( $\gamma^B$ ) terms. However, PCL, which demonstrated negligible mass loss and did not change in modulus, did not show changes in either  $\mu^C$  or  $\gamma^C$ . The nonlinearity parameter,  $\xi^C$ , increased slightly with time.

We next validated the model by combining the constituent polymer parameters into a mixture model for the Composite scaffold (**Figure 6-5**). Despite slightly underestimating stresses at the initial time point, the model provided very good approximations of the stress-strain behavior of Composite scaffolds at all subsequent stages of degradation. The poor prediction at day 0 may suggest that, initially, the Composite does not behave as a true mixture. This may be due to transient, complex behaviors such as fiber-fiber welding or sliding, which diminish with degradation. Although homotypic fiber-fiber interactions are represented by the matrix phase, heterotypic fiber-fiber interactions, like those present in the composite, are not accounted for in the model. The experimental data may underscore this point, in that the fiber to transverse modulus ratio for PCL was 10:1, while for the Blend it was only 3:1. It has previously been shown that small changes in solvent or environmental conditions can alter the degree of fiber-fiber welding that occurs with fiber deposition, changing tensile properties by as much as 4-fold (Kidoaki et al. 2006). Nevertheless, the excellent prediction of composite behavior for day 7 through 63 of incubation demonstrates that the model not only fits curves, but that it represents a true biophysical description of static and time-varying mechanics of the composite material.

With the validated model, the complete range of possible Blend and PCL combinations was simulated (**Figure 6-6**). This simulation demonstrated that the magnitude and time-dependence of Composite scaffold mechanics can be modulated in a predictable fashion by altering the initial composition. Simulations also showed that it is possible to tune not only linear region modulus (**Figure 6-6B**), but also the profile of the stress-strain curve (**Figure 6-6A**). For instance, introducing an increasing fraction of PCL fibers to the Composite reduces the modulus, while conferring nonlinearity to the overall material behavior. This model result is consistent with experimental observations of Study I where modulation of the PCL and PLGA fiber fractions tuned the resultant stress-strain behavior of composites (**Figure 6-2D**). Because many fiber reinforced soft tissues are subject to physiologic deformations below the transition strain, it is important to implement a method for scaffold design that incorporates full material nonlinearity, and not only linear region metrics such as a single modulus value (Butler et al. 2004).

## 6.5 CONCLUSIONS

Taken together, this work represents a significant advance in the formulation of nanofibrous scaffolds for load bearing applications, and sets the stage for further advance. For example, it will be of great value to characterize the full elastic behavior of a wide collection of polymers. Model parameters from each would be integrated into a “functional library” that, coupled with the specific metrics taken from a tissue of interest, could be used to determine the exact composition and combination of fiber populations that would most closely reproduce the desired stress-strain profile. Such techniques can also define polymers that are not suitable for certain applications. For example, the

polymer set employed here is not likely to be useful when rigorous load bearing is required at the time of implantation. The linear modulus of the Composites generated in this study cannot exceed 45MPa, a value far below that of many fiber-reinforced tissues. A stiffer, more slowly degrading element would be ideal as it could withstand physiologic loading and at the same time provide structural support to the construct, as other more rapidly eroding elements vacated the scaffold (in order to foster cell infiltration and matrix elaboration). We have recently made progress towards this goal with the electrospinning of select elements of a degradable poly( $\beta$ -amino ester) library spanning a wide range of mechanical and degradation profiles (Tan et al. 2008), and new elastomeric and hydrolytically degradable polymers (Ifkovits et al. 2008). Combining these new polymers with rigorous mechanical testing and validated predictive models may result in improved scaffolds for implantation. This approach represents a novel direction in the rational design and fabrication of nanofibrous scaffolds for the repair or replacement of dense connective tissues.

## ***CHAPTER 7: TISSUE ENGINEERING WITH MENISCUS CELLS DERIVED FROM SURGICAL DEBRIS***

### **7.1 INTRODUCTION**

The meniscus is a fibrocartilaginous tissue vital to knee function (Walker et al. 1975; Fithian et al. 1990; Kelly et al. 1990; Messner et al. 1998). Aligned collagen bundles within the meniscus (Petersen et al. 1998) bear tensile hoop stresses that are generated with load transmission across the tibiofemoral joint (Shrive et al. 1978). These stresses are resisted, with little deformation (Jones et al. 1996), by the high tensile properties in the circumferential direction, which range from 50-250MPa, depending on age, species, and testing parameters (Bullough et al. 1970; Proctor et al. 1989; Fithian et al. 1990; Mow et al. 1992; Tissakht et al. 1995; Sweigart et al. 2004). The meniscus is sparsely colonized by a heterogeneous cell population which continually maintains and remodels the extracellular matrix (ECM) (Arnoczky 1999; Benjamin et al. 2004). Meniscus cells transition from a fibrochondrocyte-like phenotype in the avascular inner region to a more fibroblastic phenotype in the outer rim, with ECM deposition reflective of this transition (i.e., a mix of type I and type II collagen and aggrecan in the inner zone and type I collagen in the periphery) (Cheung 1987; McDevitt et al. 1990; Adams et al. 1992; Spindler et al. 1994; Arnoczky 1999; Hellio Le Graverand et al. 2001; Nakata et al. 2001; Kambic et al. 2005; Valiyaveetil et al. 2005; Verdonk et al. 2005).

While the meniscus functions well with a lifetime of use, traumatic or degenerative injuries to the avascular, inner region fail to heal (Newman et al. 1989). Disruption of the

fibrous architecture impairs load transmission (Krause et al. 1976; Levy et al. 1989; Jones et al. 1996) and initiates erosion of the adjacent articular surfaces, or osteoarthritis (OA) (Roos et al. 1995; Roos et al. 1998; Elliott et al. 1999; Rath et al. 2000). Currently, damage to the inner zone of the meniscus is treated by resection via arthroscopic partial meniscectomy, which alleviates symptoms but similarly predisposes patients to OA. Tissue removed in this procedure is deemed surgical waste and is discarded at the time of surgery. Studies following patient outcomes after partial meniscectomy indicate that resection of larger portions of meniscus results in more rapid cartilage erosion (Cox et al. 1975; Andersson-Molina et al. 2002). Adverse changes in cartilage (as indicated by radiographic joint space narrowing) are noted within a 5-10 year period post-meniscectomy (Roos et al. 1998). This long duration before clinical symptoms arise creates a unique window of opportunity for the application of regenerative strategies to restore meniscus function and avert the onset of OA.

Over the last two decades, a number of tissue engineering strategies have emerged to replace all or part of the meniscus to improve immediate and long-term patient outcomes (reviewed in (Setton et al. 1999; Sweigart et al. 2001; Buma et al. 2004)). For example, cell-free hydrogels have been implanted in place of an entire meniscus in rabbit and sheep models (Kobayashi et al. 2005; Kelly et al. 2007). A variety of degradable porous foams have been developed (van Tienen et al. 2002; Heijkants et al. 2004), some incorporating anchors for fixation to the tibial plateau (Chiari et al. 2006), or carbon fibers to instill directionality (Veth et al. 1986). More recently, efforts have focused on natural materials such as subintestinal submucosa (Cook et al. 2006; Cook et al. 2006) as

well as collagen- and tissue- based implants (Stone et al. 1992; Rodkey et al. 1999; Izuta et al. 2005; Martinek et al. 2005; Zaffagnini et al. 2007). Many of these studies employing *in vivo* animal models reveal that some chondroprotection is afforded by the implant, but that none to date have been able to recapitulate native mechanical properties or completely abrogate cartilage degeneration (Tienen et al. 2006).

To further the field of meniscus repair, we have investigated the use of nanofibrous scaffolds combined with meniscal cells or mesenchymal stem cells for meniscus tissue engineering (Chapter 3). This strategy is founded on electrospinning, a scaffold fabrication technique that generates nanometer diameter fibers through an electrostatic process (Li et al. 2004; Li et al. 2005). While numerous biologic and synthetic polymers can be electrospun (see (Li et al. 2005) for review), we fabricate nanofibrous scaffolds using poly( $\beta$ -caprolactone), a slowly degrading polyester. This polymer was chosen as it maintains its form in a physiologic environment and can thus direct tissue formation over a long period of time (as cells deposit new ECM), as well as deform elastically over physiologic ranges experienced in the meniscus (Li et al. 2006). These fibers can further be arranged into parallel arrays (Ayres et al. 2006; Courtney et al. 2006; Li et al. 2007), creating an architecturally and mechanically anisotropic micro-pattern conducive to organized tissue growth. In Chapter 3, we showed that young bovine meniscal fibrochondrocytes (MFCs) aligned with and deposited ECM in the predominant fiber direction of these anisotropic scaffolds, and that this matrix deposition improved the construct tensile properties with time in culture. Such constructs, that possess architectural and mechanical features similar to the native tissue, may better restore

meniscus mechanics and load transmission *in vivo*, averting the onset of OA after meniscus repair.

To move this technology closer to clinical implementation, this study focused on the potential of human meniscus fibrochondrocytes isolated from surgical debris from patients undergoing either partial meniscectomy or total knee arthroplasty (TKA). Isolation of cells from native meniscus tissue has a number of advantages; the cells have the appropriate phenotype, would be autologous and so limit immune responses, and requires no secondary surgical site. In this study, we utilized cells derived from ten patients spanning a range of ages (18-84 years old) and disease conditions (traumatic or degenerative meniscus lesions, or OA of the entire joint). It has previously been shown that increases in organism age limits the ability of chondrocytes from articular cartilage to form functional ECM (Barbero et al. 2004; Tran-Khanh et al. 2005). Further, when age-matched chondrocytes derived for autologous chondrocyte implantation procedures were compared between normal and osteoarthritic donors, cells from diseased tissues showed a markedly lower ability to form collagen-rich ECM (Tallheden et al. 2005). Fibrochondrocytes are related to chondrocytes (particularly for the samples acquired from the inner avascular region of the meniscus), and so we hypothesized that while all surgical specimens would yield viable human cells, their ability to deposit functional fibrocartilaginous ECM and improve scaffold properties would depend on the donor age and/or disease status. To test this hypothesis, MFCs were seeded onto aligned nanofibrous scaffolds, cultured in a chemically defined chondrogenic medium, and

biochemical, histological, and mechanical properties were evaluated over a ten week time course.

## **7.2 MATERIALS AND METHODS**

### ***7.2.1 Scaffold Fabrication***

For each donor, a separate aligned, nanofibrous mesh was produced via electrospinning as described in Chapter 3. Briefly, a 14.3% w/v solution of poly( $\beta$ -caprolactone) (PCL) (80kD, Sigma-Aldrich, St. Louis, MO) was dissolved in a 1:1 solution of tetrahydrofuran and N,N-dimethylformamide (Fisher Chemical, Fairlawn, NJ). The solution was electrospun onto a grounded mandrel (1" diameter, 8" length) rotating at a velocity of ~10 meters/sec (Li et al. 2007). For each production run, nanofibers were collected for 8 hours, resulting in a fiber mats with an average thickness of  $0.865 \pm 0.177$ mm.

### ***7.2.2 Cell Isolation, Expansion, and Seeding***

Meniscus tissue was collected according to an approved IRB protocol from ten adult male and female patients ranging in age from 18 to 84 years (See **Table 7-1**). Resected tissue was finely minced and plated on tissue culture polystyrene in basal medium (DMEM containing 1X PSF and 10% FBS). Meniscus fibrochondrocytes (MFCs) emerged over a two week period after which the tissue pieces were removed. Adherent colonies were passaged twice to obtain  $>20 \times 10^6$  cells for scaffold seeding.

**Table 7-1: Characteristics of Human Donor Tissue: Age, Gender, Tear Type, and Anatomic Location. Surgical debris from a total of ten donors ranging in age from 18-84 years was used in this study. Tissue was derived from seven donors who underwent partial meniscectomy and three who underwent total knee replacement.**

<b>Donor</b>	<b>Age</b>	<b>Sex</b>	<b>Tear Type</b>	<b>Side</b>	<b>Location</b>
1	18	Male	Bucket handle	Medial	Inner 2/3
2	25	Male	Incomplete discoid	Lateral	Inner 1/3
3	49	Male	Radial	Medial	Inner 2/3
4	33	Male	Bucket handle	Medial	Inner 1/3
5	70	Male	TKA	Medial	Total
6	39	Male	Radial	Medial	Inner 1/3
7	81	Male	Radial-horizontal	Medial	Inner 2/3
8	84	Female	TKA	N/A	Total
9	58	Male	TKA	Lateral	Total
10	45	Female	Horizontal	Lateral	Inner 2/3

Mechanically homogeneous strips (5mm wide by 75mm long) were cut in the prevailing fiber direction of electrospun sheets and prepared for cell-seeding as in Chapter 3. Strips were disinfected in ethanol (100, 70, 50, 30%; 30 minutes per step), rinsed twice in phosphate-buffered saline (PBS), and soaked overnight in a 20µg/ml human fibronectin (Invitrogen, Carlsbad, CA). Prior to seeding, strips were rinsed twice with PBS and segmented into three 25mm long pieces, two of which were seeded with MFCs, leaving one to serve as a paired, unseeded control (USC). For seeding, each scaffold side received a 50µl aliquot containing 250,000 cells followed by one hour of incubation. After the final incubation, seeded constructs were cultured in 4mL of chemically-defined medium (high glucose DMEM with 1X PSF, 0.1µM dexamethasone, 50µg/mL ascorbate 2-phosphate, 40µg/mL L-proline, 100µg/mL sodium pyruvate, 1X ITS+ (6.25µg/ml Insulin, 6.25µg/ml Transferrin, 6.25ng/ml Selenous Acid, 1.25mg/ml Bovine Serum Albumin, and 5.35µg/ml Linoleic Acid) with 10ng/mL TGF-β3) in non-tissue culture treated 6-well plates (Mauck et al. 2006). The USCs were incubated at 37°C in PBS changed twice monthly for the study duration.

### **7.2.3 Mechanical Testing**

Uniaxial tensile testing was performed with an Instron 5848 Microtester (Instron, Canton, MA). Prior to testing, five thickness measurements along the length of each sample were taken with a custom LVDT measurement system; five width measurements were acquired with a digital caliper. Samples were clamped in serrated grips and a 0.5N preload applied for 180 seconds to ensure proper seating. After noting gauge length with a digital caliper, samples were preconditioned by cyclic extension to 0.5% of the gauge length 0.1Hz for 10 cycles. Subsequently, samples were extended beyond their yield point at a rate of 0.1% of the gauge length per second. For day 70 samples, extension was carried out until failure occurred. Stiffness was determined from the linear region of the force-elongation curve. Using the cross-sectional area and gauge length, Young's modulus was calculated from the analogous stress-strain curve. Five seeded samples were tested for each of the ten donors at each time point along with their corresponding USCs.

### **7.2.4 Biochemical Analyses**

After mechanical testing, samples were stored at -80°C until determination of biochemical composition. Samples were lyophilized (Freezone 4.5 Freeze Dry System, LabConco, Kansas City, MO) for 24 hours and massed to determine dry weights. Following this, samples were papain digested as in (Mauck et al. 2006) and DNA, sulfated glycosaminoglycan (s-GAG), and collagen content was determined using the Picogreen double-stranded DNA (dsDNA) (Molecular Probes, Eugene, OR), DMMB

dye-binding (Farndale et al. 1986), and hydroxyproline (Stegemann et al. 1967) assays, respectively. Hydroxyproline content was converted to collagen as in (Neuman et al. 1950), using a factor of 7.14. This conversion is an estimate, and susceptible to bias based on the prevailing collagen type present. Data are reported as a sample's total content or as a percentage of the sample dry weight. Five additional human meniscus samples (donor age  $62 \pm 6$  years, all TKAs) were tested to establish native tissue biochemical content ranges.

### **7.2.5 Histology**

Cytoskeletal organization was examined in MFC monolayers and cell-laden constructs one day post-seeding. Filamentous actin and nuclei were labeled with Alexa Fluor 647 phalloidin and Prolong Gold Antifade with DAPI (Invitrogen), respectively, and imaged at  $20\times$  on a Nikon T30 inverted fluorescent microscope (Nikon Instruments, Inc., Melville, NY). For analysis of matrix deposition with long-term culture, a 6mm length was cut from each paired, non-tested construct, fixed overnight at  $4^{\circ}\text{C}$  in 4% phosphate-buffered paraformaldehyde, and frozen in Optimal Cutting Temperature compound (Sakura Finetek USA, Inc., Torrance, CA). Cross-sections,  $8\mu\text{m}$  thick (spanning the depth and width of the scaffold) were cut with a Cryostat (Microm HM500, MICROM International GmbH, Waldorf, Germany). Sections were rehydrated and stained with DAPI, Alcian Blue (AB, pH 1.0), or Picrosirius Red (PSR) to visualize cell nuclei, proteoglycans, or collagen, respectively. DAPI stained sections were imaged at  $5\times$ . On separate slides, AB and PSR images were acquired at the same magnification on an upright Leica DMLP microscope (Leica Microsystems, Germany).

### **7.2.6 Statistical Analyses**

Analysis of variance (ANOVA) was carried out with SYSTAT (v10.2, Point Richmond, CA). Fisher's LSD post-hoc tests were used to make pair-wise comparisons between donors and time points, with significance set at  $p \leq 0.05$ . At least 5 samples were analyzed for each donor at each time point. Data are presented as the mean  $\pm$  standard deviation for each donor. Pearson's correlation analysis was performed with SYSTAT.

## **7.3 RESULTS**

### **7.3.1 Cell Isolation, Expansion, and Scaffold Seeding**

Cells were successfully isolated from meniscus tissue from each of the ten donors (**Table 7-1**). A total of  $20 \times 10^6$  passage 2 cells were required from each donor for construct seeding. The time from initial plating to passage 2 confluency with sufficient expansion ( $>20 \times 10^6$  cells) was  $53 \pm 9.6$  days. Cell morphology during expansion showed an increasing population of fibroblast-like cells (**Figure 7-1A**). When seeded onto aligned scaffolds, MFCs aligned their long axes and cytoskeleton with the underlying scaffold architecture (**Figure 7-1B**).

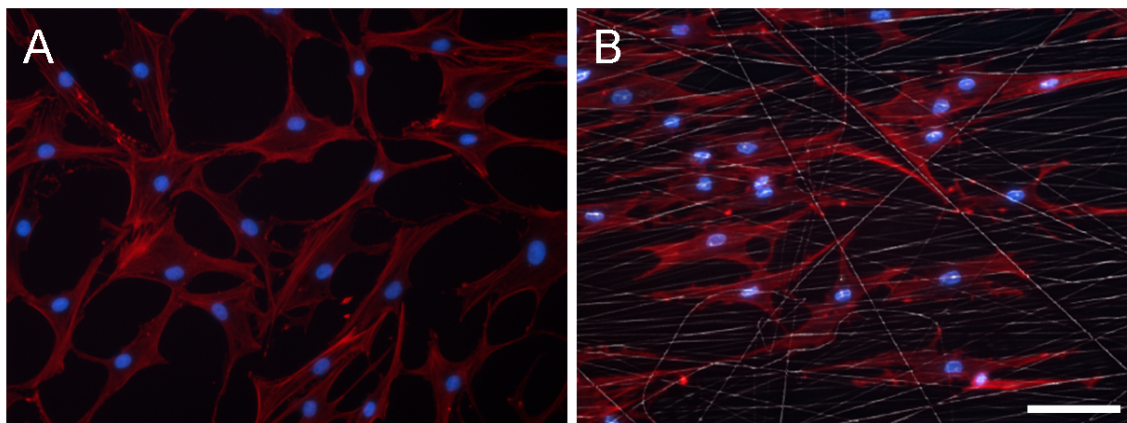


**Figure 7-1: Morphological appearance of human MFCs in monolayer and on fiber-aligned nanofibrous scaffolds. (A) Passage 2 MFCs in monolayer on tissue culture polystyrene demonstrate a fibroblast-like morphology. (B) Passage 2 MFC-seeded constructs cultured for one day reveal MFCs elongating in and aligning with the predominant fiber direction of the scaffold. Red: F-actin, white: fibers, blue: nuclei. Scale bar: 50µm.**

### **7.3.2 Mechanical Properties of MFC-Laden Constructs**

Mechanical properties of cell-seeded and paired acellular scaffolds were assessed via tensile testing. It was noted in preliminary studies that variations in scaffold mechanical properties exist both between different nanofibrous PCL batches, as well as along the length of the collection mandrel. For example, scaffold stiffness on day 14 (before appreciable matrix deposition) from different batches ranged from 2.7 to 6.1N/mm (Table 7-2). To address the issue, each donor was assigned a specific production run of nanofibrous scaffold, and each MFC-seeded sample was tested along with an unseeded control (USC) excised from the same location along the mandrel. As strips excised in such a manner begin with identical mechanical properties, the effect of cell-seeding and ECM deposition can be more accurately assessed. By normalizing the stiffness of each cell-seeded scaffold to its counterpart USC at each time point, a percentage change (as well as a magnitude change) in stiffness can be determined.

**Table 7-2: Structural and Mechanical Properties of Engineered Meniscus Constructs.** Cross-sectional area (CSA, mm<sup>2</sup>), Stiffness (N/mm), Modulus (MPa), and Maximum Stress (MPa) achieved on day 70 are provided for constructs generated from each of the ten donors. Values indicate the mean (top number in bold) and standard deviation (bottom number) of five samples tested for each measure and donor at each time point. For each parameter, the highest magnitude of change is denoted with an (H), and lowest level of change is denoted with an (L). Average change in each parameter between days 14 and 70 for all donors is provided at the bottom of each column.

Time in Culture	CSA (mm <sup>2</sup> )		Stiffness (N/mm)		Modulus (MPa)		Max Stress (MPa)	
	Day 14	Day 70	Day 14	Day 70	Day 14	Day 70	Day 70	
Donor (Age)	1 (18)	4.6 1.1	5.4 + 0.6	3.7 0.3	5.6 0.3	16.1 3.2	20.2 2.4	4.6 1.1
	2 (25)	5.0 0.5	6.3 0.6	4.2 0.3	5.9 0.5	15.3 1.3	17.2 + 1.0	5.7 0.4
	4 (33)	5.5 0.9	5.5 +,L 1.1	4.6 0.5	9.9 0.9	15.5 2.0	32.5 5.2	3.1 0.6
	6 (39)	4.0 0.5	4.7 + 0.4	3.5 0.4	5.1 L 0.5	15.4 1.2	19.2 0.6	2.8 0.4
	10 (45)	4.0 0.4	4.7 0.4	3.8 0.5	8.1 0.8	16.9 0.4	30.2 1.4	2.0 0.2
	3 (49)	5.0 0.5	6.1 0.7	4.1 0.6	7.9 0.4	15.0 0.9	23.1 1.8	3.2 0.5
	9 (58)	4.5 0.9	7.6 H 0.5	6.1 1.9	11.2 1.0	24.8 4.1	25.6 +, L 1.1	5.6 1.5
	5 (70)	4.2 0.4	5.9 0.5	4.9 0.3	10.5 1.7	21.2 1.9	31.5 3.4	3.1 0.5
	7 (81)	3.6 0.3	5.2 0.3	2.7 0.1	7.2 0.6	13.9 0.6	23.9 1.4	2.3 0.3
	8 (84)	4.3 0.4	5.5 0.4	4.2 0.7	12.5 H 1.0	17.6 1.4	39.2 H 1.6	4.8 0.6
Average Δ	1.2 0.8		4.2 2.1		9.1 6.8		3.7 1.3	

The mechanical response of engineered constructs differed markedly between USC and MFC-seeded constructs over the duration of the study. The force-displacement curve from each of the day 70 Donor 8 samples are shown in **Figure 7-2A**, with MFC-laden constructs showing a much higher stiffness and ultimate load. Quantification of these changes amongst all donors revealed that the ultimate load (**Figure 7-2B**) and stiffness (**Figure 7-2C**) of cell-seeded samples increased for 8/10 donors and 10/10 donors by day 70, respectively ( $p < 0.001$  vs. USC). Conversely, USC did not decrease over this same time course ( $p > 0.219$  vs. day 14). The average change in stiffness between day 14 and day 70 was  $4.2 \pm 2.1$  N/mm for all donors, with a maximum change of 8.1 N/mm for

Donor 8 and a minimum change of 1.6N/mm for Donor 6 (**Table 7-2**). On a percentage basis, this represents changes of up to 300% in construct stiffness compared to USC over the 70 days (**Figure 7-2C**). Cell-seeded constructs from each of the donors also increased in thickness ( $p < 0.05$  except Donors 4 and 6), resulting in an increasing cross-sectional area (**Table 7-2**,  $p < 0.05$  except donors 4 and 6). While moduli generally increased, the effect of the increase in cross-sectional area occasionally precluded these changes from reaching significance (**Table 7-2**). The average change in modulus was  $9.1 \pm 6.8$ MPa for all donors, with a maximum change of 21.6MPa for Donor 8 and a minimum change of 0.8MPa for Donor 9.

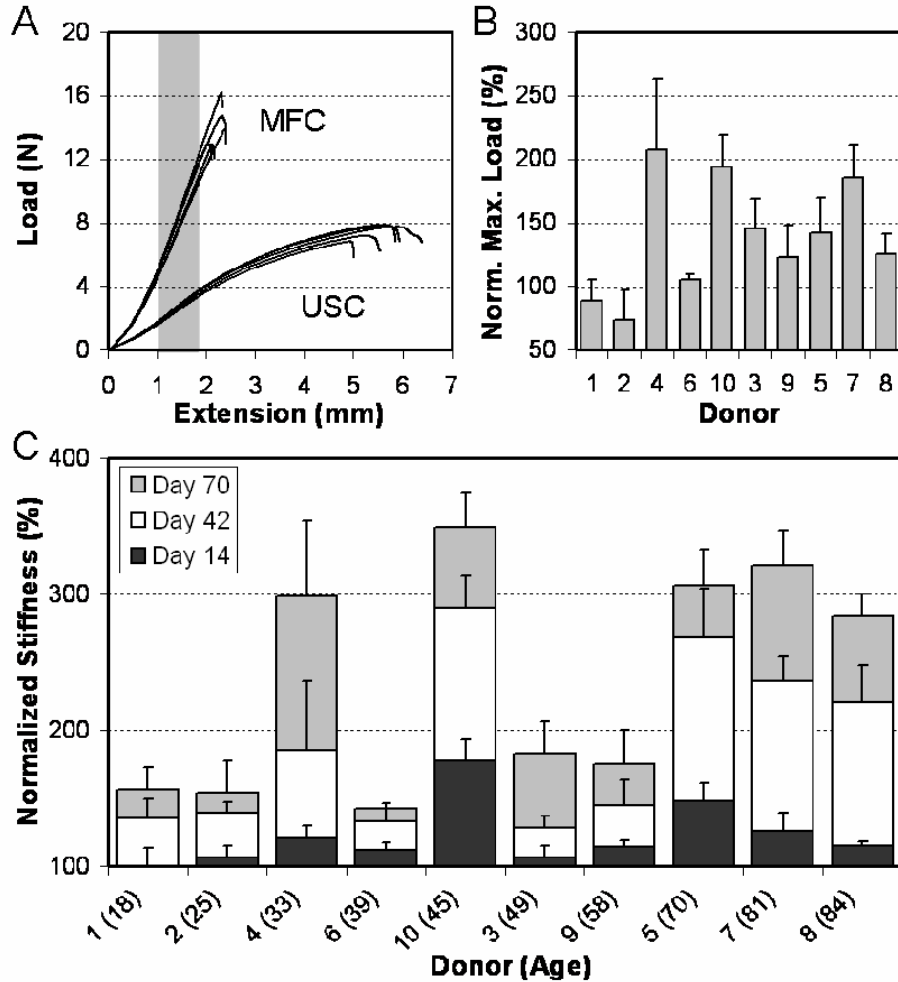


**Figure 7-2:** MFC-seeded scaffolds increase in mechanical properties with time in culture in a fibro-cartilaginous medium. (A) Force-elongation plots of five scaffolds either seeded (MFC) or maintained as unseeded controls (USC) on day 70 for Donor 8. (B) Maximum load of seeded scaffolds normalized to that of paired USC scaffolds on day 70 for all ten donors. Donor # is indicated on the x-axis. Data represent the mean and standard deviation of 5 samples per donor. (C) Normalized stiffness (indicating percentage change) of MFC-seeded scaffolds from each donor compared to their paired USC scaffolds at each time point. Donor # (and age) is indicated on the x-axis.

### 7.3.3 Biochemical Content of MFC-Laden Constructs

Construct biochemical content was determined for cell-seeded scaffolds with time in culture. Constructs seeded with MFCs from all donors increased in dry weight (Table 7-3,  $p < 0.05$  except Donor 2). This increase in mass ranged between 2.5mg (Donor 4) and 6.1mg (Donor 9) and averaged  $4.5 \pm 1.6$ mg for all donors. DNA content also increased

with time in culture ( $p < 0.001$ ) for all donors except for Donor 10 (**Table 7-3**). Collagen and s-GAG contents also increased in constructs in a time-dependent manner (**Figure 7-3A,B**,  $p < 0.001$ ). Overall, the total s-GAG and collagen per construct was highly dependent on time in culture ( $p < 0.001$ ) and donor ( $p < 0.001$ ). We normalized these results to the dry weight (DW) of the construct (**Figure 7-3C,D**) to enable comparisons to the native tissue. For collagen, native tissue values averaged  $50 \pm 18\%$  DW, and ranged from 24 to 72% DW (**Figure 7-3C**, grey region, note break in scale). S-GAG content of native tissue averaged  $0.6 \pm 0.3\%$  DW, and ranged from 0.3 to 1.1% DW (**Figure 7-3D**, grey region). The most robust deposition of collagen ( $\sim 18\%$  DW, Donor 5) was lower than the lowest native tissue level, while the largest amount of GAG ( $\sim 3.3\%$  DW, Donor 7) was above native levels.

**Table 7-3: Biochemical Composition of Engineered Meniscus Constructs.** Dry mass (mg), total DNA content ( $\mu\text{g}$ ), total sGAG content ( $\mu\text{g}$ ), and total collagen content ( $\mu\text{g}$ ) achieved on day 70 are provided for constructs generated from each of the ten donors. Values indicate the mean (top number in bold) and standard deviation (bottom number) of five samples tested for each measure and donor at each time point. For each parameter, the highest magnitude of change is denoted with an (H), and lowest level of change is denoted with an (L). Average change in each parameter between days 14 and 70 for all donors is provided at the bottom of each column. For this table, all comparisons between days 14 and 70 were significantly different with  $p < 0.05$  except when noted (+).

Time in Culture	Dry Mass (mg)		Total DNA ( $\mu\text{g}$ )		Total GAG ( $\mu\text{g}$ )		Total Collagen ( $\mu\text{g}$ )		
	Day 14	Day 70	Day 14	Day 70	Day 14	Day 70	Day 14	Day 70	
<b>Donor (Age)</b>	1 (18)	15.6 1.4	19.6 1.3	4.2 0.5	9.7 1.2	36.7 5.4	190.7 11.6	89.5 28.4	1778.6 204.1
	2 (25)	20.7 0.9	23.0 +,L 1.2	4.8 0.8	10.9 H 1.9	39.9 3.0	418.4 70.7	117.1 49.5	2065.8 461.1
	4 (33)	21.1 3.8	23.6 3.6	7.7 0.5	9.7 0.8	93.1 7.0	447.8 70.3	541.9 45.5	3175.9 350.3
	6 (39)	13.9 1.8	17.0 2.0	3.2 0.4	5.1 0.4	36.4 3.1	109.4 L 21.2	98.8 14.0	755.0 L 89.0
	10 (45)	15.3 0.8	19.0 0.5	8.1 0.7	8.4 +, L 0.6	122.0 8.0	212.8 24.3	665.3 97.1	2414.0 101.2
	3 (49)	17.9 3.1	23.7 2.5	7.0 0.9	10.1 0.5	70.6 8.0	320.2 40.6	255.3 41.4	2336.5 135.6
	9 (58)	20.1 4.0	27.2 H 1.7	11.0 0.7	13.6 0.8	132.1 4.7	877.1 H 34.6	375.4 18.1	2656.3 230.3
	5 (70)	16.9 1.3	22.7 2.0	12.8 0.7	15.2 0.8	160.3 8.8	500.3 137.9	746.6 82.5	4013.6 H 346.4
	7 (81)	14.1 1.2	19.0 1.0	8.3 0.4	10.0 0.7	80.8 6.8	641.0 158.4	279.0 30.5	3006.3 339.3
	8 (84)	16.3 1.2	22.0 1.7	7.4 0.4	12.3 0.7	93.9 8.9	455.2 99.3	267.1 62.8	3185.7 248.0
Average $\Delta$	4.5 1.6		3.0 1.9		330.7 208.2		2195.2 749.3		

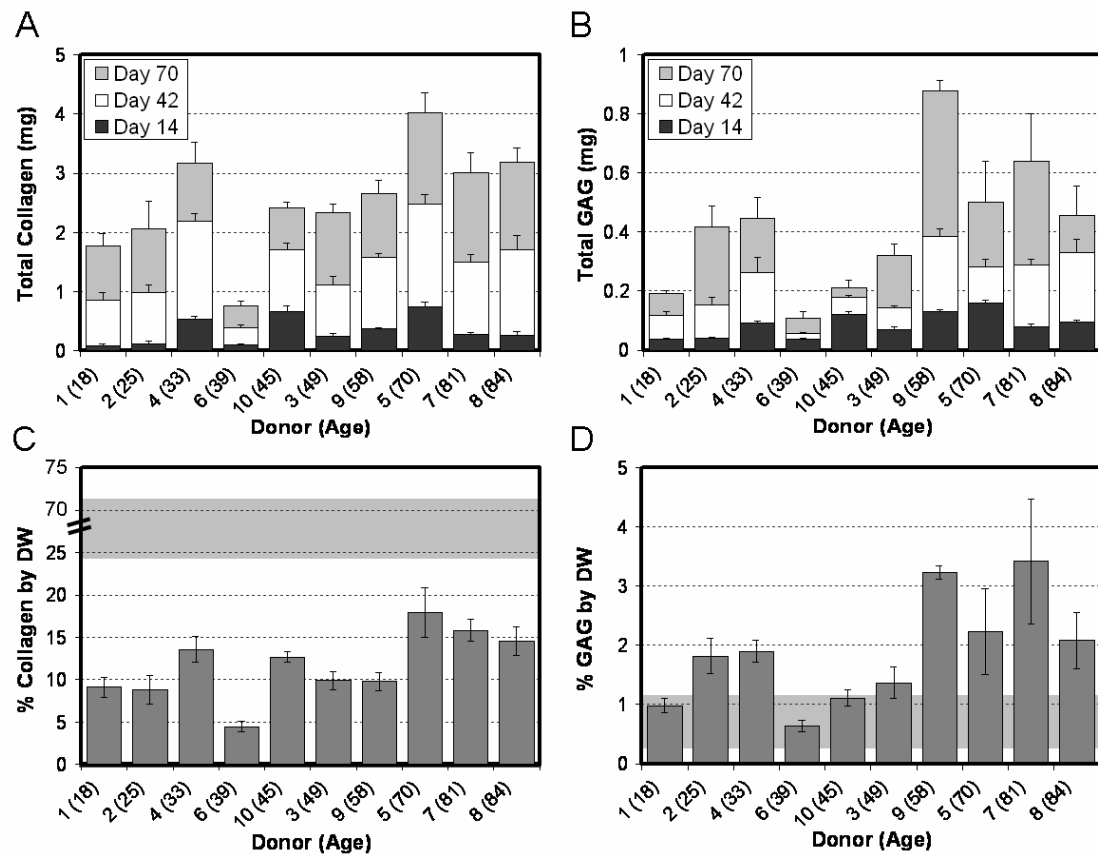


**Figure 7-3: Donor-to-donor variation in time-dependent changes in biochemical composition of MFC-seeded engineered meniscus constructs. (A) Total collagen and (B) total s-GAG accumulation in engineered constructs with time in culture for each donor. Donor # (and age) is indicated on the x-axis. Data represent the mean and standard deviation of 5 samples per donor per time point. (C) Percent dry weight (% DW) collagen and (D) % DW s-GAG for samples from each of the ten donors on day 70. Gray background in (C) and (D) indicates range of collagen and s-GAG found in 5 native tissue samples. Note the interrupted scale in (C) the % collagen by DW plot. USC constructs processed similarly showed no appreciable background content of s-GAG or collagen.**

### 7.3.4 Structure-Function Correlations of MFC-Seeded Constructs

Correlation analysis was carried out to determine the structure-function relationships within developing constructs, and the relationship between donor age and capacity to generate increasing mechanical properties (Figure 7-4A-C). Strong correlations were found between the change in stiffness of the construct with the total collagen content

(**Figure 7-4A**,  $R^2=0.81$  value,  $p<0.001$ ). Weaker (but significant) correlations were also observed for change in stiffness with total s-GAG content (**Figure 7-4B**,  $R^2=0.46$ ,  $p<0.001$ ). While there were significant differences in total DNA content between donors, no correlation was observed between this measure and mechanical performance (data not shown). Finally, correlating the change in stiffness with age showed a weak correlation toward increasing properties with donor age (**Figure 7-4C**,  $R^2=0.47$ ,  $p<0.05$ ).

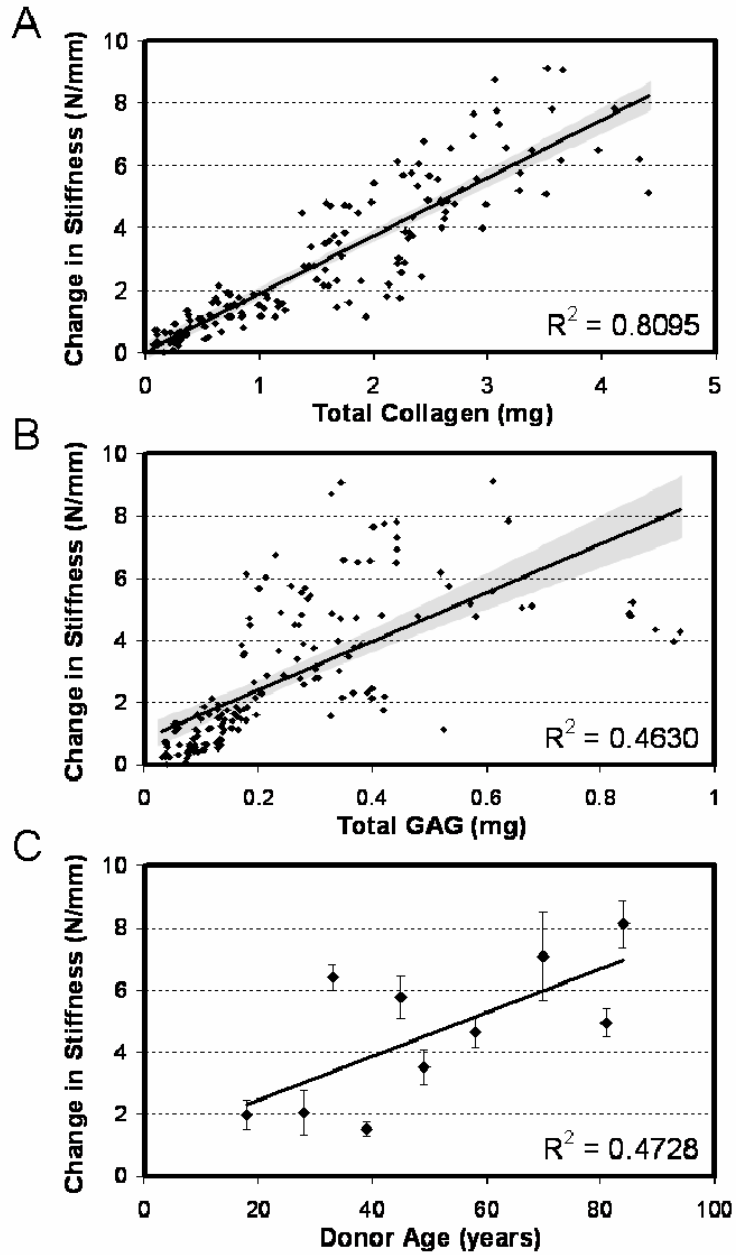


**Figure 7-4: Structure-function-composition correlations for MFC-seeded constructs with time in culture. (A) Total collagen content in constructs correlates well with change in stiffness for all donors at all time points (days 14, 42, and 70). (B) Total GAG content correlates poorly with change in stiffness for all donors at all time points (days 14, 42, and 70). (C) Donor age showed a weak correlation with change in stiffness of constructs on day 70.**

### **7.3.5 Histological Analysis**

Cellular infiltration and distribution of ECM was evaluated through histological staining of construct cross-sections. DAPI-staining showed the progressive infiltration of cells into the scaffold with culture time. Cells from different donors infiltrated to a greater or lesser degree as shown in the best-case (**Figure 7-5A**, Donor 8) and worst-case (**Figure 7-5B**, Donor 6) images of day 70 samples. Similarly, collagen and s-GAG deposition varied amongst donors and appeared to correlate with the best performing (**Figure 7-5C,E**) and worst performing (**Figure 7-5D,F**) constructs on day 70.

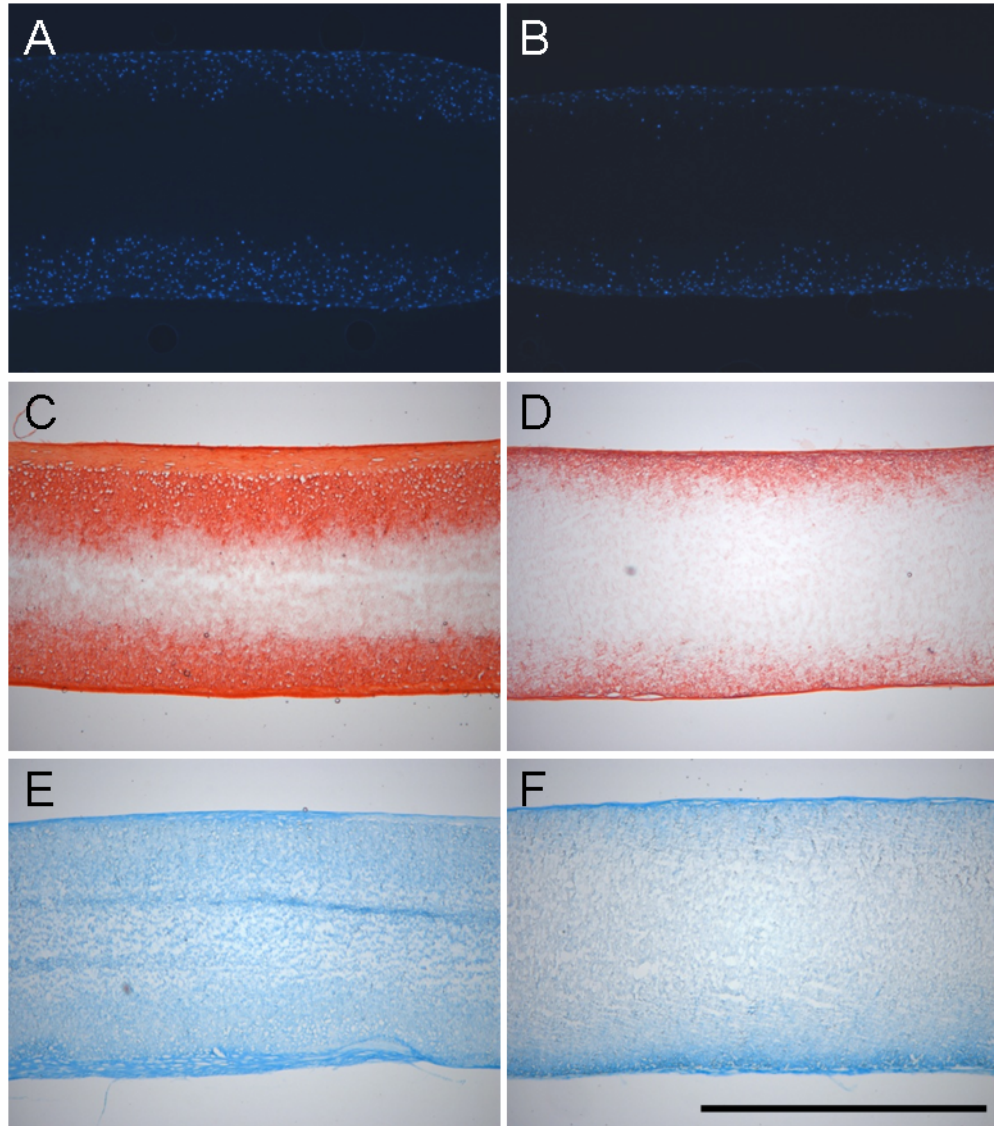


**Figure 7-5: Histological analysis of constructs from best-case (Donor 8, A,C,E) and worst-case (Donor 6, B,D,F) samples on day 70. DAPI staining of cell nuclei demonstrate infiltration into the outer two-thirds of constructs under best-case conditions (A), and limited infiltration at the periphery under worst-case conditions (B). Similar findings are observed for collagen (C,D) and proteoglycan (E,F) deposition as indicated by Picrosirius Red and Alcian Blue staining, respectively. Scale Bar: 1mm.**

#### 7.4 DISCUSSION

In this study, we assessed the ability of human meniscal derived cells (MFCs) to modulate the properties of fiber-aligned biodegradable electrospun nanofibrous scaffolds.

This scaffolding system serves as a 3D micro-pattern for directing cell orientation and

neo-tissue formation by replicating the structural and mechanical anisotropy of the native tissue. Human MFCs were isolated from surgical waste from ten human donors ranging in age from 18-84 and with differing disease status (acute versus degenerative meniscus tears or progression of knee osteoarthritis necessitating total joint replacement) (**Table 7-1**). MFCs were successfully isolated from each donor tissue, expanded in culture through passage 2, seeded onto scaffolds, and cultured in a chemically-defined, pro-fibrocartilaginous medium formulation for ten weeks. When seeded with MFCs, construct tensile properties, biochemical content, and histological features improved with time (**Figures 7-2, 7-3, 7-5**). Amongst the ten donors, variations were observed in the magnitude of these quantitative and qualitative outcome measures, but each donor MFC population yielded positive maturation of the engineered construct. Those donors whose MFCs responded most vigorously generated well infiltrated constructs containing ~25% of the collagen content of the native tissue with tensile moduli of ~40MPa. These findings indicate that native human MFCs derived from surgical debris are a potent cell source for the fabrication of mechanically functional engineered meniscus constructs.

We began this work with the hypothesis that MFCs derived from older individuals would harbor less capacity to generate functional properties *in vitro*. This idea was predicated on work demonstrating that in chondrocytes, a related cell type, collagen production decreases with age (Barbero et al. 2004; Tran-Khanh et al. 2005), and that disease states such as osteoarthritis further reduce the matrix forming capacity (Tallheden et al. 2005). In this study, MFCs were derived from the inner third of the meniscus (small avascular tears), the inner two-thirds of the meniscus (large tears or degenerate regions), or from

the entirety of the meniscus (meniscus removal with TKA). These MFCs represented a range of donor ages, spanning 18-84 years. MFCs from the inner zone of the meniscus are considered chondrocyte-like, displaying phenotypic similarities including a round cell shape and cartilage gene expression and matrix deposition (Nakata et al. 2001; Upton et al. 2006). Thus, these cells were expected to display age-dependent declines in ECM deposition capacity. However, counter our hypothesis, the age of donor MFCs showed no negative correlation with the properties of the engineered construct. In fact, in this study, change in stiffness and donor age showed a weak positive correlation (**Figure 7-6C**). This finding is perhaps due the fact that all donors were at or beyond skeletal maturity, while the most marked changes in cell biosynthetic activities occur at early ages. Interestingly, constructs with the most proteoglycan deposition, which one would expect for MFCs derived from the inner zone, actually came from Donor 9, who underwent a TKA and contributed cells from the entire meniscus. Obviously, these findings are drawn from a small set of donors, but analysis of this set reveals few strong indicators of robust growth based on standard parameters such as age and zonal source of donor cells.

In this study we focused on MFCs isolated from meniscectomy debris as a cell source for engineering replacement meniscus tissue. We focus on this overlooked cell source for a number of reasons outlined above (potential for autologous therapies, no immune response, proper cell phenotype), and not on the more commonly used mesenchymal stem cell (MSC). MSCs can undergo a fibrocartilaginous differentiation on nanofibrous scaffolds, as evidenced by increases in aggrecan and type II collagen expression and

deposition (Li et al. 2005), and we have demonstrated similar growth and maturation patterns when using MSCs compared to MFCs in a juvenile bovine model system (Chapter 3). However, MSC isolation necessitates a second surgical site not associated with primary meniscus repair. Furthermore, we have recently shown that all regions of the meniscus contain multipotential cells (Mauck et al. 2007), suggesting that endogenous cell populations may contribute to repair processes. The finding that all constructs improved in mechanical properties from ten donors, points to the potential of MFCs as a cell source for meniscus tissue engineering. With surgery, the defect that is generated to alleviate acute symptoms may be accurately characterized. As the time between meniscus injury and the onset of OA is relatively long (5-10 years), a fully conforming construct may be fabricated and matured *ex vivo* to effect autologous repair.

*In vitro* culture of meniscus implants offers a range of benefits, most importantly the ability to optimize neo-tissue growth. In this study, we used a chemically defined medium containing TGF- $\beta$ 3 to promote fibrocartilaginous ECM deposition. In our previous studies with MFCs in both pellet format (Mauck et al. 2007) and when seeded onto nanofibrous scaffolds (Chapter 3), this medium increased proteoglycan and collagen deposition. For a small subset of four donors, expression (assessed by real time PCR) of aggrecan and type I collagen was constant or increased over the culture duration, while type II collagen expression increased markedly, perhaps reflecting the reversal of dedifferentiation events that had occurred as result of monolayer expansion (data not shown). For the repair of defects in the inner avascular meniscus zone (the most common site of injury in middle-aged patients), engineered constructs would ideally match the

biochemical composition of the native tissue. This zone contains the largest level of proteoglycan, and a mixture of type I and type II collagen (Adams et al. 1992). For MFCs from all donors, GAG levels matched or were superior to native tissue. Correlations between measured GAG content and tensile properties showed only a weak correlation. Conversely, collagen content of constructs formed from all donors increased substantially, and reached a maximum of 18% of the dry weight of the native tissue, though a range is observed in samples derived from differing states of meniscal degeneration. Correlation analysis showed a very strong association between collagen deposition in constructs and the tensile properties. This suggests that maximizing the collagen content of constructs may further improve their tensile properties.

While the results of this study are promising, there are several limitations that should be addressed. First, significant variations were observed in the properties achieved amongst the ten donors. Age does not appear to be the prevailing indicator, and so other predictors of growth potential must be developed to identify suitable donors, such as short term screening in pellet cultures prior to scaffold seeding. Furthermore, while some constructs approached moduli of 40 MPa within ten weeks, further enhancement of this and other mechanical properties towards native tissue values is a priority. Another potential limiting factor is the persistence of the polymer fibers, which may impede complete cellular infiltration. While the volume fraction of polymer in these scaffolds is in the range of 10-20% (Li et al. 2007), small pores may slow matrix filling. Inclusion of faster degrading polymer elements, such as PLGA or PGA (Li et al. 2006), or biologic fiber components such as collagen (Telemeco et al. 2005), into the fibrous network may

speed this infiltration process. Alternatively, infiltration may be enhanced by creating a mixture of fiber sizes (Pham et al. 2006), utilizing salt leaching approaches to create large pores/lamellae (Nam et al. 2007), or as in the approach described in Chapter 4, evacuating sacrificial fibers to enhance porosity while maintaining overall structural anisotropy.

As a final note, we created constructs as rectangular strips to facilitate tensile testing, without considering the wedge-shaped anatomic form of the meniscus. For clinical application, engineering and fabrication technologies must be developed to enable reproduction of the anatomic form, and integration with native tissue must be achieved (Sheth et al. 2006). To this end, we have recently demonstrated that MSC-seeded multi-lamellar constructs form mechanically viable interfaces when held in apposition with one another (Nerurkar et al. 2009) and with the native tissue (Sheth et al. 2007), and that the constructs hold suture (Sheth et al. 2006) allowing fixation within a meniscus defect. Regardless of these advances, complete integration will be a significant challenge (Hennerbichler et al. 2007), and strategies that engage the outer vascular periphery (Arnoczky 1992) maybe be required to enable *in vivo* success. Long-term *in vivo* studies will address this question in detail, and explore the ability of these novel constructs to preserve articular cartilage and avert the onset of OA after partial meniscectomy.

## **7.5 CONCLUSIONS**

In summary, this study explored the utility of human meniscus-derived fibrochondrocytes for applications in engineering fibrocartilage *in vitro*. These cells, which are isolated

from surgical waste tissue, proved to be a potent cell source for tissue engineering, as cells taken from all 10 donors increased the biochemical content and mechanical properties of aligned nanofibrous scaffolds. Furthermore, and contrary to observations of related cell types, the biosynthetic capacity of these cells did not appear to be tied to the age of the donor. This finding implies that should MFCs be employed autologously, patients of all ages would be suitable for such therapies. Beyond establishing the potential of a cell type that can be considered a “gold standard” for engineering meniscal fibrocartilage, this study also highlighted the relationship between collagen production and resulting mechanical properties of tissue engineered construct. As constructs failed to achieve tensile properties on par with native meniscus, this correlation identifies the enhancing the collagen content of constructs as a key objective for future tissue engineering endeavors.

# ***CHAPTER 8: THE INFLUENCE OF AN ALIGNED NANOFIBROUS TOPOGRAPHY ON HUMAN MESENCHYMAL STEM CELL FIBROCHONDROGENESIS***

## **8.1 INTRODUCTION**

Mesenchymal stem cells (MSCs) are a self-renewing population of multipotent cells that have garnered intense interest for applications in regenerative medicine (Caplan 1991). These cells may be directed along numerous tissue-specific lineages by modulation of their chemical, mechanical, and topographical environment (Pittenger et al. 1999; Altman et al. 2002; McBeath et al. 2004; Engler et al. 2006). Furthermore, MSCs can be isolated with relative ease from adults, avoiding the ethical issues associated with the use of embryonic stem cells. Given their capacity to differentiate into an increasing number of cell types including adipocytes, osteocytes, chondrocytes, and myocytes, they have been widely investigated for use in repairing or engineering musculoskeletal tissues (Caplan 2005).

In particular, we have explored the use of MSCs for the engineering of fibrocartilaginous tissues such as the annulus fibrosus of the intervertebral disc (Nerurkar et al. 2009) and the knee meniscus as described in Chapter 3. These tissues, so-named for sharing characteristics of both articular cartilage and fibrous tissues such as tendon and ligament, fulfill mechanical roles essential to healthy joint function. Fibrocartilaginous tissues are composed primarily of highly organized collagen fibers that resist tensile forces.

Glycosaminoglycans (GAGs) are interspersed between these fibrils, enabling the tissue to resist compressive loads. In the case of both meniscus and annulus fibrosus, traumatic and/or degenerative changes disrupt mechanical function, eventually leading to altered joint loading and debilitating pain. The current standard of treatment is resection of these damaged tissues through partial or total meniscectomy in the case of the meniscus, or complete removal of the disc with subsequent fusion of the adjacent vertebrae for the annulus fibrosus.

With the eventual goal of replacing damaged tissue with engineered fibrocartilage that has architectural, mechanical, and biochemical features similar to the healthy native tissue, we have explored the use of nanofibrous scaffolds fabricated by electrospinning. With focused deposition onto a rotating mandrel, this simple electrostatic process produces three dimensional scaffolds with highly-aligned polymer fibers (Ayres et al. 2006; Courtney et al. 2006; Li et al. 2007). Importantly, these scaffolds mimic the architecture and length-scale of native anisotropic, fibrous tissues, and can even be formed with biopolymers such as elastin and collagen (Stitzel et al. 2006). In Chapter 3, we demonstrated that juvenile bovine MSCs will align with and deposit fibrocartilaginous extracellular matrix (ECM) in the predominant direction of nanofiber alignment, and that this matrix deposition leads to improvements in construct tensile properties. In that study, constructs were also derived from animal-matched meniscal fibrochondrocytes (MFCs), the resident cell type of the meniscus. MFCs led to commensurate increases in construct mechanical properties and synthesized a GAG and collagen-rich matrix, although MSCs produced slightly more of these key matrix

molecules under identical culture conditions. Results from these previous studies indicated MSC in conjunction with aligned nanofibrous scaffolds held promise for engineering anisotropic fibrocartilage.

One caveat to this earlier work was the necessity of using bovine cells in order to isolate healthy MSCs and MFCs from the same donor. Moving this technology towards clinical practice, we have also investigated human fibrochondrocytes isolated from meniscus tissue resected during meniscectomy procedures (Chapter 7). Comparable to bovine MFCs, these cells were biosynthetically active, producing abundant ECM that led to increases in the tensile properties of the constructs. Although inter-donor variability was observed, the age of the patient did not appear to be the factor responsible for these differences.

As MSCs can be readily harvested from bone marrow, their use for engineering replacement tissues would negate the need for multiple surgeries at the defect site. MSC constructs matured *in vitro* to functional equivalence with the native tissue could be implanted at the time of removal of the damaged tissue. Furthermore, the slow disease progression associated with damage to the meniscus or intervertebral disc and long duration before clinical symptoms arise may create a unique window of opportunity for intervention with regenerative strategies. Given the similar potentials of bovine MSCs and MFCs in nanofibrous microenvironments, we hypothesized that constructs formed with human MSCs would demonstrate robust matrix synthesis and increases in mechanical properties, and would do so at levels comparable to human MFCs. To test

this hypothesis and assess the utility of human MSCs for engineering fibrocartilage, MSCs were harvested from the bone marrow of patients undergoing total knee arthroplasty (TKA). As a control, MFCs were isolated from the same donors, and both cell types were seeded onto aligned nanofibrous scaffolds that were engineered to enhance cellular infiltration as in Chapter 4, with construct mechanical properties, biochemical content, and histological features assessed over long-term culture. Results showed that human MSCs were highly sensitive to their 3D microenvironment: while biosynthetically productive in pellet form, on nanofibrous scaffolds, they elaborated little matrix compared to MFCs taken from the same donor.

## **8.2 MATERIALS AND METHODS**

### ***8.2.1 Scaffold Fabrication***

Scaffolds employed in this work were dual-component, aligned nanofibrous scaffolds designed to improve cell infiltration via the removal of a subpopulation of fibers, as described in Chapter 4. These electrospun composites initially contained 40% by mass sacrificial poly(ethylene oxide) (PEO) fibers, which were dissolved from the structure prior to cell seeding (leaving behind the slow-degrading PCL fiber population). For each donor, a separate aligned, nanofibrous mesh containing a mixture of poly( $\epsilon$ -caprolactone) (PCL) and PEO fibers was produced via a dual-spinneret electrospinning setup. Briefly, a 14.3% w/v solution of PCL (80 kD, Sigma-Aldrich, St. Louis, MO) was dissolved in a 1:1 solution of tetrahydrofuran and N,N-dimethylformamide (Fisher Chemical, Fairlawn, NJ) and a 10% w/v solution of PEO was dissolved in 90% ethanol. The two solutions were co-electrospun onto a grounded mandrel (2" diameter, 8" length) rotating at a

velocity of ~10 meters/sec (Li et al. 2007) for a duration of 4 hours. Strips excised from the resulting mat were disinfected and rehydrated in decreasing concentrations of ethanol (100, 70, 50, 30%; 30 min/step) and rinsed twice in phosphate-buffered saline (PBS), to remove the water-soluble, sacrificial PEO fibers.

### 8.2.2 Cell Culture

Meniscus fibrochondrocytes (MFCs) were isolated as in Chapter 7 from human meniscus tissue collected under an approved IRB protocol. Tissue was from 4 adults ranging in age from 57 to 78 years who were undergoing total knee arthroplasties (TKA) (**Table 8-1**). Meniscal tissue was debrided of any fatty tissue or remnant capsular material, finely minced, and plated on tissue culture plastic (TCP) in basal medium (BM: DMEM containing 1X PSF and 10% FBS). MFCs emerged from the tissue and formed colonies which were expanded to passage 2 to obtain sufficient cell numbers for scaffold seeding and pellet formation.

Donor	Age	Sex	Cells	Source
1	57	Female	MFC, MSC	Tibia/Femur (Total knee arthroplasty)
<b>2</b>	<b>63</b>	<b>Male</b>	<b>MFC, MSC</b>	<b>Tibia/Femur (Total knee arthroplasty)</b>
3	78	Female	MFC, MSC	Tibia/Femur (Total knee arthroplasty)
<b>4</b>	<b>60</b>	<b>Male</b>	<b>MFC, MSC</b>	<b>Tibia/Femur (Total knee arthroplasty)</b>
5	22	Female	MSC	Iliac crest (Lonza)
<b>6</b>	<b>18</b>	<b>Male</b>	<b>MSC</b>	<b>Iliac crest</b>

**Table 8-1: MSCs were isolated from healthy and OA bone marrow sources. MSCs and MFCs isolated from the surgical waste tissue of four patients undergoing TKA were compared in this study. Healthy MSCs were examined to determine whether stem cell behavior was disease or age dependent.**

Mesenchymal stem cells (MSCs) were isolated from the same four patients. Bone marrow aspirates obtained during TKA were plated on TCP in basal medium. In separate confirmatory studies, MSCs from young, healthy donors were obtained, either from a

commercially available source (Lonza, Basel, Switzerland) or from a patient undergoing treatment for osteochondritis dissecans (**Table 8-1**). To confirm MSCs isolated from TKA bone marrow aspirate were in fact multipotent, adipogenic, osteogenic, and chondrogenic differentiation capacity was assessed using standard techniques (Pittenger et al. 1999; Mauck et al. 2007). For adipogenesis and osteogenesis, MSCs were plated at a density of 2,000/cm<sup>2</sup> in treated tissue culture 24-well plates and maintained in lineage-specific differentiation media changed twice weekly. Osteogenic medium consisted of BM supplemented with 10 nM dexamethasone, 10 mM  $\beta$ -glycerophosphate, 50 mg/ml ascorbate 2-phosphate, and 10 nM 1,25-dihydroxyvitamin D<sub>3</sub> (BIOMOL, Plymouth Meeting, PA). Adipogenic medium consisted of BM with 1 mM dexamethasone, 1 mg/ml insulin, and 0.5 mM 3-isobutyl-1-methylxanthine. For chondrogenesis, pellets containing 250,000 cells were formed by centrifugation (5 min, 300 $\times$ g) in 96-well polypropylene conical plates (Nalgene Nunc International, Rochester, NY) and maintained in chemically-defined medium (CDM: DMEM with 1X PSF, 0.1 $\mu$ M dexamethasone, 50 $\mu$ g/mL ascorbate 2-phosphate, 40 $\mu$ g/mL L-proline, 100 $\mu$ g/mL sodium pyruvate, 6.25 $\mu$ g/ml insulin, 6.25 $\mu$ g/ml transferrin, 6.25ng/ml selenous acid, 1.25mg/ml bovine serum albumin, and 5.35 $\mu$ g/ml linoleic acid) supplemented with 10ng/mL TGF- $\beta$ 3 (CDM+, R&D Systems, Minneapolis, MN).

To form constructs (cells seeded onto nanofibrous scaffolds), each side of a 4 by 25mm scaffold received a 50 $\mu$ l aliquot containing 200,000 cells followed by one hour of incubation. Once seeded with cells, constructs were cultured in 3mL of CDM+ changed twice weekly in non-treated 6-well plates. Constructs were harvested on days 21, 42, and

63 for mechanical and biochemical analysis. Additionally, pellets (250,000 cells/pellet) were formed as above from both cell types and maintained in CDM+ for up to 3 weeks. Pellets were harvested on days 7 and 21 for determination of biochemical content. Constructs and pellets at terminal time points of day 63 and 21, respectively, were examined histologically.

### ***8.2.3 Mechanical Testing***

Uniaxial tensile testing was performed with an Instron 5848 Microtester (Instron, Canton, MA). Prior to testing, the cross-sectional area was determined at four locations along the length of each construct with a custom laser-LVDT measurement system (Peltz et al. 2009). Samples were preloaded to 0.1N for 60 seconds to remove slack. After noting the gauge length with a digital caliper, samples were extended to failure at a rate of 0.1% of the gauge length per second. Stiffness was determined from the linear region of the force-elongation curve. Using the cross-sectional area and gauge length, Young's modulus was calculated from the analogous stress-strain curve.

A custom mechanical testing device was used to evaluate compressive properties of engineered constructs (Mauck et al. 2006). Disks (2mm diameter) were cored through the thickness of each planar construct. These disks were tested in unconfined compression between two impermeable platens. First, samples were equilibrated in creep under a static load of 0.02 N for 5 min. After creep deformation, samples were subjected to 10% strain (calculated from post-creep thickness values) applied at 0.05%/s followed by

relaxation for 1000s until equilibrium. The equilibrium modulus was determined from the equilibrium stress (minus tare stress) normalized to the applied strain.

#### ***8.2.4 Transcriptional and Biochemical Analyses***

Total RNA was isolated with TRIZOL-chloroform and reverse transcription was performed on pellets and nanofibrous constructs after 7 days of culture, as in (Huang et al. 2009). Real-time PCR was carried out with intron-spanning primers for type I collagen, aggrecan core protein, and glyceraldehyde 3-phosphate dehydrogenase (GAPDH). Starting quantities of collagen I and aggrecan transcripts were determined by the standard curve method and normalized to GAPDH.

Pellets and constructs after tensile testing were stored at -20°C until determination of biochemical composition. Constructs were desiccated and massed to determine dry weights. Following this, all samples were papain digested as in (Mauck et al. 2006) and DNA, sulfated glycosaminoglycan (s-GAG), and collagen content was determined using the Picogreen double-stranded DNA (dsDNA) (Molecular Probes, Eugene, OR), DMMB dye-binding (Farndale et al. 1986), and hydroxyproline (Stegemann et al. 1967) assays, respectively. Hydroxyproline content was converted to collagen as in (Neuman et al. 1950), using a factor of 7.14. This conversion is an estimate, and susceptible to slight bias based on the prevailing collagen type present.

### **8.2.5 Histology**

Adipogenic and osteogenic monolayers were stained with Oil Red O and Alizarin Red, to confirm the presence of lipid globules and mineral deposits, respectively (Mauck et al. 2007). Pellets were fixed in 4% paraformaldehyde, embedded in agarose blocks, infiltrated with paraffin, and sectioned to 16µm thickness. Nanofibrous constructs were fixed, embedded in frozen-sectioning medium, and cut in cross-section to 16µm thickness. Sections were stained with Picrosirius Red (PSR) and Alcian Blue (AB) to identify collagen and sulfated proteoglycan, respectively, and imaged on an upright Leica DMLP microscope (Leica Microsystems, Germany). Cell nuclei and F-actin were visualized with 4',6-diamidino-2-phenylindole (DAPI) and phalloidin-Alexa488 (Invitrogen, Carlsbad, CA), respectively, and imaged on a Nikon T30 inverted fluorescent microscope (Nikon Instruments, Melville, NY).

### **8.2.6 Statistical Analyses**

Analysis of variance (ANOVA) was carried out with SYSTAT (v10.2, Point Richmond, CA). Tukey post-hoc tests were used to make pair-wise comparisons between cell type and time points, with significance set at  $p < 0.05$ . Data are presented as the mean  $\pm$  standard deviation.

## **8.3 RESULTS**

### **8.3.1 Cell Isolation and Expansion**

MSCs and MFCs were successfully isolated from bone marrow aspirate and meniscus tissue, respectively, harvested from patients undergoing TKA (**Table 8-1**). Cells were

expanded to passage 3 before use in forming pellets or nanofiber-based constructs. In monolayer, MFCs proliferated at a faster rate, yielding  $42\pm 11M$  cells in  $64\pm 10$  days, while MSCs produced only  $30\pm 3M$  cells in  $90\pm 15$  days. MSCs isolated in this manner were multipotent, as evidenced by their successful induction towards adipogenic, osteogenic, and chondrogenic phenotypes (**Figure 1**).

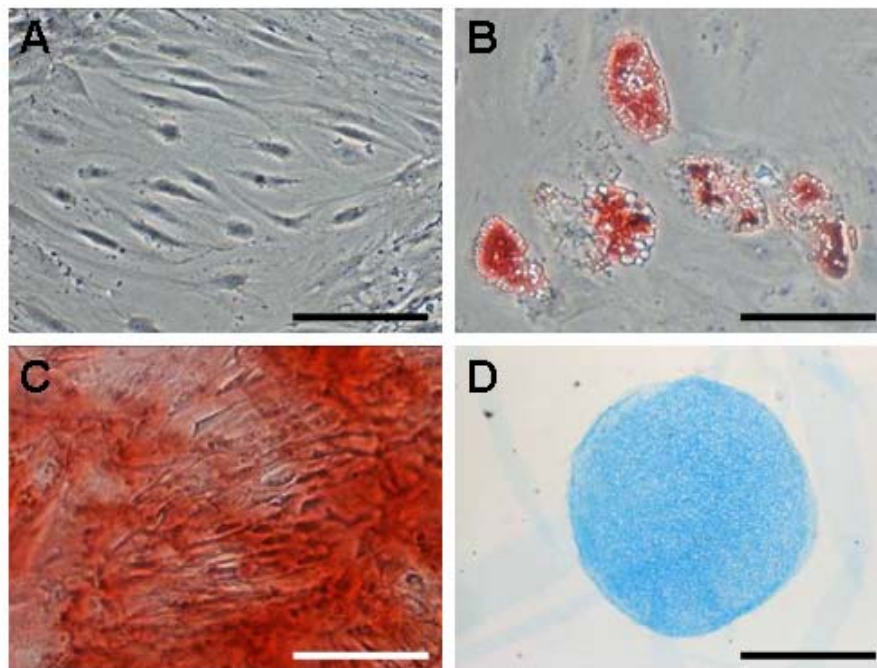


**Figure 8-1:** MSCs isolated from OA donors are multipotent. MSCs cultured for 3 weeks under control (A, unstained), adipogenic (B, stained with Oil Red O), osteogenic (C, stained with Alizarin Red), and chondrogenic (D, stained with Alcian Blue) conditions. Scale:  $100\mu m$  (A, C),  $50\mu m$  (B),  $500\mu m$  (D).

### 8.3.2 3D Pellet Culture

In order to assess the baseline behavior of these cells in a 3D environment, MSCs and MFCs were placed in pellet culture in a pro-chondrogenic chemically defined medium. On days 7 and 21, pellets were harvested and assayed for DNA, GAG, and collagen content (**Figure 8-2A-C**). In pellets, cell division was limited – DNA content did not increase with time ( $p=0.482$ ). Averaging across donors, there was no difference in the

number of cells in MSC and MFC pellets at either time point ( $p>0.170$ ). Both cell types synthesized GAG and collagen, key components of cartilage and meniscus ECM. Day 7 pellets contained comparable amounts of these matrix molecules, irrespective of cell type or donor source. However, with two additional weeks of culture, variability with respect to donor and cell type became apparent. For example, MFC pellets from three of four donors contained more GAG than their MSC counterparts, while the converse held for Donor 3. As observed in Chapter 7 and (Payne et al. ; Murphy et al. 2002), donor to donor variability was marked for both cell types and as a result, the average response of all donors was not significantly different in terms of GAG ( $p=0.925$ ) or collagen ( $p=0.054$ ) content between MSC and MFC at the terminal time point. Histological staining corroborated these biochemical measures (**Figure 8-2D**). Alcian Blue and Picrosirius Red staining, indicative of GAG and collagen, respectively, correlated well with the assay results and strengthened the general conclusion that in 3D pellet culture, MSCs and MFCs behave similarly.

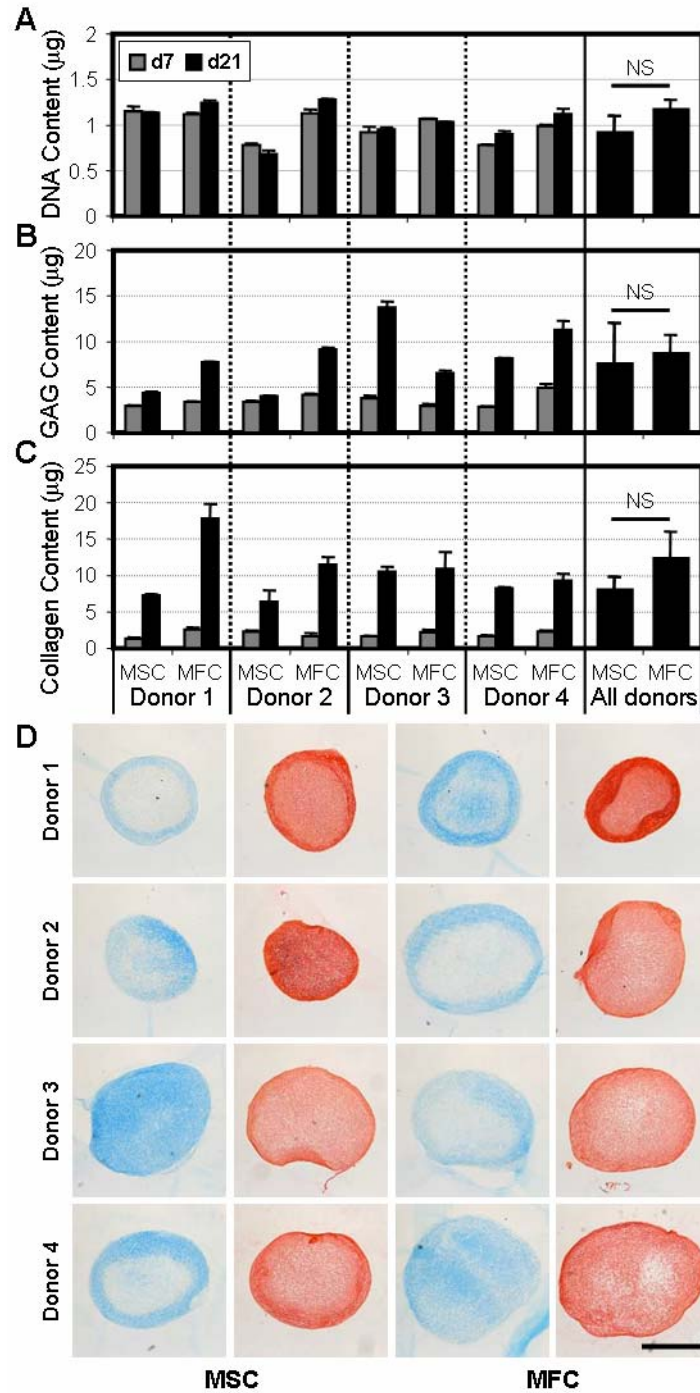


**Figure 8-2:** MSCs readily produce a GAG- and collagen-rich ECM comparable to MFCs in pellet culture. MSCs and MFCs isolated from four OA donors were formed into pellets and cultured in a pro-chondrogenic medium. On days 7 and 21, DNA (A), GAG (B), and collagen (C) contents were determined. Data is presented on a per pellet basis. 4 pellets/n, n=3. D) Representative day 21 MSC and MFC pellets stained for GAG (blue) and collagen (red). Scale: 500 $\mu\text{m}$ .

### **8.3.3 Nanofibrous Constructs**

At the time of pellet formation, the same MSC and MFC cell populations were seeded onto aligned nanofibrous scaffolds to form constructs (**Figure 8-3A**). Both cell types adopted an elongated morphology with prominent actin stress fibers (**Figure 8-3D,E**). After 7 days of culture, real-time RT-PCR was performed on MSC and MFC pellets and nanofibrous constructs to determine the expression of type I collagen and aggrecan, which are typical markers for fibrous tissues and cartilage, respectively (**Figure 8-3B,C**). MSCs seeded on aligned nanofibers underwent fibrochondrogenesis, expressing both type I collagen and aggrecan. Compared to pellets, scaffold-seeded cells demonstrated increased type I collagen expression ( $p < 0.005$ ) and trended towards decreased aggrecan expression ( $p < 0.1$ ), despite significant variability between donors. Importantly, no difference in the expression of either type I collagen or aggrecan was detected between MSCs and MFCs in either pellet form or when seeded on electrospun scaffolds ( $p > 0.582$ ).

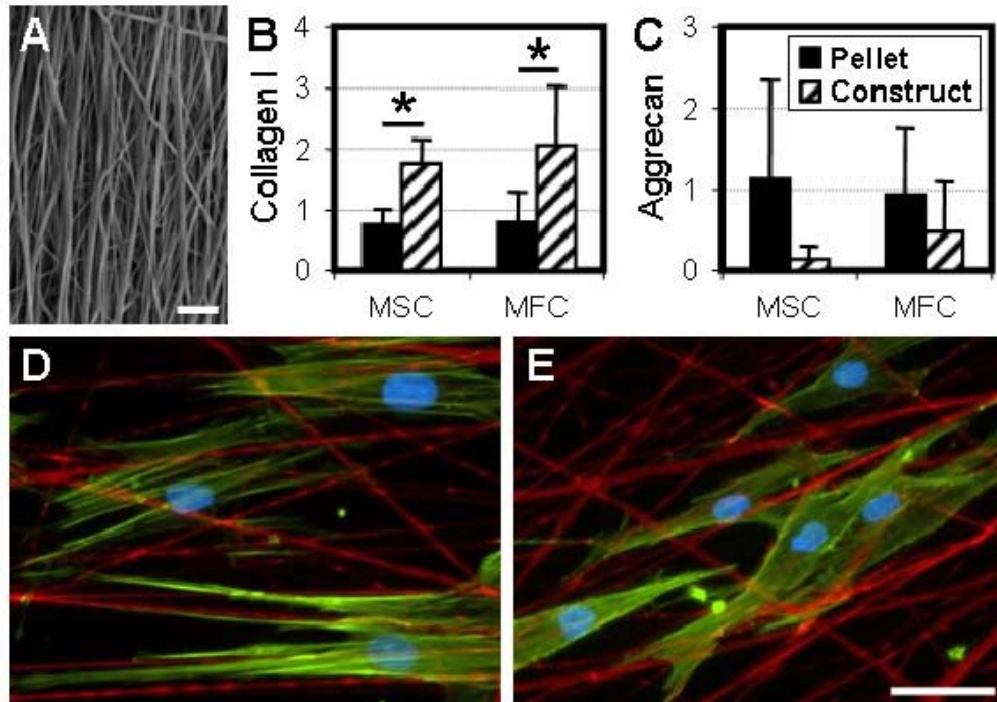


**Figure 8-3:** The nanofibrous topography defines cell morphology and modulates gene expression of key matrix constituents. A) Cells were seeded onto aligned nanofibrous scaffolds following the removal of sacrificial PEO fibers in order to hasten cell infiltration. Scale: 10 $\mu$ m. Type I collagen (B) and aggrecan (C) gene expression of MSC and MFC pellets and nanofibrous constructs after 7 days under identical culture conditions. n=4, \*: p<0.05. MSCs (D) and MFCs (E) seeded onto scaffolds (green: F-actin, red: fibers, blue: nuclei). Scale: 25 $\mu$ m.

Over a longer time course, and consistent with the studies described in Chapter 7, MFCs cultured in this microenvironment were biosynthetically active (**Figure 8-4**). MFCs proliferated considerably between the time of seeding and day 21, before leveling off by day 42. Concurrent with cell division, MFCs elaborated a robust collagen- and GAG-rich ECM with time in culture (p<0.001). In stark contrast, MSCs showed limited division and matrix biosynthesis when seeded onto electrospun scaffolds. The DNA content of MSC constructs did not change with culture duration, and remained lower than donor-matched MFC constructs at all time points (4-fold less on day 63, p<0.001). Additionally, for each donor, MSC-seeded constructs contained negligible amounts of

GAG and collagen. While the quantity of these biomolecules did increase with time in culture ( $p < 0.001$ ), MFC constructs on day 63 contained ~24 and ~10 fold more GAG and collagen, respectively, than donor-matched MSC samples.

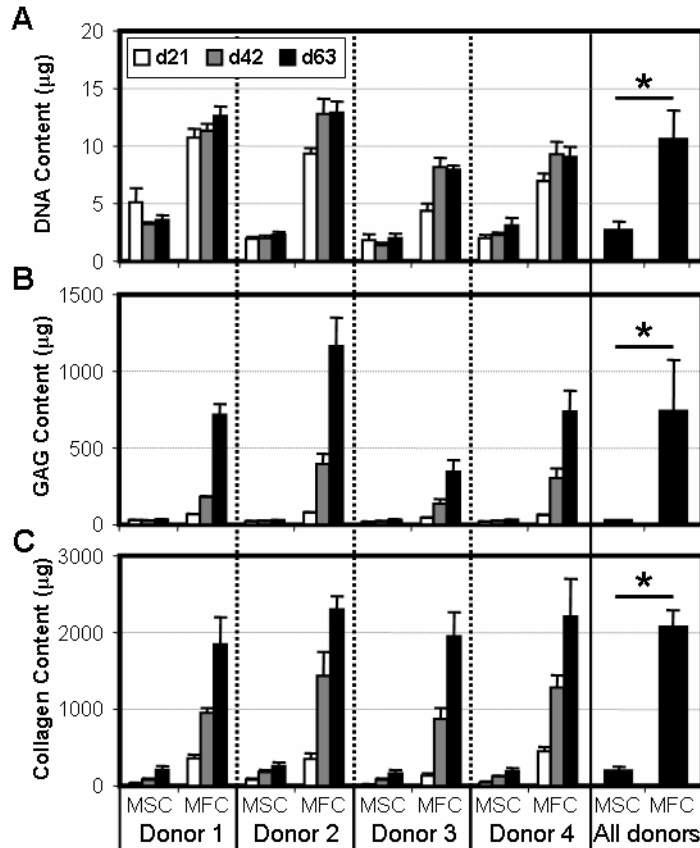


**Figure 8-4: MSCs on nanofibrous scaffolds do not proliferate and produce less ECM than donor-matched MFCs. Donor-matched MSC and MFC populations were seeded onto aligned nanofibrous scaffolds and maintained in identical culture conditions. On days 21, 42, and 63, construct DNA (A), GAG (B), and collagen (C) content was determined.  $n=5$ , \*:  $p < 0.05$ .**

Histological staining of construct cross-sections on day 63 confirmed differences in cellularity and ECM elaboration between cell types (**Figure 8-5**). DAPI staining of cell nuclei on day 63 showed that MFCs from all four donors colonized the entirety of the electrospun scaffolds. The near homogeneous distribution of cells throughout the thickness of the construct translated to better distributed ECM. As seen in other studies,

GAGs were more uniformly dispersed than collagen, which exhibited a slight density gradient weighted towards the scaffold periphery. Conversely, MSC-seeded constructs showed limited cell proliferation and matrix synthesis. Despite their limited numbers and inability to divide, cell infiltration did not appear to be inhibited as individual MSCs were observed at depths of up to ~200 $\mu$ m from the scaffold periphery. As expected given the restriction of MSCs to the surface, GAG and collagen were confined to the scaffold periphery as well.

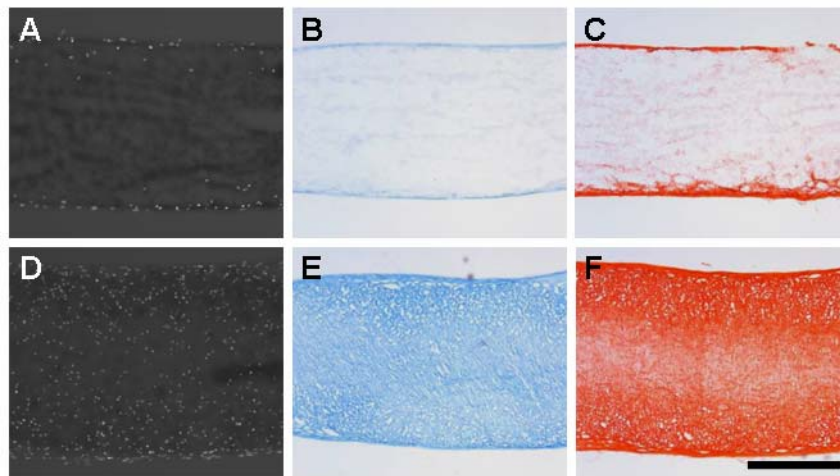


**Figure 8-5: Histological examination confirms the disparity in ECM production between MSC- and MFC-laden nanofibrous constructs. Representative cross-sections of MSC (A, B, C) and MFC (D, E, F) nanofibrous constructs on day 63 stained for cell nuclei (A, D), GAG (B, E), and collagen (C, F). Scale: 500 $\mu$ m.**

The assembly of ECM was paralleled with increases in construct mechanical properties (**Figure 8-6**). For tensile testing, every cell-seeded sample was tested with a paired unseeded control (USC) that possessed identical mechanical properties at the beginning of the study. Maintaining the gauge length across all studies, the stiffness of cell-seeded constructs was normalized to paired USCs to determine a percentage change in stiffness. Both MSC and MFC constructs increased in % stiffness with time in culture ( $p < 0.001$ ), however the magnitude of change was significantly lower for MSCs from all donors

( $p < 0.001$ ). By day 63, MFC samples ranged between 80-200% higher than USC values while MSC constructs maximally increased by 50%. The tensile moduli of all constructs increased relative to USCs by the final time point ( $p < 0.001$ ). Due to decreases and increases in MSC and MFC construct dimensions, respectively, no significant difference in modulus was found for Donors 1 and 2, while substantial increases were seen in this measure for Donors 3 and 4.

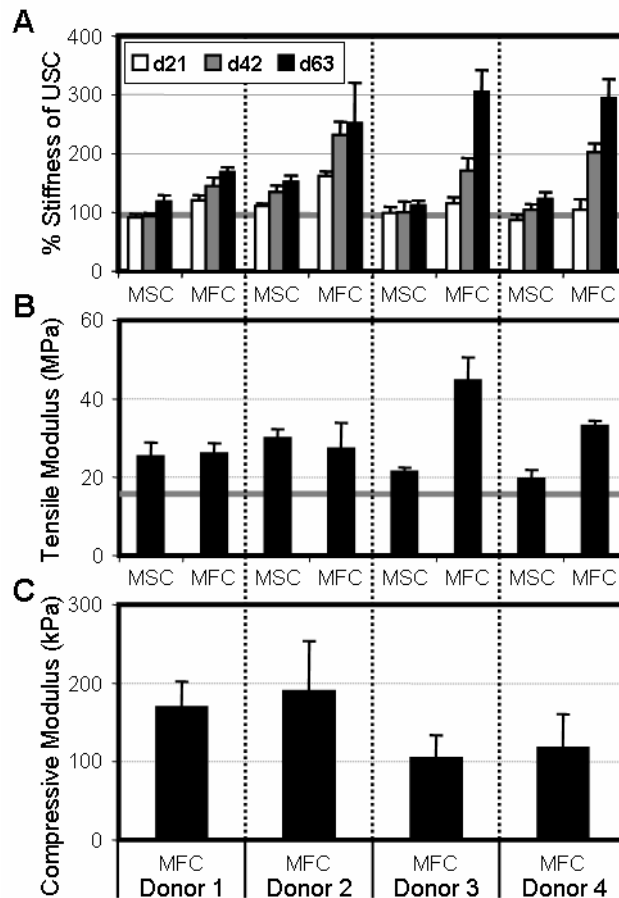


**Figure 8-6: Increases in construct biochemical content are paralleled by changes in mechanical properties. A) Tensile stiffness of MSC- and MFC-seeded constructs with time in culture, normalized to unseeded control scaffolds (grey bar). B) Tensile modulus of day 63 constructs and unseeded controls (grey bar). C) Compressive equilibrium modulus of MFC constructs on day 63. Note: MSC constructs and unseeded controls could not be tested in this manner (see Results). n=5 for tensile data, n=3 for compressive data.**

To determine compressive properties, cores were taken through the thickness of the constructs and equilibrium modulus was assessed in unconfined compression (**Figure 8-6**). Unlike MFC constructs, MSC and USC samples deformed beyond 20% of their starting thickness under nominal tare loads and did not exhibit stress-relaxation. This indicated the need for a contiguous cell-deposited matrix spanning the entire construct thickness in order to reliably assess the compressive properties of the nanofiber-reinforced matrix rather than the void volume of an empty scaffold. As such, compressive modulus is reported only for MFC constructs. MFC constructs from all four donors achieved equilibrium moduli ranging between 100-200 kPa.

#### ***8.3.4 MSCs from Healthy Donors***

To determine whether the advanced age and OA sourcing of cells from Donors 1-4 was responsible for the impaired division and matrix production observed in MSCs on nanofibrous scaffolds, identical studies were carried out using MSCs isolated from young, healthy donors (**Table 8-1**). MSCs from Donors 5 and 6 expanded in monolayer at faster rates than both MSCs and MFCs from OA donors ( $44 \pm 8.5$ M cells in  $38 \pm 4.2$  days). Pellets formed from these MSCs contained equivalent amounts of GAG and collagen, and appeared histologically similar to those formed with OA MSCs (data not shown). When seeded onto nanofibrous scaffolds, the resulting constructs matured in analogous fashion to those formed with MSC from Donors 1-4 (**Figure 8-7**). By day 63, tensile stiffness surpassed USC values, but these increases were slightly less than observed with OA MSCs (grey region and dotted line). GAG and collagen accumulated with time in culture to levels comparable to those reached with MSCs from Donors 1-4.

Histological appearance of constructs grown from Donor 5 and 6 MSCs on day 63 were comparable to constructs seeded with MSCs from Donors 1-4.

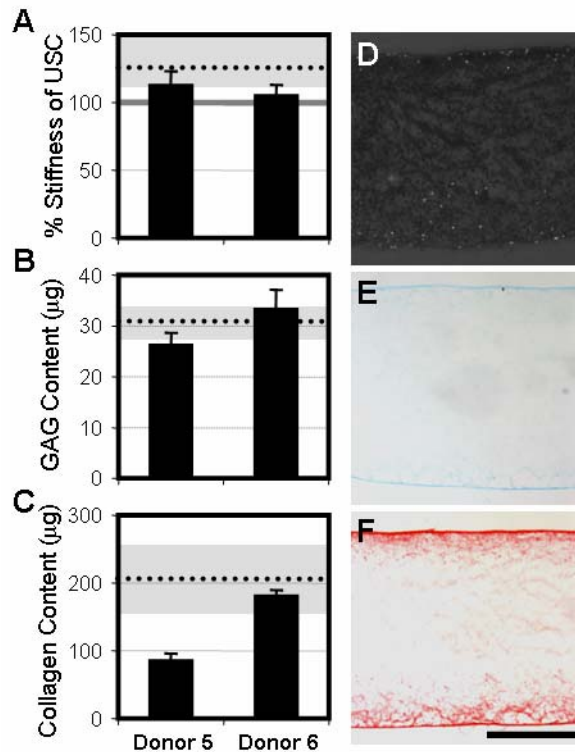


**Figure 8-7: Limitations in the maturation of human MSC-seeded nanofibrous constructs are not dependent on age or disease-status. A) Tensile stiffness of healthy MSC constructs on day 63 normalized to unseeded control scaffolds (grey bar). GAG (B) and collagen (C) content of day 63 constructs. Dotted lines and gray regions represent the average and full range of response of OA MSCs, respectively. Cross-sections of day 63 Donor 5 MSC-seeded nanofibrous constructs stained for cell nuclei (D), GAG (E), and collagen (F). Scale: 500µm.**

## 8.4 DISCUSSION

Numerous studies have demonstrated that modulation of the *in vitro* microenvironment can dictate the morphology and phenotypic transitions of both differentiated and stem cells. For instance, the plating and expansion of primary chondrocytes on tissue culture plastic triggers a loss in phenotype which can be recovered upon returning the cells to 3D hydrogel culture (Benya et al. 1982). More recent studies have shown that characteristics of the physical surroundings of stem cells, such as topography in the form of adhesive

island size and substrate elasticity, potentially regulate fate decisions (McBeath et al. 2004; Engler et al. 2006). Nanofibrous assemblies present a topography that more closely mimics naturally-occurring ECM than micropatterned features such as ridges or grooves, and as such, there has been great interest in understanding how stem cells operate in a nanofibrous context. Studies by Nur-E-Kamal et al. showed that culture of mouse embryonic stem cells on a 3D nanofibrous topography encourages self-renewal and forestalls differentiation as compared to 2D tissue culture plastic surfaces (Nur et al. 2006). Beyond simply the dimensionality (2D vs. 3D) of the microenvironment, it is now appreciated that the scale of features has unique consequences for how cells attach to and perceive their surroundings (Baker et al. 2009). Li and coworkers observed that chondrocytes remained rounded and retained their phenotype when seeded onto nanofibers, but became spread with pronounced actin stress fibers when cultured on the surface of micrometer-scale fibers comprised of the same material (Li et al. 2006). Given that terminally differentiated cells such as chondrocytes are sensitive to these topographical inputs, stem cells, which lack a defined set of preprogrammed responses, may be even more affected by the shape and scale of their surrounding microenvironment.

The current study explored the effect of a nanofibrous microenvironment on human MSCs, with the aim of directing these cells to assemble a mechanically functional fibrocartilaginous matrix. MSCs were cultured in two different 3D systems resulting in distinct cell microenvironments and consequent morphologies. In pellets, a simple culture model for chondrogenesis, the absence of a scaffold enabled aggregated cells to

remain rounded (Johnstone et al. 1998). When seeded on aligned nanofibrous scaffolds, nanofibers present a defined surface for cell attachment and elongation - MSCs adopt a highly polarized cell body with pronounced actin stress-fibers (**Figure 8-3**). Despite culture in identical media formulations, the difference in 3D microenvironments led MSCs along separate paths, culminating in the production of characteristically divergent ECM. Within one week of seeding on aligned nanofibers, MSCs shifted towards a more fibrous phenotype, significantly increasing the expression of type I collagen and trending towards down-regulation of aggrecan (**Figure 8-3**). These early changes in gene transcription were supported by bulk measures of GAG and collagen at later time points (**Figures 8-2, 8-4**). MSC pellets contained a 1:1 ratio of collagen to GAG more representative of cartilage, while this ratio for MSCs on scaffolds approached ~2, suggesting a shift towards a fibroblastic phenotype with increased collagen production (and less GAG production). MFC gene expression paralleled the differences observed with MSCs, and revealed an increase in the collagen to GAG ratio from ~1.5 in pellet form to 5 in nanofibrous format, in keeping with previous reports demonstrating the innate plasticity of this cell type (Mauck et al. 2007). This may have implications with respect to the phenotypic spectrum of MFCs found in the meniscus (Upton et al. 2006). These findings imply a change in cell behavior induced by aligned nanofibers in both differentiated and adult stem cells.

A microenvironment composed of aligned nanofibers was suitable for the production of organized fibrocartilaginous matrix by both MFCs and MSCs, leading to significant increases in tensile properties by 9 weeks for both cell types. However, the magnitude of

increase was markedly different for MFCs and MSC, owing in part to the fact that MSCs did not proliferate on nanofibrous topographies. Interestingly, the same MSCs divided normally in the identical media formulation but when cultured on tissue culture plastic (data not shown). While the underlying cause for this discrepancy requires further investigation, several obvious explanations were ruled out. The absence of proliferation may suggest that these MSCs were senescent and unable to divide, differentiate, or synthesize ECM (Wagner et al. 2008). Countering this supposition, MSCs from OA sources were multipotent (**Figure 8-1**) and when placed in pellet format, synthesized equivalent amounts of GAG and collagen as MFCs cultured similarly (**Figure 8-2**). Literature indicating that MSCs from aged or OA donors may have reduced potential raises the possibility that the observed shortcomings are not a general behavior of human MSCs (Murphy et al. 2002; Coipeau et al. 2009), but rather resulted from the OA condition. To rule out age/disease effects, MSCs were isolated from the healthy marrow of young donors and formed into pellets and seeded on to scaffolds. Paralleling MSCs from OA donors, proliferation, matrix synthesis, and changes in construct mechanical properties were modest relative to MFCs from older donors (**Figure 8-7**), despite robust matrix formation in pellets (data not shown).

The limited proliferation of MSCs on aligned nanofibrous scaffolds was evident in DAPI staining of construct cross-sections (**Figure 8-5**) and corroborated by quantification of DNA content (**Figure 8-4**). Constructs were formed by seeding the scaffold surface with cells. MFCs proliferated abundantly on the scaffold surface and gradually migrated inwards, colonizing the entirety of ~1mm thick scaffolds by 9 weeks of culture.

Although TGF- $\beta$ 3 appears to exert a mitogenic effect on human and bovine MFCs, and bovine MSCs (as seen in Chapters 3 & 7), human MSCs did not respond in the same fashion. After 9 weeks, MSCs remained sequestered primarily to the scaffold surface and the limited amount of matrix produced by this thin population was tightly localized to this region. The addition of a mitotic agent such as FGF could potentially spur MSC proliferation and improve the maturation of human MSC-seeded nanofibrous constructs (Tsutsumi et al. 2001; Farre et al. 2007).

These findings are in agreement with other studies finding differences in MSC viability and proliferation as a function of species of origin. Of note, however, proliferation deficits alone do not fully account for the discrepancy between human MSC and MFC constructs. Despite the difference in construct cell density, we observed an innate deficiency in ECM production by MSCs on aligned topographies. Normalizing biochemical measures of 9 week constructs to DNA content, MFCs synthesized 3- and 6-fold more collagen and GAG, respectively, than MSCs on a per cell basis. Recent work has revealed fundamental differences between native chondrocytes and chondrogenically-differentiated MSCs in hydrogel cultures (Mauck et al. 2006). In those studies, donor-matched MSCs generated inferior cartilage constructs compared to fully-differentiated chondrocytes. Work by Huang et al. found that functional parity could not be achieved by merely augmenting MSC seeding density (Huang et al. 2009). Furthermore, using microarrays to transcriptionally fingerprint chondrocytes and differentiated MSCs, they identified matrix-mediating genes that were either over- or under-expressed in MSC-laden constructs (Huang et al. 2010). Given the complex transcriptional topography

navigated by MSC during differentiation (Ng et al. 2008; Mrugala et al. 2009), a similar microarray approach could be employed to identify inadequacies of MSCs in this aligned nanofiber system.

While nanofibrous scaffolds present a suitable foundation for the engineering of collagen-rich tissues, one significant drawback lies in an inherently small pore size which hampers the ingress of the surface-seeded cells. In previous studies, despite extended periods of culture, the central third of ~1mm thick nanofibrous constructs remained deficient of cells and matrix (Chapter 3 & 7). To overcome this, we have developed a composite scaffold containing water soluble (PEO) fibers interspersed between slow-degrading polyester (PCL) fibers (Chapter 4). Removal of these sacrificial fibers increases the average pore size and hastens cell infiltration. In the current study, the use of such composites resulted in completely infiltrated MFC constructs by 9 wks (**Figure 8-5**). The improved distribution of cells translated to a more homogeneously distributed matrix which enabled the measurement of compressive properties.

Compressive and tensile properties were assessed in this study as these are the predominant loading modalities of tissues such as the meniscus that operate in a complex mechanical environment (**Figure 8-6**) (Shrive et al. 1978; Setton et al. 1999). MFC constructs possessed a compressive equilibrium modulus of between 100-200 kPa, values within range of native meniscus benchmarks (Chia et al. 2008; Bursac et al. 2009). Acellular and MSC seeded constructs did not stress-relax, highlighting the need for the contiguous GAG-laden matrix (enabled by the use of composite scaffolds optimized for

cell infiltration) to achieve mechanical functionality in compression. To assess changes in tensile properties, the stiffness of seeded constructs was normalized to acellular scaffolds to eliminate any artifact caused by changes in specimen geometry. While MSC constructs increased in stiffness by only 25%, MFC constructs revealed more demonstrable changes. By 9 weeks of culture, the anisotropic matrix established by MFCs translated to a 2.5-fold higher stiffness than acellular controls, a result on par with values from Chapter 7. Despite this considerable growth, 9 week constructs possessed quasistatic tensile moduli ranging from 26-45 MPa, a value below native human meniscus by a factor of 2 or more (Tissakht et al. 1995; Bursac et al. 2009). To stimulate further increases in tensile stiffness and narrow the gap between engineered constructs and native tissue, future studies will investigate cyclic tension during *in vitro* culture (Lee et al. 2005).

## **8.5 CONCLUSIONS**

Overall, this study demonstrated the potential for engineering fibrocartilage with human stem cell-seeded nanofibrous scaffolds, and highlighted key issues related to microenvironment and topography when using MSCs. Previous studies employing bovine cells demonstrated that this environment was suitable for differentiating MSCs and instructing these cells to synthesize an organized ECM. Although human MSCs did in fact generate GAG- and collagen-containing matrix, their productivity and proliferation was limited compared to native fibrochondrocytes, despite similar biosynthetic output between these cell types when cultured in pellet format (without scaffold). These results emphasize the importance of understanding how the

microenvironment impacts progenitor cell differentiation and biosynthetic activity, and may have implications for development and regenerative strategies. Clearly, a better understanding of the interplay between the cell-scaffold interface, intracellular architecture, and the regulation of transcriptional machinery is required. Future studies examining global expression patterns may further elucidate the incongruities between MSCs undergoing fibrochondrogenic differentiation on aligned nanofibrous scaffolds and tissue-derived cells that have undergone this process through normal developmental processes, and identify exploitable factors for enhancing *in vitro* tissue development with MSCs.

# ***CHAPTER 9: MECHANO-TOPOGRAPHIC MODULATION OF STEM CELL NUCLEAR SHAPE ON NANOFIBROUS SCAFFOLDS***

## **9.1 INTRODUCTION**

Adult mesenchymal stem cells (MSCs) have generated considerable interest for regenerative medicine applications given their ready isolation for autologous use, their extensive *in vitro* expansion capacity, and their ability to differentiate along a number of different tissue-specific lineages, particularly those of the musculoskeletal system (Baksh et al. 2004). Most notably, adult MSCs appropriately cultured and provided with key soluble factors can adopt differentiated functions consistent with cartilage cell (chondrogenesis), fat cell (adipogenesis) and bone cell (osteogenesis) phenotypes (Caplan 1991; Pittenger et al. 1999). Since this first conception of an adult stem cell, it has been noted that additional cues from the microenvironment, including both passive (topography, order, and substrate stiffness) and dynamic mechanical inputs can further regulate these phenotypic shifts (Discher et al. 2009; Guilak et al. 2009).

These microenvironmental cues are particularly important for tissue engineering, where stem cells must often interface with a biomaterial substrate that can instruct tissue formation or serve as a vehicle for targeted delivery of cells *in vivo*. For instance, the elasticity of the delivery material can influence fate decisions, even in the absence of defined soluble cues (Engler et al. 2006). Additionally, specific receptor-ligand

interactions can be engineered onto the material surface that can further modulate the extent to which differentiation occurs (Connelly et al. 2007; Lee et al. 2008). Similarly, the topography of the interacting surface can be altered to impact stem cell fate, whether these cells are delivered with or invade into the biomaterial post-implantation (McBeath et al. 2004; Dalby et al. 2007). While the mechanism by which these passive topographical stimuli elicit changes in stem cell activity is not yet clear, their influence occurs over a range of length scales and appears to influence the differentiation process directly.

Nanofibrous scaffolds, formed by the process of electrospinning, are commonly employed for tissue engineering with stem cells (Mauck et al. 2009). These scaffolds provide a biomimetic fibrous microenvironment with polymeric fibers that recreate the length scale encountered by cells within their normal extracellular milieu. Adult MSCs seeded onto these scaffolds can differentiate along multiple lineages (Li et al. 2005). Nanofibrous scaffolds, by virtue of their nano-scale features, also influence cell shape, and therefore biologic responses directly. For example, primary chondrocytes on nanofibrous scaffolds produce higher levels of cartilage-specific matrix compared to the same cells seeded on micron-scale fibers of the same composition (Li et al. 2006). Nanofibrillar surfaces also control mouse embryonic fibroblast morphology and cytoskeletal organization (Ahmed et al. 2007), enhance proliferation and self-renewal of mouse embryonic stem cells (Nur et al. 2006), and activate cytoskeletal remodeling through the small GTPase Rac (Nur et al. 2005). We have recently shown that alignment of this nanofibrous microenvironment can direct actin stress fiber organization in adult

human mesenchymal stem cells (Li et al. 2007). This in turn directs the ordered deposition of matrix, which in the long term translates to improved construct mechanical properties (as shown in previous chapters). Of particular note, and in comparison to traditional pellet culture, the aligned topography provided by these organized nanofibrous patterns can foster fibrous over cartilaginous differentiation of MSCs (Chapter 8).

In addition to these passive cues provided by material microenvironments, active mechanical cues likewise exert control over stem cell differentiation. Such mechanical cues are of developmental relevance; for example, blocking muscle contraction abrogates formation of critical fibrous structures within the knee joint (Mikic et al. 2000). Application of physical forces to MSCs in culture is often carried out via deformation of scaffolds with custom mechanical devices (e.g. (Huang et al. ; Mouw et al. 2007)). Dynamic tensile deformation of the substrate can, for example, increase collagen gene expression by MSCs after one day (Park et al. 2004) and improve osteogenesis and mineral deposition over several days (Simmons et al. 2003), while static substrate deformation blocks chondrogenesis in limb bud mesenchymal cells (Onodera et al. 2005). On dynamically loaded unpatterned surfaces, most cells reorient such that their long axis is perpendicular to the prevailing strain direction (Wang et al. 2000; Kaunas et al. 2005). To force cells to adopt a specific morphology with respect to the applied strain, constraints have been applied via aligned microgrooves on elastomeric substrates produced with soft lithography (Wang et al. 2000; Wang et al. 2003). Using such methods, Kurpinski and co-workers showed that with dynamic tensile deformation applied in the microgroove direction, MSCs increased both proliferation and smooth

muscle marker gene expression, while decreasing chondrogenic matrix marker expression (Kurpinski et al. 2006). Interestingly, when strain was applied perpendicular to the cell axis, a different set of genes was activated and proliferation rates were no longer altered, suggesting that mechanosensing by MSCs is anisotropic (direction dependent).

Cells are inextricably linked to their extracellular environment via complex interpenetrating cytoskeletal networks (Wang et al. 1993; Chen et al. 1999). These networks provide a rapid and efficient means by which extracellular and intracellular perturbations can be transmitted to cell structures such as the nucleus (Maniotis et al. 1997; Dahl et al. 2008; Wang et al. 2009). Nuclear shape and deformation in turn correlate with gene expression changes. For example, when pre-osteoblastic cells are confined to specific micropatterned geometries, an ideal ratio of nuclear area to height promotes collagen gene expression (Thomas et al. 2002). In tissues and tissue-like engineered constructs, nuclear deformation is associated with changes in cellular biosynthetic activities (Guilak 1995; Knight et al. 2002). In chondrocytes, de-differentiation in monolayer culture is associated with an increase in nuclear spreading as the cell flattens. Recovery towards a round nucleus with cytochalasin D treatment restores cartilage specific gene expression (Hoshiba et al. 2008). Likewise, disruption of actin networks in embryoid body-derived cells promotes the chondrogenic phenotype (Zhang et al. 2006). Furthermore, the mechanical properties of the embryonic cell nucleus change as a function of differentiation status (Buxboim et al. ; Pajeroski et al. 2007), raising the intriguing possibility that physical cues (active and passive) will be

interpreted differently by the same cell, depending on which lineage is adopted, and how far along that lineage specification the cell has processed.

To begin addressing these questions in the context of nanofibrous scaffolds, here we investigated the impact of scaffold fiber organization and deformation on nuclear morphology in both adult human mesenchymal stem cells and differentiated fibrochondrocytes from the knee meniscus. We hypothesized that the degree of order within the extracellular microenvironment would provide a ‘set point’ for nuclear morphology, and that mechanical perturbation of the fibrous network would elicit further changes via nuclear realignment and deformation. We further queried the role of cytoskeletal elements in defining the baseline nuclear shape and transmitting external loads to the nucleus as a function of both time and loading direction. Our findings demonstrate an increased sensitivity of undifferentiated cells to the alignment of the nanofibrillar matrix, and implicate the actin cytoskeleton in transmission of exogenous forces.

## **9.2 MATERIALS AND METHODS**

### ***9.2.1 Scaffold Fabrication***

Nanofibrous meshes were created using a custom electrospinning apparatus, as described in previous chapters. Briefly, poly( $\epsilon$ -caprolactone) (80kDa, Sigma-Aldrich, St. Louis, MO) was dissolved to 14.3% w/v in a 1:1 solution of tetrahydrofuran and N,N-dimethylformamide (Fisher Chemical, Fairlawn, NJ). The solution was ejected from the spinneret at 2.5ml/h via syringe pump through an 18G stainless steel blunt-ended needle

charged to +13kV with a high voltage power supply (ES30N-5W, Gamma High Voltage Research, Inc., Ormond Beach, FL). Fibers were collected on a grounded mandrel over an air gap of 15cm. To create non-aligned (NA) meshes, lacking a preferred fiber direction, the mandrel was rotated slowly through the collection process (surface velocity 0.5m/sec). To form scaffolds with aligned (AL) nanofibers, the surface velocity was increased to 17.5m/s (Li et al. 2007). Fibers were collected for 4 hours to produce mats of ~0.7mm in thickness. From NA sheets, 60mm by 5mm wide strips were excised in a random orientation. AL samples of the same dimension were excised from fiber-aligned mats in either the predominant fiber direction or perpendicular to the fiber direction. To assess fiber organization, scaffolds were sputter coated with AuPd and visualized by scanning electron microscopy (SEM).

### ***9.2.2 Cell Isolation and Seeding***

Human mesenchymal stem cells (MSCs) and meniscal fibrochondrocytes were isolated from surgical waste tissue as in Chapter 7. MSCs were isolated from tibial or femoral bone marrow aspirates via plastic adherence in basal medium (BM: DMEM containing 1X Penicillin/Streptomycin/Fungizone and 10% Fetal Bovine Serum) as in Chapter 3. Resected meniscus tissue was finely minced and plated in BM. Resident fibrochondrocytes migrated out of the tissue and after one week, the tissue fragments were removed. Adherent cells formed colonies and were subsequently expanded to passage 4 at a ratio of 1:3 in BM.

Prior to cell seeding, nanofibrous strips were sterilized and rehydrated in increasing concentrations of ethanol (100%, 70%, 50%, 30%) and soaked in a 20 $\mu$ g/ml solution of human fibronectin for 16 hours to promote cell attachment. Each surface of the scaffold received a 200 $\mu$ l aliquot containing 60K cells (either MSCs or fibrochondrocytes) followed by 2 hours of incubation to allow for attachment. Cell-seeded scaffolds were cultured in a chemically-defined medium (Mauck et al. 2006) (CDM: high glucose DMEM with 1X PSF, 0.1 $\mu$ M dexamethasone, 50 $\mu$ g/mL ascorbate 2-phosphate, 40 $\mu$ g/mL L-proline, 100 $\mu$ g/mL sodium pyruvate, 6.25 $\mu$ g/ml Insulin, 6.25 $\mu$ g/ml Transferrin, 6.25ng/ml Selenous Acid, 1.25mg/ml Bovine Serum Albumin, and 5.35 $\mu$ g/ml Linoleic Acid) for 16h prior to scaffold deformation. Where indicated, media were further supplemented with 2.0mM acrylamide (AC, National Diagnostics, Atlanta, GA), 1.7 $\mu$ M nocodazole (NO, Sigma-Aldrich, St. Louis, MO), or 1.0nM cytochalasin D (CD, Sigma-Aldrich, St. Louis, MO) to disrupt intermediate filaments, microtubules, and actin filaments, respectively (Connolly 1985; Trickey et al. 2004). These values represent the minimum concentration that visibly disrupted the element without altering normal cell morphology (see below).

### **9.2.3 Mechanical Loading**

A custom tensile stretching device was developed to apply precise static deformations to cell-seeded nanofibrous scaffolds on the stage of an inverted fluorescent microscope (**Figure 9-1A,B**). The device consisted of a linear stage outfitted with a manual actuator/micrometer (Newport, Irvine, CA), two anodized aluminum braces, and removable polysulfone grips. To determine the relationship between applied

deformations with the device and surface strain on the scaffold, acellular aligned PCL strips were speckle coated with black enamel (Nerurkar et al. 2008) and mounted in the device. Tensile deformation of up to 10% grip-to-grip strain was applied in 2.5% increments with one minute of rest between steps; images were acquired before and after each step using a digital camera (A1021, Basler, Ahrensburg, Germany). Scaffold stress-relaxation behavior was characterized using an Instron 5542 mechanical test system (Instron, Canton, MA). Speckled samples were preloaded to 0.1N, ramped to 10% of the gauge length at 0.1%/s, and held for 2 hours. Texture correlation analysis of local deformation was performed on the central third of each scaffold using Vic2D (Correlated Solutions, Columbia, SC) as in (Nerurkar et al. 2008).

To image cell and nuclear deformation, cell seeded constructs were fitted into the tensile loading device and extended to 0, 5, or 10% grip-to-grip strain at 0.1%/s. Constructs were either fixed immediately in 4% paraformaldehyde, or were cultured in CDM for an extended duration in the stretched state (5min, 15min, 30min, 1 hour, or 2 hours) prior to fixation. To visualize nuclear and cytoskeletal morphologies, cells were permeabilized with Triton X-100 and stained with either anti-vimentin (Millipore, Billerica, MA) to visualize intermediate filaments, anti- $\alpha$ -tubulin mAb-Alexa488 (Invitrogen, Carlsbad, CA) to visualize microtubules, or phalloidin-Alexa488 (Invitrogen, Carlsbad, CA) to visualize actin, according to the manufacturers' instructions. Nuclei were labeled with 4',6- diamidino-2-phenylindole (DAPI). Images were obtained on a Nikon T30 inverted fluorescent microscope equipped with a CCD camera (Nikon Instruments, Inc., Melville, NY).

#### ***9.2.4 Quantification of Nuclear Morphology***

To quantify the nuclear aspect ratio (NAR) and the orientation angle of the nucleus, a custom code was developed in MATLAB (The Mathworks, Inc., Natick, MA). Briefly, grayscale images of DAPI-stained nuclei were thresholded and each nucleus was assigned a cluster identity. Each cluster of pixels representing a nucleus was subject to principal component analysis in order to determine its long and short axis and orientation. The NAR was defined as the ratio of the long axis to the short axes and the orientation angle was defined as the angle between the long axis of the nucleus and the direction of loading (**Figure 9-2C**).

#### ***9.2.5 Statistical Analysis***

Analysis of variance was performed using the statistical software package, SYSTAT (v10.2, Point Richmond, CA) with Bonferroni post-hoc tests used to make pair-wise comparisons. Significance was set at  $p \leq 0.05$ . Data are presented as mean  $\pm$  standard deviation.

### **9.3 RESULTS**

#### ***9.3.1 Mechanical Response of Nanofibrous Scaffolds to Static Tensile Deformation***

A system for applying static tensile deformation to nanofibrous scaffolds was designed and validated (**Figure 9-1A,B**). To ensure that local strains were macroscopically homogeneous and consistent with the applied strain, the relationship between applied and surface strain was determined using texture correlation. At all levels of applied strain, the

region of interest (central third) had a relatively homogenous strain distribution (**Figure 9-1C**). Applied strain also correlated well with average surface strain (**Figure 9-1D**,  $R^2=0.997$ ,  $p<0.001$ ), with a slope of 1.15. As some studies of cellular function were conducted over the course of several hours, the time-varying mechanical behavior of nanofibrous scaffolds under static deformation was assessed. Scaffolds were extended by 10% of their initial length and held for two hours (**Figure 9-1E**). The stress peaked with the applied strain and relaxed by ~30% over the ensuing 2 hours, with the greatest decrease in stress occurring in the first 3 minutes. Surface strains determined by texture correlation remained constant over the two hour period at 10%.

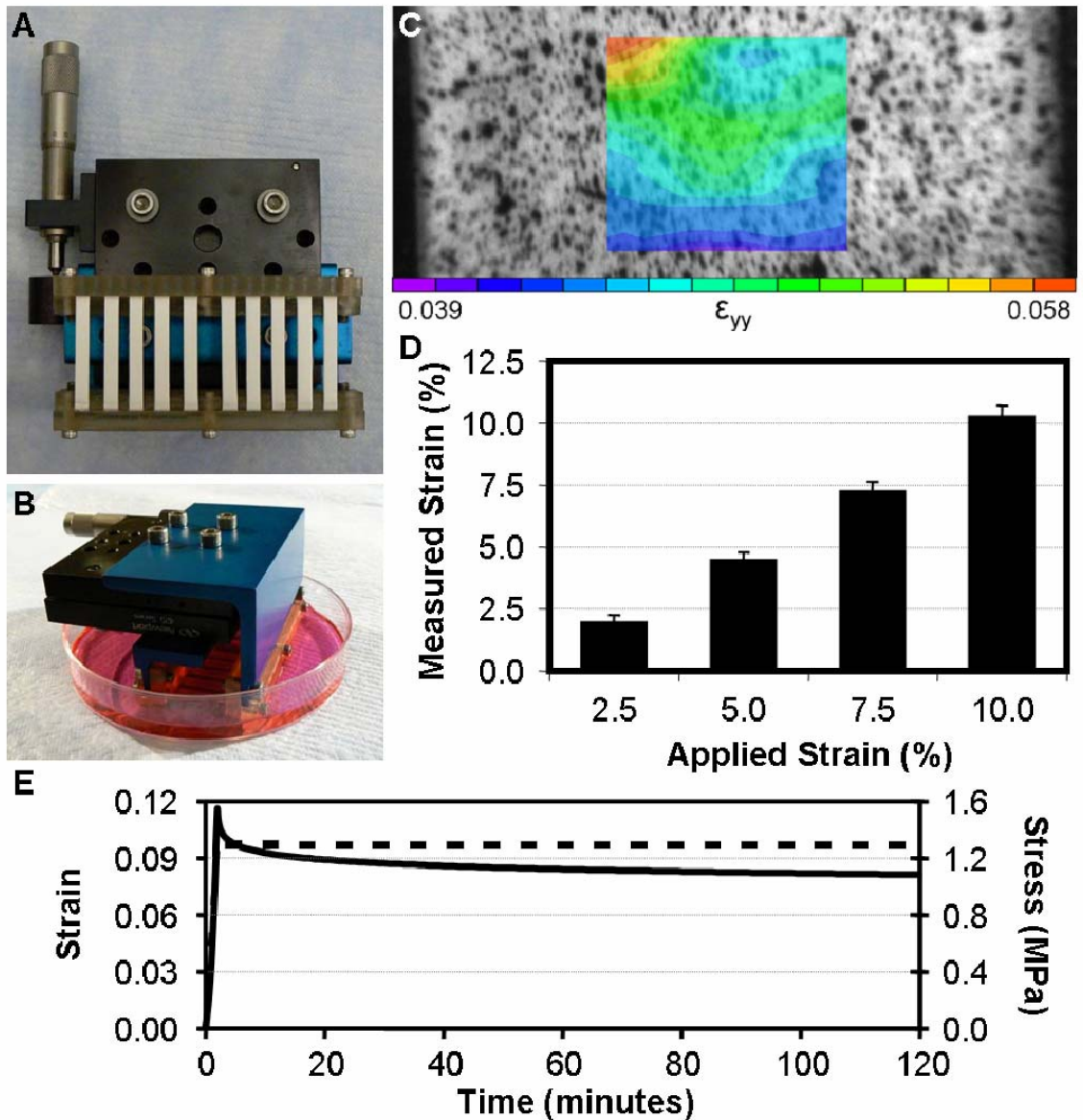


**Figure 9-1: Construction and validation of a custom system for prescribing controlled tensile deformation to cell-seeded nanofibrous scaffolds. A & B) Custom device for applying tension to constructs *in vitro*. C) Texture correlation of a speckled scaffold under 5% applied strain reveals surface strains that are relatively homogenous. D) Average surface strains correlate well with applied deformations (n=6). E) Representative stress (solid line) and strain (dashed line) response of an aligned nanofibrous scaffold held at 10% strain for 2 hours.**

### 9.3.2 Translation of Topographical and Mechanical Cues to Nuclear Deformation

SEM imaging of electrospun scaffolds confirmed the formation of randomly oriented non-aligned (Figure 9-2A), and highly aligned scaffold topographies (Figure 9-2B).

Cells seeded onto these distinct architectures adopted morphologies that reflected the underlying fiber topography. Cells on nonaligned scaffolds were well-spread, with actin-rich processes extending isotropically (**Figure 9-2D**). In contrast, cells on aligned scaffolds had fewer and larger processes, extending exclusively along the fiber direction (**Figure 9-2E**). While results are shown only for fibrochondrocytes (Fig. 2D, E), MSCs behaved similarly, as has been shown previously in Chapter 8.

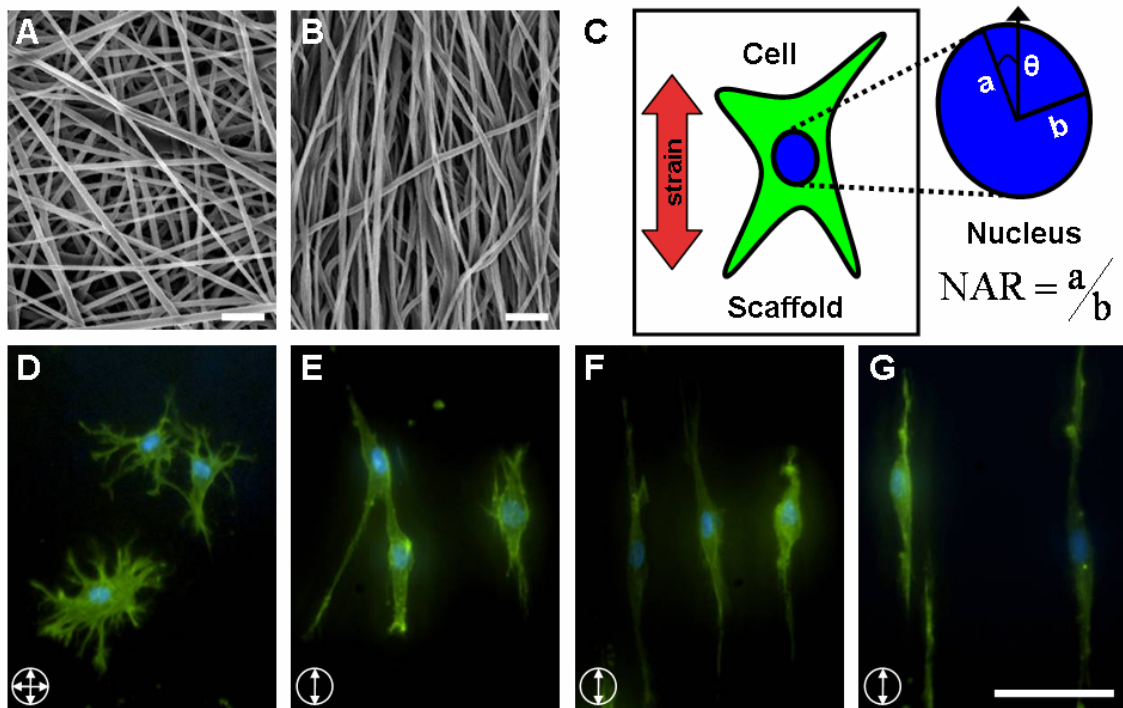


**Figure 9-2:** The organization of nanofibers dictates the initial morphology of seeded cells. SEM images of non-aligned (A) and aligned (B) PCL nanofibers (scale bar: 10 $\mu$ m). (C) To quantify subcellular morphologic changes, the nuclear aspect ratio (NAR) and orientation angle ( $\theta$ ) were quantified. The NAR was defined as the ratio of the long axis (a) to the short axis (b) of the nucleus and  $\theta$  was defined as the angle between the long axis (a) and the direction of stretch. Representative images of meniscal fibrochondrocytes seeded on NA (D) and AL (E) nanofibrous scaffolds, and AL constructs deformed to 5% (F) and 10% strain (G) (scale bar: 20  $\mu$ m). Cells were fluorescently labeled for F-actin (green) and DNA (blue).

The pronounced effect of scaffold architecture on cell morphology translated to quantifiable differences in nuclear geometry and organization. Changes in nuclear shape

were quantified by measurement of a nuclear aspect ratio (NAR) by normalizing the lengths of the long to short axes (**Figure 9-2C**). In monolayer culture on tissue culture plastic and on nonaligned nanofibrous scaffolds, the nuclei of MSCs were elliptical, possessing a NAR of  $\sim 1.5$  (**Figure 9-3A**). When the same cells were seeded on aligned scaffolds, the nuclei became more elongated in the fiber direction, increasing NAR to  $\sim 1.7$  ( $p < 0.001$ ). Compared to MSCs, fibrochondrocytes began with a lower NAR on nonaligned scaffolds [ $1.34 \pm 0.30$  vs.  $1.52 \pm 0.49$ ], and increased on aligned scaffolds, albeit to a much lesser extent than MSCs [ $1.41 \pm 0.32$  vs.  $1.71 \pm 0.44$ ] (**Figure 9-3B**). The angle between the direction of fiber alignment and the principal orientation of the nucleus was determined and binned into angular histograms (**Figure 9-3C,D**). As expected, the distribution of nuclear orientation on nonaligned scaffolds was random, with a mean angle of  $\sim 45^\circ$ . In contrast, cell nuclei on aligned scaffolds were parallel to the fiber direction (**Figure 9-3**). For both cell types, the majority of nuclei were aligned within  $\pm 25^\circ$  of the predominant fiber direction, with a mean angle of  $21^\circ$  and  $24^\circ$  for MSCs and fibrochondrocytes, respectively.

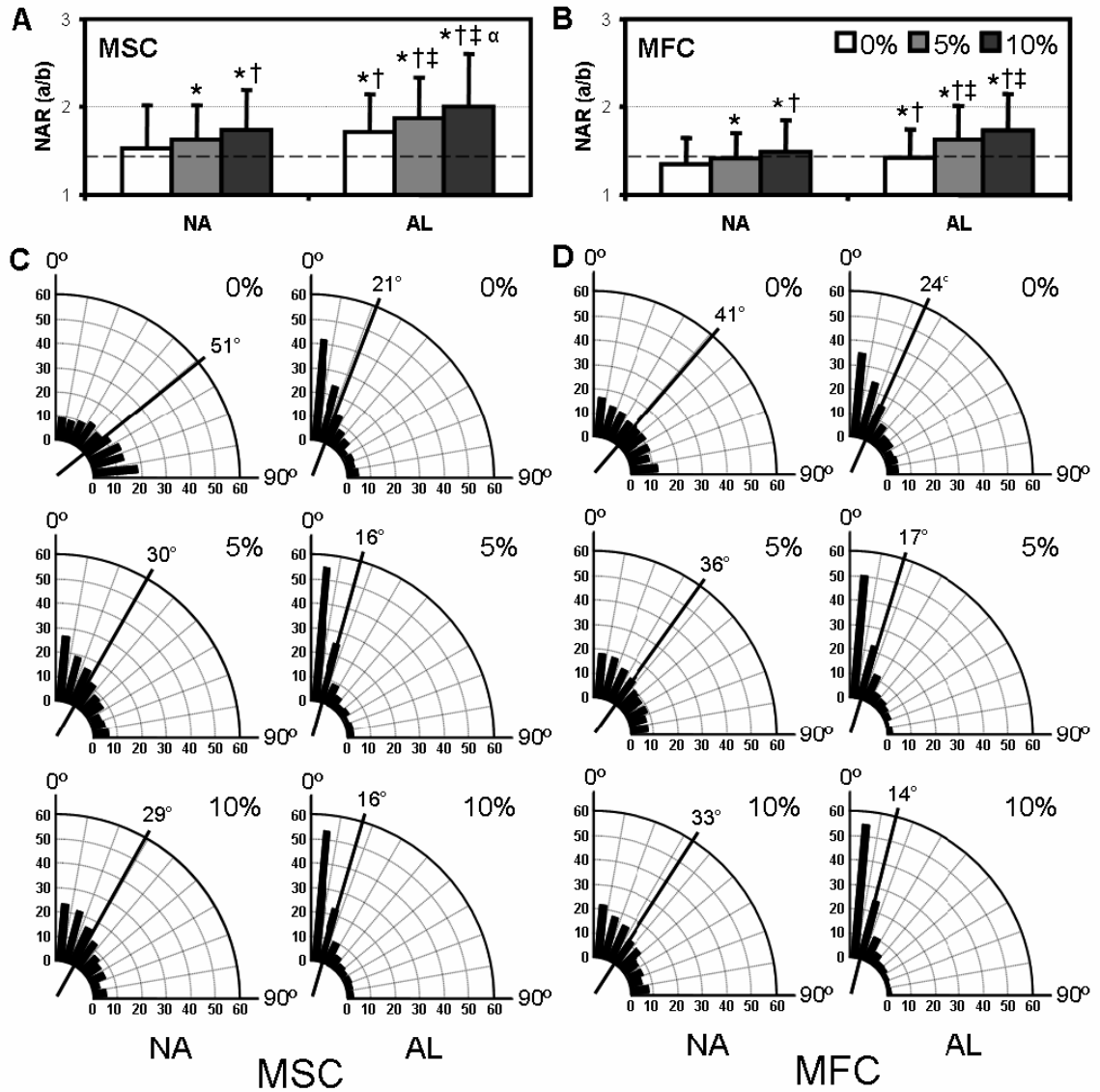


**Figure 9-3: Nuclear morphology and orientation are dependent upon scaffold architecture and applied strain.** NAR of MSC- (A) and fibrochondrocyte- (B) seeded NA and AL scaffolds with increasing levels of applied strain ( $n > 500$ , \*:  $p < 0.05$  vs. 0% NA, †:  $p < 0.05$  vs. 5% NA, ‡:  $p < 0.05$  vs. 0% AL, α:  $p < 0.05$  vs. 5% AL). Dashed lines indicate the NAR of the same cell populations cultured in monolayer. Angular histograms of nuclear orientation of MSC (C) and fibrochondrocyte (D) NA and AL constructs at 0, 5, or 10% strain. The radial axis indicates the percentage of the total cell population and the solid line represents the mean angle of the distribution.

Next, constructs were deformed by 5 or 10% of their initial length and immediately fixed to determine how deformation of the nanofibrous scaffold translated to cell and nuclear

deformation. Both cell types, which were already highly polarized on AL scaffolds, became further oriented and elongated with deformation along the direction of alignment (**Figure 9-2E-G**). On nonaligned scaffolds, both cell types lengthened to a lesser extent (not shown). Consistent with these changes in cell morphology with stretch, the nuclei of both cell types were sensitive to tensile deformation. On both nonaligned and aligned scaffolds, increasing levels of strain resulted in higher NARs, with this effect being more dramatic on aligned scaffolds. Furthermore, on both nonaligned and aligned scaffolds, tensile deformation induced nuclei to reorient in the direction of the applied load. For example, in MSC-seeded nonaligned constructs, a 10% deformation caused 30% more nuclei to align within  $\pm 20^\circ$  with respect to the direction of loading, shifting the mean angle of the population from  $51^\circ$  to  $29^\circ$ . While trends were similar between the two cell types, the NAR of fibrochondrocytes were consistently lower than MSCs. Furthermore, the NAR did not increase from 5 to 10% strain in aligned fibrochondrocyte seeded constructs, suggesting that these differentiated cells had reached a maximum in nuclear deformation.

### ***9.3.3 Temporal Changes in NAR and Orientation Angle***

While these experiments captured the instantaneous response of cells to mechanical perturbation of their underlying substrates, in many cell types, cell and nuclear shape changes are transient when the mechanical stimulus is held constant (Knight et al. 2002). To capture transient changes in nuclear deformation, fibrochondrocyte-seeded aligned scaffolds were stretched to 10% strain and incubated for increasing durations of time prior to fixation and imaging. As above, 10% strain resulted in an immediate 30%

increase in NAR relative to unstrained controls (**Figure 9-4A**). However, when the deformation was held constant, NAR decreased with time, despite no changes in scaffold deformation over this time course (**Figure 9-1E**). Notably, the NAR dropped markedly over the first 5 minutes before returning towards baseline values at a more gradual rate. After two hours, the NAR of cells on constructs strained to 10% were not different than unstrained controls ( $p=0.475$ ).

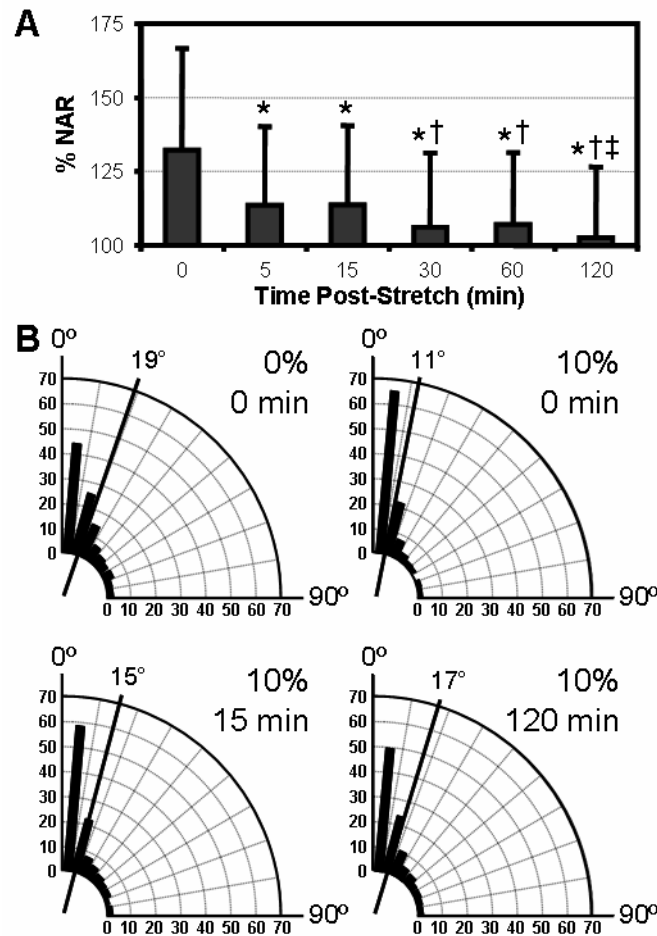


**Figure 9-4: Time dependent nuclear relaxation with static scaffold deformation.** A) The % change in NAR (relative to undeformed values) of fibrochondrocyte-seeded constructs at increasing time intervals after application of 10% strain ( $n>500$ , \*:  $p<0.05$  vs. 0min, †:  $p<0.05$  vs. 15min, ‡:  $p<0.05$  vs. 60min). B) Angular histograms of nuclear orientation prior to stretch, immediately after stretch, and after 15 or 120 minutes ( $n>500$ ).

Paralleling these temporal changes in NAR, nuclear orientation also relaxed during continuously applied static deformation (**Figure 9-4B**). Prior to strain, a large population of nuclei were already polarized as a consequence of the aligned fiber topography, translating to a mean angle of 19°. The application of 10% strain further oriented the population in the direction of load, as evidenced by an increase in the fraction of cells in the  $\pm 10^\circ$  bin and a mean angle of 11°. As the NAR decreased over the first 15 min, the nuclei also began to relax towards a wider distribution of orientation angles. The mean angle increased to 15° and the angular histogram revealed a profile intermediate to pre- and post-strain states. By 120 min, the angular profile and mean angle of the population mimicked closely the undeformed scenario.

#### ***9.3.4 Cytoskeletal Mediation of Nuclear Changes***

As demonstrated in the above studies, a deformation of the nanofibrous substrate translated through the cell to dynamic changes in the geometry and alignment of the nucleus. To investigate the role of the cytoskeleton in this nuclear deformation, actin microfilaments, microtubules, and intermediate filaments were perturbed. Fluorescent staining confirmed the presence of these subcellular structures in both MSCs and fibrochondrocytes on nanofibrous scaffolds (**Figure 9-5A-C**). Microtubules radiated outward from the center of the cell, and were highly aligned with the cell body (and direction of nanofiber alignment). Vimentin, an intermediate filament protein, did not span the entire cytoplasm, but rather was concentrated around the nucleus. Actin was present throughout the cytoplasm, forming dense stress fibers that were aligned with the long axis of the cell.

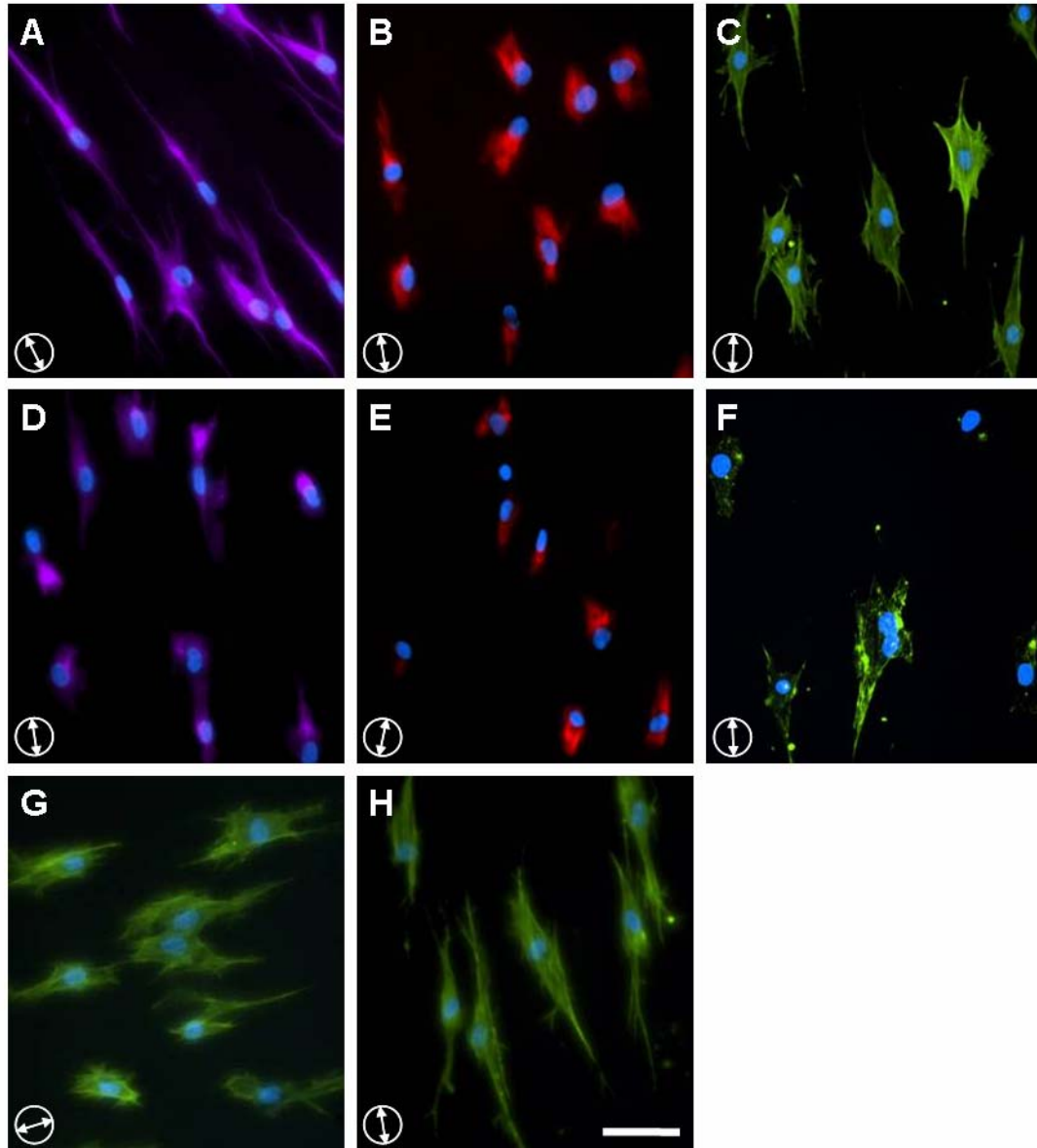


**Figure 9-5:** Selective disruption of cytoskeletal elements does not alter cell morphology on nanofibrous scaffolds. Fibrochondrocytes on AL scaffolds stained for microtubules (A, purple), intermediate filaments (B, red) and F-actin (C, green). Constructs were exposed to nocodazole (D), acrylamide (E), and cytochalasin D (F) to disrupt microtubule, intermediate filament, and F-actin networks, respectively. Additional samples were treated with nocodazole (G) or acrylamide (H) and stained with phalloidin to confirm the removal of these elements did not alter the actin cytoskeleton. All images were counterstained for cell nuclei (blue). Scale bar: 20  $\mu\text{m}$ .

To identify the cytoskeletal element responsible for the observed increase in NAR with scaffold deformation, microtubules, intermediate filaments, and filamentous actin were

depolymerized with nocodazole (NOC), acrylamide (ACR), and cytochalasin D (CYD), respectively (**Figure 9-5D-F**). In the presence of chemical inhibitors, the filamentous form of these biopolymers became less prevalent: microtubules became tightly localized to the nucleus, intermediate filament staining diminished in intensity and was completely absent in some cells, and actin stress fibers were reduced to short microfilaments visible as punctate staining. Disruption of the microtubule and intermediate filament networks did not influence the actin cytoskeleton or overall cell morphology (**Figure 9-4G,H**).

Next, the change in NAR with 10% strain was examined in nanofibrous constructs cultured in the presence of these cytoskeletal disruptors. The baseline NAR of aligned MSCs in control media prior to the application of strain was 1.7 (CTRL, **Figure 9-6A**). As before, 10% applied strain increased this value to 2.0. The same effect of strain was observed despite the disruption of microtubules and intermediate filaments (NOC and ACR, **Figure 9-6A**). However, the removal of actin completely abrogated this response – NAR did not change with scaffold deformation (CYD, **Figure 9-6A**). These same trends held for fibrochondrocyte-seeded constructs (**Figure 9-6B**). Interestingly, in the absence of applied strain, the NAR increased significantly in MSCs whose microtubules and intermediate filaments were disrupted, a behavior that was not observed in fibrochondrocytes treated similarly (**Figure 9-6**).

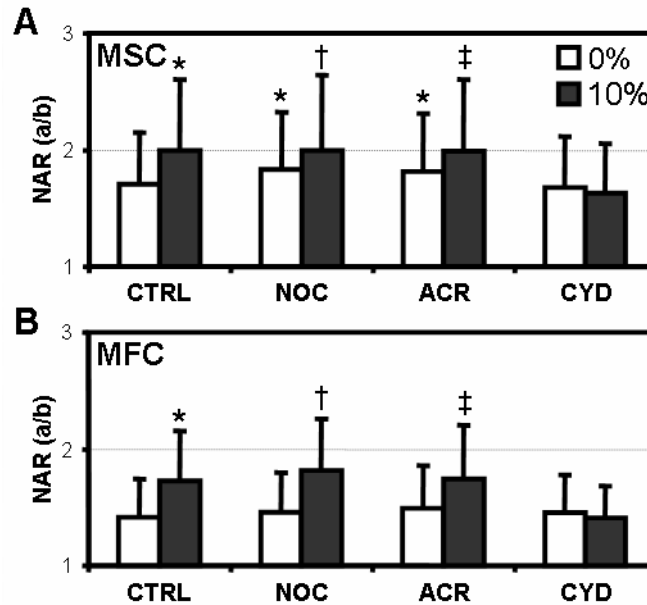


**Figure 9-6: Disruption of the actin cytoskeleton abrogates strain-induced alterations in NAR.** MSC- (A) and fibrochondrocyte- (B) seeded constructs were cultured in either control media (CT), or identical media supplemented with nocodazole (NO), acrylamide (AC) or cytochalasin D (CD) prior to the application of 10% strain ( $n > 500$ , \*:  $p < 0.05$  vs. 0% CT, †:  $p < 0.05$  vs. 0% NO, ‡:  $p < 0.05$  vs. 0% AC). NAR was determined immediately after loading.

### 9.3.5 Directional Control of NAR and Orientation Angle

To further elucidate the interplay between the scaffold topography and loading direction, cells on aligned nanofibrous scaffolds were stretched either parallel (//) or perpendicular ( $\perp$ ) to the fiber direction (**Figure 9-7A**). As in previous experiments, strain applied in the direction of the fibers increased the NAR and induced further alignment of nuclei (// CTRL, **Figure 9-7B,D**). Conversely, strain applied transverse to the fibers resulted in a minor but significant decrease in NAR, indicating that nuclei became rounder in shape ( $\perp$  CTRL, **Figure 9-7B**). Examining the magnitude rather than direction of change, an identical 10% strain applied // or  $\perp$  results in a 32% or 7% change in NAR, respectively. In contrast to // strains, angular histograms do not reveal marked reorientation of nuclei

under load ( $\perp$  CTRL, **Figure 9-7D**). In the presence of CYD, the strain-induced changes in NAR in either // or  $\perp$  directions were abrogated (// or  $\perp$  CYD, **Figure 9-7B**). Disruption of the actin cytoskeleton also prevented nuclei from reorienting with scaffold deformation in either direction, confirming the role of actin in not only transmitting mechanical forces to the nucleus, but also in dictating nuclear reorientation (**Figure 9-7D**). Further to these changes in NAR, the projected nuclear area was altered with respect to deformation. With // strain, nuclear area decreased, while in the presence of CYD no such response was evoked. With  $\perp$  strain, there was a small but significant increase in area under both control and CYD conditions.

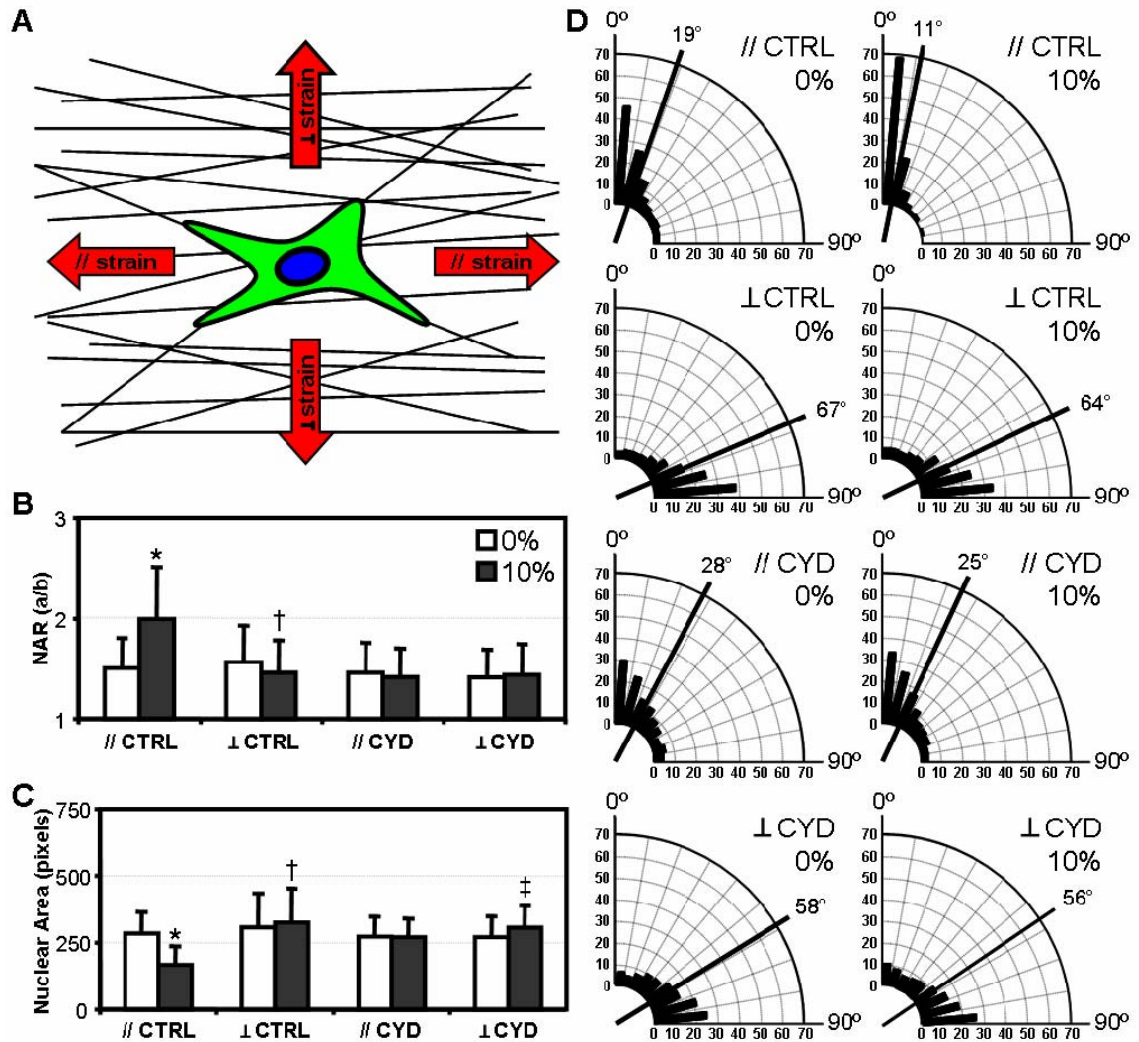


**Figure 9-7: Alterations in nuclear morphology are dependent on nanofiber stretch.** A) Schematic depicting strains applied parallel (//) and perpendicular (⊥) to the predominant fiber direction. Fibrochondrocyte-seeded constructs were loaded in either direction in the presence or absence of CD. NAR (B), nuclear area (C), and angular histograms (D) were acquired from DAPI-stained images and normalized to pre-strain values ( $n > 500$ , \*:  $p < 0.05$  vs. 0% //CT, †:  $p < 0.05$  vs. 0% ⊥CT, ‡:  $p < 0.05$  vs. ⊥CD).

## 9.4 DISCUSSION

A variety of cues presented by or transmitted through the cellular microenvironment regulate stem cell fate decisions. While the cell nucleus is the conventional center in which soluble second messengers are summed on a molecular basis, recent work has also suggested that the resting shape and deformation of the nucleus itself may directly alter

transcriptional events (Dahl et al. 2008). Indeed, precise control of nuclear shape via controlled micro-printed templates can regulate collagen expression in osteo-progenitor cells (Thomas et al. 2002). Our work with nanofibrous networks suggests that this nano-scale topography likewise alters cellular activity. For example, MSCs seeded on aligned scaffolds reduce chondrogenic, and increase fibrous marker expression, compared to traditional pellet cultures (Chapter 8). Moreover, dynamic tensile loading applied over long time periods increases expression of these same fibrous markers, and ultimately leads to more matrix production and enhanced mechanical function in engineered constructs (see Chapter 10). Based on these findings, the present study investigated how nuclear morphology is defined by nanofibrous networks of differing organization, and how this morphology changes when scaffolds are subjected to tensile deformations.

In this study, we evaluated how the nuclei of two cell types, MSCs and fibrochondrocytes respond to the presentation of differing nanofibrous topographies. These two cell types were chosen to represent an uncommitted progenitor cell population (MSCs), and a mature, differentiated cell population (fibrochondrocytes from the meniscus). Evaluation of nuclear aspect ratios (NARs) showed that simply presenting these cells with a nanofibrous topography altered nuclear shape; MSC nuclei on aligned scaffolds were more elongated (i.e., had a higher NAR) than on either non-aligned scaffolds or on tissue culture plastic (**Figure 9-3**). Notably, NAR for the differentiated fibrochondrocyte population changed only slightly with changing topography. It has recently been suggested that the quantity and quality of the MSC cytoskeleton (and so cell mechanical properties) are altered by substrate topography. Lim and coworkers showed that MSCs

are softer and contain less actin on nano-patterned tissue culture plastic (500nm gratings) compared to flat plastic (Yim et al.). In our work, fibrochondrocytes and MSCs were indistinguishable from one another on either aligned or non-aligned scaffolds, containing dense actin networks with clearly visible stress fibers (Chapter 8). As the cytoskeletal network is similar in both cell types, the observed difference in NAR may alternatively reflect changes in nuclear stiffness. While the nucleus is generally considered the stiffest element within the cell (Guilak et al. 2000), the intrinsic stiffness of the nucleus increases with differentiation, potentially due to changes in nuclear envelope protein type and amount (Pajeroski et al. 2007). Thus, the different nuclear morphology observed for MSCs compared to fibrochondrocytes may reflect the changing mechanical properties of the nucleus relative to the cytoskeletal network in which it is ensconced. Future studies will further query this possibility through direct mechanical testing of the MSC nucleus as it undergoes fibrochondrogenesis.

To investigate how exogenous deformation, superimposed on these base topographies, might further modulate nuclear shape, we developed a custom tensile loading device and validated transfer of strain to the scaffold surface (**Figure 9-1**). Increasing tensile deformation led to increases in NAR for each cell type (**Figure 9-3**). At each step (5% and 10%), NAR increased significantly for MSCs on both nonaligned and aligned scaffolds. Conversely, a significant increase was observed only for the first 5% strain step for fibrochondrocytes on aligned scaffolds. This may reflect a limit on nuclear deformation in these differentiated cells, potentially related to the maturity of the nuclear lamina (Dahl et al. 2004). Overall the findings above are consistent with those reported

by Stella and coworkers, who showed an increasing NAR in nonaligned polyurethane based nanofibrous scaffolds seeded with vascular smooth muscle cells and subjected to biaxial tensile stretch (Stella et al. 2008). In that study and the present one, nuclei were randomly oriented on nonaligned scaffolds, with a gradual alignment towards the stretch direction with increasing deformation, suggestive of fiber reorientation with load. In the present study, however, nuclei on aligned scaffolds were already highly aligned after seeding, and showed the most marked increase in NAR between 0% strain and 5% strain. This would suggest that there was an immediate engagement of fibers on these aligned scaffolds, with only slight reorientation needed to align the cells with the loading direction.

When subjected to a stretch and held in that configuration, NAR decayed to baseline levels with time, despite no time-dependent changes in the underlying scaffold (**Figure 9-4**). Indeed, the greatest decrease occurred over the first five minutes, with a steady decline to baseline levels over the next two hours. This suggests, interestingly, that cells respond to static deformation by reestablishing their homeostatic nuclear configuration within minutes. Whether this return to baseline results from reorganization of the cytoskeleton that engendered the original perturbation in NAR, or whether the relaxation was a purely viscoelastic phenomenon (Guilak et al. 2000), is not yet known. For example, Putnam and coworkers showed a rapid increase in assembly of the microtubule network within 15 minutes of 10% static stretch of cells on an unpatterned elastomeric sheet (Putnam et al. 2003). Regardless of mechanism, these findings suggest temporal limitations of static loading as a strategy for enhancing long term ECM deposition or

differentiation in engineered tissues if sustained nuclear deformation is required for these processes to occur.

Translation of scaffold deformation through the cell to nuclear deformation is mediated by the cytoskeletal network (Wang et al. 2009). To determine which component of this network was operative in sensing topography and responding to applied deformation, selective disruption of actin, microtubule, and intermediate filament networks was carried out (**Figure 9-5**). Disruption of actin filaments blocked all NAR changes with stretch in the fiber or transverse directions, while disruption of microtubules and intermediate filaments had no effect on NAR with stretch (**Figure 9-6**). This finding suggests that the primary mediator of nuclear deformation on nanofibrous scaffolds is the actin network. Interestingly, blockade of both the microtubule and intermediate filament networks in the undeformed state led to a small but significant increase in NAR in MSCs. This may suggest that these two elements act to restrain the otherwise compressive action of the dense actin fibers that surround the nucleus and traverse the cell in the long axis. This is consistent with previous reports that the intermediate filament network is tightly coupled with the nucleus, determined by micromanipulation of cytoskeletal elements within a single cell (Maniotis et al. 1997). Perturbations of the intermediate filament and microtubule network did not alter the nuclear morphology in fibrochondrocytes, again suggesting that the differentiated nucleus may be better able to resist deformation.

In each of the studies above, 10% elongation of aligned scaffolds in the fiber direction produced increases in NAR of ~30%. Conversely, when the same magnitude of strain

was applied transverse to prevailing fiber direction, NAR decreased while nuclear area increased (**Figure 9-7**). This disparate behavior between 10% strain in the fiber and perpendicular directions may be a consequence of scaffold mechanics (Nerurkar et al. 2006): loading in the fiber direction induces large lateral contractions (large Poisson's ratio), such that uniaxial extension along the fiber direction simultaneously extends the long axis of the nucleus and compresses the short axis. On the other hand, lateral contractions are very small under transverse extension, so that the cells are not subject to these compressive deformations. Indeed, under these conditions there is a small, but significant decrease in NAR, suggesting that cells spread over multiple fibers may rebound as prestress from the actin cytoskeleton is partially relieved. This observation may also explain the differential expression patterns observed in MSCs on micro-grooved surfaces when stretched along and transverse to the groove (and cell) direction (Kurpinski et al. 2006). These findings suggest that substrate architecture alters the transmission of external forces inward, differentially altering nuclear shape, indicating a clear coupling of topographic and with mechanical cues.

## **9.5 CONCLUSIONS**

Taken together, these findings demonstrate that mechanical deformation of aligned nanofibrous scaffolds translates directly to cellular and sub-cellular changes in seeded MSCs and fibrochondrocytes. These alterations, particularly those of the nucleus, are time-dependent and mediated by the actin cytoskeleton. Furthermore, differences of nuclear morphology in response to mechanical load and presented topography support the idea of a more pliable nucleus in undifferentiated compared to differentiated cells. These

data provide additional insight into potential biophysical mechanisms that may be optimized to improve fibrous tissue maturation through tailored mechanical loading regimens, as well as exploitable cues for defining and enforcing stem cell fate.

# ***CHAPTER 10: DYNAMIC TENSILE LOADING IMPROVES THE FUNCTIONAL PROPERTIES OF MSC-LADEN NANOFIBER-BASED FIBROCARILAGE***

## **10.1 INTRODUCTION**

The meniscus is a dense fibrocartilaginous tissue that plays a crucial role in normal knee function (Messner et al. 1998; Greis et al. 2002). These semi-lunar wedges, situated between the femoral condyles and tibial plateau, function to transfer and absorb loads by redirecting vertical forces laterally, efficiently converting compressive into tensile loads via a hoop-stress mechanism (Shrive et al. 1978). These forces are borne by a highly organized extracellular matrix (ECM) composed of circumferentially-oriented collagen bundles which form the bulk of the tissue and instill mechanical anisotropy, a characteristic vital to the function of the tissue (Fithian et al. 1990; Petersen et al. 1998; Setton et al. 1999). Compositionally, collagens make up 85-95% of the tissue (Eyre et al. 1983; McDevitt et al. 1990), while proteoglycans, comprising 2-3% of the dry weight, are concentrated in the more cartilage-like inner region and contribute to the compressive properties of the tissue (O'Connor 1976; Adams et al. 1992). With normal physiologic loading, forces several times body weight arise within the knee (Seedhom 1976; Ahmed et al. 1983). Given the high tensile stiffness in the circumferential direction (65-80MPa) (Bursac et al. 2009), the menisci transmit 50-100% of these forces with strains of only to 2-6% (Jones et al. 1996; Richards et al. 2003).

While the meniscus functions well with normal use, damage may occur as a result of traumatic events and/or age-related degenerative processes (MacAusland 1931; Cravener et al. 1941). Meniscal damage frequently manifests in the form of tears that disrupt the circumferentially-aligned collagen fiber architecture, thereby abrogating normal mechanical function, increasing stresses on the adjacent articular surfaces, and initiating osteoarthritic sequelae in the joint (Rath et al. 2000; Greis et al. 2002). The current standard of treatment for such tears is resection of the damaged portion of the tissue through partial or total meniscectomy, a procedure that fails to restore normal mechanics in the knee and predisposes the patient to precocious osteoarthritic changes (Englund et al. 2003; Meredith et al. 2005). Thus, there exists considerable clinical demand for a repair strategy that restores meniscal function and protects against further deleterious changes in the joint.

With the eventual goal of replacing damaged meniscus with engineered fibrocartilage that has structural, mechanical, and biochemical features similar to the healthy native tissue, this thesis has focused on the use of aligned nanofibrous scaffolds. These scaffolds are formed by the electrospinning process, wherein a polymer solution is drawn into fiber form through a voltage gradient and collected layer-by-layer on a grounded surface (Deitzel et al. 2001). With focused deposition onto a rotating mandrel, this simple electrostatic process produces three-dimensional scaffolds composed of aligned polymer fibers with tunable mechanical and structural anisotropy (Ayres et al. 2006; Courtney et al. 2006; Li et al. 2007). Beyond mimicking the microstructural features and length scales of natural collagenous ECMs, aligned nanofibrous scaffolds recapitulate the

mechanical behavior and structural organization of anisotropic fiber-reinforced soft tissues such as the meniscus (Mauck et al. 2009). Most importantly, these scaffolds serve as an instructive three-dimensional micropattern for directed cell-mediated collagen-rich ECM deposition. On poly( $\epsilon$ -caprolactone) (PCL) nanofibrous scaffolds, numerous cell types will align, deposit ordered collagen, and increase construct tensile properties in the direction of nanofiber alignment, as shown in Chapter 3. Conversely, when seeded on randomly-oriented nanofibers, cellular orientation and matrix deposition is disorganized and so the resulting changes in mechanical properties are marginal.

Mesenchymal stem cells (MSCs) are a cell type especially amenable to instruction from a nanofibrous microenvironment. MSCs are a self-renewing population of multipotent cells under widespread investigation for applications in regenerative medicine (Caplan 1991; Caplan 2005), and in particular, we have explored their utility as a cell source for engineering fibrocartilaginous tissues such as the knee meniscus as well as the annulus fibrosus of the intervertebral disc (Nerurkar et al. 2009). These cells may be directed along numerous tissue-specific lineages by modulation of their chemical, mechanical, and topographical environment (Discher et al. 2009; Guilak et al. 2009). On nanofibrous scaffolds in the presence of TGF- $\beta$ 3, MSCs adopt an elongated morphology and express fibrous over chondrogenic markers in a chemical environment permissive to both phenotypes (Chapter 8). Studies described in Chapter 3 conducted in static, free-swelling conditions showed that MSCs synthesize organized fibrocartilaginous ECM on aligned nanofibrous scaffolds, leading to increases in the tensile modulus of cell-scaffold constructs. However, even with long term culture (100 days), endpoint tensile properties

reached a maximum of 30MPa, a value below native meniscus tissue by two-fold or more (see Future Directions). While results from these studies indicate MSCs in conjunction with aligned nanofibrous scaffolds hold promise for engineering anisotropic fibrocartilage, free-swelling culture does not provide sufficient stimuli to drive tissue formation towards functional equivalence with the native meniscus.

Load transmission is not only the chief function of musculoskeletal tissues, but also a driving force vital to their development and homeostatic maintenance (Carter 1987). For instance, the absence of forces in avian hind limbs inhibited the normal patterning and formation of tendons (Kardon 1998). In forming synovial joints, contracting peripheral musculature plays a fundamental role in progenitor cell fate commitment and subsequent joint cavitation and morphogenesis (Kahn et al. 2009). In specific regards to the meniscus, while the early stages of meniscal formation proceed normally in the developing knees of immobilized chick embryos, these tissues ultimately fail to mature and are eventually resorbed in the absence of load transmission (Mikic et al. 2000). Based on these observations, there has been much interest in recapitulating physiologic forces *in vitro* towards spurring the development of engineered musculoskeletal tissues (Butler et al. 2000). Cyclic compression of cartilage constructs enhances mechanical and biochemical outcomes (Mauck et al. 2000) and repeated tensile loading promotes matrix gene expression, deposition, and tissue maturation for tendon and ligament applications (Garvin et al. 2003; Juncosa-Melvin et al. 2006). Notably, Lee and coworkers performed short-term stretching (three days) of ligament fibroblasts on thin layers of aligned nanofibers, detecting an increase in collagen production with loading

that was sensitive to cellular orientation (Lee et al. 2005). Towards enhancing the formation of MSC-based tissues, reports indicate that cyclic compression of hydrogel constructs reinforces MSC chondrogenesis (Huang et al. 2004; Mauck et al. 2007; Mouw et al. 2007), and cyclic tension of fibrin gels upregulates fibrous gene expression (Connelly et al.). Taken together, these studies demonstrate that dynamic loading representative of physiologic loading can drive MSC differentiation, modulate biosynthetic activity, and lead to the production of engineered replacement tissues that better approximate their native counterparts.

Based on these findings and the relationship between applied deformations of scaffolds and resulting strains in cells explored in Chapter 9, the current study examines the effects of dynamic tensile loading on MSC-seeded aligned nanofibrous scaffolds. After establishing a fibrochondrogenic population of aligned MSCs, we hypothesized that tensile stimulation would upregulate fibrous markers representative of fibrocartilage, increase the production of collagenous ECM, and as a result, improve the functional properties of constructs. Towards this end, a bioreactor system was designed and validated for dynamic loading of nanofibrous constructs during *in vitro* culture. The effects of cyclic tension on the long-term maturation of MSC-seeded aligned nanofibrous scaffolds was examined, with transcriptional, biochemical, and mechanical changes examined over four weeks of cyclic loading.

## 10.2 MATERIALS AND METHODS

### 10.2.1 Scaffold Fabrication

For bioreactor validation and cell-seeded studies, separate aligned, nanofibrous meshes were produced via electrospinning as described previously. Briefly, a 14.3% w/v solution of poly( $\epsilon$ -caprolactone) (PCL) (80kD, Sigma-Aldrich, St. Louis, MO) was dissolved in a 1:1 solution of tetrahydrofuran and N,N-dimethylformamide (Fisher Chemical, Fairlawn, NJ). This solution was supplied to the spinneret tip at a rate of 2ml/h via syringe pump (KDS100, KD Scientific, Holliston, MA). A power supply (ES30N-5W, Gamma High Voltage Research, Ormond Beach, FL) was used to apply a +10kV potential difference between the spinneret and the aluminum mandrel ( $\text{\O} = 2''$ ). Aluminum shields were charged to +5kV to aid in directing the transiting electrospun fibers towards the mandrel, which was charged to -3kV. To induce fiber alignment, the mandrel was rotated via a belt mechanism conjoined to an AC motor (Pacesetter 34R, Bodine Electric, Chicago, IL) to achieve a linear surface velocity of  $\sim 10\text{m/s}$ . Nanofibers were collected over a spinneret-mandrel distance of 15cm for 4h, resulting in mats of approximately 600 $\mu\text{m}$  thickness.

### 10.2.2 Cyclic Tension Bioreactor

A custom bioreactor was designed and constructed for applying cyclic sinusoidal deformations to cell-seeded nanofibrous scaffolds during *in vitro* culture (**Figure 10-1**). The device is founded on a stepper motor linked to a bi-directional lead screw which drives the opposing motion of two sliding carriages (BiSlide, Velmex, Bloomfield, NY). Prior to tensile loading, samples were mounted and cultured in custom polysulfone

fixtures (**Figure 10-1**). These autoclavable and chemically-inert sample grips engaged the sliding carriages via anodized aluminum mounting arms, and additionally served to maintain the positioning of samples during rest periods. This modular design enables ready insertion, loading, and removal of sets of samples, allowing multiple experimental groups to be loaded daily. To maintain sterility, the entire assembly was covered by an acrylic lid which also provided a means for sample visualization during loading. Heat generated by the stepper motor was removed from the incubator via a coolant-circulating heat sink (Koolance, Auburn, WA). Motion of the stepper motor was defined via control software (COSMOS, Velmex) to execute a variety of waveforms with a resolution of 6.4 $\mu$ m (defined by a single step of the motor). The maximum carriage velocity was 38mm/s and sample lengths were maintained at 48mm, translating to a maximum strain rate of 160%  $\epsilon$ /s given the linked and opposite translations of the two carriages. In this work, the device was programmed to approximate sinusoidal waveforms equating to 6% strain amplitude at a frequency of 1Hz.

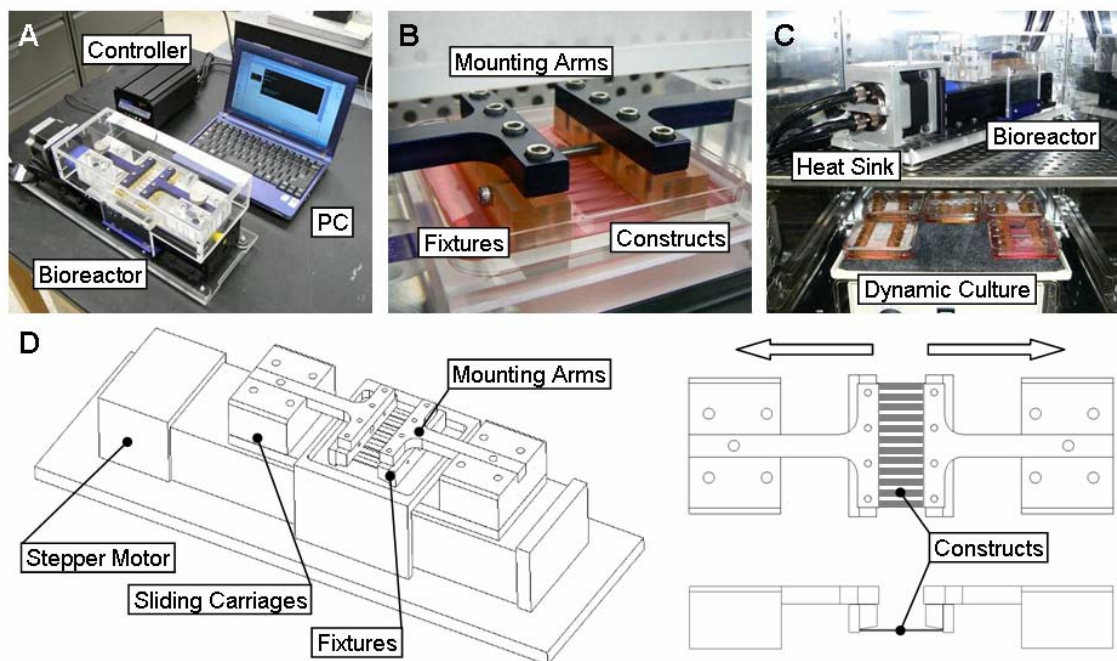


**Figure 10-1: Tensile bioreactor design. (A)** The device consists of a computer programmable stepper motor which drives the opposing motion of two linear stages. **(B)** These stages are linked to mounting arms designed to engage and distract fixtures containing multiple cell-seeded scaffolds. **(C)** A heat sink is placed on the motor to remove excess heat during operation in a standard incubator. When not loaded, samples are cultured dynamically on an orbital shaker to ensure even nutrient distribution to arrays of clamped constructs. **(D)** Schematics of the tensile bioreactor and fixture assembly.

### *10.2.3 Bioreactor Validation and Fatigue Testing*

Prior to dynamically loading cell-seeded scaffolds, programmed carriage motions were confirmed to translate to accurate and repeatable deformations of nanofibrous scaffolds. Acellular scaffolds (5×60mm) were airbrushed with black enamel to generate surface texture and placed within the bioreactor. Loading was initiated and images of the central third of each specimen were captured for subsequent texture-correlation analysis via Vic2D to determine two-dimensional Lagrangian strain (Correlation Solutions, Columbia, SC). With an applied deformation to sub-yield strains, aligned nanofibrous scaffolds develop non-recoverable slack causing the sample to move out of the plane of

focus. Therefore, samples were prestrained to 1%, and then cyclically loaded an additional 5% up to 1000 cycles. In additional studies, acellular scaffolds were loaded to 6% strain for either 108,000 or 216,000 cycles in PBS, a number of cycles equivalent to that seen in cell-seeded constructs.

#### ***10.2.4 Cell Isolation, Expansion, and Seeding***

Mesenchymal stem cells (MSCs) were isolated from tibial and femoral bone marrow of two 3-6 month old calves (Research 87, Boylston, MA) as described in (Mauck et al. 2006). Briefly, marrow was freed from the trabecular spaces via agitation in DMEM supplemented with 300units/ml heparin. After centrifugation for 5 minutes at 500g, the pelleted matter was resuspended in DMEM containing 1X Penicillin/Streptomycin/Fungizone and 10% Fetal Bovine Serum and plated in 150mm tissue culture dishes. Adherent cells formed numerous colonies through the first week, and were subsequently expanded through passage 2 at a ratio of 1:3.

Scaffolds (60×5mm, with the long axis oriented in the direction of nanofiber alignment) were sterilized and rehydrated in decreasing concentrations of ethanol (100, 70, 50, 30%; 30 minutes/step), concluding with two washes in PBS. A 100µl aliquot containing 1M MSCs was loaded onto each side of the scaffold followed by one hour of incubation to allow for cell attachment. Following seeding, cell-scaffold constructs were cultured individually in custom troughs (to accommodate the large sample length) for 6 weeks in chemically-defined medium (high glucose DMEM with 1X Penicillin/Streptomycin/Fungizone, 0.1µM dexamethasone, 50µg/mL ascorbate 2-

phosphate, 40 $\mu$ g/mL L-proline, 100 $\mu$ g/mL sodium pyruvate, 6.25 $\mu$ g/ml insulin, 6.25 $\mu$ g/ml transferrin, 6.25ng/ml selenous acid, 1.25mg/ml bovine serum albumin, and 5.35 $\mu$ g/ml linoleic acid containing 10ng/mL TGF- $\beta$ 3).

### ***10.2.5 Tensile Loading***

After this initial six week preculture period, constructs were transferred to fixtures for long-term dynamic mechanical stimulation. Each day, constructs were mounted into the bioreactor and cyclically loaded to 6% strain at a frequency of 1Hz for 3 hours. During rest periods, construct assemblies were placed on an orbital shaker to ensure even nutrient distribution to all samples. To serve as nonloaded controls, an additional set of constructs were clamped in identical fixtures and maintained for the duration of the study on the orbital shaker. Media changes occurred every two days.

### ***10.2.6 Mechanical Testing***

Acellular scaffolds from fatigue loading and cell-seeded constructs were mechanically tested through uniaxial extension to failure to determine tensile properties. Prior to testing, cross-sectional area was determined at four locations along the length of each sample with a custom laser-LVDT measurement system (Peltz et al. 2009). Testing was performed with an Instron 5848 Microtester (Instron, Canton, MA). After a 0.1N preload for 60 seconds to remove slack, gauge length was noted, and samples were extended to failure at a rate of 0.1% of the gauge length per second. Stiffness was determined over a 1% strain range from the linear region of the force-elongation curve with a custom MATLAB script. Using the cross-sectional area and gauge length, Young's modulus was

calculated from the analogous stress-strain curve. Gauge lengths were maintained across groups and time points, to enable the comparison of stiffness amongst samples.

### ***10.2.7 Biochemical and Gene Expression Analyses***

After mechanical testing, samples were stored at -20°C until processing to determine biochemical composition. Samples were digested in papain as in (Mauck et al. 2006) and assayed for DNA, sulfated glycosaminoglycan (s-GAG), and collagen content using the Picogreen double-stranded DNA (dsDNA) (Molecular Probes, Eugene, OR), DMMB dye-binding (Farndale et al. 1986), and orthohydroxyproline (Stegemann et al. 1967) assays, respectively. Hydroxyproline content was converted to collagen as in (Neuman et al. 1950), using a factor of 7.14.

An additional portion of each construct was finely minced and homogenized in TRIZOL (Invitrogen, Carlsbad, CA). Total RNA was extracted in phenol/chloroform and reverse transcribed as in (Huang et al. 2009). Real-time PCR was carried out with intron-spanning primers for type I and II collagen, fibronectin, lysyl oxidase, and glyceraldehyde 3-phosphate dehydrogenase (GAPDH). Starting quantities of target transcripts were determined by the standard curve method and normalized to GAPDH levels determined similarly.

### ***10.2.8 Statistical Analysis***

Analysis of variance were carried out with SYSTAT (v10.2, Point Richmond, CA) with Bonferroni post-hoc tests used to make pair-wise comparisons between groups.

Significance was set at  $p \leq 0.05$ . All data are presented as the mean  $\pm$  the standard deviation.

### **10.3 RESULTS**

#### ***10.3.1 Bioreactor Validation and Fatigue Loading***

A bioreactor was designed and constructed to apply sinusoidal tensile deformations to nanofibrous constructs *in vitro* (**Figure 10-1**). In validation studies, speckle-coated acellular scaffolds were mounted in the bioreactor, pre-strained to 1%, and cyclically loaded by an additional 5% strain at a frequency of 1Hz. Average surface strains, measured via texture correlation, approximated a sinusoidal waveform and consistently achieved the target strain of 6% over 1000 cycles (**Figure 10-2A**). Surface strains across the central portion of each scaffold were relatively homogeneous during both early and late loading cycles (**Figure 10-2B**).

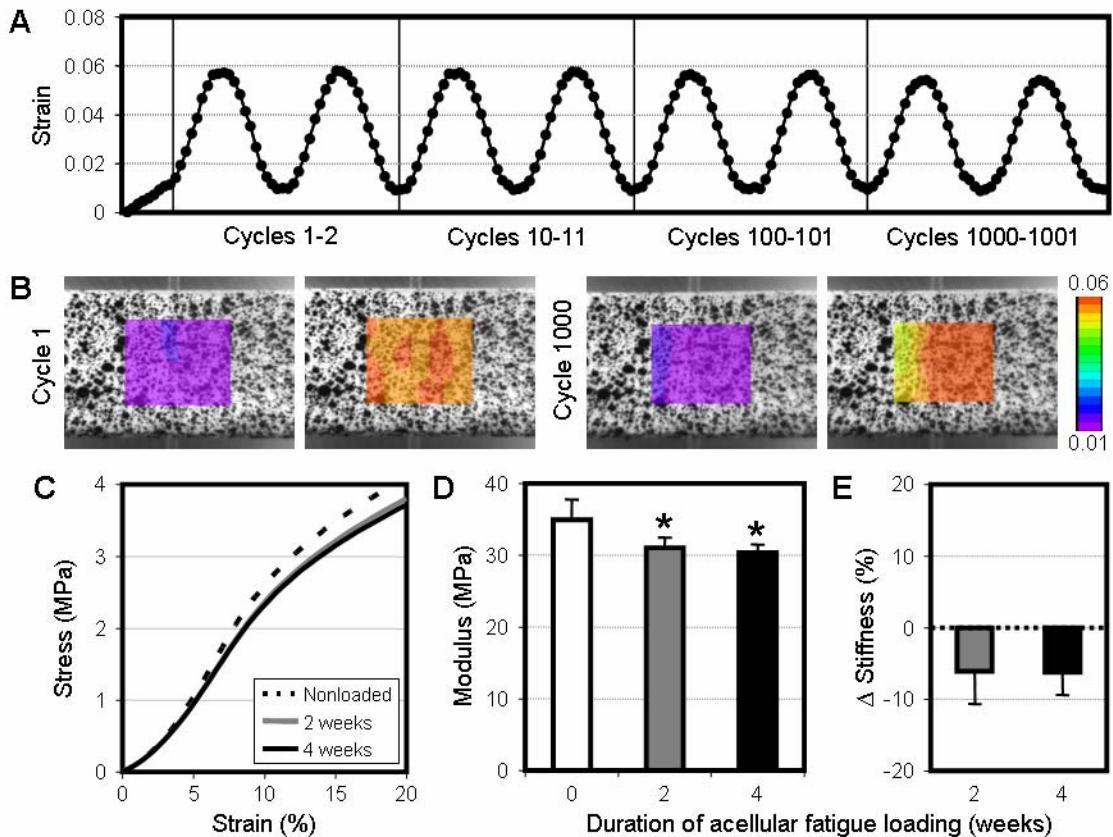


**Figure 10-2: Bioreactor validation and fatigue testing of acellular scaffolds. (A) Average surface strains determined by texture correlation of acellular scaffolds preloaded to 1% strain and cyclically loaded to 6% strain at 0.1Hz. Average stress-strain curves (B), tensile modulus (C), and percentage change in stiffness (normalized to nonloaded scaffolds) (D) after two weeks (108,000 cycles) or four weeks (216,000 cycles) of loading to 6% strain at 1Hz (n=6, \*: p<0.05 vs. nonloaded samples).**

To examine the effect of repeated deformations on scaffold mechanical properties, acellular scaffolds were cyclically loaded for either 108,000 or 216,000 cycles, equivalent to the number of loading events encountered by cell-seeded constructs with loading at 1Hz for 3 hours per day over a two or four week period. After 108,000 cycles, the tensile stress response of scaffolds decreased slightly, particularly at higher strains (5-10% region, **Figure 10-2C**), with this translating to an 11% decrease tensile modulus (p<0.01, **Figure 10-2D**). Normalizing to the stiffness of nonloaded controls, the equivalent of two weeks of

loading led to a 6% decrease in stiffness ( $p < 0.01$ , **Figure 10-2E**). An additional 108,000 cycles did not elicit further changes in the stress-strain response ( $p = 1.0$ ), suggesting that after these initial decreases, additional loading did not further compromise acellular scaffold mechanical properties.

### 10.3.2 Construct Preculture and Effect of Dynamic Culture Conditions

Fiber-aligned nanofibrous scaffolds were seeded with mesenchymal stem cells (MSCs) and precultured for a period of six weeks, after which samples were either loaded daily for an additional two or four weeks or maintained as nonloaded controls (**Figure 10-3**). During the preculture period, constructs were cultured individually under static conditions where the media remained unperturbed. Under these conditions, MSCs colonized scaffolds and simultaneously elaborated a functional fibrocartilaginous matrix, consistent with observations in Chapter 3. The production of collagen and proteoglycans, key matrix constituents of fibrocartilage, was evident from biochemical assays (**Figure 10-4B,C**) and by histologic staining (**Figure 10-5**).

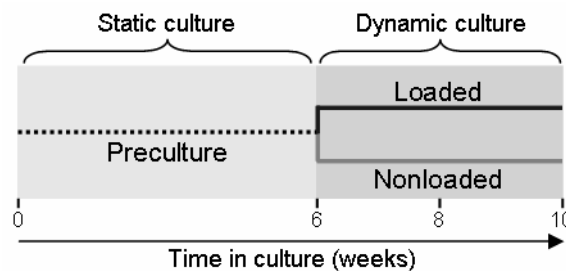


**Figure 10-3: Study design.** Aligned nanofibrous scaffolds were seeded with MSCs and precultured for an initial six week period under static culture conditions. Following this, samples were either loaded daily or maintained as nonloaded controls for up to an additional four weeks. Constructs were harvested at weeks 6, 8, and 10 for analysis.

After the initial six week preculture period, all remaining constructs were placed in fixtures designed to interface with the bioreactor and cultured upon an orbital shaker to ensure even nutrient distribution across samples. With two weeks of culture under dynamic media conditions, a marked loss in proteoglycan content of both loaded and nonloaded constructs was evident, with nearly a 50% reduction in GAG content (**Figure 10-4C**). Following this initial decline, nonloaded controls continued to lose proteoglycans ( $p < 0.001$  vs. week 8), while loaded constructs reached a steady state ( $p = 1.0$  vs. week 8). This proteoglycan loss was readily apparent when comparing cross-sections of precultured and week 10 constructs stained for proteoglycans (**Figure 10-5**). Dynamic culture did not adversely impact collagen content, as both loaded and nonloaded constructs continued to accrue collagen after the preculture period (**Figure 10-4B**).

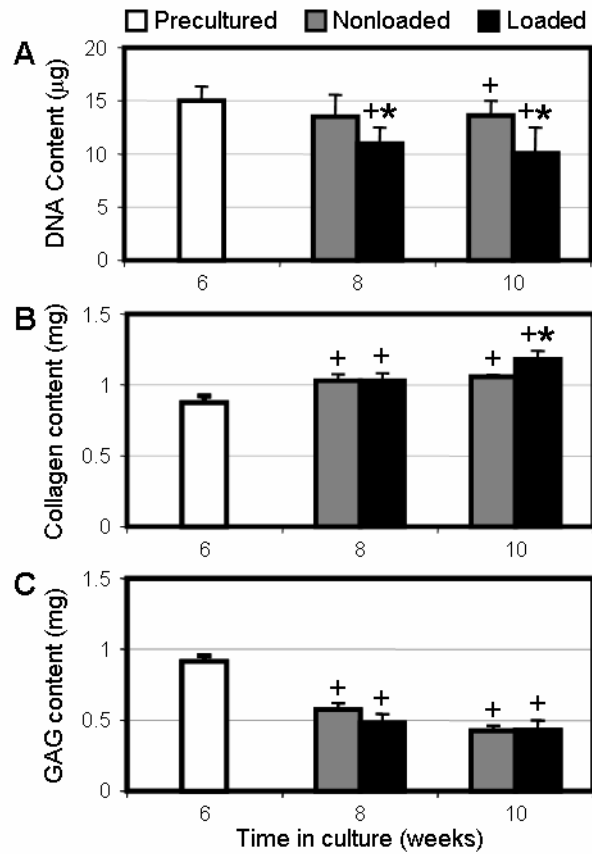


**Figure 10-4: Effect of dynamic culture and tensile loading on biochemical content. Total DNA (B), GAG (C), and collagen (D) content of MSC-seeded constructs after preculture (week 6), and with up to four weeks of daily cyclic loading (n=6, \*: p<0.05 vs. nonloaded controls, +: p<0.05 vs. precultured constructs).**

### 10.3.3 Effect of Dynamic Loading on Construct Maturation

Dynamically loaded and nonloaded control constructs were analyzed for biochemical content at weeks 8 and 10. Over the first two weeks of cyclic conditioning, there was a significant decrease in DNA content in loaded constructs compared to both preculture samples and nonloaded controls (p<0.001, **Figure 10-4A**). DNA content did not decrease further with an additional two weeks of loading (p=0.62). Despite a decrease in cellularity due to loading, cells continued to secrete collagenous matrix. At week 8, both loaded and nonloaded constructs increased in collagen content relative to preculture values, with no difference between groups at this time point (p=1.0, **Figure 10-4B**). However, while the

collagen content of nonloaded controls plateaued by week 10 ( $p=1.0$  vs. week 8), mechanically conditioned constructs continued to accrue collagen ( $p<0.001$  vs. week 8). At the terminal time point, dynamically loaded constructs contained more collagen than nonloaded controls ( $p<0.005$ ). Construct cross-sections stained for collagen revealed slightly more intense staining in loaded constructs as compared to nonloaded controls (**Figure 10-5**). No differences in proteoglycan content were observed with mechanical loading ( $p>0.79$ , **Figure 10-4C**), consistent with Alcian blue staining (**Figure 10-5**).

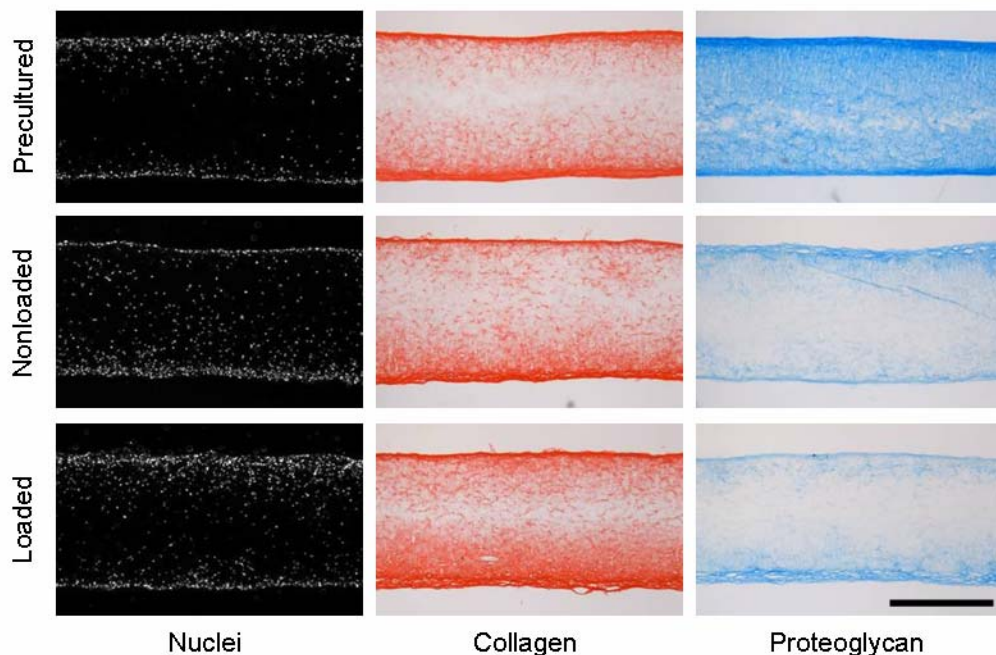


**Figure 10-5:** Histological assessment of long-term dynamically loaded MSC constructs. Representative cross-sections of precultured samples (week 6), and nonloaded controls and loaded constructs at week 10 stained with DAPI for cell nuclei, Picrosirius Red for collagens, and Alcian Blue for proteoglycans (scale: 500 $\mu$ m).

Mechanical properties of constructs at the beginning and end of the preculture period, and loaded samples and nonloaded counterparts at weeks 8 and 10 were evaluated in tension. Overall, increases in construct tensile properties were reflective of changes in collagen content. As constructs accumulated ECM throughout the preculture period, the

mechanical properties of week 6 constructs increased relative to week 0 values ( $p < 0.05$ , **Figure 10-6A**). By week 8 (two weeks after loading started), all samples had increased in modulus relative to preculture values, although no difference was detected between loaded and nonloaded constructs ( $p = 1.0$ ). However, an additional two weeks of cyclic conditioning induced a 16% increase in the tensile modulus of loaded samples compared to nonloaded controls ( $p < 0.001$ ). This increase in modulus was evident in average stress-strain plots of week 10 constructs, where loaded samples revealed a higher stress response at each level of strain beyond the toe region (**Figure 10-6B**).

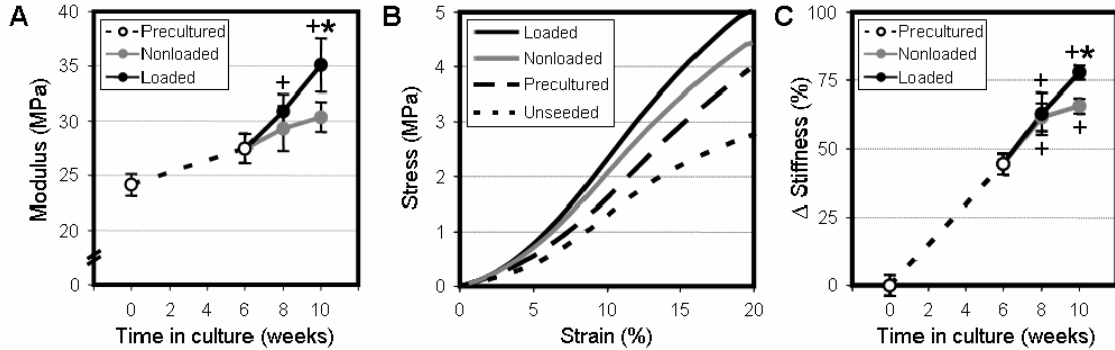


**Figure 10-6: Mechanical stimulation increases construct tensile properties.** (A) Tensile modulus of precultured samples at through week 6, and dynamically loaded constructs or nonloaded controls through week 10. (B) Changes in stiffness normalized to initial (week 0) values ( $n=6$ , \*:  $p < 0.05$  vs. nonloaded controls, +:  $p < 0.05$  vs. precultured constructs). (C) Average stress-strain curves of loaded and nonloaded constructs at the terminal time point, precultured samples at week 6, and acellular controls maintained in PBS for the duration of the study.

While modulus is an intrinsic property of a material, changes in sample cross-sectional areas can preclude this measure from representing the actual changes in stiffness due to the production of load-bearing matrix. To eliminate any error introduced by alterations in cross-sectional area (observed in loaded constructs), gauge lengths were maintained identically across the entire study to enable the fair comparison of stiffness. Quantifying the percentage change relative to scaffold stiffness at week 0, the tensile contribution of

newly synthesized ECM due to dynamic loading was isolated (**Figure 10-6C**). While differences in stiffness were less exaggerated than those observed with tensile modulus, the identical trend was observed. Following an initial increase in stiffness over the preculture period, two weeks of loading revealed no differences as a result of cyclic conditioning ( $p=1.0$ ). However, with an additional two weeks of conditioning, loaded constructs continued to increase in stiffness ( $p<0.001$  vs. week 8) while nonloaded controls plateaued at 8 week levels ( $p=1.0$  vs. week 8).

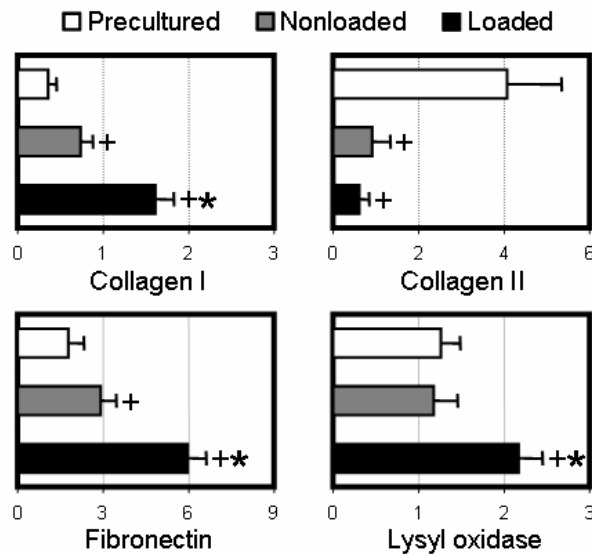


**Figure 10-7: Modulation of matrix-associated gene expression.** Expression of collagen I, collagen II, fibronectin, and lysyl oxidase normalized to GAPDH for precultured samples (week 6) and loaded constructs or nonloaded controls at week 10 ( $n=6$ , \*:  $p<0.05$  vs. nonloaded controls, +:  $p<0.05$  vs. precultured constructs).

#### 10.3.4 Transcriptional Changes with Dynamic Tensile Loading

To better understand the molecular underpinnings of these biochemical and mechanical changes with tensile conditioning and dynamic culture, real-time RT-PCR was performed on MSC-laden precultured constructs (week 6) and loaded/nonloaded constructs (week 10). Consistent with the increases in matrix content and tensile properties, cyclic loading had a pronounced effect on the expression of matrix and matrix-associated genes (**Figure**

**10-7).** Four weeks of loading resulted in a two-fold increase in collagen I expression compared to nonloaded controls ( $p < 0.001$ ), with no effect on collagen II expression ( $p = 1.0$ ). Fibronectin, which is responsible for cell binding to the surrounding ECM and is a precursor to collagen deposition (Li et al. 2003), increased by two-fold with conditioning ( $p < 0.001$ ). Likewise, lysyl oxidase, an enzyme that cross-links collagen fibrils, was significantly upregulated in loaded constructs compared to nonloaded controls ( $p < 0.001$ ). Interestingly, compared to precultured samples, collagen II expression decreased markedly in both loaded and nonloaded samples ( $p < 0.001$ , **Figure 10-7**) and collagen I and fibronectin increased in nonloaded controls ( $p < 0.05$ ). Whether these changes were due to media agitation or are characteristic of the natural evolution of nanofibrous constructs remains to be determined.

#### **10.4 DISCUSSION**

With the goal of engineering *in vitro* tissues with biochemical and mechanical properties approximating native meniscal fibrocartilage, this study explored the effects of dynamic tensile stimulation on MSC-laden nanofibrous constructs. These constructs are founded on biocompatible and biodegradable scaffolds composed of aligned polymer nanofibers. The organization of nanofibers, which mimics the architecture of fibrous tissues such as the meniscus, dictates cell alignment and the organization of cell-deposited ECM as shown in Chapter 3. In previous studies, the deposition of anisotropic fibrocartilaginous matrix under free-swelling, static culture conditions lead to demonstrable increases in the tensile properties of aligned nanofibrous constructs. However, even with long-term culture, the mechanical properties of constructs failed to achieve parity with native

meniscus. Based upon abundant evidence that mechanical forces are necessary for the development and maintenance of load-bearing tissues, this study explored the effect of cyclic tension, the predominant loading modality of the meniscus, on the maturation of engineered constructs. With dynamic tensile stimulation that approximates the strains seen by meniscal fibrocartilage *in vivo*, we observed upregulation of fibrous gene expression, increases in the production of collagen (**Figure 10-4**), and demonstrated, for the first time, increases in the functional properties of tissue engineered nanofibrous constructs (**Figure 10-6**).

In this work, we employed MSCs, a multipotent and readily available cell source that can be expanded *in vitro* for construct formation and can be induced to undergo fibrochondrogenic differentiation. MSC activity and fate decisions are sensitive to the cues they receive from their surrounding microenvironment, which may arise from soluble or matrix-bound signaling molecules (Pittenger et al. 1999), topographical features that inform cell shape and cytoskeletal organization (McBeath et al. 2004), passive mechanics such as matrix elasticity (Engler et al. 2006), as well as active mechanical inputs (Huang et al. ; Simmons et al. 2003) (for review, see (Discher et al. 2009; Guilak et al. 2009)). In this study, the microenvironment is both complex and dynamic, as MSCs respond to and modulate their surroundings over the course of culture. MSC-laden nanofibrous constructs were cultured in the presence of TGF- $\beta$ 3, which promotes matrix synthesis (Li et al. 2005) and can modulate MSC phenotype (Gao et al.). Beyond soluble factors, a topography of aligned nanofibers drives MSCs to adopt an elongated cell body with prominent actin stress fibers oriented in the direction of nanofiber alignment (Chapter 8).

Coincident with these changes in shape, MSCs reduce chondrogenic markers, and upregulate fibrous gene expression compared to traditional pellet cultures. In addition to these passive cues, MSCs are highly sensitive to external mechanical perturbations, which can modulate MSC phenotype depending on the modality of loading (i.e. compression versus tension) (Guilak et al. 2009), as well as the direction of loading (Kurpinski et al. 2006). Connelly and coworkers dynamically loaded MSCs within fibrin gels in tension and observed increases in type I collagen gene expression and protein production and no changes in traditional chondrogenic markers such as collagen II or aggrecan transcription or proteoglycan synthesis (Connelly et al.). Paralleling these results, MSCs in this study responded to dynamic tensile stimulation with an increase in the expression of type I collagen, fibronectin (a precursor to collagen production (Li et al. 2003)), and lysyl oxidase (a collagen fibril stabilizer and cross-linker) (**Figure 10-7**), with no difference in collagen II expression or proteoglycan synthesis. These observations, combined with studies showing upregulation of chondrogenic factors under dynamic compression (Huang et al. 2004; Mauck et al. 2007; Mouw et al. 2007), provide further evidence that MSCs will respond differently in terms of matrix biosynthesis depending on the loading modality to which they are exposed.

While MSC phenotype and alterations in gene expression are important considerations, the functional performance of ECM-rich, load-bearing engineered tissues arises from a complex cascade of protein translation, post-translational modifications, extracellular secretion and assembly, incorporation into the biomaterial scaffolding, and finally higher-order assembly and stabilization (e.g. collagen fibrillogenesis and crosslinking).

Concurrent with the upregulation of collagen I gene expression, we observed increases in the production and incorporation of collagen with dynamic tensile loading (**Figure 10-4**). These increases in total collagen content contributed to improvements in the tensile properties of nanofibrous constructs at week 10 (**Figure 10-6**). Importantly, these increases occurred despite decreases in stiffness (6%) and modulus (13%) observed in acellular scaffolds exposed to the same loading regimen. Although the increase in stiffness can be partially accounted for by the increased collagen content as demonstrated in Chapter 7, dynamic loading also upregulated the expression of lysyl oxidase, which serves to cross-link and stabilize collagen networks. The degree of collagen fibril assembly that occurs within aligned nanofibrous scaffolds, and the activity of matrix-modifiers such as lysyl oxidase both likely contribute to the resultant mechanical properties of tissue engineered constructs, and as such, are current subjects of investigation. Understanding the effect of mechanical forces at both the cellular (phenotype and biosynthetic activity) and tissue (matrix assembly, modification, and remodeling) levels in the context an engineered construct may provide insights into how development proceeds in normal or diseased states, and will ultimately allows us to engineer tissues that better approximate the hierarchy, organization, and functional properties of native tissues.

The bioreactor employed in this study was designed with several features to enable ease of operation (**Figure 10-1**). Specifically, the modular design enabled simultaneous loading of multiple samples and straightforward insertion and removal of experimental groups. However, this design required the placement of constructs in fixtures in close proximity,

presenting limitations in media diffusion under static culture conditions described in Chapter 5. To maintain such arrayed constructs for the four week loading period while providing nutrient/waste transfer to centrally located constructs, dynamic culture conditions were employed during periods of rest. Perpetual agitation of the culture medium triggered a marked loss in GAG content (**Figure 10-4, 10-5**), an ECM component crucial to tissue compressive properties. Furthermore, the depletion of GAGs may have impacted MSC gene expression, as collagen II expression decreased markedly in both loaded and nonloaded samples (**Figure 10-7**). As meniscal fibrocartilage experiences both tensile and compressive forces at the same time, the removal of GAG from the ECM should be considered. Nerurkar et al. investigated the use of dynamic culture conditions towards enhancing cell infiltration and observed an identical loss of GAGs to the culture medium (Nerurkar et al. 2010). However, within two weeks of returning constructs to static conditions, GAGs were restored to levels on par with controls cultured statically for the duration of the study, suggesting the ready capacity of MSCs to synthesize this key matrix component

While the positive changes in mechanical properties elicited by dynamic loading are encouraging (**Figure 10-6**), the improvement in tensile modulus was 16% (compared to nonloaded controls), only slightly narrowing the gap between engineered fibrocartilage (35MPa) and native meniscus tissue which possesses a fiber direction modulus between 65-80MPa (Bursac et al. 2009). That being said, this study explored only one possible loading regimen (6%, 1hz, 3h/day). It is plausible that a different combination of strain amplitude, frequency, and duty cycle applied over a longer duration, would elicit a more dramatic

cellular response and subsequent tissue maturation. In this work, 6% strain was chosen based on the deformations seen in the circumferential direction of the meniscus (Jones et al. 1996; Richards et al. 2003), a value that is not necessarily optimized for MSCs on these scaffolds or at their current differentiation state. More recent studies in the meniscus have demonstrated that relative to macroscale tissue deformations, the microscale strains experienced by resident cells is highly varied and dependent upon the location of the cell relative to collagen fiber bundles and interstitial matrix (Upton et al. 2008). In Chapter 9, we investigated how macroscale scaffold deformations translate to cellular and subcellular changes in MSCs on nanofibrous topographies. While these studies were limited to surface-seeded cells, future studies employing such a macro-to-microscale approach to investigate MSCs deformations in three-dimensional constructs will provide insights on how strain is transduced at the cellular level. Provided an understanding of this relationship, a systematic parameterization of loading regimens could then be explored to identify the strain levels and frequencies that best drive ECM biosynthesis and assembly by resident MSCs.

An additional parameter that may play a role in determining how MSCs respond to tensile loading is the duration of preculture. In this study, six weeks of preculture was selected as it was a duration sufficient for cell colonization and elaboration of a functional, load bearing ECM. MSCs will likely respond differently to external forces depending on the amount and character of their surrounding matrix. These differences could arise from the evolving mechanical properties of the surrounding matrix, which would dictate how loads are transferred through the ECM and to constituent cells. Alternatively, the presence and

quantity of specific matrix components modulates cell-matrix adhesions, and this in turn will likely regulate mechanotransduction (Chen et al. 2004). For example, Huang et al. found that MSCs responded favorably to dynamic compression in a 3D hydrogel only after chondrogenesis had occurred (Huang et al.). Thus, the ideal preculture period and phenotypic status of the cells at the onset of loading requires further investigation.

As in previous studies, cell infiltration was limited over the six week preculture period, with cells located 200 $\mu$ m maximally from the scaffold surface. As such, ECM deposition was localized to the scaffold periphery, although proteoglycans were observed to be more homogeneously distributed than collagen. Towards hastening cell infiltration so that loading may be initiated earlier, Chapter 4 described composite scaffolds composed of interspersed slow-eroding PCL (used in this study) and sacrificial poly(ethylene oxide) fiber elements which increase scaffold pore size and void volume upon removal. The use of such composites may not only allow for better cell colonization and more homogeneously distributed ECM as shown in Chapter 5, but may also provide an open structure more amenable to matrix deposition, modification, and remodeling with dynamic loading than the single polymer scaffolds employed in this study.

Beyond demonstrating the potential for improving tissue construct maturation with mechanical stimulation, results from this study may have implications outside the realm of engineering *in vitro* tissues. In the case of implantation of an acellular scaffold into a load-bearing site, questions regarding patient rehabilitation arise. The improvements in construct development observed with mechanical stimulation in this study imply that as

host cells colonize the implant, the dynamic tensile loading experienced with physiologic motion may have a beneficial effect in accelerating tissue regeneration and restoring mechanical function to the tissue. Indeed, the minimal loss in mechanical properties with repetitive loading suggests that the scaffolds are sufficiently robust to bear load when situated in a meniscal defect. On a more fundamental level, dynamic loading of aligned nanofibrous constructs can serve as model system for understanding how three-dimensional tissues composed of aligned arrays of cells embedded within organized ECM respond to mechanical stimuli and modulate their extracellular environment. Such a system provides a more controlled and experimentally compliant approach to studying mechanotransduction, as compared to studies performed with native tissues which are susceptible to donor variability and intra-tissue regional variability. Future studies using this system will provide insights into the intricate interplay between cells, the extracellular microenvironment, and mechanical perturbations. Coming full circle, eventual elucidation of the signaling mechanisms underlying the biosynthetic response of MSCs to mechanical inputs could then be applied in identifying the timing and parameters of an optimized loading regimen for improving the *in vitro maturation of* engineered tissues for meniscus and other fibrous tissue repair.

## **10.5 CONCLUSIONS**

This study demonstrated positive effects of long-term dynamic tension on the maturation of MSC-laden engineered fibrocartilage. Specifically, we show for the first time that cyclic tensile loading of nanofibrous constructs hastens the synthesis and incorporation of collagenous ECM matrix which contributes to increases in the tensile properties of

constructs. These mechanically-induced improvements in tissue constructs properties were echoed by transcriptional changes of resident MSCs. In response to dynamic loading, the expression of collagen I, fibronectin, and lysyl oxidase were significantly upregulated. In summary, this work demonstrates that replication of both the structural (through the aligned nanofibrous scaffold) and mechanical (through dynamic tensile stimulation) environment of load-bearing fibrous tissues is a viable tissue engineering strategy. Furthermore, this work lays the foundation for future studies investigating how mechanical loads are perceived by organized arrays of cells, and how these cells respond in modifying their surrounding extracellular matrix.

## ***CHAPTER 11: SUMMARY AND FUTURE DIRECTIONS***

### **11.1 SUMMARY**

The fibrocartilaginous menisci dwell between the articular surfaces of the knee and play a key role in joint function (as described in detail in Chapter 2). By virtue of the organization of circumferentially-aligned collagen bundles and the unique wedge-shape of the tissue, with joint loading, the meniscus converts axial forces into tensile hoop stresses. Through this unique load-transfer mechanism, the contact area of loading is distributed across the underlying tibial articular surface, a condition necessary to the healthy homeostasis of the articulating surfaces. Damage through trauma or degenerative changes is the most common orthopaedic injury, disrupts the mechanical function of these structures, and leads to the precocious development of osteoarthritis. The current standard of treatment is removal of the damaged tissue, a procedure that does not re-establish normal knee mechanics. Given the frequency of meniscal injury, a restorative repair strategy remains a major unmet need in orthopaedic medicine. With the goal of replacing damaged meniscus with engineered biologic tissue that can restore normal joint loading, this thesis focused on the exploration of scaffolds composed of aligned biocompatible and biodegradable nanofibers that mimic the length scale and organization of anisotropic fibrous tissues such as the meniscus.

Demonstrating the utility of these scaffolds for engineering anisotropic fibrous tissues such as fibrocartilage, Chapter 3 investigated the effect of nanofiber alignment on the organization of cells and cell-deposited collagen. MSCs and MFCs were seeded onto

either scaffolds where the nanofibers were randomly organized (nonaligned), or ones where the fibers were uniformly aligned in the same direction. While the production of ECM was similar in nonaligned and aligned constructs, only aligned constructs revealed increases in tensile modulus with time in culture. Identifying the source of the disparity in functional properties, disorganized collagen was identified in nonaligned constructs, while collagen deposition was parallel to the predominant direction of nanofibers in aligned constructs. Importantly, this chapter demonstrated that nanofiber alignment dictates the organization of collagen, leading to profound consequences for the load-bearing properties of the resultant tissue. The ability to generate organized collagen-rich tissues serves as the foundation for the remainder of the work.

A significant limitation observed in these initial studies was the slow rates at which cells infiltrate these three-dimensional matrices. This problem arises from small pore sizes arising from the dense packing of fibers during the electrospinning process, a problem that's further exacerbated by nanofiber alignment. To increase pore sizes and hasten cell ingress, Chapters 4 and 5 developed composites containing both slow-eroding structural fibers, and water-soluble elements that serve to hold space during the formation of the scaffold. Chapter 4 detailed the design and mechanics of these composite scaffolds, and showed that the inclusion of sacrificial fiber elements led to improvements in cell infiltration over short-term culture. In Chapter 5, the longer-term ramifications of sacrificial fiber inclusion on construct maturation were explored. With high sacrificial fiber content, increases in collagen distribution and content led to more marked improvements in tensile properties, with constructs achieving tensile moduli of ~50MPa

by 12 weeks of culture, the highest value to date of an *in vitro* fibrocartilaginous construct. To underscore the utility of this strategy for both *in vitro* tissue engineering as well as acellular implantation, host cell colonization was shown to be dramatically improved with sacrificial fiber content in a rat subcutaneous model.

Chapters 4 and 5 demonstrated the benefits of combining multiple polymer fibers into a composite, and motivated the addition of third fiber population that erodes concomitant with cellular infiltration and tissue formation. Thus, Chapter 6 focused on engineering a tri-polymer composite with temporally dynamic mechanical properties. While the experimental aspects of this work focused on integrating a particular polymer with specific degradation rates and mechanical properties, the overall composite strategy could have relevance to numerous tissue engineering applications. To generalize this strategy, a theoretical model that describes the temporal mechanical behavior of composites was developed and validated with experimental data. This model was employed in simulating time-dependent stress-strain behavior of scaffolds of hypothetical formulations, and demonstrated a novel approach to the intelligent design of nanofibrous composites with dynamic mechanical properties.

Beyond an appropriately designed scaffold, an essential component to generating fibrocartilage *in vitro* is a cell type that can reconstitute the extracellular content of the meniscus. The two most accessible options are meniscal fibrochondrocytes (MFCs), the cells indigenous to the meniscus that assemble and maintain its extracellular matrix, and mesenchymal stem cells (MSCs), a multipotent cell type under widespread investigation

for applications in musculoskeletal tissue engineering (as described in Chapter 2). Moving this technology closer to clinical implementation, Chapter 7 examined the tissue engineering potential of human MFCs in conjunction with aligned nanofibrous scaffolds. MFCs were isolated from ten human donors, seeded on scaffolds, and biochemical, mechanical, and histological features were assessed over long-term culture. Despite considerable donor-donor variability, all ten cell lines enhanced construct mechanical and biochemical properties, demonstrating that MFCs isolated from surgical waste are a pertinent cell source for *in vitro* meniscus tissue engineering. Along similar lines, Chapter 8 assessed the ability of human marrow-derived MSCs to elaborate a mechanically functional, fibrocartilaginous matrix in a nanofibrous context. While we hypothesized that these cells would perform similarly to donor-matched MFCs (based on results from Chapter 3), MSCs instead demonstrated limited proliferation and synthesized sparse extracellular matrix, leading to negligible increases in construct mechanical properties as compared to donor-matched MFCs. Highlighting the sensitivity of human MSCs to their three-dimensional microenvironment, there was no difference in matrix production of MSCs and FCs when cultured in pellet form.

In the previous chapters, the highest tensile modulus achieved in a nanofibrous construct after long-term free-swelling culture was approximately 50MPa, a value below adult meniscus by a factor of 2 or more. As these tissues require exposure to mechanical forces *in vivo* for proper formation and maintenance, Chapter 9 and 10 investigated the effects of tensile deformations on nanofibrous constructs, as this is the primary loading modality of the meniscus. In Chapter 9, we began at the cellular level and examined how

applied tensile strains translated to gross morphological changes in the cell as well as alterations in nuclear shape and orientation. With applied deformation, the response of cells and their nuclei was found to be time-dependent and sensitive to the underlying scaffold architecture. With a basic understanding of how applied strains affect cells on aligned nanofibrous scaffolds, we next examined the effect of cyclic tensile loading on precultured fibrocartilaginous constructs, a scenario that better approximates the dynamic mechanical environment of the meniscus. Chapter 10 described the design and validation of a custom tensile bioreactor for applying cyclic strains to nanofibrous constructs during *in vitro* culture. Using this system, we found that dynamic loading led to increases in the tensile stiffness and total collagen content of MSC-laden constructs, and modulated the expression of matrix and matrix-associated genes. These results have relevance to strategies for fibrocartilage tissue engineering, but also provide new insights on how stem cells can respond to external mechanical stimuli and modify their microenvironment.

Towards recapitulating the structural features of the meniscus, this work focuses on scaffolds composed of aligned arrays of polymeric nanofibers fabricated with the electrospinning process. These biocompatible and biodegradable nanofibers can be formulated to mimic the length scale and organization of collagenous tissues, and as such, serve as a suitable foundation for engineering meniscal fibrocartilage. Using a multi-faceted approach, this work investigated aspects of scaffold design, cell source selection, and modulation of the mechanical environment with the aim of engineering fibrocartilage that approximates the organization, composition, and mechanical function of the native meniscus. While significant progress was made on all of these fronts, much

work remains to be done before a nanofibrous construct will be ready for clinical implementation. Outlined briefly below are some potential avenues of future investigation inspired by this thesis.

## **11.2 LIMITATIONS AND FUTURE DIRECTIONS**

### ***11.2.1 Identifying Shortcomings in MSC Fibrochondrogenesis***

It remains to be determined which cell type is the most appropriate for engineering meniscus tissue for the purpose of clinical intervention. In this work, we examined the construct forming potential of both MSCs and MFCs isolated from human donors. In our hands, MFCs significantly outperformed MSCs in all respects, proving more capable in infiltrating nanofibrous scaffolds, synthesizing extracellular matrix (ECM), and increasing construct tensile properties with time in culture (Chapter 8). Indeed, constructs formed from human MFCs led to a 2.5-fold increase in the tensile modulus of scaffolds over 12 weeks of culture, resulting in an endpoint modulus of ~50MPa (Chapter 5). Despite these promising results, the isolation of MFCs require an initial arthroscopic resection of meniscus tissue before these cells can be isolated and expanded for use. In the scenario of growing a fibrocartilage construct *in vitro* for subsequent implantation, this would require two surgeries at the defect site. Conversely, MSCs, which can be isolated from a bone marrow tap of the Iliac crest, could be expanded, formed into nanofibrous construct, and implanted at the time of tear resection, thereby requiring only a single invasive procedure.

However, based on the results presented in Chapter 8, MSCs under identical growth conditions as donor-matched MFCs failed to proliferate when seeded on nanofibrous scaffolds. As the most straightforward way of populating nanofibrous scaffolds is by surface seeding, the evolution of the construct is dependent both upon the differentiation and biosynthetic activity of each cell, as well as the proliferation and colonization of the overall population of cells. While MSCs in Chapter 8 responded to topographic and chemical cues, underwent fibrochondrogenesis (as assessed by gene expression), and synthesized a collagen- and glycosaminoglycan-containing ECM, the absence of proliferation appeared to be a significant contributor to the inferior tensile properties of MSC-based constructs. Other studies have encountered limitations in MSC viability or proliferation in three-dimensional constructs (Salinas et al. 2008), and numerous studies have demonstrated the need for fibroblast growth factor (FGF) for the efficient expansion (Martin et al. 2001; Tsutsumi et al. 2001; Farre et al. 2007) and 3D culture of MSCs (Solchaga et al. 2005). Based on these studies, we recently assessed the use of basic FGF (bFGF or FGF-1) on the maturation of adult human MSC-seeded nanofibrous scaffolds (**Figure 11-1**). In this study, aligned pure PCL scaffolds were seeded with MSCs and cultured in media containing TGF- $\beta$ 3, bFGF, or a combination of both growth factors for up to 9 weeks.

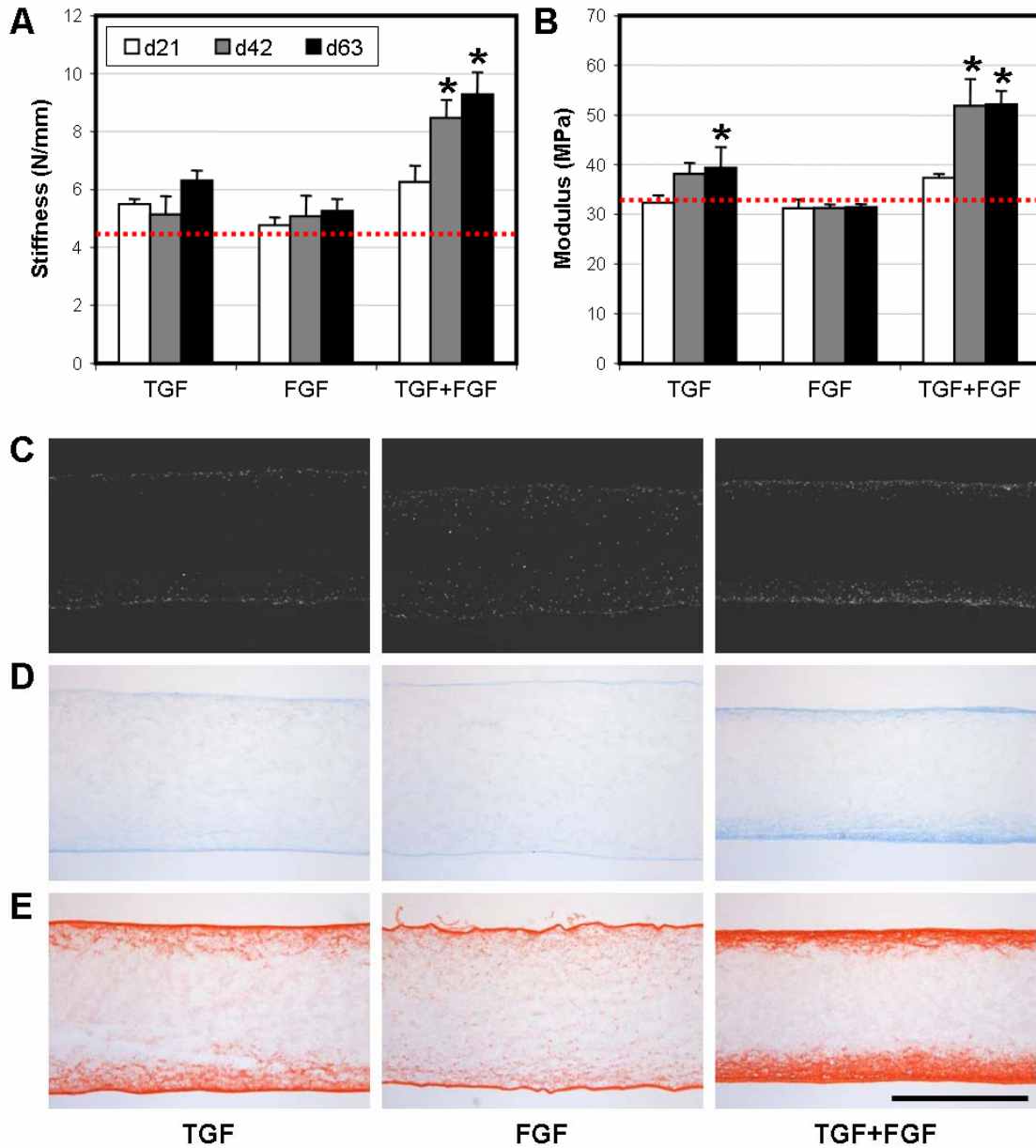


**Figure 11-1: The effect of growth factors on MSC construct maturation. Tensile stiffness (A) and modulus (B) of adult human MSC-seeded constructs cultured with TGF- $\beta$ 3, bFGF, or a combination of both growth factors. Dashed lines indicate day 0 values. \*:  $p < 0.05$  vs. day 21. Day 63 cross-sections stained for cell nuclei (C), proteoglycan (D), and collagen (E). Scale: 500 $\mu$ m.**

In the presence of TGF- $\beta$ 3, MSCs demonstrated limited proliferation as seen in Chapter 8. Despite this, cells elaborated an ECM which contributed to increases in the tensile properties of constructs after 9 weeks of culture. In chemically-defined medium

containing both bFGF and TGF- $\beta$ 3, MSCs proliferated and colonized the periphery of scaffolds, although infiltration into the depths of scaffolds was not observed. The expanded population of cells synthesized markedly more ECM which in turn led to more marked improvements in construct tensile properties. Interestingly, in conditions with bFGF alone, MSCs proliferated and appeared to be more migratory as cells were identified at the center of scaffolds. However, the production of ECM was severely limited such that the tensile modulus of bFGF constructs did not increase with time. These preliminary results demonstrate the need for inclusion of a mitogenic agent in addition to an inducer of matrix synthesis when culturing MSC-based constructs, and pave the way for future studies focusing on the formation of functional fibrocartilage constructs derived from adult human MSCs.

Adult human MSCs can undergo fibrochondrogenic differentiation on nanofibrous scaffolds, as evidenced by an increase in collagen I and decrease in aggrecan expression compared to in pellet culture (Chapter 8). However the production of ECM when normalized to cell number appeared to be impaired in comparison to donor-matched MFCs. To identify the disparities between matrix production by MFCs and that of MSCs, a more in-depth understanding of MSC fibrochondrogenesis is necessary. Recognizing shortcomings in the functional properties of MSC-encapsulated hydrogels compared to differentiated chondrocytes (Mauck et al. 2006), Huang et al. examined the molecular underpinnings of MSC chondrogenesis using a microarray approach (Huang et al. 2009). Employing a genome-wide screen for differentially-regulated genes, they identified several transcripts that were severely up- or down-regulated as compared to

chondrocyte controls. Adopting a similar approach with MSCs and MFCs in the context of an aligned nanofibrous scaffold may elucidate misregulated genes, and may identify potential molecules that play a fundamental role in the development of functional fibrocartilage. On a related note, examining the transcriptional behavior of human MFCs in juxtaposition to the functional properties of constructs formed from these cells may shed some light on what characterizes an efficacious cell line, as considerable donor-donor variability was noted in Chapter 7.

### ***11.2.2 Approximating the Mechanical Environment of the Meniscus***

The meniscus is exposed to a combination of tension and compression, where compression occurs predominantly in the inner region and tension occurs throughout the meniscus. This complex loading environment is evident in the spatially varying biochemical content of the tissue, with the inner region composed of both a dense aligned collagen element (a mix of type I and type II collagen), as well as a rich proteoglycan component that resists compressive deformation. In this work, we focused on cyclic tension as an inducer of fibrocartilage formation, as this loading modality represents the primary function of the tissue. However, the potential effects of compression on fibrocartilage formation should not be ignored. For example, a fibrocartilage zone can be found at the site where tendons wrap around bone pulleys or bony protrusions and experience significant compressive forces with loading. Highlighting the role of compression in the formation of a fibrocartilaginous zone, Malaviya et al. translocated the flexor digitorum profundus tendon in rabbits, thereby removing compressive forces from the portion of tendon that wraps around the ankle. Within 4 weeks of surgery, the

tissue demonstrated significant remodeling with decreases in compressive mechanical properties and glycosaminoglycan content, along with a loss in the organization of constituent collagen fibers. Clearly, compressive forces play a central role in the maintenance of fibrocartilage.

In order to better recapitulate the mechanical environment of fibrocartilaginous tissues such as the meniscus, bioreactors that exert both tensile and compressive loads may prove insightful. Shown in **Figure 11-2A** is a schematic depicting a custom tension-compression bioreactor that mimics the wrap-around tendon-bone pulley system. This bioreactor is designed to produce tensile stress throughout the entirety of the construct, as well as compressive stress at a circular post over which the scaffold changes directions. In future studies, ECM expression, biochemical composition, and mechanical (tensile and compressive) properties could be evaluated in these constructs both within the compressive domain, and along the tensile regions. Additionally, to examine the effect of sliding motion on developing engineered fibrocartilage, this post could be rotated in order to replicate the motion of the condyle on the proximal surface of the meniscus. Finite element modeling can be used to predict the locations and magnitudes of compressive and tensile strains, and could be informative in designing efficacious loading regimens (**Figure 11-2B**).

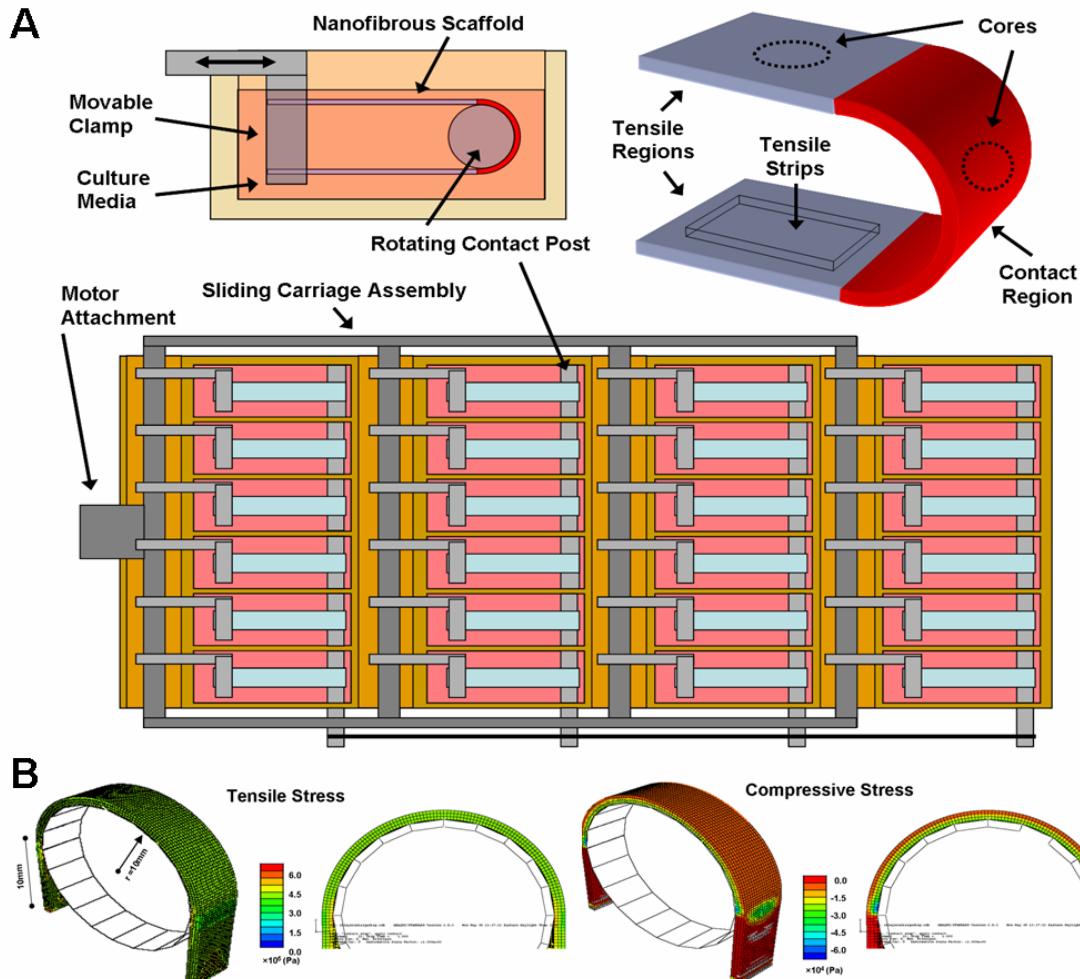


**Figure 11-2: Tension-compression bioreactor.** A) Schematics of a combined tension-compression bioreactor featuring a unit culture cell (top left), locations of the tensile and compressive regions (top right), and the overall assembly capable of mechanically loading 24 samples simultaneously (bottom). B) Finite element modeling of scaffolds deformed against a cylindrical post, depicting magnitudes of tensile (left) and compressive (right) stresses.

Ultimately, the use of bioreactors that impart multiple loading modalities could provide a fundamental understanding the how cells sense different types of forces and respond in modulating the character of their surrounding ECM. The use of nanofibrous scaffolds provides a suitable microenvironment amenable to exerting both tensile and compressive forces to constituent cells (as compared to hydrogels, where transducing tensile loads to encapsulated cells may prove difficult). In fact, an aligned nanofibrous construct

deformed against a pulley may best approximate the wrap-around tendon scenario, as cells within these zones are highly aligned and morphologically similar to those in purely tensile zones (Malaviya et al. 2000). *In vitro* studies using this system could allow for the identification of key pathways that regulate the production of fibrous versus cartilaginous ECM, which would have tremendous relevance not only for the fabrication of fibrocartilage, but bearing on the engineering of both articular cartilage and fibrous tissues such as tendon and ligament. Furthermore, while studies thus far have confirmed the role of compressive (Huang et al.) and tensile (Chapter 10) forces in MSC phenotypic commitment and matrix synthesis, these results have been obtained using different culture systems (hydrogels versus nanofibrous scaffolds) and are arguably anecdotal in nature. A controlled study employing the identical scaffold and chemical environment where the sole difference lies in the types of loads experienced by MSCs would definitively confirm the differential effects of compressive and tensile forces on MSC fate decision.

### ***11.2.3 Dynamic Mechanical Properties of Engineered Fibrocartilage***

Although electrospun materials are commonly applied to the engineering of viscoelastic and cyclically loaded tissues, the typical mechanical testing procedure (and that employed throughout this thesis) is a quasistatic continuous ramp to failure at a nominal strain rate so as to eliminate rate dependent effects. While quasistatic uniaxial tensile properties serve as a suitable standard and provide a framework that enables comparisons across studies and laboratories, in truth, load-bearing musculoskeletal tissues are seldom if ever loaded at such low strain rates. No data exists on the strain rates occurring in the

meniscus with physiologic loading, although several studies indicate strain magnitudes of between 2-6% in *ex vivo* studies approximating normal loading (Jones et al. 1996; Richards et al. 2003). A frequency of 1Hz is often used to represent normal gait, but the point in each stride at which axial loading is initiated and the duration over which load is applied to the meniscus is clearly less than 1 second (especially when considering more extreme motions such as running or jumping) (Chia et al. 2008). Given the dynamic and repeated mechanical loading experienced by the meniscus over a lifetime of use, eventually it will be necessary to go beyond quasistatic tensile properties and begin to consider the rate-dependent characteristics of engineered constructs.

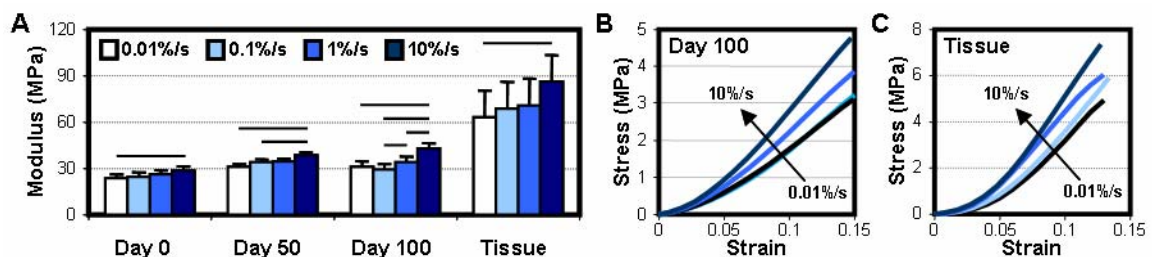


**Figure 11-3: A) Tensile modulus of meniscus and engineered constructs cultured for 0, 50, or 100 days tested in the fiber direction at different strain rates. Average stress-strain response of day 100 constructs (B) and meniscus tissue (C) at each strain rate; note difference in scaling. Bars denote significant comparisons with  $p < 0.05$ ; constructs:  $n=5$ /group, tissue:  $n=10$ /group.**

Based on some theoretical models, there is evidence that electrospun fibers may slide relative to one another (Li et al. 2007; Nerurkar et al. 2007), generating frictional interactions that may be a source of rate-dependent effects. Moreover, as resident cells deposit ECM within electrospun scaffolds, there is an increase in water content and concentration of potentially viscoelastic ECM elements. In a preliminary study, we assessed the rate-dependent tensile properties of bovine MSC-seeded aligned nanofibrous scaffolds with time in culture, and compared this behavior with strips of bovine meniscus

taken in the circumferential direction of the tissue (**Figure 11-3**). The tensile modulus of meniscus was dependent upon strain rate, where samples tested at 10%/s possessed a significantly higher modulus than those tested at the slowest strain rate, a result that underscores the need for examining dynamic properties of engineered replacements. Substantiating the aforementioned claims of viscoelastic behavior in electrospun materials, acellular scaffolds (day 0) also revealed viscoelastic behavior. With ensuing matrix synthesis and construct maturation, the correspondence between strain rate and tensile modulus became more pronounced, where by day 100, each rate beyond 0.1%/s resulted in a significant increases in modulus. Calculating the % difference between moduli at the highest and lowest rates, the effect becomes more apparent – the difference was 22% in acellular scaffolds but nearly doubled to 38% by day 100, suggesting that matrix deposition reinforces this phenomenon. Taken together, the similar viscoelastic behavior of engineered constructs and native meniscus is encouraging, but additional studies examining fatigue characteristics with cyclic loading will be vital in predicting how these constructs will function post-implantation.

#### ***11.2.4 Tailorable, Smart Electrospun Materials***

Despite the plethora of materials that can be processed into nanofibers (reviewed in Chapter 2), there remains a significant need for new polymers that can better approximate the mechanical behavior of fibrous tissues. Shown in **Figure 11-4**, is the average stress-strain profile of healthy meniscus tissue tested in the circumferential direction along with lower- and upper-bounds to this response which define a “meniscus domain.” This domain represents a functional benchmark that we should strive to replicate in a suitable

biomaterial for meniscus replacement. Juxtaposed upon this plot are the tensile behaviors of fiber-aligned scaffolds formed from several polymers explored throughout this thesis (Chapter 6). Despite the considerable variation observed between different polymers, none of these materials reveal a stress-strain behavior that falls within the “meniscus domain.” In this thesis, we chose to focus on the use of poly( $\epsilon$ -caprolactone) (PCL), as this polymer demonstrates a toe region akin to that of collagenous tissues, is more distensible than other members of the polyester family, and can serve as a long-standing structural element during *in vitro* or *in vivo* culture due to its slow erosion via hydrolysis. While this polymer has shown promise and may serve as an adequate foundation for the *in vitro* development of fibrocartilage, a polymer that is equally distensible but stiffer may better approximate the mechanical properties of the meniscus and prove a more sensible choice.

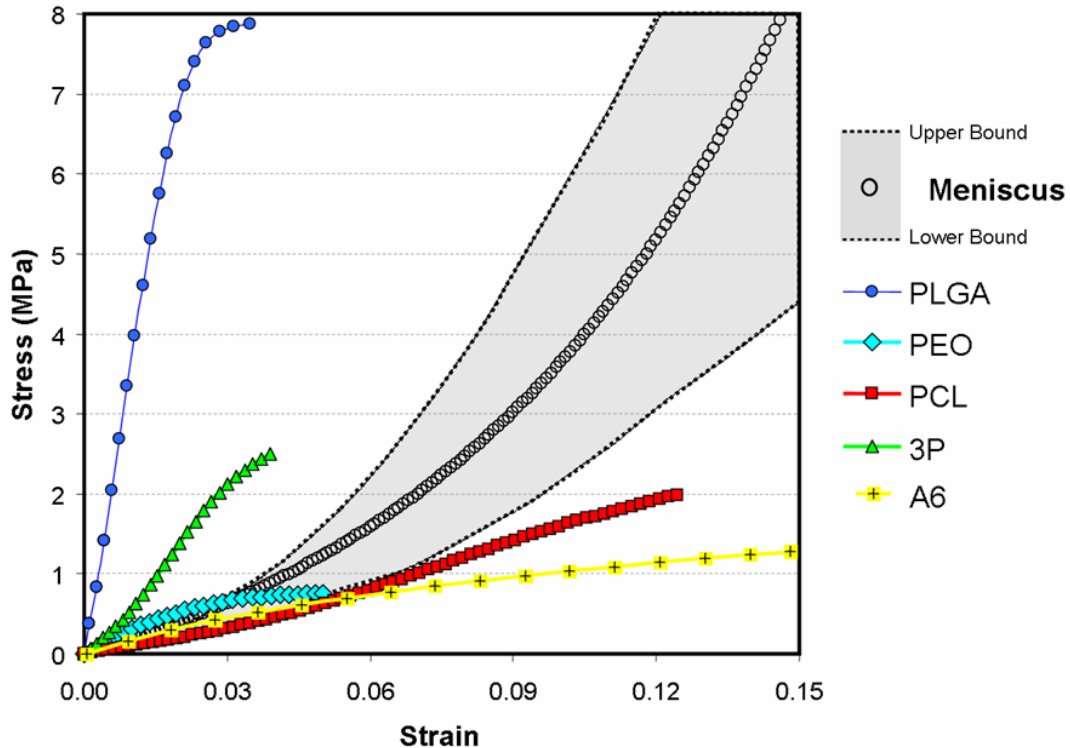


**Figure 11-4: Benchmarks for the engineering of fibrous tissues. Healthy meniscus tissue tested in the fiber direction produces a non-linear stress-strain response (circles indicate average response; boundaries indicate high and low range of responses from 10 separate samples). Superimposed on this physiologic range are the stress-strain responses of nanofibrous scaffolds of varying polymer composition.**

We have recently reported on the electrospinning of several elements of a library of 120 poly( $\beta$ -aminoester)s that were photo-polymerized after formation (Tan et al. 2008) as well as new photocrosslinkable and hydrolytically degradable elastomers (Ifkovits et al. 2008). These novel materials, produced by a combinatorial approach to polymer synthesis, have a wide range of mechanical properties and degradation rates, and will be assessed in future work for their applicability in engineering fibrous tissues. Additionally, there is great potential for electrospun materials that have added functionalities such as MMP-cleavable domains or the ability to carry growth factors. Recent work by Ionescu et al. demonstrated the delivery of molecules of interest from

microspheres embedded within a nanofibrous scaffold (Ionescu et al.). Overall, access to a wide selection of electrospinnable materials with diverse characteristics (ie. mechanics, degradation rates, and innovative functionalities) in conjunction with the composite approach described in Chapter 6 will enable the design of “smarter” nanofibrous scaffolds that can better effect fibrous tissue repair.

### ***11.2.5 Scaling Up to Anatomic Form***

While the results presented in this thesis indicate the potential of fiber-aligned electrospun scaffolds to guide neo-tissue growth, clinical application will require the fabrication of constructs with anatomic relevance. The meniscus fills a unique anatomic space, ensuring congruency between the rounded femoral condyle and the flat tibial plateau. Indeed, the wedge shape of the meniscus is a key feature enabling the conversion of axial compressive loads to tensile hoop stresses (see **Figure 2-4** in Chapter 2). Tissue engineering strategies must therefore recapitulate not only the micro- and nano-scale topography of the tissue, but the macro-scale anatomic form in order to effectively restore joint function.

The goal of scaling up to larger structures poses a rather difficult problem as electrospun materials are formed as sheets on the order of a millimeter in thickness, which already demonstrate limitations in cellular infiltration. We have recently begun to explore methods to develop nanofibrous constructs with anatomic relevance by fabricating wedge-shaped constructs using a novel folding technique (**Figure 11-5A**). This approach preserves the circumferential fiber orientation while approximating the wedge form of

the meniscus. To stabilize constructs initially, a spot welding approach was adopted in which a heated probe fused adjacent acellular layers (**Figure 11-5B**). In preliminary studies, nanofiber-based anatomic wedges were formed and seeded with 10 million MSCs via syringe. After 3 weeks in culture, wedges were harvested and stained for cell localization and matrix deposition. As shown in **Figure 11-5C,D**, the lamellar wedge construct takes on a tissue-like appearance with matrix deposition occurring at each layer. Collectively, these results show that nanofibrous constructs can be formed into structures with anatomic relevance while preserving anisotropic mechanical and architectural features.

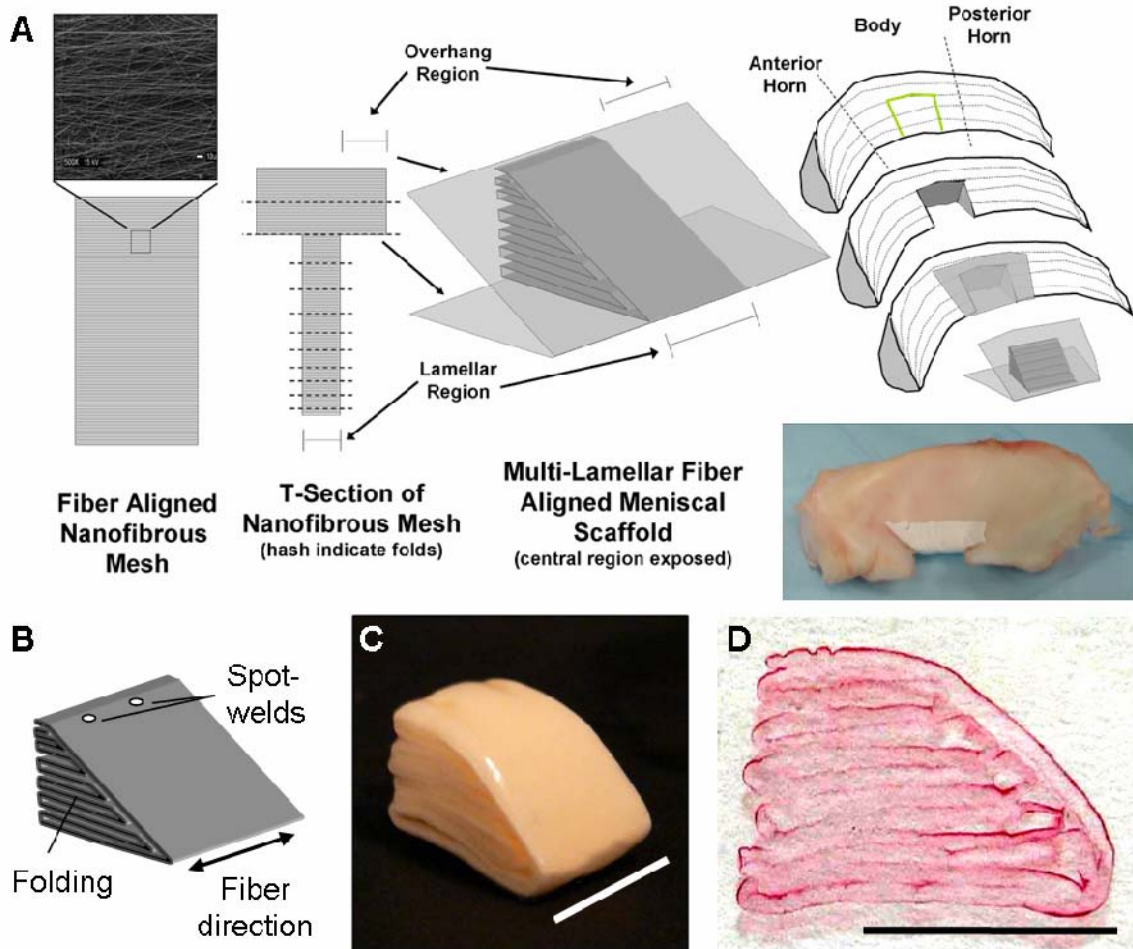


**Figure 11-5: Approximating anatomic form.** Fabrication algorithms involving lamellar folding (A) and spot-welding (B) were developed to generate constructs with 3D anatomic form (wedge shape) while preserving the orientation of nanofibers with respect to the circumferential collagen fibers of the meniscus. MSC-seeded wedge-shaped constructs took on a meniscus-like appearance after three weeks in culture (C), with collagen deposition occurring between each layer (D). Scale bar: 1 cm.

Beyond the production of three-dimensional structures that appropriately fill meniscal defects, the issue arises of implant integration with the native tissue, especially relevant in the case of a sub-total resection. To address both this question and to assess the interfaces formed within lamellar wedge constructs (Figure 11-5C,D), we've examined the mechanical integration of cell-seeded constructs when held in apposition to meniscal tissue or to another construct, respectively. In these studies, scaffold-scaffold or scaffold-

meniscus interfaces were formed, and integration strength between layers was assessed using a lap test, with maximum force normalized to the overlap area (**Figure 11-6A,E**). Results from these preliminary studies demonstrate that after two weeks, a stable union between cell-seeded scaffolds formed and continued to increase in strength with further time in culture (**Figure 11-6B**). In fact, scaffold-scaffold interfaces after 24 weeks reached several hundred kilopascals and numerous samples failed not at the interface but within the midsubstance of one of the scaffolds. Histological analysis of these forming interfaces showed a steady increase in ECM deposition with time (**Figure 11-6C,D**). In contrast, the strength of scaffold-meniscus interfaces remained markedly lower regardless of cell seeding (**Figure 11-6F**). Histological examination reveals a clear demarcation between native and engineered tissues and limited matrix production despite the presence of cells (**Figure 11-6G,H**). The inferior interface formed between scaffold and meniscus is likely due to the dense, impenetrable ECM of the native tissue. Future exploration of methods to roughen this surface either mechanically or enzymatically may enhance the integration of meniscus tissue with implanted constructs.

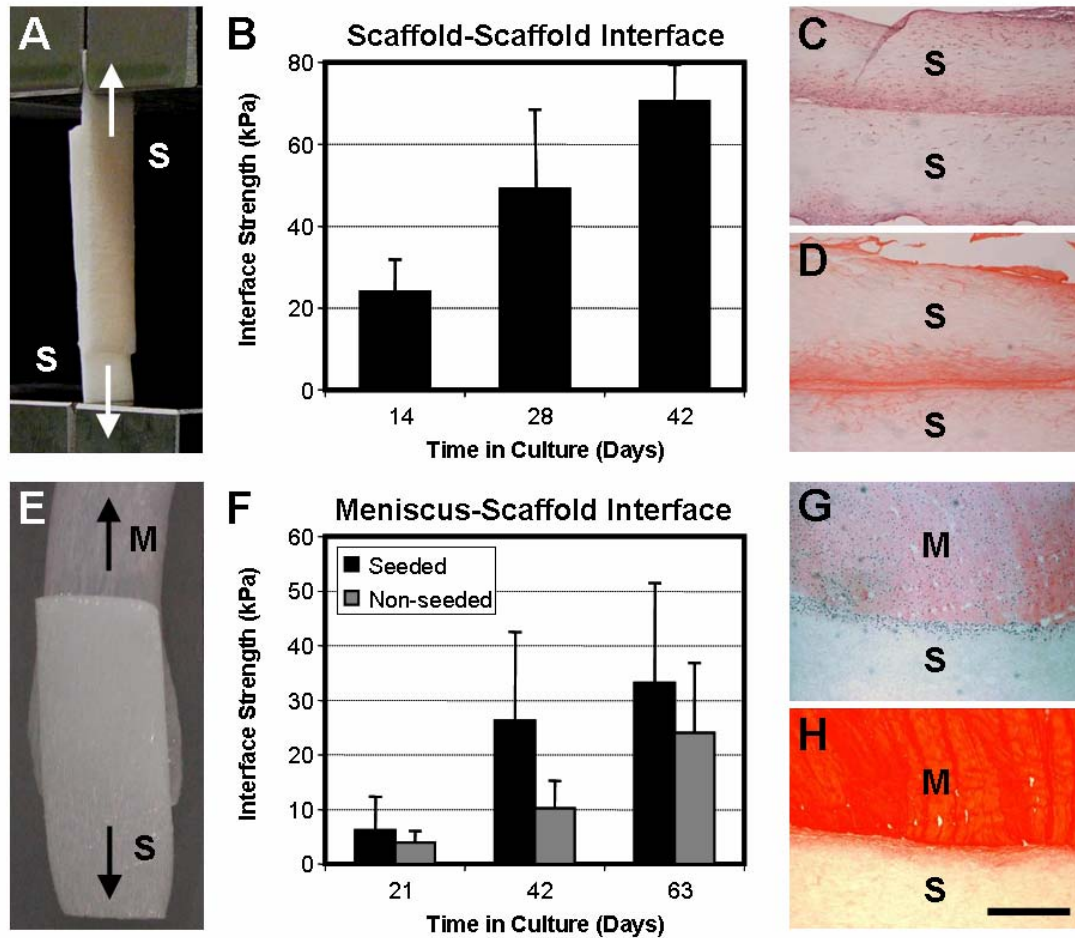


**Figure 11-6: Interfacing nanofibrous constructs.** Scaffold-scaffold (A, S-S) and scaffold-menisus (E, S-M) constructs were formed and cultured for up to 9 weeks *in vitro*. In both cases, mechanical strength of the interface increased with time (B and F), and new matrix was deposited at the interface (C: H&E and D: PSR for S-S constructs, G: H&E and H: PSR for S-M constructs).

In addition to the challenge of integrating scaffolds with adjacent meniscus tissue, a lamellar approach to forming wedge constructs presents a limitation in the size of the defect that can be filled. For complex meniscal tears where a total meniscectomy is performed, folding a replacement for the entire meniscus is impossible given the starting material of a uniformly aligned nanofibrous sheet. In such cases, a different approach may be adopted to directly electrospin wedge-shaped annuli. To enable this fabrication process, we have modified our rotating collecting mandrel to form an annular wedge

shaped crevice (**Figure 11-7A-D**). By grounding the internal margin of this crevice while insulating the outer surfaces, nanofibers will be attracted to the annular cleft space and will build up with collection time (**Figure 11-7E**). This will produce an annular scaffold with a wedge cross-section, which can then be bisected to form semi-circular segments (**Figure 11-7F**). Given the larger scale of these structures, the use of sacrificial fiber as described in Chapters 4-5 may be especially relevant for these constructs, whether they be seeded and cultured *in vitro* or directly implanted acellularly.

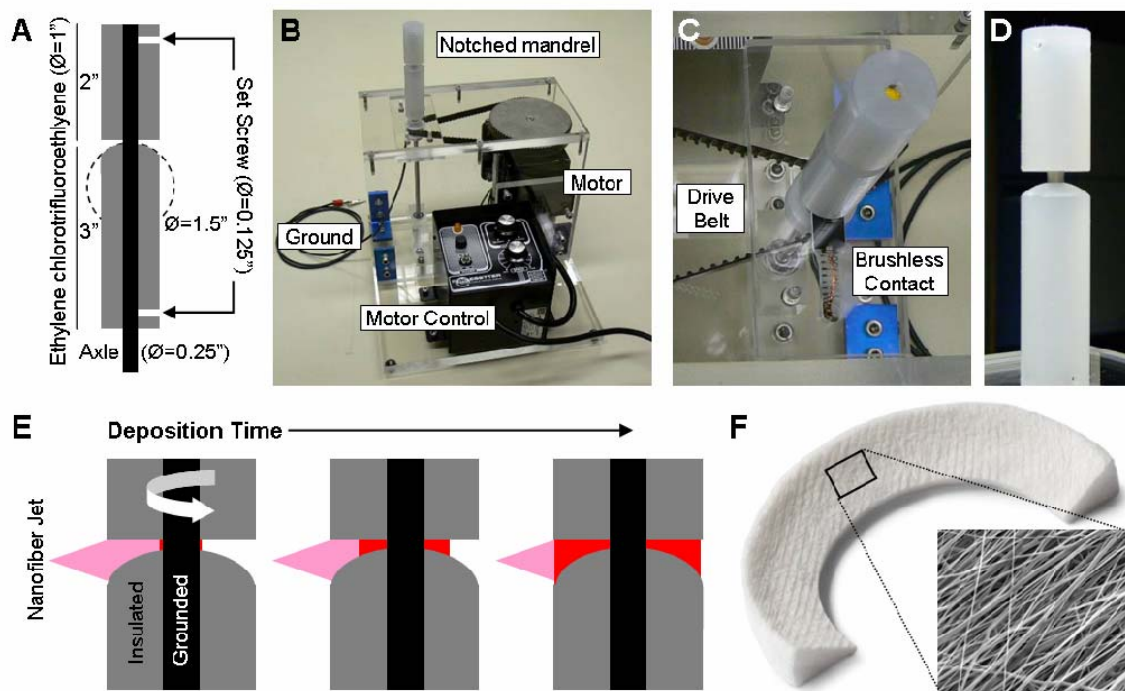


**Figure 11-7: Direct electrospinning of a wedge-shaped annulus. A) Schematic of a modified collection mandrel for direct electrospinning of meniscus implants. B-D) Images of the novel electrospinning device. E) Formation of a meniscus-shaped scaffold with gradual nanofiber deposition into the wedge-shaped crevice. F) Resulting semi-annular meniscus scaffold depicting the direction of constituent aligned nanofibers.**

### 11.2.6 Animal Models of Meniscus Repair

As new enabling technologies are developed to restore the function of the meniscus, appropriate animal models are required to test engineered construct efficacy in the

context of the demanding load-bearing environment of the native tissue. Further, since the primary role of the meniscus is to protect the underlying cartilage, engineered constructs must be tested in a model that is sufficiently aggressive to demonstrate cartilage preservation. A number of animals have been used to study meniscus structure, function, and mechanobiology. For example, rabbit MFC biosynthetic activities are altered with joint instability (Hellio Le Graverand et al. 2001; Hellio Le Graverand et al. 2001). In rats, exercise changes meniscus biochemical content (Vailas et al. 1986). While useful, these animal models are generally too small to assess changes in the mechanical properties of the meniscus and adjacent tissues, or to evaluate meniscus repair devices. Thus most meniscus repair studies use large animals such as canine, caprine, or ovine models. Compared to canine, ovine models are particularly useful for evaluating meniscus injury and repair as their menisci are closer in size to that of the human, and show similar loading patterns (Jackson et al. 1992). Consistent with smaller mammals, proteoglycan production is decreased in canine meniscus with immobilization (Djurasovic et al. 1998) and cartilage erodes with meniscus damage or removal in dogs and sheep (Elliott et al. 1999; Wyland et al. 2002).

Moving towards clinical implementation of a meniscal repair strategy predicated on nanofibrous scaffolds, we have begun to develop a suitable large animal model to assess the mechanical and joint preserving features of these novel constructs. In this endeavor, we have devised a new surgical approach to expose the central aspect of the medial meniscus (**Figure 11-8**). The surgical approach involves a block osteotomy of the medial femoral condyle, which provides a birds-eye view of the meniscus and reveals a

straightforward surgical path for the creation of a defect and subsequent repair with a nanofibrous construct. Most importantly, it preserves the intra-articular cruciate ligaments which do not heal readily and whose transection directly spurs osteoarthritic changes in the articular surfaces (McDevitt et al. 1977; Johnson et al. 1990; Brandt et al. 1991; Batiste et al. 2004). Despite the invasiveness of the procedure, the block osteotomy can be readily reduced to restore normal loading of the medial compartment of the knee. Implanted constructs are initially protected by an Achilles tenotomy, which enforces non-load bearing conditions in the operated joint for up to 8 weeks.

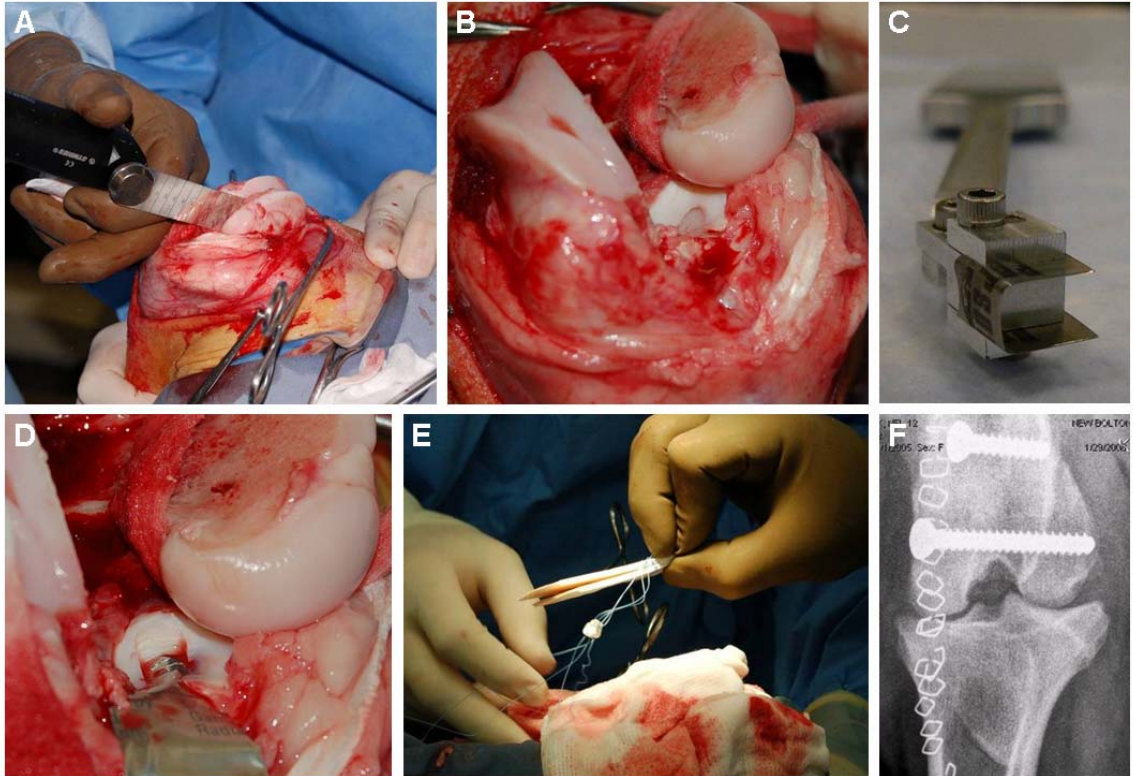


**Figure 11-8: Ovine meniscal defect model. A block osteotomy is performed on the medial femoral condyle (A), providing a birds-eye view of the meniscus (B). Using a custom defect tool (C) a 6×6mm portion of the inner medial meniscus is removed (D) and replaced with a suture-ready wedge-shaped construct (E). F) Radiograph of the sheep stifle following reduction of the osteotomy.**

The model has been explored with a four month study of joint stability and cartilage integrity following osteotomy. Adequate reduction of the osteotomy was achieved, with all animals beginning normal weight bearing within 6-8 weeks of surgery and showing no evidence of cartilage erosion over the course of four months. Ongoing studies are now evaluating changes in mechanical and histological properties of the tibial plateau cartilage with sham (osteotomy) and meniscal defect conditions, as well as with repair using nanofibrous scaffolds. Validation of this large animal model will provide a sound testbed for the future assessment of novel construct formulations (such as those described above), as well as new approaches to the surgical fixation of implants.

#### ***11.2.7 Outcome Assessments for Meniscus Tissue Engineering Strategies***

The animal studies outlined above show promise for the evaluation of new meniscus repair devices for both partial defect repair as well as whole meniscus implantation. Standard measures of meniscus volume and cartilage health, including India ink staining of surfaces, histological analysis of both the implant and the integration site, and mechanical assessment of neo-meniscus and cartilage tissue all provide valuable information regarding the efficacy of the engineered repair. Additionally, clinical methods of analysis (lameness scores) provide information about recovery of function after implantation. A drawback to these studies, however, is the long time course required to demonstrate real efficacy. In humans, while removal of increasing amounts of meniscus tissue during meniscectomy procedures hastens the rate of cartilage erosion and joint space narrowing, this process still takes years to fully develop into symptomatic OA. Outcomes for most animal studies, while thorough and rigorous, do not generally

test these long time periods due to cost considerations. These long time intervals also lengthen the crucial engineering process of design and revision. To expedite this engineering process, new methods should be adopted. For example, a recent study by Maher and co-workers used a sheep model of partial and complete meniscectomy to map pressure distribution with meniscus removal (Cottrell et al. 2008). In this study, sheep knee joints were mounted in a knee testing device programmed to apply normal sheep gait dynamics and forces across the joint, while simultaneously recording location and magnitude of load transmission with an electronic pressure sensor. Such techniques can readily be converted to assay the load transmission in engineered constructs immediately upon implantation, as well as in joints after various periods of *in vivo* integration and maturation. Correlating long-term clinical, mechanical, and histological outcomes from studies such as these with changing design parameters in the original implant may decrease the revision time in technology development, and expedite development and refinement of repair methods. When technologies transition to human application, as has recently occurred for the CMI implant (Rodkey et al. 2008), thorough evaluation is limited to patient surveys of function, second-look arthroscopies and biopsies of neo-tissue, as well as MRI imaging of joint structures. Incorporating these same analysis tools into animal models may help to unite these model systems with clinical application.

### **11.3 CONCLUSION**

Numerous cell- and biomaterial-based strategies have been developed for enhancing meniscus repair. Natural and synthetic scaffolds have shown some promise in creating replacement constructs *in vitro* and *in vivo*. In this thesis, we present one novel

fabrication methodology that has potential to direct the formation of organized ECM that better recapitulates the native tissue. An additional hurdle is the identification of the most appropriate cell source, and/or the mobilization of endogenous cells. We have demonstrated the potential of meniscus fibrochondrocytes from native tissue, as well as the ability of mesenchymal stem cells to elaborate a fibrocartilaginous matrix. Clinical application will require evaluation of the most appropriate cell source, as well as the most efficient means of their isolation and application. Currently, it remains to be established whether a cell-based strategy is essential to success and divergent strategies all hold potential. As examples, acellular scaffolds could be implanted and colonized *in situ* by endogenous cells, previously isolated bone marrow derived stem cells could be incorporated at the time of resection and repair, or MFCs could be isolated during meniscectomy and used in cultivating a functional meniscus construct to be implanted in a second repair surgery. Continued optimization of these tissue engineering efforts may also include the use of *in vitro* bioreactors and anabolic culture environments to produce constructs that more completely recapitulate the form and function of the native tissue. Additional practical considerations, such as scale-up and quality control of fabricated constructs, and new surgical approaches to enable arthroscopic replacement must be investigated. Furthermore, methodologies for the fixation of these constructs into the repair site, as well as the proper rehabilitation regimen that allows for continued *in vivo* maturation and integration will also be required. While still in its early stages, the realization of a functional engineered meniscus construct based on nanofibrous scaffolds may enhance the repair of damaged meniscus, correcting what is otherwise a progressively debilitating and untreatable orthopaedic condition. Moreover, while the

focus of the work described in this thesis is the knee meniscus, these same enabling technologies may be incorporated into strategies for the repair of other fiber-reinforced tissues, such as tendon, ligament, and the intervertebral disc. These tissues all share a common developmental process, wherein fiber alignment is established early in development, and adult function relies on increasing fiber-reinforcement through guided ECM deposition. Thus overcoming limitation in meniscus tissue engineering with these novel scaffolds may have significant impact on the development of engineered replacements for these other similar tissues, and together, dramatically enhance the future of allograft science and tissue engineering via the provision of novel fiber-reinforced constructs for implantation.

# ***APPENDIX I: MATLAB SCRIPTS***

## **11.4 TENSILE STIFFNESS CALCULATION**

```
% title: bmod.m
% author: brendon baker
% contact: bambren@seas.upenn.edu
% description: reads, displays, and calculates stiffness from
% force/displacement data

% data format, from instron output
% column 1 = time
% column 2 = displacement
% column 3 = load

% clear existing workspace
clear
close all

% PARSE DATA
% open file prompt
[filename, pathname, filterindex] = uigetfile('*.csv', 'Open Data
File');
cd(pathname);

% if user hits cancel, exits script
if filterindex == 0
    break;
else
    strcat(pathname, filename);
end

% acquire numerical data as variable RAWDATA, this is a 3 column matrix
% data column1 = time
% data column2 = displacement
% data column3 = force
data = xlsread(filename);

% remove all data after failure
[value, maxloadindex] = max(data(:,3));
data = data(1:maxloadindex,:);

% PLOT FORCE VS DISP AND ALLOW USER TO PICK POINTS
% gui placement and dimension
resolution = get(0, 'ScreenSize');
set_y = resolution(4) - 600;
figure(1)
set(1, 'Position', [100 set_y 600 600]);

% setup gui buttons and callbacks
currentfile = uicontrol('Position', [30 570 400 20], 'Style', 'text');
set(currentfile, 'BackgroundColor', [0.8 0.8 0.8], 'String', filename);
set(currentfile, 'FontSize', 12.0, 'HorizontalAlignment', 'left');
```

```

leftboundradio = uicontrol('Position',[30 50 160
25],'BackgroundColor',[0.8 0.8 0.8],'Style','radio');
set(leftboundradio,'String','Left
boundary','Callback','radiochoice=1;','ForegroundColor','green');

rightboundradio = uicontrol('Position',[30 30 160
25],'BackgroundColor',[0.8 0.8 0.8],'Style','radio');
set(rightboundradio,'String','Right
boundary','Callback','radiochoice=2;','ForegroundColor','cyan');

resultframe = uicontrol('Position',[240 10 200
60],'BackgroundColor',[0.8 0.8 0.8],'Style','frame');
resultbox = uicontrol('Position',[245 15 190 50],'BackgroundColor',[0.8
0.8 0.8],'Style','text','HorizontalAlignment','left');

calculatebutton = uicontrol('Position',[480 45 100
25],'BackgroundColor',[0.8 0.8 0.8]);
set(calculatebutton,'String','Calculate','Callback','calculate=1;');

okbutton = uicontrol('Position',[480 10 100 25],'BackgroundColor',[0.8
0.8 0.8]);
set(okbutton,'String','OK','Callback','done=1;');

% initial values for callback variables
done = 0;
calculate = 1;
radiochoice = 0;

% estimates max slope between bounds
% leftbound and rightbound index the range over which slope is
calculated
leftbound_index = 1;
rightbound_index = length(data);

% calculations of initial points
step = 10; % movement made for each calculation
interval = 100; %10hz sampling at .1%/s -> 100pts = 1% strain range

% initialize variables
start = 1;
total_steps = floor((length(data)-interval)/step);
linear_stiffness = 0;

% GUI CONTROL
while done ~= 1

    % calculate button functions
    if calculate == 1
        % iterate through truncated data set performing robustfit at
set interval,
        % find max slope and store that range
start = leftbound_index;
stop = start + interval;

```

```

        total_steps = floor(((rightbound_index-leftbound_index)-
interval)/step);
        linear_stiffness = 0;
        for i=1:total_steps
            fit = robustfit(data(start:stop,2),data(start:stop,3));
            if fit(2,1) >= linear_stiffness
                linear_stiffness = fit(2,1);
                left_index = start;
                right_index = stop;
            end
            start = start + step;
            stop = stop + step;
        end

        % show results
        set(resultbox,'String',strvcat(['linear stiffness: ',
num2str(linear_stiffness),'MPa']));

        % plot data and boundaries
        figure(1)
        subplot('Position',[.10 .20 .80 .73]);
        plot(data(:,2), data(:,3))
        hold on;
        plot(data(leftbound_index,2),data(leftbound_index,3),'go',
data(rightbound_index,2), data(rightbound_index,3),'co');
        plot(data(left_index,2),data(left_index,3),'ro',
data(right_index,2), data(right_index,3),'ro');
        xlabel('displacement');
        ylabel('load');
        hold off;

        % reset the calculate button
        calculate = 0;
    end

    % reset radiochoice to turn off ginput
    radiochoice = 0;

    % pause needed so that clicks have time to change variable values
    pause(.3)

    % change ginput with radio button choice, also make radio buttons
mutually exclusive
    switch radiochoice
        case 1
            set(rightboundradio,'Value',0);
            [xclick, yclick] = ginput(1);
            [distance, leftbound_index] = min(abs(data(:,2) - xclick));
        case 2
            set(leftboundradio,'Value',0);
            [xclick, yclick] = ginput(1);
            [distance, rightbound_index] = min(abs(data(:,2) -
xclick));
    end
end

```

```

end

% calculate toe stiffness (initial 1% strain)
fit = robustfit(data(1:100,2),data(1:100,3));
toe_stiffness = fit(2,1)

% determine intersection of toe and linear regions using
intersections.m
x = [0:0.01:5];

% define line for toe region (assume intersects at origin)
for i=1:length(x)
    toe_y(i) = toe_stiffness*x(i);
end

% define line for linear region
x1 = data(left_index,2);
y1 = data(left_index,3);
x2 = data(right_index,2);
y2 = data(right_index,3);
b = (y1*x2-x1*y2)/(x2-x1);
for i=1:length(x)
    linear_y(i) = linear_stiffness*x(i) + b;
end

% find intersection using intersections.m
[heal_x heal_y] = intersections(x, toe_y, x, linear_y);

% outputs to csv file
fid2 = fopen('bmod_data.csv','a+');
fprintf(fid2,'%s %g %g %g \n',filename, toe_stiffness,
linear_stiffness, heal_x);

% prompt user to run the program again
ButtonName = questdlg('Run bmod again?', filename, 'Yes','No','Yes');

switch ButtonName,
    case 'Yes',
        bmod
    case 'No',
        disp('Data exported to bmod_data.csv')
        type bmod_data.csv
end

fclose('all');

% clean up
close all

```

## 11.5 CROSS-SECTIONAL AREA CALCULATION

```

% title: giz.m
% author: brendon baker

```

```

% contact: bambren@seas.upenn.edu
% description: simplified code for gizmo sample measuring device,
% includes a correction algorithm to adjust for slants in the table

% clean up
clear all
close all

% DATA ACQUISITION AND SORTING
% open file and parse data
[filename, pathname] = uigetfile('*.','Choose Data File');
rawdatafile = fullfile(pathname, filename)
rawdata = load(rawdatafile); % [t, x, y]
index = [1:1:length(rawdata)];
tdata = rawdata(:,1);
xdata = rawdata(:,2);
ydata = rawdata(:,3);

% make new figure and maximize its size
figure(1);
units = get(1,'units');
set(1,'units','normalized','outerposition',[0 0 1 1]);
set(1,'units',units);

% PASS DISCRIMINATION, user defines the starts/ends of each pass
plot(index,xdata);
pass_start = [];
pass_end = [];
[xclick, yclick] = ginput;
for i=1:2:length(xclick)
    pass_start = [pass_start; round(xclick(i))];
    pass_end = [pass_end; round(xclick(i+1))];
end
num_passes = length(xclick)/2;

% SORT INTO DISTINCT DATASETS CONTAINING A PASS EACH
for i=1:num_passes
    pass{i} = rawdata(pass_start(i):pass_end(i),:);
    % flip certain passes to make them all progress in the same
    direction
    if pass{i}(1,2)>pass{i}(length(pass{i}),2)
        pass{i} = flipud(pass{i});
    end
end

% SAMPLE DISCRIMINATION, user defines portion of each pass on sample
for i=1:num_passes
    % user picks points
    plot(pass{i}(:,2),pass{i}(:,1));
    grid on;
    [xclick, yclick] = ginput(1);

```

```

[trash location] = min(abs(pass{i}(:,2) - xclick));
sample_left(i) = location;
[xclick, yclick] = ginput(1);
[trash location] = min(abs(pass{i}(:,2) - xclick));
sample_right(i) = location;

% CORRECTION - try to normalize the left side to zero and adjust
% the rest accordingly, and adjust the entire pass by the table's
slope

% calculate slope across all points within a pass + outside of
sample
xcorr_data = [pass{i}(1:sample_left(i),2);
pass{i}(sample_right(i):length(pass{i}),2)];
tcorr_data = [pass{i}(1:sample_left(i),1);
pass{i}(sample_right(i):length(pass{i}),1)];
fit = robustfit(xcorr_data,tcorr_data);
slope(i) = fit(2);

% correct whole pass by avg height of left side
corr_height(i) = mean(pass{i}(1:sample_left(i),1));
corr_pass{i} = pass{i} - corr_height(i);

% correct by the slope
slope_corr = 0;
delta_x{i} = diff(corr_pass{i}(:,2));
for j=1:length(delta_x{i})
    corr_pass{i}(j,1) = corr_pass{i}(j,1) - slope_corr;
    slope_corr = slope_corr + delta_x{i}(j)*slope(i);
end

% replot corrected data
plot(corr_pass{i}(:,2),corr_pass{i}(:,1));
grid on;
pause(1);

% isolate portion of pass that is sample
sample{i} = corr_pass{i}(sample_left(i):sample_right(i),1:2);

end

% CSA PLOTS & CALCULATION, using defaults of trapz
% replot corrected data, sample portion, and calculate csa of each one
for i=1:num_passes
    plot(corr_pass{i}(:,2),corr_pass{i}(:,1), 'b-');
    plot(sample{i}(:,2),sample{i}(:,1), 'r-')
    axis equal;
    grid on;
    hold on;
    csa(i) = abs(trapz(sample{i}(:,2),sample{i}(:,1)));
    thickness(i) = mean(sample{i}(200:length(sample{i}))-200);
end
hold off;
csa_avg = mean(csa);

```

```

csa_std = std(csa);
thickness_avg = mean(thickness);

% OUTPUT AND CLOSURE
% outputs to csv file
fid = fopen('giz_data.csv','a+');
fprintf(fid,'%s %g %g %g %i %s\n', rawdatafile, csa_avg, csa_std,
thickness_avg, num_passes, num2str(csa));

csa
waitforbuttonpress;

% prompt user to run the program again
ButtonName = questdlg('giz again?', filename, 'Yes','No','Yes');

switch ButtonName,
    case 'Yes',
        giz
    case 'No',
        disp('Data exported to giz_data.csv')
        close(1);
        type giz_data.csv
end

```

## 11.6 CYCLIC TENSION DATA ANALYSIS

```

% title: cycl.m
% description: analysis of cyclic loading tests
% authors : amy silverstein and brendon baker
% description: determines max load, hysteresis, and dynamic modulus
from
% cyclic tensile data

close all

% PARSE DATA
% open file prompt
[filename, pathname, filterindex] = uigetfile('*.csv', 'Open Data
File');
cd(pathname);

% generates strain and stress in the 5th and 6th columns
data = xlsread(filename);
data(:,5) = data(:,5)/lngth;
data(:,6) = data(:,6)/csa;

% CALCULATIONS
counter = length(data)/100;
startpt = 1
endpt = 100
for i=1:counter
    xaxis(i) = mean(data(startpt:endpt,4));
    cycle{i} = data(startpt:endpt,5:6);
end

```

```

startpt = startpt + 100;
endpt = endpt + 100;
start = 1;
stop = 8;

% slope of the curve to get modulus
modulus = 0;
for j=1:40
    fit =
robustfit(cycle{i}(start:stop,1),cycle{i}(start:stop,2));
    if fit(2,1) >= modulus
        modulus = fit(2,1);
    end
    start = start + 1;
    stop = stop + 1;
end
mod(i)=modulus;

% hysteresis is the difference in the areas of the upstroke and
% downstroke curves
hyst(i) = trapz(cycle{i}(1:50,1),cycle{i}(1:50,2)) -
trapz(cycle{i}(51:100,1),cycle{i}(51:100,2));

% max load is maximum pt of each stroke
max_load(i)= max(cycle{i}(:,2));

end

% PLOTTING
figure
plot(xaxis,hyst)
figure
plot(xaxis,max_load)
figure
plot(xaxis,mod)

% OUTPUTS
output = [xaxis; hyst; max_load; mod];

% outputs to csv file
outputfilename = strcat('cycl3_',filename);
csvwrite(outputfilename,output.');
```

## 11.7 COMPRESSIVE EQUILIBRIUM MODULUS CALCULATION

```

% title: pest.m
% author: brendon baker
% contact: bambren@seas.upenn.edu
% description: analyzes stress-relaxation data from compressive tests,
% called with the thickness in mm, and core size in mm

function modulus = pest(thickness)
```

```

core = 2;

% PARSE DATA
% open file prompt
[filename, pathname, filterindex] = uigetfile('*.*', 'Open Data File');

% if user hits cancel, exits script
if filterindex == 0
    return
else
    strcat(pathname, filename);
end

% open the file
fid = fopen(strcat(pathname, filename), 'r');

% go through the whole file and count the numbers in each line
line_count = 1;
line = fgetl(fid);
while mean(line ~= -1) ~= 0
    line_size(line_count) = length(str2num(line));
    line_count = line_count + 1;
    line = fgetl(fid);
end
close
end_line = line_count - 1;

% close and reopen the file and parse into 'data'
fclose(fid);
fid = fopen(strcat(pathname, filename), 'r');

% acquire numerical data as variable RAWDATA, this is a 3 column matrix
for counter = 1:end_line
    rawdata(counter, :) = str2num(fgetl(fid));
end

time = rawdata(1:end_line, 1);
force = rawdata(1:end_line, 2);
disp = rawdata(1:end_line, 3);

% clean up
fclose(fid);
% clear filterindex fid line line_size trash_line counter

% CALCULATIONS
Fi = mean(force(1:25));
Ff = mean(force(end_line-50:end_line));
Di = mean(disp(1:25));
Df = mean(disp(end_line-50:end_line));

% converting to g to N and um to mm
stiffness = (Ff-Fi)*9.80665/(Df-Di);
CSA = (core/2)^2*3.14159;

% output modulus in kPa

```

```

modulus = stiffness * thickness / CSA *1000;

% outputs to csv file
fid2=fopen('pest_data.csv','a+');
fprintf(fid2,'%s %s %g %g \n',pathname, filename, thickness,
modulus);

fclose('all');

type pest_data.csv

```

## 11.8 SIMPLE MODEL OF COMPOSITE SCAFFOLDS

```

% Modeling ElectroSpun Scaffolds = MESS
% author: brendon baker
% email: bambren@seas.upenn.edu
% description: a simple model of randomly, but oriented fibers and
% calculations for the resulting pore sizes

% clean up
clear all
close all

% hard-coded variables
angle = 20; % max angle defining range of angles present
diameter = 3; % fiber diameter in pixels
fiber_count = 10;
iterations = 20;

% define empty space of scaffold
scaffold = ones(1000);

% add fibers in k iterations, each time adding fiber_count # of fibers
for k=1:iterations
    for i=1:fiber_count
        slope(i)= tand((rand-.5)*angle);
        start_pt(i) = rand*1000;
        for j=1:1000
            fiber_y{i}(j) = round(start_pt(i) + slope(i)*j);
            if fiber_y{i}(j)<2 || fiber_y{i}(j)>999
                break;
            end
            scaffold(j, (fiber_y{i}(j)-1))=0;
            scaffold(j, fiber_y{i}(j))=0;
            scaffold(j, (fiber_y{i}(j)+1))=0;
        end
    end
end

% display scaffold
imshow(scaffold);

% break up pores into discrete
pore_label = bwlabeln(scaffold);

```

```

pore_count(k) = max(max(pore_label));

% figure out pixel size of each pore
for i=1:pore_count(k)
    pore_size{k}(i) = length(find(pore_label==i));
end
avg_pore_size(k) = mean(pore_size{k});

% outputs
output_filename = strcat('mess_bin_',num2str(k),'.csv');
fid2 = fopen(output_filename,'a+');
for i=1:pore_count(k)
    fprintf(fid2,'%g \r',pore_size{k}(i));
end
fclose(fid2);

% to make figure pics
% if k==2 || k==10 || k==18
%     waitforbuttonpress
% end

end

```

## 11.9 NUCLEAR ASPECT RATIO AND ORIENTATION DETERMINATION

```

% title: NARC (nuclear aspect ratio calculator)
% author: brendon baker, brendon.baker@gmail.com
% description: determines the nuclear aspect ratio (long/short axis) and
% orientation angle with respect to the horizontal axis of the image,
% via principle component analysis
% note: for use with 10X images dapi-stained images

% clean up
clear all
close all

% DAPI IMAGE - AUTOMATED NAR AND ANGLE CALCULATION
% open file prompt, if user hits cancel exits script
[filename, pathname, filterindex] = uigetfile('*.*jpg', 'Open DAPI
Image');
cd(pathname)
if filterindex == 0
    return
else
    name = strcat(pathname,filename);
end

% open the file, convert to gray scale and threshold
orig_dapi_img = imread(name); % 3D matrix
gray_dapi_img = rgb2gray(orig_dapi_img); % 2D matrix
threshlvl = graythresh(gray_dapi_img)
%threshlvl = .15;
thresh_dapi_img = im2bw(gray_dapi_img,threshlvl);

```

```

% image display
figure(1); imshow(orig_dapi_img, 'Border', 'tight');
figure(2); imshow(thresh_dapi_img, 'Border', 'tight');
final_dapi_img = thresh_dapi_img;

% initializations
k=1;

% cluster each nucleus and determine centroid
[nucleus_cluster_matrix, nucleus_cluster_number] =
bwlabeln(thresh_dapi_img);

% determines centroid of each nucleus, uses PCA to find the long and
short
% axis of the shape, and finds the angle between the long axis a
for i=1:nucleus_cluster_number
    [row,col] = find(nucleus_cluster_matrix == i);
    if length(row)> 100 && length(row)<300 % excludes any cluster
that's likely not a nucleus
        nucleus_cluster_centroid{k} =
[round(mean(row)), round(mean(col))];
        nucleus_set{k} = [row,col];
        total_matrix = zeros(2);
        for j=1:length(nucleus_set{k})
            point_vector = nucleus_set{k}(j,:) -
nucleus_cluster_centroid{k};
            point_matrix = point_vector.*point_vector;
            total_matrix = total_matrix + point_matrix;
        end
        % find eigenvalues/vectors and sort
[eigenvectors,eigenvalues] = eig(total_matrix);
        if max(eigenvalues(:,1))>max(eigenvalues(:,2))
            long_axis = max(eigenvalues(:,1)).^0.5;
            short_axis = max(eigenvalues(:,2)).^0.5;
        else
            long_axis = max(eigenvalues(:,2)).^0.5;
            short_axis = max(eigenvalues(:,1)).^0.5;
        end
        % NAR and angle calculation
area(k) = length(row);
NAR(k) = long_axis/short_axis;
angle(k) = acosd(dot(eigenvectors(:,1), [1;0]));
k=k+1;

        clear total_matrix point_matrix point_vector long_axis
short_axis
    else
        for l=1:length(row) % remove that cluster from the image
            final_dapi_img(row(l),col(l))=0; % remember, matrix vs img
coord
        end
    end
    clear row col
end

```

```

figure(3); imshow(final_dapi_img, 'Border', 'tight');

% OUTPUTS
% calculations
NAR_mean = mean(NAR)
NAR_std = std(NAR)
angle_mean = mean(angle)
NAR = transpose(NAR);
angle = transpose(angle);
data_out = [NAR, angle];
area = transpose(area);

% outputs to excel file
output_filename = strcat(filename, '.xls');
xlswrite(output_filename, NAR, 'Sheet1', 'A1');
xlswrite(output_filename, angle, 'Sheet1', 'B1');
xlswrite(output_filename, area, 'Sheet1', 'C1');

% write images
imwrite(thresh_dapi_img, strcat(filename, '_', num2str(threshlvl), '_thresh
.jpg'), 'jpeg')
imwrite(final_dapi_img, strcat(filename, '_final.jpg'), 'jpeg')

% prompt user to run the program again
waitforbuttonpress;
ButtonName=questdlg('Run NARC again?', filename, 'Yes', 'No', 'Yes');
switch ButtonName,
    case 'Yes',
        narcwar
    case 'No',
        disp('Data exported to current directory')
end

```

## 11.10 SEMI-QUANTITATIVE HISTOLOGY

```

% title: doh.m (densitometry of histology)
% author: brendon baker, brendon.baker@gmail.com
% description: determines intensity profiles at 20 intervals
% horizontally-oriented across an image

% clean up
clear all
close all

% open file prompt, if user hits cancel exits script
[filename, pathname, filterindex] = uigetfile('*.tif', 'Open Image');
cd(pathname)
if filterindex == 0
    return
else
    name = strcat(pathname, filename);
end

```

```

% open the file and convert to gray scale
gray_img = rgb2gray(imread(name));

% convert to bw
threshlvl = graythresh(gray_img);
bw_img = im2bw(gray_img, threshlvl);

% grab data
for i=1:20
    gray_line(i,:) = gray_img(40*i,:);
    bw_line(i,:) = bw_img(40*i,:);
end

for i=1:1100
    gray_avg(i) = mean(gray_line(:,i));
    inv_gray_avg = 255-gray_avg;
    bw_avg(i) = mean(bw_line(:,i));
    inv_bw_avg = 1-bw_avg;
end

% output
filename_out = strcat(filename, '_doh.xls');
[success,message] = xlswrite(filename_out,inv_gray_avg', 'Sheet1', 'A1');
[success,message] = xlswrite(filename_out,inv_bw_avg', 'Sheet1', 'B1');

figure
plot(inv_gray_avg)
waitforbuttonpress
figure
plot(inv_bw_avg)
waitforbuttonpress

% rerun?
ButtonName = questdlg(filename, 'run again?', 'Yes', 'No', 'Yes');
switch ButtonName,
    case 'Yes',
        doh
    case 'No',
        close all
end

```

## 11.11 COMPILATION OF MECHANICAL AND VIC2D STRAIN DATA

```

% name: vic2d.m (vic2d/instron collate to data)
% author: brendon baker, an nguyen
% description: compiles the vic2d-derived strain files and instron
% csv's into one output xls
% required file naming scheme:
%   -all vic2d csv's need to be of the form: 'samplename_#.csv',
%     where # = 001, 002, 003, etc.
%   -instron csv needs to be in the form 'samplename.csv'

```

```

clear

% hardcoded variables
frame_rate = 2 % seconds between pictures

% get vic2d file names, should be of the form CF1_1_01.csv
[vic_filename vic_pathname, filterindex] = uigetfile('*.csv');
prefix = vic_filename(1:length(vic_filename)-6)
cd(vic_pathname)

% have user enter the CSA of the sample
csa = input('Enter the cross sectional area (mm^2): ');

% VIC2D PARSING
% generate suffixes 01, 02, etc
for i=1:9
    num_suffix{i}=strcat('0',num2str(i));
end
for i=10:100
    num_suffix{i}=strcat('',num2str(i));
end

% initialize variables
step = 1;
exx = [];
eyy = [];
exy = [];
e1 = [];
e2 = [];
disp = [];
load = [];

% iterate through vic2d output csv files so long as they exist
while exist(strcat(prefix,num_suffix{step},'.csv'), 'file') ~= 0,
    % grab all data in each file and store as a maxtrix
    mixed_data = csvread([prefix,num_suffix{step},'.csv'],1,0);

    % find the mean of each variable and add to array.  each array
contains
    % the mean from each of the output files
    exx = [exx; mean(mixed_data(:, 6))];
    eyy = [eyy; mean(mixed_data(:, 7))];
    exy = [exy; mean(mixed_data(:, 8))];
    e1 = [e1; mean(mixed_data(:, 9))];
    e2 = [e2; mean(mixed_data(:, 10))];
    step = step + 1;
end

% total number of analyzed pictures
total_pts = step - 1;

% INSTRON PARSING
% open the instron csv file

```

```

[ins_filename ins_pathname, filterindex] = uigetfile('*.csv');
cd(ins_pathname)
fid = fopen(ins_filename);

% hardcoded number of header lines for instron 5848 output
header_lines = 2;

% get rid of unwanted headers
for i = 1:header_lines
    trash_line = fgetl(fid);
end

% acquire numerical data as variable RAWDATA, this is a 3 column matrix
counter = 1;
next_line = fgetl(fid);
while next_line ~= -1
    rawdata(counter,:) = str2num(next_line);
    next_line = fgetl(fid);
    counter = counter + 1;
end

% initialize variables
filtered_data = [];
time = [];
disp = [];
load = [];
stress = [];

% filter data to only include data corresponding to acquired pictures
for i=1:total_pts
    [minvalue location] = min(abs(rawdata(:,1)-i*frame_rate));
    filtered_data = [filtered_data; rawdata(location,:)];
end

% distribute data from FILTERED_DATA
time = filtered_data(:,1);
disp = filtered_data(:,2);
load = filtered_data(:,3);

% calculate stress
stress = load/csa;

% combine all data into one matrix
temp = [time(1:total_pts) eyy(1:total_pts) stress(1:total_pts)
exx(1:total_pts) exy(1:total_pts) e1(1:total_pts) e2(1:total_pts)
disp(1:total_pts) load(1:total_pts)];
dim = size(temp);

% generate output matrix DATA_OUT with column titles
data_out = cell(dim(1)+1, dim(2));
data_out(1,1) = {'time (s)'};
data_out(1,2) = {'eyy'};
data_out(1,3) = {'stress (MPa)'};
data_out(1,4) = {'exx'};
data_out(1,5) = {'exy'};

```

```

data_out(1,6) = {'e1'};
data_out(1,7) = {'e2'};
data_out(1,8) = {'disp (mm)'};
data_out(1,9) = {'load (N)'};

for row=2:(dim(1)+1)
    for col=1:dim(2)
        data_out(row,col) = num2cell(temp(row-1, col));
    end
end

% save the data to an excel spreadsheet
cd ..
xlswrite([prefix,'_compiled_data.xls'], data_out);

filtered_data
prefix

```

## 11.12 POISSON RATIO CALCULATION

```

% title: pson.m
% author: brendon baker
% contact: bambren@seas.upenn.edu
% description: calculates poisson ratio data
% notes: need to hand it array 'data', two columns of exx and eyy

% clear existing workspace
close all

% gui placement and dimension
resolution = get(0,'ScreenSize');
set_y = resolution(4) - 600;
figure(2)
set(2,'Position',[400 set_y 600 600]);
clear resolution set_y

% unpack data
exx = data(:,1)*-1;
eyy = data(:,2);

% estimation of linear range with maximum slope
% calculations of initial points
step = 1;
interval = 3;
start = 1;
stop = start + interval;
total_steps = length(data)-(interval+1);
max_slope = 0;

% iterate through entire data set performing robustfit over INTERVAL
number of points,

```

```

% find max slope and store that range
for i=1:total_steps
    fit = robustfit(eyy(start:stop),exx(start:stop));
    if fit(2,1) >= max_slope
        max_slope = fit(2,1);
        maxslope1_index = start;
        maxslope2_index = stop;
    end
    start = start + step;
    stop = stop + step;
end

poisson_ratio = max_slope;

% make plot
subplot('Position',[.10 .20 .80 .73]);
plot(eyy, exx)
hold on;
plot(eyy(maxslope1_index),exx(maxslope1_index),'ro',
eyy(maxslope2_index), exx(maxslope2_index),'ro');
xlabel('eyy');
ylabel('-exx');
hold off;

waitforbuttonpress;

% outputs to commandline and csv
fid=fopen('pson_data.csv','a+');
fprintf(fid,'%g \n',poisson_ratio);
fclose(fid)
type pson_data.csv

% clean up
close

```

### 11.13 CELL INFILTRATION ANALYSIS

```

% CELL INFILTRATION ANALYSIS
% description: clusters each nucleus and determines distance from
% closest point on boundary. allows user to select scaffold boundary
% to exclude all cells in the capsule

% clean up
clear all
close all

% PHASE IMAGE ANALYSIS
% open file prompt, if user hits cancel exits script
[filename, pathname, filterindex] = uigetfile('*.jpg', 'Open PHASE
Image');
cd(pathname)
if filterindex == 0

```

```

    return
else
    name = strcat(pathname,filename);
end

% open the file and convert to gray scale
phase_img = rgb2gray(imread(name));

% create matrix the same size as picture full of zeros
[height, width] = size(phase_img);
lined_img = zeros(height,width);

% user defines TOP edge of the sample
figure(1); imshow(phase_img);
[click_x,click_y] = ginput;
click_count = length(click_x);
for i=1:click_count
    if click_x(i) < 1
        click_x(i) = 1;
    end
    if click_x(i) > 1392
        click_x(i) = 1392;
    end
end

% connect the dots for TOP
for i=1:(click_count-1)
    slope = (click_y(i)-click_y(i+1))/(click_x(i)-click_x(i+1));
    width = click_x(i+1)-click_x(i);

    % go through each x-coord, figure out the y-coord and change the
    % pixel value to the whatever is assigned to 'color'
    for j=1:width+1
        xtarget = floor(click_x(i)) + j;
        ytarget = click_y(i) + slope*j;
        lined_img(floor(ytarget), xtarget) = 255;
        phase_img(floor(ytarget), xtarget) = 255;
    end
end

% user defines BOTTOM edge of the sample
figure(1); imshow(phase_img);
[click_x,click_y] = ginput;
click_count = length(click_x);
for i=1:click_count
    if click_x(i) < 1
        click_x(i) = 1;
    end
    if click_x(i) > 1392
        click_x(i) = 1392;
    end
end

% connect the dots for BOTTOM

```

```

for i=1:(click_count-1)
    slope = (click_y(i)-click_y(i+1))/(click_x(i)-click_x(i+1));
    width = click_x(i+1)-click_x(i);

    % go through each x-coord, figure out the y-coord and change the
    closest
    % pixel value to white
    for j=1:(width+1)
        xtarget = floor(click_x(i)) + j;
        ytarget = click_y(i) + slope*j;
        lined_img(floor(ytarget), xtarget) = 255;
        phase_img(floor(ytarget), xtarget) = 255;
    end
end
figure(1); imshow(phase_img);
waitforbuttonpress;

% cluster each line and put coordinates of each line in cluster_cell
[border_cluster_matrix,border_cluster_number] = bwlabeln(lined_img);
border_count = 1;
for i=1:border_cluster_number
    [row,col] = find(border_cluster_matrix == i);
    temp_border_cluster_cell{i} = [row,col];
    [temp_border_cluster_length(i) columns] =
size(temp_border_cluster_cell{i});
    if temp_border_cluster_length(i) > 500
        border_cluster_cell{border_count} =
temp_border_cluster_cell{i};
        border_cluster_length(border_count) =
temp_border_cluster_length(i);
        border_count = border_count + 1;
    end
end

% THICKNESS ANALYSIS
% determines thickness by finding shortest distance at 10 points along
top
interval = round(border_cluster_length(1)/11);
min_thickness = 1392;
for i=1:10
    for j=1:border_cluster_length(2)
        temp_thickness =
((abs(border_cluster_cell{1}(round(interval*i),1)-
border_cluster_cell{2}(j,1)))^2+(abs(border_cluster_cell{1}(round(inter
val*i),2)-border_cluster_cell{2}(j,2)))^2)^.5;
        if temp_thickness < min_thickness
            min_thickness = temp_thickness;
            temp_thickness_index = j;
        end
    end
    thickness(i) = min_thickness;
    top_index(i) = round(interval*i);
    bot_index(i) = temp_thickness_index;
    min_thickness = 1392;
end

```

```

% connect points in top_index and bot_index
for i=1:10
    slope(i) = 1/((border_cluster_cell{1}(top_index(i),1)-
border_cluster_cell{2}(bot_index(i),1))/(border_cluster_cell{1}(top_ind
ex(i),2)-border_cluster_cell{2}(bot_index(i),2)));
    width(i) = border_cluster_cell{2}(bot_index(i),1) -
border_cluster_cell{1}(top_index(i),1);
    % go through each y-coord, figure out the x-coord and change the
closest
    % pixel value to white
    for j=1:width(i)
        y_target = round(border_cluster_cell{1}(top_index(i),1) + j);
        x_target = round(border_cluster_cell{1}(top_index(i),2) +
slope(i)*j);
        lined_img(y_target, x_target) = 255;
    end
end

% DAPI IMAGE ANALYSIS
% open file prompt, if user hits cancel, exits script
[filename, pathname, filterindex] = uigetfile('*.jpg', 'Open DAPI
Image');
if filterindex == 0
    return
else
    name = strcat(pathname,filename);
end

% open the file and binary convert with threshold=.15
orig_dapi_img = imread(name);
dapi_img = im2bw(orig_dapi_img,.15);

% cluster each nucleus and determine centroid
[nucleus_cluster_matrix,nucleus_cluster_number] = bwlabeln(dapi_img);
for i=1:nucleus_cluster_number
    [row,col] = find(nucleus_cluster_matrix == i);
    nucleus_cluster_centroid{i} = [round(mean(row)),round(mean(col))];
end

% FIND THE MINIMUM DISTANCE BETWEEN EACH NUCLEUS AND A BORDER
min_distance = 1392;
cell_count = 1;
for i=1:nucleus_cluster_number
    % exclusion criteria (outside of top and bottom lines)
    if nucleus_cluster_centroid{i}(1) >
mean(border_cluster_cell{1}(find(nucleus_cluster_centroid{i}(1)==border
_cluster_cell{1}(:,2)),1)) && nucleus_cluster_centroid{i}(1) <
mean(border_cluster_cell{2}(find(nucleus_cluster_centroid{i}(1)==border
_cluster_cell{2}(:,2)),1))
        cell_count = cell_count + 1;
        min_distance = 1392;
        for j=1:2
            for k=1:border_cluster_length(j)

```

```

        distance = (abs(nucleus_cluster_centroid{i}(1)-
border_cluster_cell{j}(k,1))^2+(abs(nucleus_cluster_centroid{i}(2)-
border_cluster_cell{j}(k,2))^2)^.5;
        if distance < min_distance
            min_distance = distance;
        end
    end
end
cell_infiltration(cell_count) = min_distance;
end
end

% convert into um distances and bin
% conversion factors:
% T30 @ 4x: 1.61um/pixel
conversion_factor = 1.62
cell_distance = cell_infiltration * conversion_factor;
bin_num = 6;
bin_interval = 100;
bin = 0;
um_binned_count(1:bin_num) = 0;
for i=1:bin_num
    for j=1:cell_count
        if cell_distance(j) >= bin && cell_distance(j) < (bin +
bin_interval)
            um_binned_count(i) = um_binned_count(i) + 1;
        end
    end
    bin = bin + bin_interval;
end

%convert into percentage infiltration and bin
percent_infiltration = cell_infiltration/(mean(thickness)/2)*100;
perc_bin_num = 4;
perc_bin_interval = 25;
bin = 0;
percent_binned_count(1:perc_bin_num) = 0;
for i=1:perc_bin_num
    for j=1:cell_count
        if percent_infiltration(j) >= bin && percent_infiltration(j) <
(bin + perc_bin_interval)
            percent_binned_count(i) = percent_binned_count(i) + 1;
        end
    end
    bin = bin + perc_bin_interval;
end

% FINAL IMAGE DISPLAY
figure(1); imshow(phase_img);
figure(2); imshow(imread(name));

final_lined_img = im2double(lined_img);
final_img = dapi_img;
for i=1:1040
    for j=1:1392

```

```

        if lined_img(i,j)==255
            final_img(i,j)=255;
        end
    end
end
figure(3); imshow(final_img);

% DATA OUTPUT
% calculate outputs
cell_infiltration = transpose(cell_infiltration);
cell_distance = transpose(cell_distance);
percent_infiltration = transpose(cell_infiltration);
avg_infiltration = conversion_factor * mean(cell_infiltration);
avg_thickness = conversion_factor * mean(thickness);

% outputs to csv file
output_filename = strcat(filename, '.csv');
fid2=fopen(output_filename, 'a+');

fprintf(fid2, 'average infiltration in um: \r');
fprintf(fid2, '%g \r', avg_infiltration);

fprintf(fid2, 'average thickness in um: \r');
fprintf(fid2, '%g \r', avg_thickness);

fprintf(fid2, 'um binned counts: \r');
for i=1:bin_num
    fprintf(fid2, '%g \r', um_binned_count(i));
end

fprintf(fid2, 'percent binned counts: \r');
for i=1:perc_bin_num
    fprintf(fid2, '%g \r', percent_binned_count(i));
end

fprintf(fid2, 'raw values: \r');
for i=1:cell_count
    fprintf(fid2, '%g \r', cell_infiltration(i));
end
fclose(fid2);

```

## ***APPENDIX II: RELATED PUBLICATIONS***

1. **Baker BM**, Shah RP, Huang AH, Mauck RL. “Dynamic Tensile Loading Improves the Functional Properties of MSC-Laden Nanofiber-Based Fibrocartilage,” *Tissue Engineering, Part A*, submitted.
2. Nathan AS, **Baker BM**, Nerurkar NL, Mauck RL. “Mechano-Topographic Modulation of Stem Cell Nuclear Shape on Nanofibrous Scaffolds,” *Acta Biomaterialia*, submitted.
3. **Baker BM**, Nathan AS, Gee AO, Mauck RL. “The Influence of an Aligned Nanofibrous Topography on Human Mesenchymal Stem Cell Fibrochondrogenesis,” 2010, *Biomaterials*, PMID: 20494438.
4. Nerurkar NL, **Baker BM**, Sen S, Wible EW, Elliott DM, Mauck RL. “Nanofibrous Biologic Laminates Replicate the Form and Function of the Annulus Fibrosus,” *Nature Materials*, 8(12):986-92 [\*\*Selected for cover art, December 2009\*\*].
5. **Baker BM**, Handorf AM, Ionescu LC, Li W-J, Mauck RL. “New Directions in Nanofibrous Scaffolds for Soft Tissue Engineering and Regeneration,” 2009, *Expert Review of Medical Devices*, 6(5):515-32.
6. **Baker BM**, Nerurkar NL, Burdick JA, Elliott DM, and Mauck RL. “Fabrication and Modeling of Dynamic Multi-Polymer Nanofibrous Scaffolds,” 2009, *Journal of Biomechanical Engineering*, 131(10):101012 [\*\*Selected for cover art, October 2009\*\*].
7. Mauck RL, **Baker BM**, Nerurkar NL, Burdick JA, Li WJ, Tuan RS, Elliott DM. “Engineering on the Straight and Narrow: The Mechanics of Nanofibrous Assemblies for Fiber-Reinforced Tissue Regeneration,” 2009, *Tissue Engineering: Part B*, 15(2):171-93.
8. **Baker BM**, Gee AO, Sheth NP, Huffman GR, Sennett BJ, Schaefer TP, Mauck RL. “Meniscus Tissue Engineering on the Nanoscale: From Basic Principles to Clinical Application,” 2009, *Journal of Knee Surgery*, 22(1):45-59.
9. **Baker BM**, Nathan AS, Huffman GR, Mauck RL. “Tissue Engineering with Meniscus Cells Derived from Surgical Debris,” 2009, *Osteoarthritis and Cartilage*, 17(3):336-45.
10. **Baker BM**, Gee AO, Metter RB, Nathan AS, Marklein RA, Burdick JA, Mauck RL. “Selective Removal of Sacrificial Fibers Improves Cell Infiltration in Composite Fiber-Aligned Nanofibrous Scaffolds,” 2008, *Biomaterials*, 29(15):2348-58.

11. Tan AR, Ifkovits JL, **Baker BM**, Brey DM, Mauck RL, Burdick JA. “Electrospinning of Photocrosslinked and Degradable Fibrous Scaffolds,” 2008, *Journal of Biomedical Materials Research A*, 87(4):1034-43.
12. **Baker BM**, Mauck RL. “Alignment Enhances the Maturation of Nanofiber-Based Engineered Meniscus Constructs,” 2007, *Biomaterials*, 28(11):1967-77.
13. Sheth NP, **Baker BM**, Huffman GR, Mauck RL, “Emerging Strategies for Meniscus Repair,” 2006, *University of Pennsylvania Orthopaedic Journal*, 18:59-72.

### ***APPENDIX III: RELATED CONFERENCE ABSTRACTS***

1. **Baker BM**, Shah RP, Silverstein AM, Mauck RL. “Tunable nanofibrous composites with sacrificial content enhance cellular colonization and functional tissue formation,” Gordon-Kenan Research Seminar: Signal Transduction by Engineered Extracellular Matrices, June 26-27, 2010, podium.
2. **Baker BM**, Shah RP, Huang AH, Mauck RL. “Dynamic Tensile Stimulation of MSC-Seeded Nanofibrous Constructs,” *6<sup>th</sup> World Congress on Biomechanics*, Singapore, August 1-6, 2010, podium.
3. Huang AH, Farrell MJ, **Baker BM**, Kim MW, Mauck RL. “Mechanical Stimulation Enhances Functional Mesenchymal Stem Cell Chondrogenesis,” *6<sup>th</sup> World Congress on Biomechanics*, Singapore, August 1-6, 2010, podium.
4. **Baker BM**, Shah RP, Mauck RL. “Dynamic Tensile Loading Improves the Mechanical Properties of MSC-Laden Aligned Nanofibrous Scaffolds,” *Proceedings of ASME 2010 Summer Bioengineering Conference*, Naples, FL, June 16-19, paper #19685, podium.
5. **Baker BM**, Silverstein AM, Shah RP, Mauck RL. “Engineering the Functional Maturation of Nanofiber-Based Human Meniscus Tissue,” *Proceedings of ASME 2010 Summer Bioengineering Conference*, Naples, FL, June 16-19, paper #19447, poster.
6. Huang AH, **Baker BM**, Ateshian GA, Mauck RL. “Sliding Contact Loading Improves the Tensile Properties of MSC-Based Engineered Cartilage,” *Proceedings of ASME 2010 Summer Bioengineering Conference*, Naples, FL, June 16-19, 2010, podium.
7. **Baker BM**, Shah RP, Silverstein AM, Mauck RL. “Dynamic Tension Improves the Mechanical Properties of Nanofiber-Based Engineered Meniscus Constructs,” *Transactions of the 56th Annual Meeting of the Orthopaedic Research Society*, New Orleans, LA, March 6-9, 2010, podium.
8. **Baker BM**, Silverstein AM, Shah RP, Mauck RL. “Matrix Deposition Modulates Dynamic Mechanical Behavior of Nanofiber-Based Fibrocartilage,” *Transactions of the 56th Annual Meeting of the Orthopaedic Research Society*, New Orleans, LA, March 6-9, 2010, poster.
9. Nathan AS, **Baker BM**, Nerurkar NL, Mauck RL. “Time-Dependent and Anisotropic Nuclear Deformations on Aligned Nanofibrous Scaffolds,” *Transactions of the 56th Annual Meeting of the Orthopaedic Research Society*, New Orleans, LA, March 6-9, 2010, podium.

10. Huang AH, **Baker BM**, Ateshian GA, Mauck RL. "Sliding Contact Enhances Mesenchymal Stem Cell Chondrogenesis in 3D Culture," Transactions of the 56th Annual Meeting of the Orthopaedic Research Society, New Orleans, LA, March 6-9, 2010, podium.
11. Gee AO, **Baker BM**, Montero G, Silverstein AM, Mauck RL. "Fabrication and Evaluation of Biomimetic-Biosynthetic Nanofibrous Composites," Transactions of the 56th Annual Meeting of the Orthopaedic Research Society, New Orleans, LA, March 6-9, 2010, poster.
12. Nerurkar NL, Sen S, **Baker BM**, Zachary TL, Elliott DM, Mauck RL. "Dynamic Culture Enhances Stem Cell Ingress and Extracellular Matrix Deposition on Electrospun Nanofibrous Scaffolds," Transactions of the 56th Annual Meeting of the Orthopaedic Research Society, New Orleans, LA, March 6-9, 2010, poster.
13. DeCoons RM, Shah RP, Gee AO, **Baker BM**, Guevara JL, Modesto RB, Schaer TP, Mauck RL. "*In vivo* Meniscus Repair with Anatomic Nanofibrous Scaffolds: A Preliminary Report," Transactions of the 56th Annual Meeting of the Orthopaedic Research Society, New Orleans, LA, March 6-9, 2010, poster.
14. **Baker BM**, Silverstein AM, Mauck RL. "Engineering Dense Connective Tissues via Anisotropic Nanofibrous Scaffolds with High Sacrificial Fiber Content," *Proceedings of the ASME 2010 First Global Congress on NanoEngineering for Medicine and Biology*, Houston, TX, February 7-10, 2010, paper #13371, podium.
15. **Baker BM**, Nathan AS, DeCoons RM, Gee AO, Mauck RL. "Human Meniscus Fibrochondrocytes Yield Superior Tissue Compared to Donor-Matched Mesenchymal Stem Cells on Nanofibrous Scaffolds," *Proceedings of the 2009 BMES Annual Meeting*, Pittsburgh, PA, October 7-10, 2009, paper #1325, podium, awarded graduate research award.
16. **Baker BM**, Montero G, Mauck RL. "Removal of Sacrificial Fibers Enhances Long Term Cell and Matrix Distribution in Aligned Nanofibrous Scaffolds," *Proceedings of ASME 2009 Summer Bioengineering Conference*, Lake Tahoe, CA, June 17-21, paper #206856, podium.
17. Nathan AS, **Baker BM**, Mauck RL. "Cytoskeletal Control of Mesenchymal Stem Cell Nuclear Deformation on Nanofibrous Scaffolds," *Proceedings of ASME 2009 Summer Bioengineering Conference*, Lake Tahoe, CA, June 17-21, paper #206855, 1<sup>st</sup> place in student poster competition.
18. **Baker BM**, Nerurkar NL, Burdick JA, Elliott DM, Mauck RL. "Instilling Time-Dependent Behavior in Electrospun, Multi-Polymer Nanofibrous Composites," *Transactions of the 55th Annual Meeting of the Orthopaedic Research Society*, Las Vegas, NV, February 22-25, 2009, 34:473, poster.

19. **Baker BM**, Gee AO, Nathan AS, Mauck RL. "Meniscus Tissue Engineering with Fibrochondrocytes and MSCs from Osteoarthritic Donors," *Transactions of the 55th Annual Meeting of the Orthopaedic Research Society*, Las Vegas, NV, February 22-25, 2009, 34:1293, poster.
20. Nathan AS, **Baker BM**, Mauck RL. "Static Deformation Modulates Stem Cell Architecture and Morphology on Aligned Nanofibrous Scaffolds" *Transactions of the 55th Annual Meeting of the Orthopaedic Research Society*, Las Vegas, NV, February 22-25, 2009, 34:1293, podium.
21. **Baker BM**, Nerurkar NL, Burdick JA, Mauck RL. "The Temporal Behavior of Electrospun, Multi-Polymer Nanofibrous Composites," *Proceedings of TERMIS-NA 2008 Conference*, San Diego, CA, December 7-11, paper #574, podium.
22. **Baker BM**, Nerurkar NL, Burdick JA, Elliott DM, Mauck RL. "Fabrication and Modeling of an Electrospun Tri-Polymer Composite for the Engineering of Fibrous Tissues," *Proceedings of ASME 2008 Summer Bioengineering Conference*, Marco Island, FL, June 25-29, paper #193174, podium.
23. Gee AO, **Baker BM**, Mauck RL. "Mechanics and Cytocompatibility of Genepin Crosslinked Type I Collagen Nanofibrous Scaffolds," *Proceedings of ASME 2008 Summer Bioengineering Conference*, Marco Island, FL, June 25-29, paper #193220, poster.
24. **Baker BM**, Nathan AS, Mauck RL. "Tensile Loading Modulates Collagen Gene Expression in MSC-Laden Nanofibrous Scaffolds," *Transactions of the 54th Annual Meeting of the Orthopaedic Research Society*, San Francisco, CA, March 2-5, 2008, 33:1465, poster.
25. **Baker BM**, Gee AO, Jennings MW, Nathan AS, Huffman GR, Mauck RL. "Engineering Anatomically-Shaped Meniscus Constructs: Biologic and Mechanical Integration," *Transactions of the 54th Annual Meeting of the Orthopaedic Research Society*, San Francisco, CA, March 2-5, 2008, 33:1460, poster.
26. **Baker BM**, Gee AO, Marklein RA, Nathan AS, Burdick JA, Mauck RL. "Tuning Nanofibrous Scaffold Mechanics and Porosity to Promote Cell Infiltration," *Transactions of the 54th Annual Meeting of the Orthopaedic Research Society*, San Francisco, CA, March 2-5, 2008, 33:132, podium.
27. **Baker BM**, Nathan AS, Huffman GR, Mauck RL. "Structure-Function Correlations of Young and Aged Human Fibrochondrocyte-Seeded Engineered Meniscus Constructs," *Transactions of the 54th Annual Meeting of the Orthopaedic Research Society*, San Francisco, CA, March 2-5, 2008, 33:321, podium.

28. **Baker BM**, Nathan AS, Sheth NP, Huffman GR, Mauck RL. “Autologous Human Fibrochondrocytes from Meniscectomy Debris are a Potent Cell Source for Meniscus Tissue Engineering,” *Proceedings of ASME 2007 Summer Bioengineering Conference*, Keystone, CO, June 20-24, paper #176525, 2<sup>nd</sup> prize in student poster competition.
29. **Baker BM**, O’Connell GD, Sen S, Nathan AS, Elliott DM, Mauck RL. “Multi-Lamellar and Multi-Axial Maturation of Cell-Seeded Fiber-Reinforced Tissue Engineered Constructs,” *Proceedings of ASME 2007 Summer Bioengineering Conference*, Keystone, CO, June 20-24, paper #176434, podium.
30. O’Connell GD, Sen S, **Baker BM**, Mauck RL, Elliott DM. “Biaxial Mechanics of Native and Engineered Fiber-Reinforced Musculoskeletal Tissues,” *Proceedings of ASME 2007 Summer Bioengineering Conference*, Keystone, CO, June 20-24, paper #176540, podium.
31. Metter RB, **Baker BM**, Burdick JA, Mauck RL. “Enhanced Cellular Infiltration with Removal of Sacrificial Fibers from a Dual-Polymer Nanofibrous Scaffold,” *Proceedings of ASME 2007 Summer Bioengineering Conference*, Keystone, CO, June 20-24, paper #176487, poster.
32. Tan AR, Ifkovits JL, **Baker BM**, Mauck RL, Burdick JA. “Electrospinning of Photopolymerizable Poly(Beta-Amino Ester) Networks for Fibrous Tissue Engineering,” *Proceedings of ASME 2007 Summer Bioengineering Conference*, Keystone, CO, June 20-24, paper #176206, poster.
33. **Baker BM**, Tan AR, Metter RB, Nathan AS, Mauck RL. “Nanofiber Alignment Enhances the Development of Engineered Meniscus Constructs,” *Transactions of the 53rd Annual Meeting of the Orthopaedic Research Society*, San Diego, CA, February 11-14, 2007, 32:779, poster.
34. Sheth NP, **Baker BM**, Nathan AS, Mauck RL. “Biologic Integration of Fiber-Aligned Nanofibrous Scaffolds with Native Meniscus,” *Transactions of the 53rd Annual Meeting of the Orthopaedic Research Society*, San Diego, CA, February 11-14, 2007, 32:780, poster.
35. Nerurkar NL, **Baker BM**, Chen CY, Elliott DM, Mauck RL. “Engineering of Fiber-Reinforced Tissues with Anisotropic Biodegradable Nanofibrous Scaffolds,” *IEEE-EMBS Meeting*, New York, NY, Aug 30-Sept 3, 2006, pp. 787-790, podium.
36. **Baker BM**, Sheth NP, Mauck RL. “Maturation of MFC- and MSC-Laden Nanofibrous Scaffolds for Meniscus Tissue Engineering,” *University of Pennsylvania IME Symposium*, Philadelphia, PA, May 19, 2006, pp. 47, poster.

37. **Baker BM**, Sheth NP, and Mauck RL. “Maturation of MFC- and MSC-Laden Nanofibrous Scaffolds for Meniscus Tissue Engineering,” *Proceedings of ASME 2006 Summer Bioengineering Conference*, Amelia Island, FL, June 21-25, paper #157580, podium.

## ***BIBLIOGRAPHY***

Adams, M. E. and D. W. L. Hukins (1992). The extracellular matrix of the meniscus. Knee meniscus: basic and clinical foundations. V. C. Mow, S. P. Arnoczky and D. W. Jackson. New York, Raven Press, Ltd.: 15-28.

Agung, M., M. Ochi, et al. (2006). "Mobilization of bone marrow-derived mesenchymal stem cells into the injured tissues after intraarticular injection and their contribution to tissue regeneration." Knee Surg Sports Traumatol Arthrosc **14**(12): 1307-14.

Ahmed, A. M. and D. L. Burke (1983). "In-vitro measurement of static pressure distribution in synovial joints--Part I: Tibial surface of the knee." J Biomech Eng **105**(3): 216-25.

Ahmed, I., A. S. Ponery, et al. (2007). "Morphology, cytoskeletal organization, and myosin dynamics of mouse embryonic fibroblasts cultured on nanofibrillar surfaces." Mol Cell Biochem **301**(1-2): 241-9.

Altman, G. H., R. L. Horan, et al. (2002). "Silk matrix for tissue engineered anterior cruciate ligaments." Biomaterials **23**(20): 4131-41.

Altman, G. H., R. L. Horan, et al. (2002). "Cell differentiation by mechanical stress." Faseb J **16**(2): 270-2.

Anderson, D. G., C. A. Tweedie, et al. (2006). "A Combinatorial Library of Photocrosslinkable and Degradable Materials." Advanced Materials **18**: 2614-2618.

Andersson-Molina, H., H. Karlsson, et al. (2002). "Arthroscopic partial and total meniscectomy: A long-term follow-up study with matched controls." Arthroscopy **18**(2): 183-9.

Angele, P., B. Johnstone, et al. (2008). "Stem cell based tissue engineering for meniscus repair." J Biomed Mater Res A **85**(2): 445-55.

Arnoczky, S. P. (1992). Gross and vascular anatomy of the meniscus and its role in meniscal healing, regeneration, and remodeling. Knee meniscus: basic and clinical foundations. V. C. Mow, S. P. Arnoczky and D. W. Jackson. New York, Raven Press, Ltd.: 1-14.

Arnoczky, S. P. (1999). "Building a meniscus. Biologic considerations." Clin Orthop Relat Res(367 Suppl): S244-53.

Arnoczky, S. P., M. E. Adams, et al. (1988). Meniscus. Injury and repair of the musculoskeletal soft tissues. S. L. Woo and J. A. Buckwalter, Amer Acad Orthop Surg: 487-537.

Arnoczky, S. P. and R. F. Warren (1983). "The microvasculature of the meniscus and its response to injury. An experimental study in the dog." Am J Sports Med **11**(3): 131-41.

Arnoczky, S. P., R. F. Warren, et al. (1985). "Meniscal remodeling following partial meniscectomy--an experimental study in the dog." Arthroscopy **1**(4): 247-52.

Arnoczky, S. P., R. F. Warren, et al. (1988). "Meniscal repair using an exogenous fibrin clot. An experimental study in dogs." J Bone Joint Surg Am **70**(8): 1209-17.

Ateshian, G. A. (2007). "Anisotropy of fibrous tissues in relation to the distribution of tensed and buckled fibers." J Biomech Eng **129**(2): 240-9.

Aufderheide, A. C. and K. A. Athanasiou (2007). "Assessment of a Bovine Co-culture, Scaffold-Free Method for Growing Meniscus-Shaped Constructs." Tissue Eng **13**(9): 2195-205.

Awad, H. A., D. L. Butler, et al. (2000). "In vitro characterization of mesenchymal stem cell-seeded collagen scaffolds for tendon repair: effects of initial seeding density on contraction kinetics." J Biomed Mater Res **51**(2): 233-40.

Ayres, C., G. L. Bowlin, et al. (2006). "Modulation of anisotropy in electrospun tissue-engineering scaffolds: Analysis of fiber alignment by the fast Fourier transform." Biomaterials **27**(32): 5524-34.

Ayres, C. E., G. L. Bowlin, et al. (2007). "Incremental changes in anisotropy induce incremental changes in the material properties of electrospun scaffolds." Acta Biomater **3**(5): 651-61.

Baker, B. M., A. M. Handorf, et al. (2009). "New directions in nanofibrous scaffolds for soft tissue engineering and regeneration." Expert Rev Med Devices **6**(5): 515-32.

Baksh, D., L. Song, et al. (2004). "Adult mesenchymal stem cells: characterization, differentiation, and application in cell and gene therapy." J Cell Mol Med **8**(3): 301-16.

Ballyns, J. J., J. P. Gleghorn, et al. (2008). "Image-guided tissue engineering of anatomically shaped implants via MRI and micro-CT using injection molding." Tissue Eng Part A **14**(7): 1195-202.

Baratz, M. E., F. H. Fu, et al. (1986). "Meniscal tears: the effect of meniscectomy and of repair on intraarticular contact areas and stress in the human knee. A preliminary report." Am J Sports Med **14**(4): 270-5.

Barbero, A., S. Grogan, et al. (2004). "Age related changes in human articular chondrocyte yield, proliferation and post-expansion chondrogenic capacity." Osteoarthritis Cartilage **12**(6): 476-84.

Barnes, C. P., C. W. Pemble, et al. (2007). "Cross-linking electrospun type II collagen tissue engineering scaffolds with carbodiimide in ethanol." Tissue Eng **13**(7): 1593-605.

Barnes, C. P., S. A. Sell, et al. (2007). "Nanofiber technology: designing the next generation of tissue engineering scaffolds." Adv Drug Deliv Rev **59**(14): 1413-33.

Barry, F., R. E. Boynton, et al. (2001). "Chondrogenic differentiation of mesenchymal stem cells from bone marrow: differentiation-dependent gene expression of matrix components." Exp Cell Res **268**(2): 189-200.

Batiste, D. L., A. Kirkley, et al. (2004). "Ex vivo characterization of articular cartilage and bone lesions in a rabbit ACL transection model of osteoarthritis using MRI and micro-CT." Osteoarthritis Cartilage **12**(12): 986-96.

Benjamin, M. and J. R. Ralphs (2004). "Biology of fibrocartilage cells." Int Rev Cytol **233**: 1-45.

Benya, P. D. and J. D. Shaffer (1982). "Dedifferentiated chondrocytes reexpress the differentiated collagen phenotype when cultured in agarose gels." Cell **30**(1): 215-24.

Beredjikian, P. K., M. Favata, et al. (2003). "Regenerative versus reparative healing in tendon: a study of biomechanical and histological properties in fetal sheep." Ann Biomed Eng **31**(10): 1143-52.

Bhattacharai, N., D. Edmondson, et al. (2005). "Electrospun chitosan-based nanofibers and their cellular compatibility." Biomaterials **26**(31): 6176-84.

Birk, D. E., E. I. Zycband, et al. (1989). "Collagen fibrillogenesis in situ: fibril segments are intermediates in matrix assembly." Proc Natl Acad Sci U S A **86**(12): 4549-53.

Bland, J. M. and D. G. Altman (1986). "Statistical methods for assessing agreement between two methods of clinical measurement." Lancet **1**(8476): 307-10.

Bodin, A., S. Concaro, et al. (2007). "Bacterial cellulose as a potential meniscus implant." J Tissue Eng Regen Med **1**(5): 406-8.

Boland, E. D., B. D. Coleman, et al. (2005). "Electrospinning polydioxanone for biomedical applications." Acta Biomater **1**(1): 115-23.

Boland, E. D., T. A. Telemeco, et al. (2004). "Utilizing acid pretreatment and electrospinning to improve biocompatibility of poly(glycolic acid) for tissue engineering." J Biomed Mater Res B Appl Biomater **71**(1): 144-52.

Boland, E. D., G. E. Wnek, et al. (2001). "Tailoring tissue engineering scaffolds using electrostatic processing techniques: A study of poly(glycolic acid) electrospinning." J Macromol Sci **A38**(12): 1231-1243.

- Bolgen, N., Y. Z. Menciloglu, et al. (2005). "In vitro and in vivo degradation of non-woven materials made of poly(epsilon-caprolactone) nanofibers prepared by electrospinning under different conditions." J Biomater Sci Polym Ed **16**(12): 1537-55.
- Bonneux, I. and B. Vandekerckhove (2002). "Arthroscopic partial lateral meniscectomy long-term results in athletes." Acta Orthop Belg **68**(4): 356-61.
- Brandt, K. D., E. M. Braunstein, et al. (1991). "Anterior (cranial) cruciate ligament transection in the dog: a bona fide model of osteoarthritis, not merely of cartilage injury and repair." J Rheumatol **18**(3): 436-46.
- Bruehlmann, S. B., J. R. Matyas, et al. (2004). "ISSLS prize winner: Collagen fibril sliding governs cell mechanics in the annulus fibrosus: an in situ confocal microscopy study of bovine discs." Spine (Phila Pa 1976) **29**(23): 2612-20.
- Bruns, J., J. Kahrs, et al. (1998). "Autologous perichondral tissue for meniscal replacement." J Bone Joint Surg Br **80**(5): 918-23.
- Bullough, P. G., L. Munuera, et al. (1970). "The strength of the menisci of the knee as it relates to their fine structure." J Bone Joint Surg Br **52**(3): 564-7.
- Buma, P., N. N. Ramrattan, et al. (2004). "Tissue engineering of the meniscus." Biomaterials **25**(9): 1523-32.
- Burger, C., B. S. Hsiao, et al. (2006). "Nanofibrous materials and their applications." Annual Review of Materials Research **36**: 333-368.
- Bursac, P., S. Arnoczky, et al. (2009). "Dynamic compressive behavior of human meniscus correlates with its extra-cellular matrix composition." Biorheology **46**(3): 227-37.
- Bursac, P., A. York, et al. (2009). "Influence of donor age on the biomechanical and biochemical properties of human meniscal allografts." Am J Sports Med **37**(5): 884-9.
- Butler, D. L., S. A. Goldstein, et al. (2000). "Functional tissue engineering: the role of biomechanics." J Biomech Eng **122**(6): 570-5.
- Butler, D. L., J. T. Shearn, et al. (2004). "Functional tissue engineering parameters toward designing repair and replacement strategies." Clin Orthop Relat Res(427 Suppl): S190-9.
- Buttafoco, L., N. G. Kolkman, et al. (2006). "Electrospinning of collagen and elastin for tissue engineering applications." Biomaterials **27**(5): 724-34.

- Buxboim, A., I. L. Ivanovska, et al. "Matrix elasticity, cytoskeletal forces and physics of the nucleus: how deeply do cells 'feel' outside and in?" J Cell Sci **123**(Pt 3): 297-308.
- Campbell, S. E., T. G. Sanders, et al. (2001). "MR imaging of meniscal cysts: incidence, location, and clinical significance." AJR Am J Roentgenol **177**(2): 409-13.
- Caplan, A. I. (1991). "Mesenchymal stem cells." J Orthop Res **9**(5): 641-50.
- Caplan, A. I. (2005). "Review: mesenchymal stem cells: cell-based reconstructive therapy in orthopedics." Tissue Eng **11**(7-8): 1198-211.
- Caplan, A. I. (2007). "Adult mesenchymal stem cells for tissue engineering versus regenerative medicine." J Cell Physiol **213**(2): 341-7.
- Caplan, A. I. and J. E. Dennis (2006). "Mesenchymal stem cells as trophic mediators." J Cell Biochem **98**(5): 1076-84.
- Carter, D. R. (1987). "Mechanical loading history and skeletal biology." J Biomech **20**(11-12): 1095-109.
- Casper, C. L., N. Yamaguchi, et al. (2005). "Functionalizing electrospun fibers with biologically relevant macromolecules." Biomacromolecules **6**(4): 1998-2007.
- Casper, C. L., W. Yang, et al. (2007). "Coating electrospun collagen and gelatin fibers with perlecan domain I for increased growth factor binding." Biomacromolecules **8**(4): 1116-23.
- Centeno, C. J., D. Busse, et al. (2008). "Regeneration of meniscus cartilage in a knee treated with percutaneously implanted autologous mesenchymal stem cells." Med Hypotheses **71**(6): 900-8.
- Chen, C. S. and D. E. Ingber (1999). "Tensegrity and mechanoregulation: from skeleton to cytoskeleton." Osteoarthritis Cartilage **7**(1): 81-94.
- Chen, C. S., J. Tan, et al. (2004). "Mechanotransduction at cell-matrix and cell-cell contacts." Annu Rev Biomed Eng **6**: 275-302.
- Cheung, H. S. (1987). "Distribution of type I, II, III and V in the pepsin solubilized collagens in bovine menisci." Connect Tissue Res **16**(4): 343-56.
- Chia, H. N. and M. L. Hull (2008). "Compressive moduli of the human medial meniscus in the axial and radial directions at equilibrium and at a physiological strain rate." J Orthop Res **26**(7): 951-6.
- Chiari, C., U. Koller, et al. (2006). "A tissue engineering approach to meniscus regeneration in a sheep model." Osteoarthritis Cartilage **14**(10): 1056-65.

- Clark, C. R. and J. A. Ogden (1983). "Development of the menisci of the human knee joint. Morphological changes and their potential role in childhood meniscal injury." J Bone Joint Surg Am **65**(4): 538-47.
- Coipeau, P., P. Rosset, et al. (2009). "Impaired differentiation potential of human trabecular bone mesenchymal stromal cells from elderly patients." Cytotherapy **11**(5): 584-94.
- Connelly, J. T., A. J. Garcia, et al. (2007). "Inhibition of in vitro chondrogenesis in RGD-modified three-dimensional alginate gels." Biomaterials **28**(6): 1071-83.
- Connelly, J. T., E. J. Vanderploeg, et al. "Tensile Loading Modulates Bone Marrow Stromal Cell Differentiation and the Development of Engineered Fibrocartilage Constructs." Tissue Eng Part A.
- Connolly, J. A. (1985). "Microtubules, microfilaments and the transport of acetylcholine receptors in embryonic myotubes." Exp Cell Res **159**(2): 430-40.
- Cook, J. L., D. B. Fox, et al. (2006). "Evaluation of small intestinal submucosa grafts for meniscal regeneration in a clinically relevant posterior meniscectomy model in dogs." J Knee Surg **19**(3): 159-67.
- Cook, J. L., D. B. Fox, et al. (2006). "Long-term Outcome for Large Meniscal Defects Treated With Small Intestinal Submucosa in a Dog Model." Am J Sports Med **34**(1): 32-42.
- Cooper, J. A., H. H. Lu, et al. (2005). "Fiber-based tissue-engineered scaffold for ligament replacement: design considerations and in vitro evaluation." Biomaterials **26**(13): 1523-32.
- Costa, K. D., E. J. Lee, et al. (2003). "Creating alignment and anisotropy in engineered heart tissue: role of boundary conditions in a model three-dimensional culture system." Tissue Eng **9**(4): 567-77.
- Cottrell, J. M., P. Scholten, et al. (2008). "A new technique to measure the dynamic contact pressures on the Tibial Plateau." J Biomech **41**(10): 2324-9.
- Courtney, T., M. S. Sacks, et al. (2006). "Design and analysis of tissue engineering scaffolds that mimic soft tissue mechanical anisotropy." Biomaterials **27**(19): 3631-8.
- Cox, J. S., C. E. Nye, et al. (1975). "The degenerative effects of partial and total resection of the medial meniscus in dogs' knees." Clin Orthop Relat Res(109): 178-83.
- Cravener, E. K. and D. G. MacElroy (1941). "Injuries of the internal semilunar cartilage." JAMA **117**(20): 1695-1700.

- Cremer, T. and C. Cremer (2001). "Chromosome territories, nuclear architecture and gene regulation in mammalian cells." Nat Rev Genet **2**(4): 292-301.
- da Silva Meirelles, L., P. C. Chagastelles, et al. (2006). "Mesenchymal stem cells reside in virtually all post-natal organs and tissues." J Cell Sci **119**(Pt 11): 2204-13.
- Dahl, K. N., S. M. Kahn, et al. (2004). "The nuclear envelope lamina network has elasticity and a compressibility limit suggestive of a molecular shock absorber." J Cell Sci **117**(Pt 20): 4779-86.
- Dahl, K. N., A. J. Ribeiro, et al. (2008). "Nuclear shape, mechanics, and mechanotransduction." Circ Res **102**(11): 1307-18.
- Dalby, M. J., N. Gadegaard, et al. (2007). "Nanotopographical control of human osteoprogenitor differentiation." Curr Stem Cell Res Ther **2**(2): 129-38.
- Dalton, P. D., K. Klinkhammer, et al. (2006). "Direct in vitro electrospinning with polymer melts." Biomacromolecules **7**(3): 686-90.
- De Vita, R., D. J. Leo, et al. (2006). "A constitutive law for poly(butylene terephthalate) nanofibers mats." Journal of Applied Polymer Science **102**(6): 5280-5283.
- DeHaven, K. E. (1999). "Meniscus repair." Am J Sports Med **27**(2): 242-50.
- Deitzel, J. M., J. Kleinmeyer, et al. (2001). "The effect of processing variables on the morphology of electrospun nanofibers and textiles." Polymer **42**: 261-272.
- Dejardin, L. M., S. P. Arnoczky, et al. (2001). "Tissue-engineered rotator cuff tendon using porcine small intestine submucosa. Histologic and mechanical evaluation in dogs." Am J Sports Med **29**(2): 175-84.
- Dienst, M., P. E. Greis, et al. (2007). "Effect of lateral meniscal allograft sizing on contact mechanics of the lateral tibial plateau: an experimental study in human cadaveric knee joints." Am J Sports Med **35**(1): 34-42.
- Ding, B., E. Kimura, et al. (2004). "Fabrication of blend biodegradable nanofibrous nonwoven mats via multi-jet electrospinning." Polymer **45**(6): 1895-1902.
- Discher, D. E., D. J. Mooney, et al. (2009). "Growth factors, matrices, and forces combine and control stem cells." Science **324**(5935): 1673-7.
- Djurasovic, M., J. W. Aldridge, et al. (1998). "Knee joint immobilization decreases aggrecan gene expression in the meniscus." Am J Sports Med **26**(3): 460-6.

- Dosunmu, O. O., G. G. Chase, et al. (2006). "Electrospinning of polymer nanofibres from multiple jets on a porous tubular surface." Nanotechnology **17**(4): 1123-1127.
- Eberline, R., G. A. Holzapfel, et al. (2001). "An anisotropic constitutive model for annulus tissue and enhanced finite element analyses of intact lumbar disc bodies." Comput Methods Biomech Biomed Engin **4**: 209-230.
- Egerbacher, M., S. P. Arnoczky, et al. (2008). "Loss of homeostatic tension induces apoptosis in tendon cells: an in vitro study." Clin Orthop Relat Res **466**(7): 1562-8.
- Elliott, D. M., F. Guilak, et al. (1999). "Tensile properties of articular cartilage are altered by meniscectomy in a canine model of osteoarthritis." J Orthop Res **17**(4): 503-8.
- Elliott, D. M., R. Jones, 3rd, et al. (2002). "Joint degeneration following meniscal allograft transplantation in a canine model: mechanical properties and semiquantitative histology of articular cartilage." Knee Surg Sports Traumatol Arthrosc **10**(2): 109-18.
- Engler, A. J., S. Sen, et al. (2006). "Matrix elasticity directs stem cell lineage specification." Cell **126**(4): 677-89.
- Englund, M., E. M. Roos, et al. (2003). "Impact of type of meniscal tear on radiographic and symptomatic knee osteoarthritis: a sixteen-year followup of meniscectomy with matched controls." Arthritis Rheum **48**(8): 2178-87.
- Eyre, D. R. and J. J. Wu (1983). "Collagen of fibrocartilage: a distinctive molecular phenotype in bovine meniscus." FEBS Lett **158**(2): 265-70.
- Farndale, R. W., D. J. Buttle, et al. (1986). "Improved quantitation and discrimination of sulphated glycosaminoglycans by use of dimethylmethylene blue." Biochim Biophys Acta **883**(2): 173-7.
- Farre, J., S. Roura, et al. (2007). "FGF-4 increases in vitro expansion rate of human adult bone marrow-derived mesenchymal stem cells." Growth Factors **25**(2): 71-6.
- Fithian, D. C., M. A. Kelly, et al. (1990). "Material properties and structure-function relationships in the menisci." Clin Orthop(252): 19-31.
- Formhals, A. (1934). Process and apparatus for preparing artificial threads, United States Patent Office. **1,975,504** 1,975,504
- Freedman, K. B., S. J. Nho, et al. (2003). "Marrow stimulating technique to augment meniscus repair." Arthroscopy **19**(7): 794-8.
- Fridrikh, S. V., J. H. Yu, et al. (2003). "Controlling the fiber diameter during electrospinning." Phys Rev Lett **90**(14): 144502.

- Fung, Y. C. (1982). "Biomechanics: Mechanical Properties of Living Tissues."
- Gao, L., R. McBeath, et al. "Stem cell shape regulates a chondrogenic versus myogenic fate through Rac1 and N-cadherin." Stem Cells **28**(3): 564-72.
- Garrett, J. C. (1992). Meniscal transplantation. Knee surgery, current practice. P. M. Aichroth and W. D. Canon. New York, Raven Press, Ltd.: 95-102.
- Garvin, J., J. Qi, et al. (2003). "Novel system for engineering bioartificial tendons and application of mechanical load." Tissue Eng **9**(5): 967-79.
- Gastel, J. A., W. R. Muirhead, et al. (2001). "Meniscal tissue regeneration using a collagenous biomaterial derived from porcine small intestine submucosa." Arthroscopy **17**(2): 151-9.
- Geng, X., O. H. Kwon, et al. (2005). "Electrospinning of chitosan dissolved in concentrated acetic acid solution." Biomaterials **26**(27): 5427-32.
- Ghosh, P. and T. K. Taylor (1987). "The knee joint meniscus. A fibrocartilage of some distinction." Clin Orthop Relat Res(224): 52-63.
- Greis, P. E., D. D. Bardana, et al. (2002). "Meniscal injury: I. Basic science and evaluation." J Am Acad Orthop Surg **10**(3): 168-76.
- Gruber, H. E., D. Mauerhan, et al. (2008). "Three-dimensional culture of human meniscal cells: extracellular matrix and proteoglycan production." BMC Biotechnol **8**: 54.
- Guerin, H. A. and D. M. Elliott (2005). "The role of fiber-matrix interactions in a nonlinear fiber-reinforced strain energy model of tendon." J Biomech Eng **127**(2): 345-50.
- Guilak, F. (1995). "Compression-induced changes in the shape and volume of the chondrocyte nucleus." J Biomech **28**(12): 1529-41.
- Guilak, F., D. M. Cohen, et al. (2009). "Control of stem cell fate by physical interactions with the extracellular matrix." Cell Stem Cell **5**(1): 17-26.
- Guilak, F., J. R. Tedrow, et al. (2000). "Viscoelastic properties of the cell nucleus." Biochem Biophys Res Commun **269**(3): 781-6.
- Gunja, N. J. and K. A. Athanasiou (2009). "Effects of co-cultures of meniscus cells and articular chondrocytes on PLLA scaffolds." Biotechnol Bioeng **103**(4): 808-16.
- Gunja, N. J., D. J. Huey, et al. (2009). "Effects of agarose mould compliance and surface roughness on self-assembled meniscus-shaped constructs." J Tissue Eng Regen Med **3**(7): 521-30.

- Guo, Z. Y., X. Q. Peng, et al. (2006). "A composites-based hyperelastic constitutive model for soft tissue with application to the human annulus fibrosus." Journal of the mechanics and physics of solids **54**(9): 1952-71.
- Hayes, A. J., M. Benjamin, et al. (1999). "Role of actin stress fibres in the development of the intervertebral disc: cytoskeletal control of extracellular matrix assembly." Dev Dyn **215**(3): 179-89.
- Hede, A., S. Hempel-Poulsen, et al. (1990). "Symptoms and level of sports activity in patients awaiting arthroscopy for meniscal lesions of the knee." J Bone Joint Surg Am **72**(4): 550-2.
- Heijkants, R. G., R. V. van Calck, et al. (2004). "Design, synthesis and properties of a degradable polyurethane scaffold for meniscus regeneration." J Mater Sci Mater Med **15**(4): 423-7.
- Hellio Le Graverand, M. P., Y. Ou, et al. (2001). "The cells of the rabbit meniscus: their arrangement, interrelationship, morphological variations and cytoarchitecture." J Anat **198**(Pt 5): 525-35.
- Hellio Le Graverand, M. P., E. Vignon, et al. (2001). "Early changes in lapine menisci during osteoarthritis development: Part I: cellular and matrix alterations." Osteoarthritis Cartilage **9**(1): 56-64.
- Hellio Le Graverand, M. P., E. Vignon, et al. (2001). "Early changes in lapine menisci during osteoarthritis development: Part II: molecular alterations." Osteoarthritis Cartilage **9**(1): 65-72.
- Hennerbichler, A., F. T. Moutos, et al. (2007). "Repair Response of the Inner and Outer Regions of the Porcine Meniscus In Vitro." Am J Sports Med.
- Higuchi, H., M. Kimura, et al. (2000). "Factors affecting long-term results after arthroscopic partial meniscectomy." Clin Orthop Relat Res(377): 161-8.
- Hoben, G. M., J. C. Hu, et al. (2007). "Self-assembly of fibrochondrocytes and chondrocytes for tissue engineering of the knee meniscus." Tissue Eng **13**(5): 939-46.
- Holzappel, G. A. (2000). "Nonlinear Solid Mechanics: A Continuum Approach for Engineering." 455.
- Holzappel, G. A., C. A. Schulze-Bauer, et al. (2005). "Single lamellar mechanics of the human lumbar anulus fibrosus." Biomech Model Mechanobiol **3**(3): 125-40.
- Hommen, J. P., G. R. Applegate, et al. (2007). "Meniscus allograft transplantation: ten-year results of cryopreserved allografts." Arthroscopy **23**(4): 388-93.

- Horie, M., I. Sekiya, et al. (2009). "Intra-articular Injected synovial stem cells differentiate into meniscal cells directly and promote meniscal regeneration without mobilization to distant organs in rat massive meniscal defect." Stem Cells **27**(4): 878-87.
- Hoser, C., C. Fink, et al. (2001). "Long-term results of arthroscopic partial lateral meniscectomy in knees without associated damage." J Bone Joint Surg Br **83**(4): 513-6.
- Hoshiya, T., T. Yamada, et al. (2008). "Nuclear deformation and expression change of cartilaginous genes during in vitro expansion of chondrocytes." Biochem Biophys Res Commun **374**(4): 688-92.
- Huang, A. H., M. J. Farrell, et al. "Long-term dynamic loading improves the mechanical properties of chondrogenic mesenchymal stem cell-laden hydrogel." Eur Cell Mater **19**: 72-85.
- Huang, A. H., A. Stein, et al. (2009 ). "Genome wide analysis to identify functional determinants of mesenchymal stem cell chondrogenesis." Trans Orthop Res Soc **34**: 279.
- Huang, A. H., A. Stein, et al. (2010). "Evaluation of the Complex Transcriptional Topography of Mesenchymal Stem Cell Chondrogenesis for Cartilage Tissue Engineering." Tissue Eng Part A.
- Huang, A. H., A. Stein, et al. (2009). "Transient exposure to transforming growth factor beta 3 improves the mechanical properties of mesenchymal stem cell-laden cartilage constructs in a density-dependent manner." Tissue Eng Part A **15**(11): 3461-72.
- Huang, C. Y., P. M. Reuben, et al. (2004). "Chondrogenesis of human bone marrow-derived mesenchymal stem cells in agarose culture." Anat Rec A Discov Mol Cell Evol Biol **278**(1): 428-36.
- Iatridis, J. C., J. J. MaClean, et al. (2005). "Mechanical damage to the intervertebral disc annulus fibrosus subjected to tensile loading." J Biomech **38**(3): 557-65.
- Ibarra, C., J. A. Koski, et al. (2000). "Tissue engineering meniscus: cells and matrix." Orthop Clin North Am **31**(3): 411-8.
- Ifkovits, J. L., R. F. Padera, et al. (2008). "Biodegradable and radically polymerized elastomers with enhanced processing capabilities." Biomed Mater **3**(3): 034104.
- Ionescu, L. C., G. C. Lee, et al. "An anisotropic nanofiber/microsphere composite with controlled release of biomolecules for fibrous tissue engineering." Biomaterials **31**(14): 4113-20.

- Izuta, Y., M. Ochi, et al. (2005). "Meniscal repair using bone marrow-derived mesenchymal stem cells: experimental study using green fluorescent protein transgenic rats." Knee **12**(3): 217-23.
- Jackson, D. W., C. A. McDevitt, et al. (1992). "Meniscal transplantation using fresh and cryopreserved allografts. An experimental study in goats." Am J Sports Med **20**(6): 644-56.
- Jackson, D. W. and T. M. Simon (1992). Biology of meniscal Allograft. Knee meniscus: basic and clinical foundations. V. C. Mow, S. P. Arnoczky and D. W. Jackson. New York, Raven Press, Ltd.: 141-152.
- Jiang, H., D. Fang, et al. (2004). "Optimization and characterization of dextran membranes prepared by electrospinning." Biomacromolecules **5**(2): 326-33.
- Johnson, R. G. and A. R. Poole (1990). "The early response of articular cartilage to ACL transection in a canine model." Exp Pathol **38**(1): 37-52.
- Johnstone, B., T. M. Hering, et al. (1998). "In vitro chondrogenesis of bone marrow-derived mesenchymal progenitor cells." Exp Cell Res **238**(1): 265-72.
- Jones, R. S., G. C. Keene, et al. (1996). "Direct measurement of hoop strains in the intact and torn human medial meniscus." Clin Biomech (Bristol, Avon) **11**(5): 295-300.
- Juncosa-Melvin, N., J. T. Shearn, et al. (2006). "Effects of mechanical stimulation on the biomechanics and histology of stem cell-collagen sponge constructs for rabbit patellar tendon repair." Tissue Eng **12**(8): 2291-300.
- Kahn, J., Y. Shwartz, et al. (2009). "Muscle contraction is necessary to maintain joint progenitor cell fate." Dev Cell **16**(5): 734-43.
- Kambic, H. E. and C. A. McDevitt (2005). "Spatial organization of types I and II collagen in the canine meniscus." J Orthop Res **23**(1): 142-9.
- Kardon, G. (1998). "Muscle and tendon morphogenesis in the avian hind limb." Development **125**(20): 4019-32.
- Kaunas, R., P. Nguyen, et al. (2005). "Cooperative effects of Rho and mechanical stretch on stress fiber organization." Proc Natl Acad Sci U S A **102**(44): 15895-900.
- Kelly, B. T., W. Robertson, et al. (2007). "Hydrogel meniscal replacement in the sheep knee - Preliminary evaluation of chondroprotective effects." American Journal of Sports Medicine **35**(1): 43-52.

- Kelly, M. A., D. C. Fithian, et al. (1990). Structure and function of the meniscus: basic and clinical applications. Biomechanics of Diarthrodial Joints. V. C. Mow, A. Ratcliffe and S. L.-Y. Woo. New York, Springer-Verlag. **1**: 191-211.
- Khil, M. S., D. I. Cha, et al. (2003). "Electrospun nanofibrous polyurethane membrane as wound dressing." J Biomed Mater Res B Appl Biomater **67**(2): 675-9.
- Kidoaki, S., I. K. Kwon, et al. (2005). "Mesoscopic spatial designs of nano- and microfiber meshes for tissue-engineering matrix and scaffold based on newly devised multilayering and mixing electrospinning techniques." Biomaterials **26**(1): 37-46.
- Kidoaki, S., I. K. Kwon, et al. (2006). "Structural features and mechanical properties of in situ-bonded meshes of segmented polyurethane electrospun from mixed solvents." J Biomed Mater Res B Appl Biomater **76**(1): 219-29.
- Kim, S. H., S. Nair, et al. (2005). "Reactive electrospinning of cross-linked poly(2-hydroxyethyl methacrylate) nanofibers and elastic properties of individual hydrogel nanofibers in aqueous solutions." Macromolecules **38**(9): 3719-3723.
- Klompaker, J., R. P. Veth, et al. (1996). "Meniscal replacement using a porous polymer prosthesis: a preliminary study in the dog." Biomaterials **17**(12): 1169-75.
- Knight, M. M., J. van de Breevaart Bravenboer, et al. (2002). "Cell and nucleus deformation in compressed chondrocyte-alginate constructs: temporal changes and calculation of cell modulus." Biochim Biophys Acta **1570**(1): 1-8.
- Kobayashi, M., Y. S. Chang, et al. (2005). "A two year in vivo study of polyvinyl alcohol-hydrogel (PVA-H) artificial meniscus." Biomaterials **26**(16): 3243-8.
- Kowalewski, T. A., S. Blonski, and S. Barral (2005). "Experiments and modelling of electrospinning process. ." Bull. Pol. Acad. Sci. Tech. Sci. **53**: 385.
- Krause, W. R., M. H. Pope, et al. (1976). "Mechanical changes in the knee after meniscectomy." J Bone Joint Surg Am **58**(5): 599-604.
- Kurpinski, K., J. Chu, et al. (2006). "Anisotropic mechanosensing by mesenchymal stem cells." Proc Natl Acad Sci U S A **103**(44): 16095-100.
- Kwon, I. K., S. Kidoaki, et al. (2005). "Electrospun nano- to microfiber fabrics made of biodegradable copolyesters: structural characteristics, mechanical properties and cell adhesion potential." Biomaterials **26**(18): 3929-39.
- Lee, C. H., H. J. Shin, et al. (2005). "Nanofiber alignment and direction of mechanical strain affect the ECM production of human ACL fibroblast." Biomaterials **26**(11): 1261-70.

- Lee, H. J., C. Yu, et al. (2008). "Enhanced chondrogenesis of mesenchymal stem cells in collagen mimetic peptide-mediated microenvironment." Tissue Eng Part A **14**(11): 1843-51.
- Lee, S. J., J. J. Yoo, et al. (2007). "In vitro evaluation of electrospun nanofiber scaffolds for vascular graft application." J Biomed Mater Res A.
- Levy, I. M., P. A. Torzilli, et al. (1989). "The effect of lateral meniscectomy on motion of the knee." J Bone Joint Surg Am **71**(3): 401-6.
- Li, D., G. Ouyang, et al. (2005). "Collecting electrospun nanofibers with patterned electrodes." Nano Lett **5**(5): 913-6.
- Li, D., Y. L. Wang, et al. (2004). "Electrospinning nanofibers as uniaxially aligned arrays and layer-by-layer stacked films." Advanced Materials **16**(4): 361-366.
- Li, D. and Y. N. Xia (2004). "Electrospinning of nanofibers: Reinventing the wheel?" Advanced Materials **16**(14): 1151-1170.
- Li, M., M. J. Mondrinos, et al. (2005). "Electrospun protein fibers as matrices for tissue engineering." Biomaterials **26**(30): 5999-6008.
- Li, S., C. Van Den Diepstraten, et al. (2003). "Vascular smooth muscle cells orchestrate the assembly of type I collagen via alpha2beta1 integrin, RhoA, and fibronectin polymerization." Am J Pathol **163**(3): 1045-56.
- Li, W. J., J. A. Cooper, Jr., et al. (2006). "Fabrication and characterization of six electrospun poly(alpha-hydroxy ester)-based fibrous scaffolds for tissue engineering applications." Acta Biomater **2**(4): 377-85.
- Li, W. J., Y. J. Jiang, et al. (2006). "Chondrocyte phenotype in engineered fibrous matrix is regulated by fiber size." Tissue Eng **12**(7): 1775-85.
- Li, W. J., C. T. Laurencin, et al. (2002). "Electrospun nanofibrous structure: a novel scaffold for tissue engineering." J Biomed Mater Res **60**(4): 613-21.
- Li, W. J., R. L. Mauck, et al. (2007). "Engineering controllable anisotropy in electrospun biodegradable nanofibrous scaffolds for musculoskeletal tissue engineering." J Biomech **40**(8): 1686-93.
- Li, W. J., R. L. Mauck, et al. (2005). "Electrospun nanofibrous scaffolds: production, characterization, and applications for tissue engineering and drug delivery." J Biomed Nanotech **1** (3): 259-275.
- Li, W. J., R. Tuli, et al. (2005). "Multilineage differentiation of human mesenchymal stem cells in a three-dimensional nanofibrous scaffold." Biomaterials **26**(25): 5158-66.

- Li, W. J., R. Tuli, et al. (2005). "A three-dimensional nanofibrous scaffold for cartilage tissue engineering using human mesenchymal stem cells." Biomaterials **26**(6): 599-609.
- Linder-Ganz, E., J. J. Elsner, et al. "A novel quantitative approach for evaluating contact mechanics of meniscal replacements." J Biomech Eng **132**(2): 024501.
- Lynch, H. A., W. Johannessen, et al. (2003). "Effect of fiber orientation and strain rate on the nonlinear uniaxial tensile material properties of tendon." J Biomech Eng **125**(5): 726-31.
- Ma, Z., W. He, et al. (2005). "Grafting of gelatin on electrospun poly(caprolactone) nanofibers to improve endothelial cell spreading and proliferation and to control cell Orientation." Tissue Eng **11**(7-8): 1149-58.
- MacAusland, W. R. (1931). "Derangements of the semilunar cartilages." Ann Surg **93**: 649-682.
- Madhugiri, S., A. Dalton, et al. (2003). "Electrospun MEH-PPV/SBA-15 composite nanofibers using a dual syringe method." J Am Chem Soc **125**(47): 14531-8.
- Malaviya, P., D. L. Butler, et al. (2000). "An in vivo model for load-modulated remodeling in the rabbit flexor tendon." J. Orthop. Res. **18**: 116-25.
- Maniotis, A. J., C. S. Chen, et al. (1997). "Demonstration of mechanical connections between integrins, cytoskeletal filaments, and nucleoplasm that stabilize nuclear structure." Proc Natl Acad Sci U S A **94**(3): 849-54.
- Manwaring, M. E., J. F. Walsh, et al. (2004). "Contact guidance induced organization of extracellular matrix." Biomaterials **25**(17): 3631-8.
- Martin, I., R. Suetterlin, et al. (2001). "Enhanced cartilage tissue engineering by sequential exposure of chondrocytes to FGF-2 during 2D expansion and BMP-2 during 3D cultivation." J Cell Biochem **83**(1): 121-8.
- Martinek, V., P. Ueblacker, et al. (2005). "Second generation of meniscus transplantation: in-vivo study with tissue engineered meniscus replacement." Arch Orthop Trauma Surg: 1-7.
- Mathew, G., J. P. Hong, et al. (2006). "Preparation and anisotropic mechanical behavior of highly-oriented electrospun poly(butylene terephthalate) fibers." Journal of applied polymer science **101**(3): 2017-2021.
- Matthews, J. A., G. E. Wnek, et al. (2002). "Electrospinning of collagen nanofibers." Biomacromolecules **3**(2): 232-8.

- Mauck, R. L., B. M. Baker, et al. (2009). "Engineering on the Straight and Narrow: The Mechanics of Nanofibrous Assemblies for Fiber-Reinforced Tissue Regeneration." Tissue Eng Part B Rev.
- Mauck, R. L., B. A. Byers, et al. (2007). "Regulation of Cartilaginous ECM Gene Transcription by Chondrocytes and MSCs in 3D Culture in Response to Dynamic Loading." Biomech Model Mechanobiol **6**(1-2): 113-125.
- Mauck, R. L., G. J. Martinez-Diaz, et al. (2007). "Regional variation in meniscal fibrochondrocyte multi-lineage differentiation potential: implications for meniscal repair." Anatomical Record **290**: 48-58.
- Mauck, R. L., M. A. Soltz, et al. (2000). "Functional tissue engineering of articular cartilage through dynamic loading of chondrocyte-seeded agarose gels." J Biomech Eng **122**(3): 252-60.
- Mauck, R. L., X. Yuan, et al. (2006). "Chondrogenic differentiation and functional maturation of bovine mesenchymal stem cells in long-term agarose culture." Osteoarthritis Cartilage **14**(2): 179-89.
- McBeath, R., D. M. Pirone, et al. (2004). "Cell shape, cytoskeletal tension, and RhoA regulate stem cell lineage commitment." Dev Cell **6**(4): 483-95.
- McDermott, I. D. and A. A. Amis (2006). "The consequences of meniscectomy." J Bone Joint Surg Br **88**(12): 1549-56.
- McDevitt, C., E. Gilbertson, et al. (1977). "An experimental model of osteoarthritis; early morphological and biochemical changes." J Bone Joint Surg Br **59**(1): 24-35.
- McDevitt, C. A. and R. J. Webber (1990). "The ultrastructure and biochemistry of meniscal cartilage." Clin Orthop Relat Res(252): 8-18.
- McGinity, J. B., L. F. Geuss, et al. (1977). "Partial or total meniscectomy: a comparative analysis." J Bone Joint Surg Am **59**(6): 763-6.
- McManus, M. C., E. D. Boland, et al. (2006). "Mechanical properties of electrospun fibrinogen structures." Acta Biomater **2**(1): 19-28.
- Meredith, D. S., E. Losina, et al. (2005). "Factors predicting functional and radiographic outcomes after arthroscopic partial meniscectomy: a review of the literature." Arthroscopy **21**(2): 211-23.
- Messner, K. and J. Gao (1998). "The menisci of the knee joint. Anatomical and functional characteristics, and a rationale for clinical treatment." J Anat **193 ( Pt 2)**: 161-78.

- Mikic, B., T. L. Johnson, et al. (2000). "Differential effects of embryonic immobilization on the development of fibrocartilaginous skeletal elements." J Rehabil Res Dev **37**(2): 127-33.
- Min, B. M., L. Jeong, et al. (2004). "Formation of silk fibroin matrices with different texture and its cellular response to normal human keratinocytes." Int J Biol Macromol **34**(5): 281-8.
- Min, B. M., G. Lee, et al. (2004). "Electrospinning of silk fibroin nanofibers and its effect on the adhesion and spreading of normal human keratinocytes and fibroblasts in vitro." Biomaterials **25**(7-8): 1289-97.
- Minas, T. (1998). "Chondrocyte implantation in the repair of chondral lesions of the knee: economics and quality of life." Am J Orthop (Belle Mead NJ) **27**(11): 739-44.
- Moffat, K. L., A. S. Kwei, et al. (2008). "Novel Nanofiber-Based Scaffold for Rotator Cuff Repair and Augmentation." Tissue Eng Part A.
- Mora, G., E. Alvarez, et al. (2003). "Articular cartilage degeneration after frozen meniscus and Achilles tendon allograft transplantation: experimental study in sheep." Arthroscopy **19**(8): 833-41.
- Moutos, F. T., L. E. Freed, et al. (2007). "A biomimetic three-dimensional woven composite scaffold for functional tissue engineering of cartilage." Nat Mater.
- Mouw, J. K., J. T. Connelly, et al. (2007). "Dynamic compression regulates the expression and synthesis of chondrocyte-specific matrix molecules in bone marrow stromal cells." Stem Cells **25**(3): 655-63.
- Mow, V. C., A. Ratcliffe, et al. (1992). Structure and function relationships of the menisci of the knee. Knee meniscus: basic and clinical foundations. V. C. Mow, S. P. Arnoczky and D. W. Jackson. New York, Raven Press, Ltd.: 37-57.
- Mrksich, M., L. E. Dike, et al. (1997). "Using microcontact printing to pattern the attachment of mammalian cells to self-assembled monolayers of alkanethiolates on transparent films of gold and silver." Exp Cell Res **235**(2): 305-13.
- Mrugala, D., N. Dossat, et al. (2009). "Gene expression profile of multipotent mesenchymal stromal cells: Identification of pathways common to TGFbeta3/BMP2-induced chondrogenesis." Cloning Stem Cells **11**(1): 61-76.
- Mueller, S. M., T. O. Schneider, et al. (1999). "alpha-smooth muscle actin and contractile behavior of bovine meniscus cells seeded in type I and type II collagen-GAG matrices." J Biomed Mater Res **45**(3): 157-66.

- Murphy, J. M., K. Dixon, et al. (2002). "Reduced chondrogenic and adipogenic activity of mesenchymal stem cells from patients with advanced osteoarthritis." Arthritis Rheum **46**(3): 704-13.
- Murphy, J. M., D. J. Fink, et al. (2003). "Stem cell therapy in a caprine model of osteoarthritis." Arthritis Rheum **48**(12): 3464-74.
- Nakata, K., K. Shino, et al. (2001). "Human meniscus cell: characterization of the primary culture and use for tissue engineering." Clin Orthop Relat Res(391 Suppl): S208-18.
- Nam, J., Y. Huang, et al. (2007). "Improved cellular infiltration in electrospun fiber via engineered porosity." Tissue Eng **13**(9): 2249-57.
- Nerurkar, N. L., B. M. Baker, et al. (2006). "Engineering of fiber-reinforced tissues with anisotropic biodegradable nanofibrous scaffolds." Conf Proc IEEE Eng Med Biol Soc **1**: 787-90.
- Nerurkar, N. L., B. M. Baker, et al. (2009). "Nanofibrous biologic laminates replicate the form and function of the annulus fibrosus." Nat Mater **8**(12): 986-92.
- Nerurkar, N. L., D. M. Elliott, et al. (2007). "Mechanics of oriented electrospun nanofibrous scaffolds for annulus fibrosus tissue engineering." J Orthop Res **25**(8): 1018-28.
- Nerurkar, N. L., R. L. Mauck, et al. (2008). "ISSLS prize winner: Integrating theoretical and experimental methods for functional tissue engineering of the annulus fibrosus." Spine **33**(25): 2691-701.
- Nerurkar, N. L., S. Sen, et al. (2010). "Dynamic Culture Enhances Stem Cell Infiltration and Modulates Extracellular Matrix Production on Aligned Electrospun Nanofibrous Scaffolds." Acta Biomater.
- Neuman, R. E. and M. A. Logan (1950). "The determination of hydroxyproline." J Biol Chem **184**(1): 299-306.
- Newman, A. P., D. R. Anderson, et al. (1989). "Mechanics of the healed meniscus in a canine model." Am J Sports Med **17**(2): 164-75.
- Ng, F., S. Boucher, et al. (2008). "PDGF, TGF-beta, and FGF signaling is important for differentiation and growth of mesenchymal stem cells (MSCs): transcriptional profiling can identify markers and signaling pathways important in differentiation of MSCs into adipogenic, chondrogenic, and osteogenic lineages." Blood **112**(2): 295-307.
- Nielsen, A. B. and J. Yde (1991). "Epidemiology of acute knee injuries: a prospective hospital investigation." J Trauma **31**(12): 1644-8.

- Nur, E. K. A., I. Ahmed, et al. (2005). "Three dimensional nanofibrillar surfaces induce activation of Rac." Biochem Biophys Res Commun **331**(2): 428-34.
- Nur, E. K. A., I. Ahmed, et al. (2006). "Three-dimensional nanofibrillar surfaces promote self-renewal in mouse embryonic stem cells." Stem Cells **24**(2): 426-33.
- O'Connor, B. L. (1976). "The histological structure of dog knee menisci with comments on its possible significance." Am J Anat **147**(4): 407-17.
- Ogden, R. W. (1997). Non-linear elastic deformations. Chichester New York, E. Horwood ; Halsted Press.
- Okuda, K., M. Ochi, et al. (1999). "Meniscal rasping for repair of meniscal tear in the avascular zone." Arthroscopy **15**(3): 281-6.
- Onodera, K., I. Takahashi, et al. (2005). "Stepwise mechanical stretching inhibits chondrogenesis through cell-matrix adhesion mediated by integrins in embryonic rat limb-bud mesenchymal cells." Eur J Cell Biol **84**(1): 45-58.
- Pajerowski, J. D., K. N. Dahl, et al. (2007). "Physical plasticity of the nucleus in stem cell differentiation." Proc Natl Acad Sci U S A **104**(40): 15619-24.
- Pangborn, C. A. and K. A. Athanasiou (2005). "Effects of growth factors on meniscal fibrochondrocytes." Tissue Eng **11**(7-8): 1141-8.
- Pangborn, C. A. and K. A. Athanasiou (2005). "Growth factors and fibrochondrocytes in scaffolds." J Orthop Res **23**(5): 1184-90.
- Park, J. S., J. S. Chu, et al. (2004). "Differential effects of equiaxial and uniaxial strain on mesenchymal stem cells." Biotechnol Bioeng **88**(3): 359-68.
- Payne, K. A., D. M. Didiano, et al. "Donor sex and age influence the chondrogenic potential of human femoral bone marrow stem cells." Osteoarthritis Cartilage **18**(5): 705-13.
- Peltz, C. D., S. M. Perry, et al. (2009). "Mechanical properties of the long-head of the biceps tendon are altered in the presence of rotator cuff tears in a rat model." J Orthop Res **27**(3): 416-20.
- Peretti, G. M., E. M. Caruso, et al. (2001). "Meniscal repair using engineered tissue." J Orthop Res **19**(2): 278-85.
- Peretti, G. M., T. J. Gill, et al. (2004). "Cell-based therapy for meniscal repair: a large animal study." Am J Sports Med **32**(1): 146-58.

- Petersen, W., G. Hohmann, et al. (2004). "Structure of the human tibialis posterior tendon." Arch Orthop Trauma Surg **124**(4): 237-42.
- Petersen, W. and B. Tillmann (1998). "Collagenous fibril texture of the human knee joint menisci." Anat Embryol (Berl) **197**(4): 317-24.
- Petrosini, A. V. and O. H. Sherman (1996). "A historical perspective on meniscal repair." Clin Sports Med **15**(3): 445-53.
- Pham, Q. P., U. Sharma, et al. (2006). "Electrospinning of polymeric nanofibers for tissue engineering applications: a review." Tissue Eng **12**(5): 1197-211.
- Pham, Q. P., U. Sharma, et al. (2006). "Electrospun Poly(epsilon-caprolactone) Microfiber and Multilayer Nanofiber/Microfiber Scaffolds: Characterization of Scaffolds and Measurement of Cellular Infiltration." Biomacromolecules **7**(10): 2796-805.
- Pittenger, M. F., A. M. Mackay, et al. (1999). "Multilineage potential of adult human mesenchymal stem cells." Science **284**: 143-147.
- Pornsopone, V., P. Supaphol, et al. (2005). "Electrospinning of methacrylate-based copolymers: Effects of solution concentration and applied electrical potential on morphological appearance of as-spun fibers." Polymer Engineering and Science **45**(8): 1073-1080.
- Port, J., D. W. Jackson, et al. (1996). "Meniscal repair supplemented with exogenous fibrin clot and autogenous cultured marrow cells in the goat model." Am J Sports Med **24**(4): 547-55.
- Proctor, C. S., M. B. Schmidt, et al. (1989). "Material properties of the normal medial bovine meniscus." J Orthop Res **7**(6): 771-82.
- Putnam, A. J., J. J. Cunningham, et al. (2003). "External mechanical strain regulates membrane targeting of Rho GTPases by controlling microtubule assembly." Am J Physiol Cell Physiol **284**(3): C627-39.
- Rath, E. and J. C. Richmond (2000). "The menisci: basic science and advances in treatment." Br J Sports Med **34**(4): 252-7.
- Rath, E., J. C. Richmond, et al. (2001). "Meniscal allograft transplantation. Two- to eight-year results." Am J Sports Med **29**(4): 410-4.
- Reneker, D. H. and I. Chun (1996). "Nanometre diameter fibres of polymer, produced by electrospinning." Nanotech **7**: 216-223.

- Renstrom, P. and R. J. Johnson (1990). "Anatomy and biomechanics of the menisci." Clin Sports Med **9**(3): 523-38.
- Rho, K. S., L. Jeong, et al. (2006). "Electrospinning of collagen nanofibers: Effects on the behavior of normal human keratinocytes and early-stage wound healing." Biomaterials **27**(8): 1452-61.
- Richards, C. J., C. J. Gatt, et al. (2003). "Quantitative measurement of human meniscal strain." Trans Orthop Res Soc **28**: 649.
- Riesle, J., A. P. Hollander, et al. (1998). "Collagen in tissue-engineered cartilage: types, structure, and crosslinks." J Cell Biochem **71**(3): 313-27.
- Rodeo, S. A. (2000). "Arthroscopic meniscal repair with use of the outside-in technique." Instr Course Lect **49**: 195-206.
- Rodkey, W. G., K. E. DeHaven, et al. (2008). "Comparison of the collagen meniscus implant with partial meniscectomy. A prospective randomized trial." J Bone Joint Surg Am **90**(7): 1413-26.
- Rodkey, W. G., J. R. Steadman, et al. (1999). "A clinical study of collagen meniscus implants to restore the injured meniscus." Clin Orthop Relat Res(367 Suppl): S281-92.
- Roos, H., T. Adalberth, et al. (1995). "Osteoarthritis of the knee after injury to the anterior cruciate ligament or meniscus: the influence of time and age." Osteoarthritis Cartilage **3**(4): 261-7.
- Roos, H., M. Lauren, et al. (1998). "Knee osteoarthritis after meniscectomy: prevalence of radiographic changes after twenty-one years, compared with matched controls." Arthritis Rheum **41**(4): 687-93.
- Salinas, C. N. and K. S. Anseth (2008). "The influence of the RGD peptide motif and its contextual presentation in PEG gels on human mesenchymal stem cell viability." J Tissue Eng Regen Med **2**(5): 296-304.
- Seedhom, B. B. (1976). "Loadbearing function of the menisci." Physiotherapy **62**(7): 223.
- Sell, S. A., M. J. McClure, et al. (2006). "Electrospun polydioxanone-elastin blends: potential for bioresorbable vascular grafts." Biomed Mater **1**(2): 72-80.
- Setton, L. A., F. Guilak, et al. (1999). "Biomechanical factors in tissue engineered meniscal repair." Clin Orthop(367 Suppl): S254-72.
- Sheth, N. P., B. M. Baker, et al. (2006). "Emerging Strategies for Meniscus Repair." University of Pennsylvania Orthopaedic Journal **18**: 59-72.

- Sheth, N. P., B. M. Baker, et al. (2007). "Biologic Integration of Fiber-Aligned Nanofibrous Scaffolds with Native Meniscus." Trans Orthop Res Soc **32**: 711.
- Sheth, N. P., W. J. Li, et al. (2006). "Fixation of anisotropic biodegradable nanofibrous poly-caprolactone scaffolds to bovine meniscus with non-absorbable suture: A strategy for meniscal repair." Trans Orthop Res Soc **31**: 800.
- Shields, K. J., M. J. Beckman, et al. (2004). "Mechanical properties and cellular proliferation of electrospun collagen type II." Tissue Eng **10**(9-10): 1510-7.
- Shin, Y. M., M. M. Hohman, et al. (2001). "Experimental characterization of electrospinning: the electrically forced jet and instabilities." Polymer **42**: 9955-9967.
- Shrive, N. G., J. J. O'Connor, et al. (1978). "Load-bearing in the knee joint." Clin Orthop(131): 279-87.
- Simmons, C. A., S. Matlis, et al. (2003). "Cyclic strain enhances matrix mineralization by adult human mesenchymal stem cells via the extracellular signal-regulated kinase (ERK1/2) signaling pathway." J. Biomech. **36**(8): 1087-96.
- Solchaga, L. A., K. Penick, et al. (2005). "FGF-2 enhances the mitotic and chondrogenic potentials of human adult bone marrow-derived mesenchymal stem cells." J Cell Physiol **203**(2): 398-409.
- Sommerlath, K. and J. Gillquist (1993). "The effects of an artificial meniscus substitute in a knee joint with a resected anterior cruciate ligament. An experimental study in rabbits." Clin Orthop Relat Res(289): 276-84.
- Spencer, A. J. M. (1972). Deformations of Fibre-reinforced Materials. London, Oxford University Press.
- Spindler, K. P., R. R. Miller, et al. (1994). "Comparison of collagen synthesis in the peripheral and central region of the canine meniscus." Clin Orthop Relat Res(303): 256-63.
- Stankus, J. J., J. Guan, et al. (2006). "Microintegrating smooth muscle cells into a biodegradable, elastomeric fiber matrix." Biomaterials **27**(5): 735-44.
- Stegemann, H. and K. Stalder (1967). "Determination of hydroxyproline." Clin Chim Acta **18**(2): 267-73.
- Stella, J. A., J. Liao, et al. (2008). "Tissue-to-cellular level deformation coupling in cell micro-integrated elastomeric scaffolds." Biomaterials **29**(22): 3228-36.

- Stitzel, J., J. Liu, et al. (2006). "Controlled fabrication of a biological vascular substitute." Biomaterials **27**(7): 1088-94.
- Stone, K. R., W. G. Rodkey, et al. (1992). Development of a prosthetic meniscal replacement. Knee meniscus: basic and clinical foundations. V. C. Mow, S. P. Arnoczky and D. W. Jackson. New York, Raven Press, Ltd.: 165-173.
- Sundaray, B., V. Subramanian, et al. (2004). "Electrospinning of continuous aligned polymer fibers." APPLIED PHYSICS LETTERS **84**(7): 1222-1224.
- Sweigart, M. A. and K. A. Athanasiou (2001). "Toward tissue engineering of the knee meniscus." Tissue Eng **7**(2): 111-29.
- Sweigart, M. A., C. F. Zhu, et al. (2004). "Intraspecies and interspecies comparison of the compressive properties of the medial meniscus." Ann Biomed Eng **32**(11): 1569-79.
- Tallheden, T., C. Bengtsson, et al. (2005). "Proliferation and differentiation potential of chondrocytes from osteoarthritic patients." Arthritis Res Ther **7**(3): R560-8.
- Tan, A. R., J. L. Ifkovits, et al. (2008). "Electrospinning of photocrosslinked and degradable fibrous scaffolds." J Biomed Mater Res A **87**(4): 1034-43.
- Tan, G. K., D. L. Dinnes, et al. "Interactions between meniscal cells and a self assembled biomimetic surface composed of hyaluronic acid, chitosan and meniscal extracellular matrix molecules." Biomaterials.
- Tanaka, T., K. Fujii, et al. (1999). "Comparison of biochemical characteristics of cultured fibrochondrocytes isolated from the inner and outer regions of human meniscus." Knee Surg Sports Traumatol Arthrosc **7**(2): 75-80.
- Telemeco, T. A., C. Ayres, et al. (2005). "Regulation of cellular infiltration into tissue engineering scaffolds composed of submicron diameter fibrils produced by electrospinning." Acta Biomater **1**(4): 377-85.
- Teo, W. E. and S. Ramakrishna (2006). "A review on electrospinning design and nanofibre assemblies." Nanotechnology **17**(14): R89-R106.
- Theron, A., E. Zussman, et al. (2001). "Electrostatic field-assisted alignment of electrospun nanofibres." Nanotechnology **12**(3): 384-390.
- Theron, S. A., A. L. Yarin, et al. (2005). "Multiple jets in electrospinning: experiment and modeling." Polymer **46**(9): 2889-2899.
- Thomas, C. H., J. H. Collier, et al. (2002). "Engineering gene expression and protein synthesis by modulation of nuclear shape." Proc Natl Acad Sci U S A **99**(4): 1972-7.

- Thomopoulos, S., G. M. Fomovsky, et al. (2005). "The development of structural and mechanical anisotropy in fibroblast populated collagen gels." J Biomech Eng **127**(5): 742-50.
- Thomopoulos, S., G. R. Williams, et al. (2003). "Variation of biomechanical, structural, and compositional properties along the tendon to bone insertion site." J Orthop Res **21**: 413-19.
- Tienen, T. G., R. G. Heijkants, et al. (2006). "Replacement of the knee meniscus by a porous polymer implant: a study in dogs." Am J Sports Med **34**(1): 64-71.
- Tissakht, M. and A. M. Ahmed (1995). "Tensile stress-strain characteristics of the human meniscal material." J Biomech **28**(4): 411-22.
- Tran-Khanh, N., C. D. Hoemann, et al. (2005). "Aged bovine chondrocytes display a diminished capacity to produce a collagen-rich, mechanically functional cartilage extracellular matrix." J Orthop Res **23**(6): 1354-62.
- Trickey, W. R., T. P. Vail, et al. (2004). "The role of the cytoskeleton in the viscoelastic properties of human articular chondrocytes." J Orthop Res **22**(1): 131-9.
- Tsutsumi, S., A. Shimazu, et al. (2001). "Retention of multilineage differentiation potential of mesenchymal cells during proliferation in response to FGF." Biochem Biophys Res Commun **288**(2): 413-9.
- Tumia, N. S. and A. J. Johnstone (2004). "Promoting the proliferative and synthetic activity of knee meniscal fibrochondrocytes using basic fibroblast growth factor in vitro." Am J Sports Med **32**(4): 915-20.
- Upton, M. L., J. Chen, et al. (2006). "Region-specific constitutive gene expression in the adult porcine meniscus." J Orthop Res **24**(7): 1562-70.
- Upton, M. L., C. L. Gilchrist, et al. (2008). "Transfer of macroscale tissue strain to microscale cell regions in the deformed meniscus." Biophys J **95**(4): 2116-24.
- Upton, M. L., A. Hennerbichler, et al. (2006). "Biaxial strain effects on cells from the inner and outer regions of the meniscus." Connect Tissue Res **47**(4): 207-14.
- Vailas, A. C., R. F. Zernicke, et al. (1986). "Adaptation of rat knee meniscus to prolonged exercise." J Appl Physiol **60**(3): 1031-4.
- Valiyaveetil, M., J. S. Mort, et al. (2005). "The concentration, gene expression, and spatial distribution of aggrecan in canine articular cartilage, meniscus, and anterior and posterior cruciate ligaments: a new molecular distinction between hyaline cartilage and fibrocartilage in the knee joint." Connect Tissue Res **46**(2): 83-91.

van Tienen, T. G., R. G. Heijkants, et al. (2002). "Tissue ingrowth and degradation of two biodegradable porous polymers with different porosities and pore sizes." Biomaterials **23**(8): 1731-8.

Vanderploeg, E. J., S. M. Imler, et al. (2004). "Oscillatory tension differentially modulates matrix metabolism and cytoskeletal organization in chondrocytes and fibrochondrocytes." J Biomech **37**(12): 1941-52.

Venkatachalam, S., S. P. Godsiff, et al. (2001). "Review of the clinical results of arthroscopic meniscal repair." Knee **8**(2): 129-33.

Venugopal, J., L. L. Ma, et al. (2005). "In vitro study of smooth muscle cells on polycaprolactone and collagen nanofibrous matrices." Cell Biol Int **29**(10): 861-7.

Verdonk, P. C., R. G. Forsyth, et al. (2005). "Characterisation of human knee meniscus cell phenotype." Osteoarthritis Cartilage **13**(7): 548-60.

Veth, R. P., H. W. Jansen, et al. (1986). "Experimental meniscal lesions reconstructed with a carbon fiber-polyurethane-poly(L-lactide) graft." Clin Orthop Relat Res(202): 286-93.

von Lewinski, G., D. Kohn, et al. (2008). "The influence of nonanatomical insertion and incongruence of meniscal transplants on the articular cartilage in an ovine model." Am J Sports Med **36**(5): 841-50.

Wagner, W., P. Horn, et al. (2008). "Replicative senescence of mesenchymal stem cells: a continuous and organized process." PLoS One **3**(5): e2213.

Walker, P. S. and M. J. Erkman (1975). "The role of the menisci in force transmission across the knee." Clin Orthop Relat Res(109): 184-92.

Walsh, C. J., D. Goodman, et al. (1999). "Meniscus regeneration in a rabbit partial meniscectomy model." Tissue Eng **5**(4): 327-37.

Wang, J. H. and E. S. Grood (2000). "The strain magnitude and contact guidance determine orientation response of fibroblasts to cyclic substrate strains." Connect Tissue Res **41**(1): 29-36.

Wang, J. H., F. Jia, et al. (2003). "Cell orientation determines the alignment of cell-produced collagenous matrix." J Biomech **36**(1): 97-102.

Wang, N., J. P. Butler, et al. (1993). "Mechanotransduction across the cell surface and through the cytoskeleton." Science **260**: 1124-1127.

Wang, N., J. D. Tytell, et al. (2009). "Mechanotransduction at a distance: mechanically coupling the extracellular matrix with the nucleus." Nat Rev Mol Cell Biol **10**(1): 75-82.

- Webber, R. J., M. G. Harris, et al. (1985). "Cell culture of rabbit meniscal fibrochondrocytes: proliferative and synthetic response to growth factors and ascorbate." J Orthop Res **3**(1): 36-42.
- Wheeler, B. C., J. M. Corey, et al. (1999). "Microcontact printing for precise control of nerve cell growth in culture." J Biomech Eng **121**(1): 73-8.
- Woerdeman, D. L., P. Ye, et al. (2005). "Electrospun fibers from wheat protein: investigation of the interplay between molecular structure and the fluid dynamics of the electrospinning process." Biomacromolecules **6**(2): 707-12.
- Wyland, D. J., F. Guilak, et al. (2002). "Chondropathy after meniscal tear or partial meniscectomy in a canine model." J Orthop Res **20**(5): 996-1002.
- Xu, C., R. Inai, et al. (2004). "Electrospun nanofiber fabrication as synthetic extracellular matrix and its potential for vascular tissue engineering." Tissue Eng **10**(7-8): 1160-8.
- Yamasaki, T., M. Deie, et al. (2008). "Transplantation of meniscus regenerated by tissue engineering with a scaffold derived from a rat meniscus and mesenchymal stromal cells derived from rat bone marrow." Artif Organs **32**(7): 519-24.
- Yang, F., R. Murugan, et al. (2005). "Electrospinning of nano/micro scale poly(L-lactic acid) aligned fibers and their potential in neural tissue engineering." Biomaterials **26**(15): 2603-10.
- Yang, F., C. Y. Xu, et al. (2004). "Characterization of neural stem cells on electrospun poly(L-lactic acid) nanofibrous scaffold." J Biomater Sci Polym Ed **15**(12): 1483-97.
- Yarin, A. L. and E. Zussman (2004). "Upward needleless electrospinning of multiple nanofibers." Polymer **45**(9): 2977-2980.
- Yim, E. K., E. M. Darling, et al. "Nanotopography-induced changes in focal adhesions, cytoskeletal organization, and mechanical properties of human mesenchymal stem cells." Biomaterials **31**(6): 1299-306.
- Yoshimoto, H., Y. M. Shin, et al. (2003). "A biodegradable nanofiber scaffold by electrospinning and its potential for bone tissue engineering." Biomaterials **24**(12): 2077-82.
- Zaffagnini, S., G. Giordano, et al. (2007). "Arthroscopic collagen meniscus implant results at 6 to 8 years follow up." Knee Surg Sports Traumatol Arthrosc **15**(2): 175-83.
- Zhang, Y., J. R. Venugopal, et al. (2008). "Electrospun biomimetic nanocomposite nanofibers of hydroxyapatite/chitosan for bone tissue engineering." Biomaterials **29**(32): 4314-22.

Zhang, Z., J. Messana, et al. (2006). "Reorganization of actin filaments enhances chondrogenic differentiation of cells derived from murine embryonic stem cells." Biochem Biophys Res Commun **348**(2): 421-7.